

DISS. ETH NO. 29638

# **Nature and catalytic activity of Lewis acid extra-framework species in zeolites**

A thesis submitted to attain the degree of  
DOCTOR OF SCIENCES of ETH ZURICH  
(Dr. Sc. ETH Zurich)

presented by

**Syeda Rabia Batool**

M.Phil. in Chemistry

Bahauddin Zakariya University, Pakistan

born on 15.01.1994

accepted on the recommendation of

Prof. Dr. Jeroen A. van Bokhoven

Prof. Dr. Prof. Dr. Ralph Spolenak

Dr. Vitaly Sushkevich

2023



If they give you ruled paper, write the other way.

*Juan Ramón Jiménez*

It is impossible to convey completely the excitement of discovery, of seeing the result of an experiment and knowing that you know something new, something fundamental and that for this moment at least, only you, in the entire world, know it.

*Stuart Firestein*





# Table of Contents

Abstract.....	i
Zusammenfassung .....	iv
Acronyms and Abbreviations .....	viii
<b>1. Introduction.....</b>	<b>10</b>
<b>2. Scope of the thesis .....</b>	<b>30</b>
<b>3. Materials and Methods.....</b>	<b>33</b>
<b>4. Correlating Lewis acid activity to extra-framework aluminum species in zeolite Y introduced by ion-exchange.....</b>	<b>45</b>
<b>5. Role of Si/Al ratio, co-cation and experimental conditions on the generation of extra- framework aluminum Lewis acid sites .....</b>	<b>66</b>
<b>6. Factors affecting the generation and catalytic activity of extra-framework aluminum Lewis acid sites in aluminum-exchanged zeolites.....</b>	<b>92</b>
<b>7. Butane dehydrogenation over aluminum-exchanged Lewis acidic zeolites.....</b>	<b>112</b>
<b>8. Distribution of aluminum Lewis acid sites during alumination and dealumination- realumination of BEA.....</b>	<b>134</b>
<b>9. Revisiting the “Very High Frequency” hydroxyls in zeolites .....</b>	<b>154</b>
<b>10. Conclusions and Outlook.....</b>	<b>170</b>
References .....	178
Publications and presentations.....	194
Appendix to Chapter 4.....	196
Appendix to Chapter 5.....	200
Appendix to Chapter 6.....	205
Appendix to Chapter 7.....	210
Appendix to Chapter 8.....	215
Appendix to Chapter 9 .....	219

## Abstract

Zeolites are aluminosilicate materials possessing well-defined pore sizes, hydrothermal stability, and structural tunability. Due to the combination of unique characteristics, they hold a central place in heterogeneous catalysis and continue to find an impressive number of potential applications. The role of zeolites as acid catalysts originates from the co-presence of Lewis acid sites (LAS) and Brønsted acid sites (BAS). The structure of BAS is well defined as the hydroxyls bridging the framework of silicon and aluminum. In contrast, LAS is less defined owing to the multiplicity of their structure and origin. Understanding the nature, origin, and activity of acid sites is crucial in tuning the structure of zeolites for end applications. The Lewis acidity of zeolites remains an extensive area of research and application. In comparison, the Lewis acidity of aluminum in zeolites is ambiguous and demands thorough investigation. In particular, many essential questions about the nature and the quantitative structure-performance relations of extra-framework aluminum (EFAI) motifs must be carefully addressed.

The present work, thus, explores the Lewis acidity of aluminum in zeolites while emphasizing the dedicated design of EFAI LAS and understanding their structure, acidity, and catalytic performance. Chapters 1 and 2 discuss the existent literature about the structure and applications of Lewis acidic zeolites, different ways of incorporating Lewis acidity, and open questions related to the Lewis acidity of EFAI species. Chapter 3 explains the required characterization techniques and synthesis protocols employed in the present work. These chapters determine the scope of the thesis.

The ultra-stable zeolite Y (USY), prepared by post-synthetic steaming, shows much higher hydrothermal stability and catalytic activity than non-steamed Y. In Chapter 4, Lewis acidity was introduced into zeolite Y by facile ion-exchange of aluminum cations. FTIR and NMR spectroscopies were employed to evaluate the Lewis acidity and coordination of introduced aluminum. A quantitative agreement was observed between the concentration of these introduced EFAI species with the total Lewis acid content from pyridine-FTIR and with the catalytic activity in Meerwein–Ponndorf–Verley (MPV) reduction of 4-*tert* butyl cyclohexanone. This illustrates that the newly introduced aluminum LAS adopt octahedral coordination under the conditions of NMR measurement and are responsible for enhanced Lewis acid catalytic activity of the aluminum exchanged zeolites. The preservation of Brønsted

acid sites after treatments further endorses the charge neutrality of these extra-framework aluminum complexes.

The efficiency of the aluminum-exchange route to introduce the EFAI LAS while retaining the zeolite's framework and inherent porous characteristics depends on many factors. The work presented in Chapter 5 explores the generation of aluminum-exchanged EFAI LAS in zeolite Y employing different Si/Al ratios and cationic forms of parent zeolite and different aluminum-exchange conditions. A constant stirring of the zeolite in an aluminum-exchange solution and higher Si/Al ratios of parent zeolite favor the maximum incorporation of catalytically active EFAI LAS, followed by maximum zeolite structure retention. The presence of sodium co-cation not only hampers the incorporation of acid sites but also negatively affects the crystallinity and pore structure. The catalytic performance depends equally on the number of EFAI LAS and the retention of the inherent framework of zeolite.

These fundamental insights about the rational design of EFAI LAS were employed in Chapter 6 to introduce Lewis acidity into zeolites of different morphologies. This work aimed to evaluate the factors affecting the generation and activity EFAI LAS in zeolites. The increase in EFAI LAS in BEA and Y was appreciable, whereas MOR and MFI showed minimal uptake of aluminum. This quantitatively follows the catalytic activity for MPV reduction of 4-*tert* butyl cyclohexanone. The incorporation of EFAI LAS and their catalytic activity depend on the zeolite framework type, pore size, and aluminum location within the framework. Likewise, the selectivity towards *cis* and *trans* 4-*tert* butyl cyclohexanols was affected by the zeolite's pore size and framework type and not by the number or structure of LAS. Irrespective of zeolite morphology, aluminum-exchange incorporates neutral LAS.

The MPV reduction of ketones occurs under mild conditions as it uses secondary alcohols for the hydride transfer reaction; thus, it can also be catalyzed by weak and medium-strength LAS (Chapters 4-6). Therefore, Chapter 7 explores the strength and hydrothermal stability of aluminum-exchanged EFAI LAS in activating the C-H bond during n-butane dehydrogenation. Aluminum-exchange significantly increases the conversion of n-butane with enhanced selectivity to dehydrogenation products. No significant change in selectivity by lowering the BAS content of aluminum-exchanged samples by Na-IE proposes that dehydrogenation occurs on EFAI LAS. The preservation of structure and Lewis acidity of EFAI species in the regenerated catalysts confirms that the thermal stability and strength of neutral EFAI LAS, produced by Al-IE, are capable of cleaving the C-H bonds of alkanes.

Zeolite BEA is an efficient catalyst for MPV reaction, and the aluminum species partly connected to the framework (FA-Al) (and not the EFAl) are usually reported as active sites. The aluminum-exchange produces EFAl LAS without affecting the content of FA-Al. In Chapter 6, an increase in EFAl LAS in BEA follows an increase in MPV activity. Therefore, Chapter 8 explores the distribution of aluminum LAS and the associated activity of BEA after alumination (by aluminum-exchange), dealumination (by acid treatment), and realumination by aluminum-exchange). The aluminated and dealuminated-realuminated BEA significantly increase the activity during MPV reduction. The correlations of catalytic activity with the total content of LAS from pyridine- and CO-FTIR and the content of EFAl and FA-Al species from  $^{27}\text{Al}$  NMR suggest that both EFAl and FA-Al can serve as MPV active sites. The Lewis acidity and catalytic activity of parent BEA are mainly due to FA-Al species. In contrast, the alumination and realumination by aluminum-exchange increase the catalytic activity and the number of LAS due to the introduction of EFAl. The EF-Al were systematically distinguished from EFAl by characterizing the zeolites under different cations forms.

The insights about the structure of the MPV active site were employed to revisit the so-called ‘very high frequency’ (VHF) hydroxyls at  $\sim 3780\text{ cm}^{-1}$  of zeolites and the structure of aluminum species attached (Chapter 9). The literature describes These hydroxyls in many ways, but the exact assignment is unclear. In BEA, these hydroxyls are considered highly acidic as they are proposed to be connected to the MPV active site. Therefore, this chapter aims to systematically explore the evolution of VHF in hydroxyl and base stretching regions under different conditions. The FTIR spectroscopy of adsorbed carbon monoxide and pyridine on dehydrated zeolites, in combination with  $^{27}\text{Al}$ - $^1\text{H}$  HETCOR NMR spectroscopy on evacuated zeolites, describes that the VHF-OH band correlates neither to the strongly acidic FA-Al species nor to the EFAl species generated by aluminum-exchange.

In conclusion, this work provides significant insights into the rational design of EFAl LAS in zeolites without Brønsted acidity of zeolite. Evaluating the factors affecting the generation of aluminum-exchanged LAS guides the pathways towards maximizing the Lewis acidity yet preserving the intrinsic properties of zeolite. A combination of different spectroscopic techniques, catalytic evaluation, and diverse treatment conditions can be used to quantitatively discern the different Lewis acidic aluminum species and address the open questions related to the Lewis acidity of extra-framework aluminum in zeolites.

## Zusammenfassung

Zeolithe sind Aluminosilikatmaterialien mit genau definierten Porengrößen, hydrothermischer Stabilität und struktureller Einstellbarkeit. Aufgrund der Kombination einzigartiger Eigenschaften nehmen sie eine zentrale Stellung in der heterogenen Katalyse ein und finden weiterhin eine beeindruckende Anzahl potenzieller Anwendungen. Die Rolle von Zeolithen als Säurekatalysatoren beruht auf der gleichzeitigen Anwesenheit von Lewis-Säure-Zentren (LAS) und Brønsted-Säure-Zentren (BAS). Die Struktur von BAS ist gut definiert als die Hydroxylgruppen, die das Gerüst aus Silizium und Aluminium überbrücken. Im Gegensatz dazu sind LAS aufgrund der Vielfalt ihrer Struktur und Herkunft weniger definiert. Das Verständnis der Natur, Herkunft und Aktivität saurer Zentren ist entscheidend für die Abstimmung der Struktur von Zeolithen für Endanwendungen. Die Lewis-Acidität von Zeolithen bleibt ein umfangreiches Forschungs- und Anwendungsgebiet. Im Vergleich dazu ist die Lewis-Acidität von Aluminium in Zeolithen nicht eindeutig und erfordert eine gründliche Untersuchung. Insbesondere müssen viele wesentliche Fragen zur Natur und den quantitativen Struktur-Leistungs-Beziehungen von Extra-Framework-Aluminium-Motiven (EFAl) sorgfältig beantwortet werden.

Die vorliegende Arbeit untersucht daher die Lewis-Acidität von Aluminium in Zeolithen und betont gleichzeitig das spezielle Design von EFAl LAS sowie das Verständnis ihrer Struktur, Acidität und katalytischen Leistung. In den Kapiteln 1 und 2 wird die vorhandene Literatur über die Struktur und Anwendungen von Lewis-sauren Zeolithen, verschiedene Möglichkeiten zur Einbeziehung der Lewis-Acidität und offene Fragen im Zusammenhang mit der Lewis-Acidität von EFAl-Spezies besprochen. Kapitel 3 erläutern die erforderlichen Charakterisierungstechniken und Syntheseprotokolle, die in der vorliegenden Arbeit verwendet werden. Diese Kapitel bestimmen den Umfang der Arbeit.

Der ultrastabile Zeolith Y (USY), der durch postsynthetisches Dämpfen hergestellt wurde, zeigt eine viel höhere hydrothermale Stabilität und katalytische Aktivität als nicht gedämpftes Y. In Kapitel 4 wurde die Lewis-Acidität durch einfachen Ionenaustausch von Aluminiumkationen in Zeolith Y eingeführt. FTIR- und NMR-Spektroskopien wurden eingesetzt, um die Lewis-Acidität und Koordination des eingeführten Aluminiums zu bewerten. Es wurde eine quantitative Übereinstimmung zwischen der Konzentration dieser eingeführten EFAl-Spezies und dem gesamten Lewis-Säure-Gehalt aus Pyridin-FTIR und mit der katalytischen Aktivität bei der Meerwein-Ponndorf-Verley (MPV) -Reduktion von 4-*tert*-Butylcyclohexanon

beobachtet. Dies zeigt, dass die neu eingeführten Aluminium-LAS unter den Bedingungen der NMR-Messung eine oktaedrische Koordination annehmen und für eine erhöhte Lewis-Säurekatalytische Aktivität der mit Aluminium ausgetauschten Zeolithe verantwortlich sind. Die Erhaltung der Brønsted-Säure-Zentren nach der Behandlung bestätigt zusätzlich die Ladungsneutralität dieser Aluminiumkomplexe außerhalb des Gerüsts.

Die Effizienz des Aluminiumaustauschweges zur Einführung des EFAl-LAS unter Beibehaltung des Gerüsts und der inhärenten porösen Eigenschaften des Zeoliths hängt von vielen Faktoren ab. Die in Kapitel 5 vorgestellte Arbeit untersucht die Erzeugung von mit Aluminium ausgetauschtem EFAl LAS in Zeolith Y unter Verwendung verschiedener Si/Al-Verhältnisse und kationischer Formen des Ausgangszeoliths sowie verschiedener Aluminiumaustauschbedingungen. Ein ständiges Rühren des Zeoliths in einer Aluminiumaustauschlösung und höhere Si/Al-Verhältnisse des Ausgangszeoliths begünstigen die maximale Einbindung von katalytisch aktivem EFAl LAS, gefolgt von einer maximalen Beibehaltung der Zeolithstruktur. Das Vorhandensein von Natrium-Co-Kationen erschwert nicht nur den Einbau von Säurezentren, sondern wirkt sich auch negativ auf die Kristallinität und Porenstruktur aus. Die katalytische Leistung hängt gleichermaßen von der Anzahl der EFAl-LAS und der Beibehaltung des inhärenten Gerüsts des Zeoliths ab.

Lewis-Acidität in Zeolithe unterschiedlicher Morphologie einzuführen. Ziel dieser Arbeit war es, die Faktoren zu bewerten, die die Erzeugung und Aktivität von EFAl LAS in Zeolithen beeinflussen. Der Anstieg von EFAl LAS in BEA und Y war deutlich, wohingegen MOR und MFI eine minimale Aluminiumaufnahme zeigten. Dies folgt quantitativ der katalytischen Aktivität für die MPV-Reduktion von 4-*tert.*-Butylcyclohexanon. Der Einbau von EFAl LAS und ihre katalytische Aktivität hängen vom Typ des Zeolithgerüsts, der Porengröße und der Position des Aluminiums innerhalb des Gerüsts ab. Ebenso wurde die Selektivität gegenüber *cis*- und *trans*-4-*tert*-Butylcyclohexanolen durch die Porengröße und den Gerüsttyp des Zeoliths und nicht durch die Anzahl oder Struktur von LAS beeinflusst. Unabhängig von der Zeolithmorphologie wird beim Aluminiumaustausch neutrales LAS eingebaut.

Die MPV-Reduktion von Ketonen erfolgt unter milden Bedingungen, da sekundäre Alkohole für die Hydridtransferreaktion verwendet werden; daher kann es auch durch schwache und mittelstarke LAS katalysiert werden (Kapitel 4-6). Daher untersucht Kapitel 7 die Stärke und hydrothermale Stabilität von mit Aluminium ausgetauschtem EFAl LAS bei der Aktivierung der CH-Bindung während der n-Butan-Dehydrierung. Durch den Aluminiumaustausch wird die

Umwandlung von n-Butan deutlich erhöht und die Selektivität gegenüber Dehydrierungsprodukten erhöht. Keine signifikante Änderung der Selektivität durch Senkung des BAS-Gehalts von mit Aluminium ausgetauschten Proben durch Na-IE lässt darauf schließen, dass eine Dehydrierung auf EFAl-LAS stattfindet. Die Erhaltung der Struktur und der Lewis-Acidität der EFAl-Spezies in den regenerierten Katalysatoren bestätigt, dass die thermische Stabilität und Festigkeit des neutralen EFAl-LAS, hergestellt durch Al-IE, in der Lage ist, die CH-Bindungen von Alkanen zu spalten.

Zeolith BEA ist ein effizienter Katalysator für die MPV-Reaktion, und die teilweise mit dem Gerüst verbundenen Aluminiumspezies (FA-Al) (und nicht das EFAl) werden normalerweise als aktive Zentren angegeben. Der Aluminiumaustausch erzeugt EFAl LAS, ohne den Gehalt an FA-Al zu beeinflussen. In Kapitel 6 folgt ein Anstieg von EFAl LAS in BEA einem Anstieg der MPV-Aktivität. Daher untersucht Kapitel 8 die Verteilung von Aluminium-LAS und die damit verbundene Aktivität von BEA nach Aluminierung (durch Aluminiumaustausch), Dealuminierung (durch Säurebehandlung) und Realuminierung durch Aluminiumaustausch. Das aluminierete und dealuminierte-realuminierte BEA erhöht die Aktivität während der MPV-Reduktion deutlich. Die Korrelationen der katalytischen Aktivität mit dem Gesamtgehalt an LAS aus Pyridin- und CO-FTIR und dem Gehalt an EFAl- und FA-Al-Spezies aus dem <sup>27</sup>Al-NMR legen nahe, dass sowohl EFAl als auch FA-Al als aktive MPV-Zentren dienen können. Die Lewis-Acidität und die katalytische Aktivität des Ausgangs-BEA sind hauptsächlich auf FA-Al-Spezies zurückzuführen. Im Gegensatz dazu erhöhen die Aluminierung und Realuminierung durch Aluminiumaustausch die katalytische Aktivität und die Anzahl der LAS aufgrund der Einführung von EFAl. Die EF-Al wurden systematisch von EFAl unterschieden, indem die Zeolithe unter verschiedenen Kationenformen charakterisiert wurden.

Die Erkenntnisse über die Struktur des aktiven Zentrums von MPV wurden genutzt, um die sogenannten „Very High Frequency“ (VHF)-Hydroxylgruppen bei ~3780 cm<sup>-1</sup> von Zeolithen und die Struktur der gebundenen Aluminiumspezies erneut zu untersuchen (Kapitel 9). In der Literatur werden diese Hydroxyle auf vielfältige Weise beschrieben, die genaue Zuordnung ist jedoch unklar. In BEA gelten diese Hydroxylgruppen als stark sauer, da angenommen wird, dass sie mit dem aktiven Zentrum von MPV verbunden sind. Daher zielt dieses Kapitel darauf ab, die Entwicklung von VHF in Hydroxyl- und Basenstreckungsregionen unter verschiedenen Bedingungen systematisch zu untersuchen. Die FTIR-Spektroskopie von adsorbiertem Kohlenmonoxid und Pyridin auf dehydrierten Zeolithen in Kombination mit <sup>27</sup>Al-<sup>1</sup>H HETCOR-NMR-Spektroskopie auf evakuierten Zeolithen beschreibt, dass die VHF-OH-Bande

weder mit der stark sauren FA-Al-Spezies noch mit der EFAl-Spezies korreliert erzeugt durch Aluminium-Austausch.

Zusammenfassend liefert diese Arbeit wichtige Einblicke in das rationale Design von EFAl LAS in Zeolithen ohne Brønsted-Acidität von Zeolithen. Die Bewertung der Faktoren, die die Erzeugung von Aluminium-ausgetauschtem LAS beeinflussen, weist den Weg zur Maximierung des Lewis-Aciditätsgrads bei gleichzeitiger Wahrung der intrinsischen Eigenschaften von Zeolithen. Eine Kombination verschiedener spektroskopischer Techniken, katalytischer Auswertung und verschiedener Behandlungsbedingungen kann verwendet werden, um die verschiedenen Lewis-sauren Aluminiumspezies quantitativ zu unterscheiden und die offenen Fragen im Zusammenhang mit der Lewis-Azidität von Aluminium außerhalb des Gerüsts in Zeolithen zu beantworten.



## Acronyms and Abbreviations

Al-IE	Aluminum ion-exchange
BAS	Brønsted acid sites
BET	Brunner-Emmett-Teller
BVO	Baeyer–Villiger oxidation
CO	Carbon monoxide
EF LAS	Extra-framework Lewis acid sites
EFAI	Extra-framework Aluminum
FA-Al	Framework-associated Aluminum
F-Al	Framework Aluminum
FCC	Fluid Catalytic Cracking
FTIR	Fourier-transform infrared spectroscopy
HETCOR	Heteronuclear Correlation
ICP	Inductively Coupled Plasma
IUPAC	International Union of Pure and Applied Chemistry
LAS	Lewis Acid Sites
MAS	Magic Angle Spinning
OES	Optical Emission Spectroscopy
MPV	Meerwein–Ponndorf–Verley reduction
MQ	Multiple Quantum
NMR	Nuclear Magnetic Resonance
Py	Pyridine
TPD	Temperature programmed Desorption
USY	Ultra Stable Y

VHF	Very High Frequency
XRD	X-ray Diffraction
XPS	X-ray photoelectron
XAS	X-ray absorption spectroscopy

# Chapter 1

## Introduction

### 1.1. Zeolites

Zeolites represent a broad range of crystalline aluminosilicate materials of natural or synthetic origin and belong to tectosilicate-type minerals <sup>1</sup>. Due to their three-dimensional (3D) framework structures, they form well-defined pores of molecular dimensions. They exhibit unique physical and chemical properties, including large micropore volume, thermal stability, compositional tunability, and commercial availability. These features put zeolite materials in the hotspot of many applications in different domains, predominantly catalysis reactions <sup>2, 3</sup>, ion-exchange <sup>4</sup>, gas adsorption <sup>5</sup>, and separation <sup>6-9</sup>.

#### 1.1.1. Structure and Composition

The skeleton of aluminosilicate zeolite comprises  $TO_4$  tetrahedra as the primary building blocks, where T are usually Al or Si atoms <sup>10, 11</sup>. The silicon and aluminum tetrahedra are interconnected through the bridged oxygen atoms to form secondary and more complex structures with uniform channels and cages (**Figure 1.1**). While silicon tetrahedra are neutral, the presence of tetrahedrally coordinated aluminum creates a negative charge in the zeolite framework. The negative charge is balanced by extra-framework cations located in the cavities or channels <sup>12</sup>.

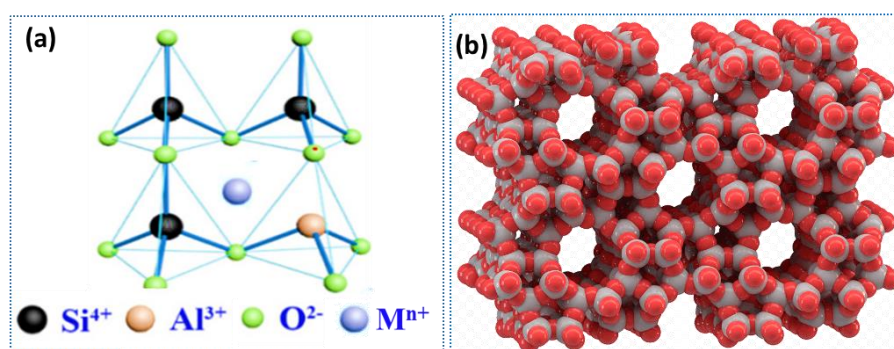


Figure 1.1: (a) Structural representation of corner-sharing silicon and aluminum tetrahedra in aluminosilicate zeolites<sup>13</sup>. (b) 3D structure of zeolite ZSM5 representing well-defined channels and cages.

If the cation compensating for the negative charge of the framework is a proton located on the oxygen bridge between the silicon and oxygen atoms (Si - O - Al), an Brønsted acid site (BAS) is formed <sup>14,15</sup>. If the negative charge is compensated by another inorganic cation or a structural defect has occurred, a Lewis acid center (LAS) is formed (**Figure 1.2**). The empirical formula of an aluminosilicate zeolite is represented by  $M_{2/n}O \cdot Al_2O_3 \cdot xSiO_2 \cdot yH_2O$ , where 'M' is a cation with an 'n' positive charge (i.e.,  $H^+$ ,  $K^+$ ,  $Mg^{2+}$ ,  $Na^+$ ) or a proton. As Al-O-Al bonds are not allowed in aluminosilicates according to Lowenstein's rule, the value of 'x' is typically limited to  $0 \leq x \leq 0.5$  <sup>16</sup>. The aluminosilicate zeolites are classified as low-, medium- and high-silica zeolites, having Si/Al ratios < 2, between 2-5, and > 5, respectively. As the T atoms can differ from Si and Al, many compositional variants of zeolites also exist with structures analogous to or different from aluminosilicate zeolites <sup>17,18</sup>.

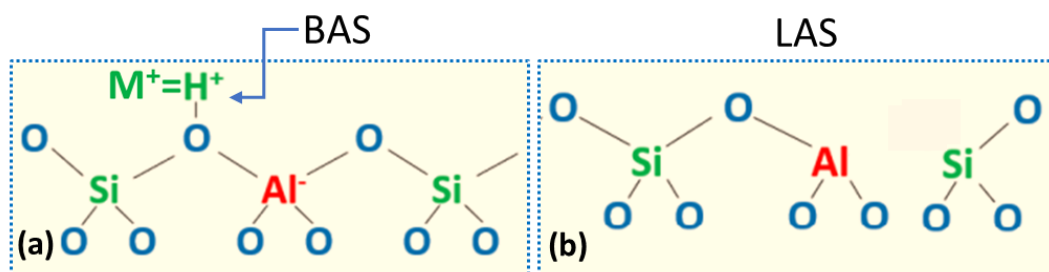


Figure 1.2: Structural representation of the generation of typical (a) Brønsted acid sites (BAS) and (b) Lewis acid sites (LAS) in zeolites. The structure of LAS is debated.

### 1.1.2. Pore structure of zeolites

The fundamental property of zeolites that makes them applicable as catalysts, adsorbents, and ion exchangers is their structural porosity <sup>19</sup>. The pores of zeolite are the void spaces inside the framework, not occupied by framework atoms. With their pore dimensions typically below 2 nm, zeolites are microporous materials, according to the classification of porous materials by the International Union of Pure and Applied Chemistry (IUPAC) <sup>20,21</sup>.

Table 1.1: Classification of zeolites according to their pore size <sup>22</sup>.

Pore Size	Structure type	Cage Size (Å)	Example
Small	8-MR	4	SSZ-13
Medium	10-MR	5.5	ZSM5
Large	12-MR	7.5	FAU
Extra-large	>12-MR	>7.5	NUD-1

The accessibility of zeolite pores to different molecular motifs differs based on their size, connectivity, topology, and geometry. The pores with window sizes smaller or equal to 6-membered rings (6R) are called cages, whereas the cavities are the polyhedral units with a maximum window aperture larger than 6R. Channels are the pores that extend indefinitely in one direction and allow the diffusion of guest motifs. Each zeolite type has a unique yet precisely defined microporous structure with pores of one or more dimensions. Based on the minimum window size of the largest pores in their system, zeolites are classified as small-pore, medium pore large pore and extra-large-pore zeolites, as presented in **Table 1.1**. Within these groups are many zeolite structures with different pore sizes and shapes. Typical examples of zeolites belonging to these classes are presented in **Figure 1.3**.

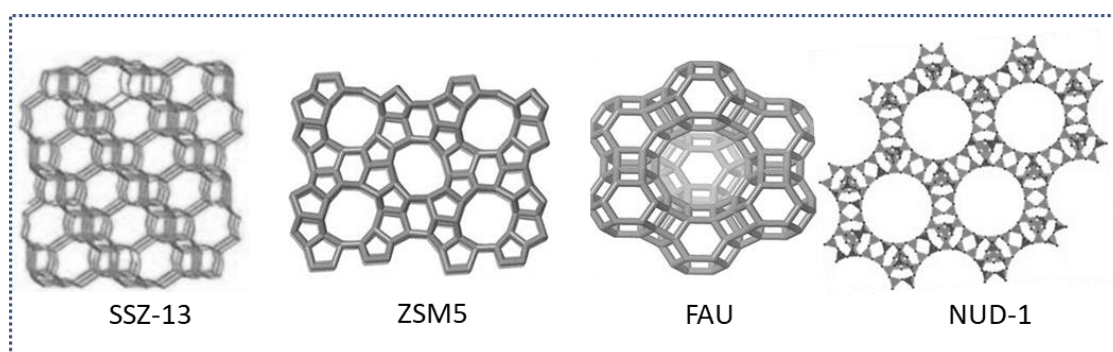


Figure 1.3: Representation of typical examples of small, medium large, and extra-large pore zeolites listed in Table 1.1.

### 1.1.3. Zeolites in catalysis

Zeolites are an essential class of heterogeneous catalysts because of their intrinsic characteristics, such as catalytic activity, hydrothermal and thermal stability, large micropore volume, and the structural pores' suitability and/or tunability for catalytic reactions. Their catalytic activity originates from the crystalline aluminosilicate structure, which yields Brønsted acid sites (BAS), and defects may give rise to Lewis acid sites (LAS)<sup>23, 24</sup>. The combination of unique chemical features and catalytic flexibility makes zeolites the backbone of the catalytic industry, especially in oil refining, petrochemistry, and processes at their interface. The replacement of conventional catalysts in many processes by zeolites is due to improvements that these materials introduce in the catalytic activity and selectivity<sup>19, 25, 26</sup>. Zeolites with BEA, MFI, FAU, and MOR topologies are the ones that have found more application niches. **Figure 1.4** gives an overview of some important catalytic processes employing zeolites.

Zeolites were used as industrial catalysts for the first time in the 1950s when zeolite X was established to outperform the available amorphous silica-alumina catalysts in the cracking of hydrocarbons. Soon after that, zeolites emerged as the benchmark catalysts in oil refineries<sup>27, 28</sup> particularly in fluid catalytic cracking (FCC) reactions<sup>2, 3</sup>, hydrocracking<sup>29</sup>, dewaxing of lubricants and fuels<sup>30</sup>, and catalytic reforming of naphtha<sup>31</sup>. The petrochemical industry extensively utilizes zeolites for some important catalytic processes, i.e., alkylation and isomerization of hydrocarbons<sup>32-34</sup>, hydro-liquefaction, methanol-to-olefins<sup>35</sup>, and methanol-to-gasoline<sup>36</sup> and biomass conversion<sup>37-40</sup>. Especially zeolites are widely utilized for sustainable intention and renewable energy generation. Typical examples include (1) sustainable hydrogen production via ethanol/bioethanol reforming<sup>41, 42</sup> (2) Conversion of CO<sub>2</sub> to methanol and hydrocarbons via modified Fischer-Tropsch synthesis<sup>43-45</sup> and methanol-mediated route<sup>46, 47</sup>.

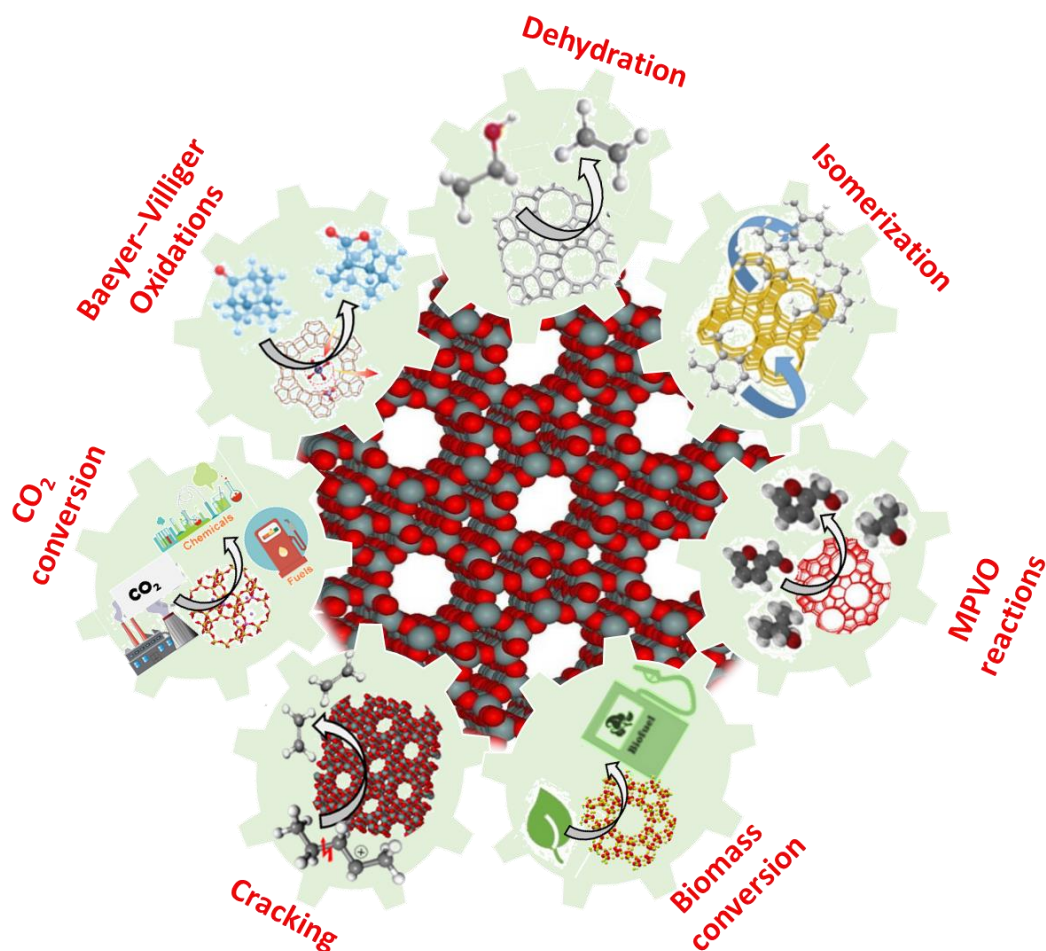


Figure 1.4: Representation of some important catalytic applications of zeolites<sup>2, 3, 28, 32-40</sup>.

#### 1.1.4. Characterizing the structure and acidity of zeolites

To understand the catalytic performance of zeolites, it is imperative to characterize and quantify the structure and geometry of their active sites. Similarly, information about the acidity associated with these active sites and the strength, concentration, and type of the acidic centers is also essential to design a suitable zeolite for the given catalytic process. Many characterization tools are used for this purpose such as temperature programmed desorption of ammonia, X-ray absorption spectroscopy (XAS)<sup>48</sup>, FTIR spectroscopy of adsorbed molecules<sup>49</sup>, MAS NMR aluminum<sup>50</sup>, X-ray photoelectron spectroscopy (XPS)<sup>51, 52</sup>, UV-Vis IR<sup>52</sup>. Following section discusses the MAS NMR spectroscopy and FTIR spectroscopy in detail.

**Magic Angle Spinning Nuclear Magnetic Resonance (MAS NMR) Spectroscopy:** Solid-state <sup>27</sup>Al MAS NMR is the most extensively employed characterization technique to identify the aluminum species in different coordinative environments in zeolites<sup>53-59</sup>. The typical <sup>27</sup>Al MQMAS NMR spectrum of a hydrated zeolite typically shows two resonances, one due to tetrahedrally coordinated framework aluminum and the other due to octahedrally coordinated aluminum around 0 ppm. However, different overlapping resonances also appear depending upon the nature of the zeolite and post-synthetic conditions<sup>55, 60</sup>. Due to the quadrupolar nature of the aluminum nucleus, it is not easy to quantify aluminum in different geometric environments, which appear as overlapping MAS NMR signals. Therefore, <sup>27</sup>Al MQMAS NMR spectroscopy is usually performed to calculate the quadrupolar coupling constants and isotropic chemical shifts. This information is utilized to deconvolute and quantify species in different coordination. **Figures 1.5a and 1.5b** show an example of a typical <sup>27</sup>Al MAS NMR and <sup>27</sup>Al MAS MQNMR spectrum of a zeolite in proton form, respectively. Zeolites typically show a sharp resonance in the region ~55-60 ppm due to tetrahedral aluminum species and at 0.1-1 ppm due to octahedral aluminum, which appears on the diagonal in <sup>27</sup>Al MQMAS NMR spectra (where F1=F2)<sup>61, 62</sup>. Furthermore, zeolites also show a broad resonance at ~60.0-64 ppm due to distorted-tetrahedral aluminum and a small peak at ~30-35 ppm due to pentahedral aluminum<sup>50 63-66</sup>. Apart from NMR of Al, the <sup>29</sup>Si and <sup>1</sup>H MAS NMR spectroscopy is also performed to evaluate the structure of and acidity of zeolites respectively. While <sup>29</sup>Si NMR gives useful insights about structural environment of silicon and aluminum, <sup>1</sup>H MAS NMR differentiates the hydroxyl groups based on their acidic strength<sup>67, 68</sup>.

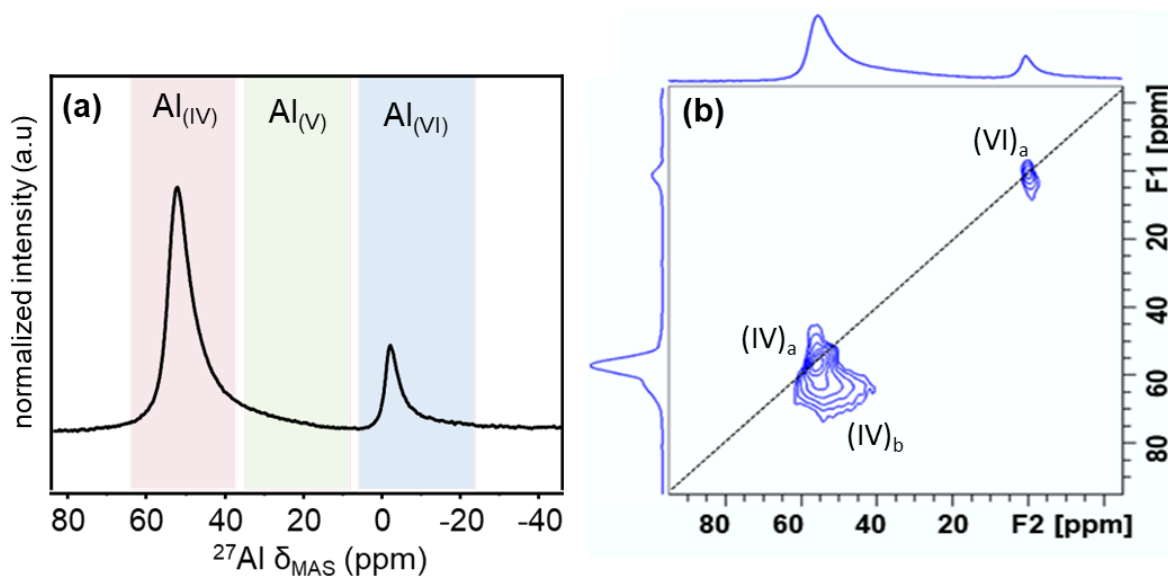


Figure 1.5: Typical (a)  $^{27}\text{Al}$  MAS NMR spectrum and (b)  $^{27}\text{Al}$  MAS MQNMR spectrum of MOR zeolite in proton form; the F1 axis is an isotropic dimension, and the F2 axis is the anisotropic dimension with second-order quadrupolar interactions.

**Fourier Transform Infrared (FTIR) spectroscopy:** The types of individual acidic sites and their concentrations can be determined by infrared spectroscopy, with the help of the adsorption of specific molecules and knowledge of their extinction coefficient. Thus, FTIR spectroscopy of adsorbed molecules is a well-established and powerful tool to study the acidic properties of zeolites, yielding their nature, number, and strength<sup>69-71</sup>. The acidity of zeolites is analyzed based on the interaction of acidic centers with a base molecule. Strongly basic molecules, which form a conjugated ion pair with the acid center, are also often used to measure the strength of acid centers. Pyridine is among the most widely used probe molecules; it can withstand a broad range of analysis conditions, form distinguishable complexes with acid sites differentiating BAS and LAS, and its use provides quantitative information<sup>49</sup>. However, due to its high basicity, it equally probes the acid sites of variable strength, and, at times, it cannot access some of the acid sites in the smaller zeolite channels because of its bulkiness.

Choosing a probe molecule of relatively weaker basicity and smaller size, such as carbon monoxide and nitrogen, is helpful in distinguishing acids sites of varying strength<sup>72, 73</sup>. Weak basic molecules interact with the acidic center by electrostatic forces, which do not lead to proton detachment but hydrogen bond formation. Usually, the vibration of the OH group shifts due to the binding of the probe molecule. Weaker bases, such as nitrogen and carbon monoxide, can differentiate multiple Lewis acid sites, including three-coordinated and octahedral aluminum species<sup>74-76</sup>.



**Figure 1.6a** illustrate the typical FTIR spectrum on an evacuated FAU zeolite which shows distinct bands at  $3747\text{ cm}^{-1}$ ,  $3630\text{ cm}^{-1}$ ,  $3565\text{ cm}^{-1}$ , and  $3597\text{ cm}^{-1}$ . These bands correspond to terminal Si-OH groups, low frequency (LF) bridging Si-OH-Al, high frequency (HF) bridging Si-OH-and EF species interacting with OH/Si-OH groups, respectively <sup>77-79</sup>. The typical FTIR difference spectra in the pyridine and carbon monoxide vibrations regions are presented in **Figures 1.6b and 1.6c**, respectively. In the region of pyridine vibrations, the bands at  $1455\text{ cm}^{-1}$  and  $1621\text{ cm}^{-1}$  are due to LAS, and the bands at  $1545\text{ cm}^{-1}$  and  $1634\text{ cm}^{-1}$  correspond to BAS. The band at  $1500\text{ cm}^{-1}$  is a superposition of LAS and BAS and is structure-insensitive ((**Figure 1.6b**)).

In the region of carbon monoxide vibrations, the bands at  $2230$ ,  $2195$ ,  $2180\text{ cm}^{-1}$ , and  $2157\text{ cm}^{-1}$  are due to three-coordinate LAS, five-coordinate LAS, BAS, and CO-SiOH, respectively. All the other bands below  $2180\text{ cm}^{-1}$  are due to physisorbed carbon monoxide <sup>77, 80</sup> (**Figure 1.6c**).

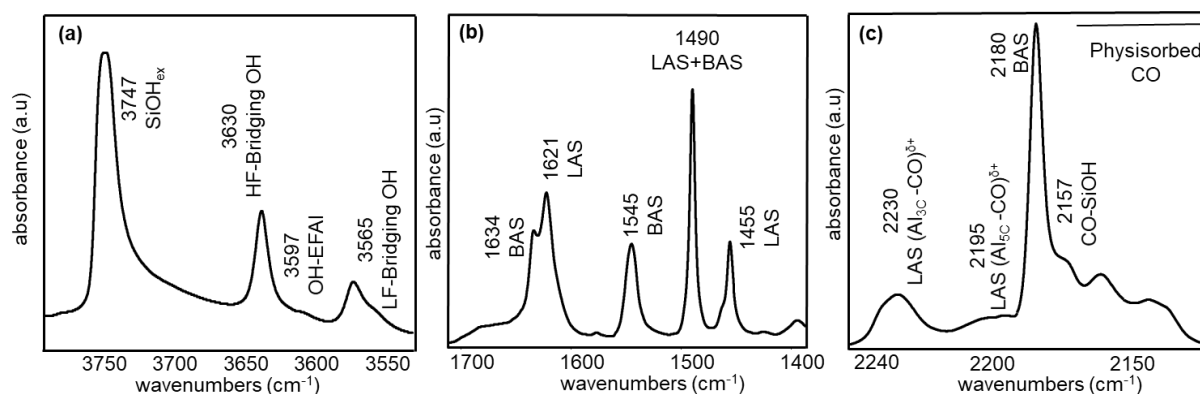


Figure 1.6: Typical FTIR spectra of a zeolite (a) in the hydroxyl stretching region of an evacuated zeolite. The difference FTIR spectrum in (b) pyridine ring deformation region (c) carbon monoxide stretching region.

## 1.2. Lewis acidic zeolites

Lewis acid zeolites are versatile catalysts used to activate and convert oxygenated molecules. Over the years, much research has been devoted to Lewis acid zeolites in terms of structural analysis and tailoring their potential in catalysis. Following sections focus on the applications of Lewis acidic zeolites in heterogeneous catalysis and the most established ways of incorporating Lewis acidity in zeolites.

### 1.2.1. Applications of Lewis acidic zeolites

Lewis acidic zeolites are extensively explored for biomass valorization reactions, such as hydride transfer reactions<sup>81</sup>, conversion of cellulose to glucose<sup>82</sup>, glucose to fructose<sup>83</sup>, trioses to alkyl lactates, and Baeyer-Villiger (BV) oxidation of ketones and aromatic aldehydes<sup>84, 85</sup> and Meerwein–Ponndorf–Verley reduction of aldehydes and ketones and Oppenauer's oxidation of alcohols (MPVO reactions)<sup>86</sup>. Some examples of zeolites for the conversion of renewables to chemicals are listed in **Table 1.2**. The following section discusses the characteristics of alkane dehydrogenation and MPV reduction in detail.

Table 1.2: Applications of Lewis acidic zeolites for biomass valorization reactions. Adapted with permission from ref.<sup>87</sup> [Copyright Royal Society Of Chemistry, Etc.]

Nature of Transformation	Reactant	Product	Ref.
1,2-H shift	Glyceraldehyde	Dihydroxyacetone	88
	Glyoxal	Glycolic acid	89
		Alkyl glycolates	89
	Dihydroxyacetone	Lactic acid	90
	Erythrose	Erythrulose	91
	Galactose	Tagatose	92
	Glucose	Fructose	93
Oxidation + 1,2-H shift	Glycerol	Lactic acid	94
1,2-C shift	Glucose	Mannose	95
	Arabinose	Ribose	96
1,5-H shift	Glucose	Sorbose	97
(Retro)-aldolisation	Sugars	Methyl lactate	98
H-transfer with solvent donor	5-HMF	Furan derivatives	99
	Methyl levulinate	Valerolactone	100
	alkyl cyclohexanones	alkyl cyclohexanols	81
Diels–Alder cycloaddition + dehydration	Furan derivative ethylene	+ p-Xylene derivative	88

**Meerwein–Ponndorf–Verley reductions and Oppenauer's oxidations:** Meerwein–Ponndorf–Verley reduction of aldehydes/ketones and Oppenauer's oxidation of alcohols

(MPVO reactions) are the traditional technologies for redox reactions to realize the selective hydrogenation of carbonyl groups through hydrogen transfer between ketones/aldehydes and alcohols <sup>86</sup>. In MPV reduction (a mechanism of transfer hydrogenation or hydrogenolysis), a carbonyl group (C=O) is reduced with an alcohol reductant, whereas in Oppenauer oxidations, an alcohol is oxidized with a ketone oxidant<sup>101</sup>. Owing to the use of secondary alcohol as a hydrogen source, MPV reduction is a milder hydrogenation technique when compared with hydrogenation under H<sub>2</sub> atmosphere <sup>102</sup>.

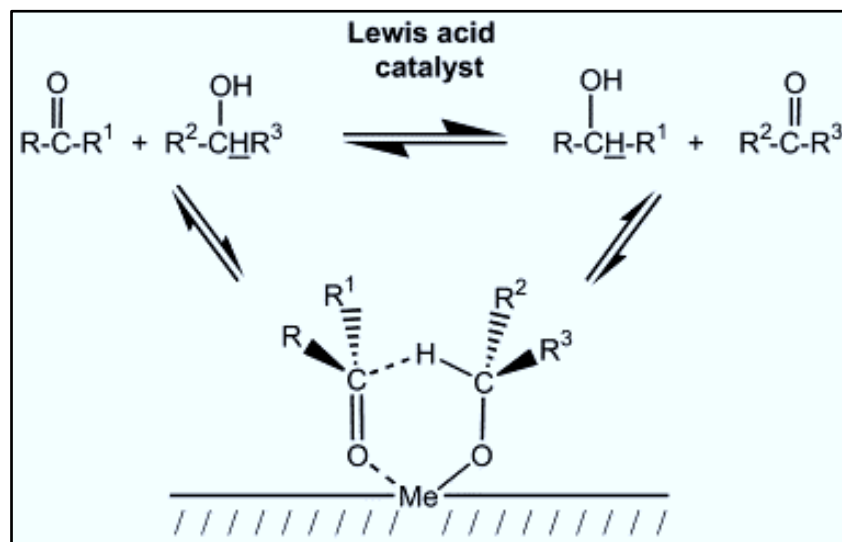


Figure 1.7: Schematic representation of a general mechanism of MPVO reactions over a Lewis acidic center.

An easily oxidizable secondary alcohol, e.g., isopropanol, serves as the reductant of a hydrogen donor, whereas simple ketones, e.g., acetone, are employed as oxidants <sup>100</sup>. The homogeneous MPV reductions use Lewis acidic metal alkoxides such as, e.g. aluminum and titanium alkoxide derived from secondary alcohols <sup>103</sup>, whereas metal *tert*-butoxides are used for oxidations <sup>104</sup>. A significant advantage of heterogeneous over homogeneous catalyzed MPVO reactions is the easy separation of catalysts from the liquid reaction mixture. Different Lewis acidic zeolites have been utilized as heterogeneous catalysts for MPVO reactions, including zeolite X, Y, Beta, MOR, and ZSM5 <sup>105 72, 103, 106</sup>. In particular, Beta zeolite with Al, Sn, and Ti Lewis acid sites exhibit excellent catalytic activity, compared with other MPVO heterogeneous catalysts <sup>81, 88, 102</sup>.

**Figure 1.7** presents the schematic of a generally accepted heterogeneous MPVO reaction mechanism. The reaction initiates by the coordination of the reducing alcohol on a Lewis acidic center to form an alkoxide species. This is followed by the coordination of the ketone, resulting

in a six-membered ring transition state, to undergo hydride ion transfer from the alkoxide to the carbonyl group of the ketone <sup>100</sup>. The MPVO reactions are widely involved in organic synthesis to produce valuable chemicals, especially in asymmetric synthesis and biomass conversion. Additionally, Lewis acid sites of zeolites are extensively evaluated utilizing MPVO reactions as the benchmark Lewis acid-catalyzed reactions. The widespread use of these reactions to explore Lewis acidic zeolites is due to the following reasons: (i) these reactions are highly selective, and any reducible group, except carbonyls (e.g., unsaturated carbon-carbon bonds and carbon-halogen groups) does not react <sup>81</sup> (ii) Lewis acid sites provide the precursor to form the active site for the hydride transfer mechanism <sup>86</sup>.

**Dehydrogenation of light alkanes:** The dehydrogenation of light alkanes involves the breaking of two carbon–hydrogen bonds with a simultaneous release of a corresponding alkene together with a molecular hydrogen <sup>107</sup>. This process is of prime significance as lower alkanes are readily available feedstocks from petroleum and gas resources and can serve as precursors to many value-added chemicals. However, non-polar C–C and C–H bonds of alkanes, with strongly localized electron pairs, can only be activated under severe reaction conditions, which makes the direct dehydrogenation of alkanes an energy-intensive process <sup>108</sup>. A non-oxidative heterogeneous dehydrogenation of alkanes has the following reaction scheme;



This endothermic reaction requires ~110–140 kJ/mol of energy to activate the C-H bond and remove two hydrogen atoms. The C-H bond activation of alkanes can lead to several essential reactions useful for the petrochemical industry, i.e., cracking, isomerization, alkylation, and aromatization. Commercially, several solid acid catalysts are employed for the catalytic dehydrogenation of light alkanes, including oxides based on platinum and chromium <sup>109, 110</sup>. However, using zeolite catalysts becomes more advantageous because of a well-defined structure, making <sup>111, 112</sup>it easy to deduce the structure-activity relationships. Activating C-H bonds in light alkanes involves cooperative catalysis of LAS and BAS of zeolites.

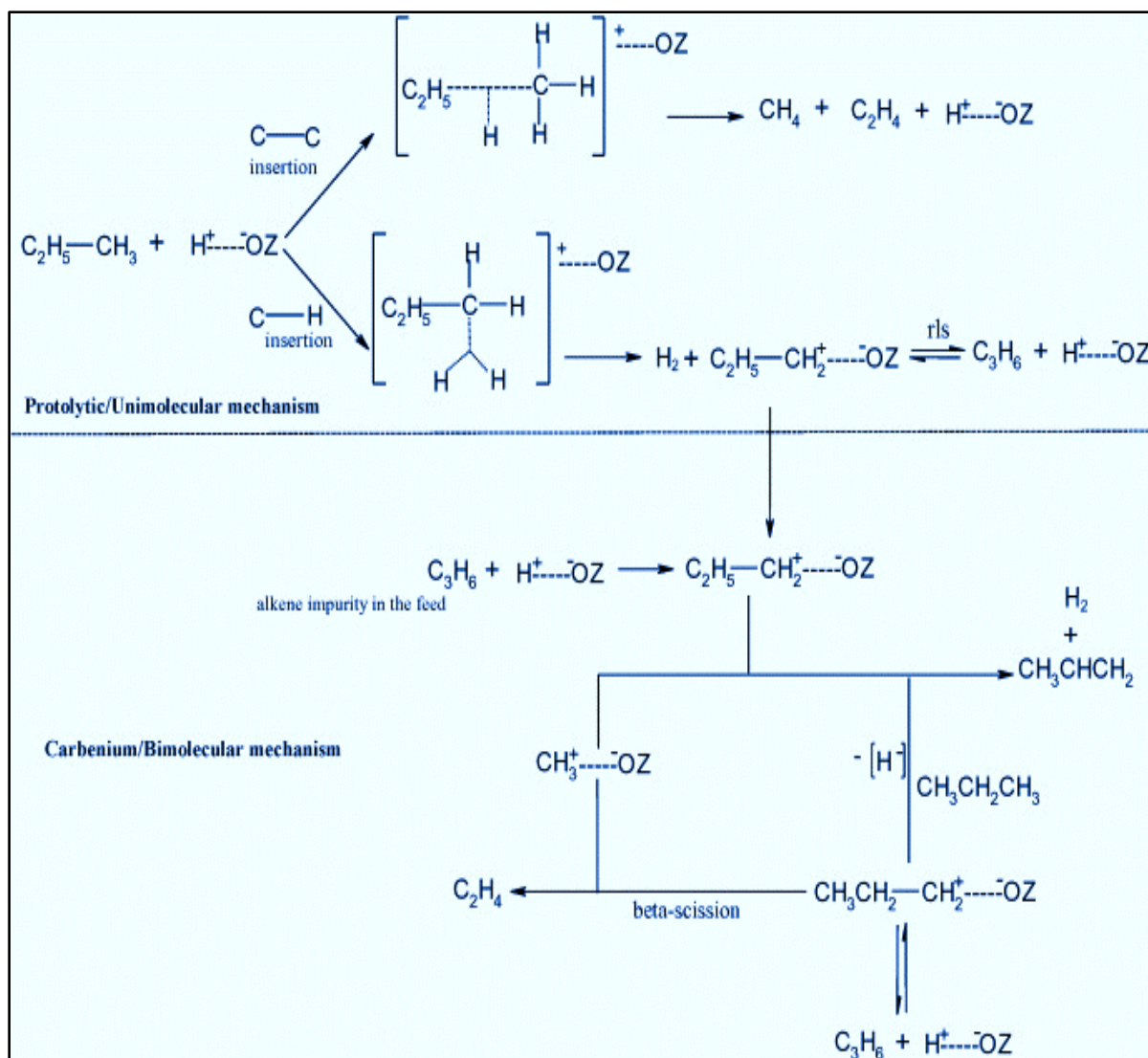


Figure 1.7: Schematic representation of C-H activation paths in propane using zeolites. Reproduced with permission from Ref. <sup>108</sup> Copyright 2016 Elsevier B.V. All rights reserved.

**Figure 1.7** presents the schematic of C-H bond activation pathways in zeolite catalysts. The two generally documented pathways for C-H activation over zeolites are the monomolecular (protolytic) mechanism and the bimolecular (carbenium chain) mechanism. High temperature and lower partial pressures of reactant usually favor unimolecular dehydrogenation mechanism, whereas low temperature and high partial pressures favor bimolecular mechanism for the dehydrogenation of alkane on zeolites. However, in the presence of BAS, each mechanism undergoes some side reactions, including dimerization, oligomerization, isomerization & aromatization <sup>113</sup>. In the unimolecular <sup>113</sup>. In the unimolecular mechanism, an alkane is directly protonated, forming a carbonium-ion intermediate. The mechanism involves the insertion of a proton either to a C-C bond or a C-H bond of an alkane. The insertion of proton to a C-C bond results in the cracking of alkane followed by the regeneration of acid sites <sup>109</sup>. In contrast, the protonation of a C-H bond generates a carbenium ion and H<sub>2</sub>. From here, the alkene can desorb from the intermediate

to regenerate the active site. Alternatively, the carbenium ion intermediate enters the bimolecular conversion path: the active site remains attached to alkoxide, whereas the C-H bond activates by another alkane molecule by hydride transfer, thus forming another alkoxide. The cycle may be terminated by olefin desorption<sup>114, 115</sup>.

### 1.2.2. Generation of Lewis acidity in Zeolites

**Incorporation of heteroatoms into zeolite framework:** Lewis acidity in zeolites can be created by hydrothermal synthesis<sup>116</sup> and post-synthetic incorporation of heteroatom into the framework of zeolites, wherein isolated acid sites serve as LAS<sup>117-119</sup>. This approach usually involves the insertion of heteroatoms, such as zirconium, tin, and titanium, into the framework of as-synthesized zeolites in liquid-solid, solid-solid, or gas-solid systems. This method is based on the framework dealumination or desilication combined with the isomorphous substitution of framework atoms by post-synthetic treatment under certain conditions. During the removal of Si or Al species by desilication or dealumination, certain types of voids or defect sites are created in the zeolite framework. Hence, the incorporation of appropriate metal complexes into the zeolite framework becomes favorable. For example, selective dealumination of zeolite BEA was performed by acid leaching, using nitric acid as a dealuminating agent. The solid-state incorporation (SSI) method incorporated Lewis acidic Sn metal in a dealuminated zeolitic framework (**Figure 1.8**)<sup>120</sup>. However, generating isolated acid sites via heteroatom substitution is not trivial and has been limited to a few zeolite frameworks<sup>117, 118, 121, 122</sup>. Additionally, depending on the dealuminating/desilicating agent and the conditions applied, these methods may lead to imperfect zeolite structures and generation of inadequate defect sites, i.e., ‘hydroxyl nest,’ which can thus create secondary mesoporous zeolites<sup>123</sup>.

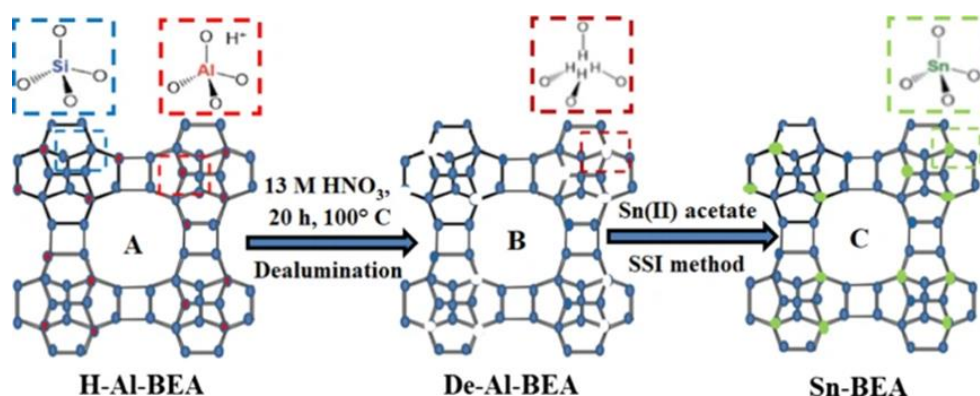


Figure 1.8: Typical example of incorporating heteroatom into zeolite framework. Reproduced with permission from Ref.<sup>120</sup> Copyright 2021, King Fahd University of Petroleum & Minerals.

**Incorporation of heteroatoms at extra-framework positions:** Another most important emerging way of adding or enhancing the intrinsic Lewis acidity is by introducing heteroatoms at extra-framework positions of zeolites by ion exchange or impregnation. This method is based on the ability of zeolite lattices to act as ligands stabilizing cationic species in their micropores. The acidic protons inside zeolite micropores can be replaced by other cationic species, including transition metal-containing complexes or multinuclear species, giving rise to well-defined Lewis acid or/and redox sites in zeolite micropores <sup>124</sup>.

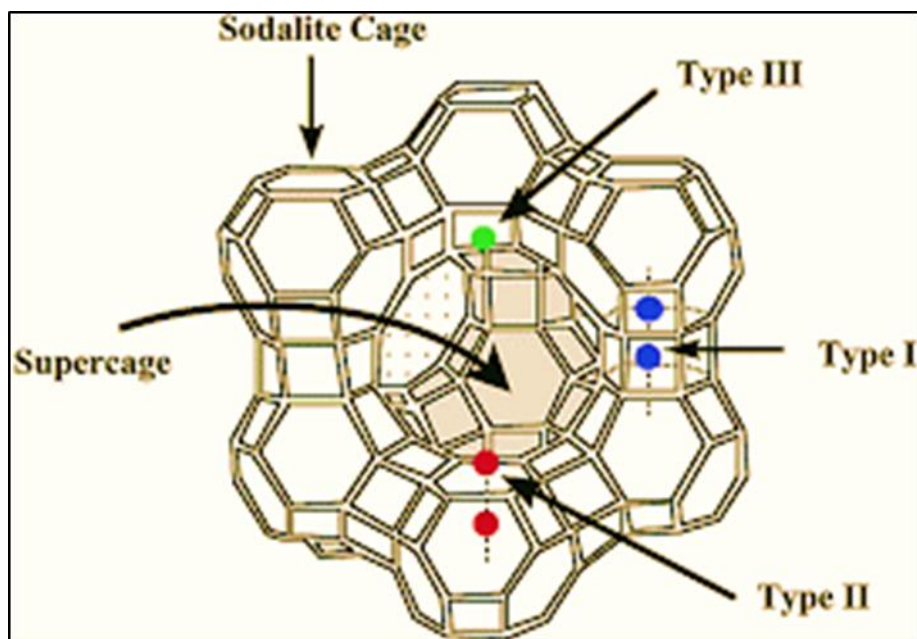


Figure 1.9: Structure of Faujasite showing central super-cage surrounded by sodalite cages, along with positions of exchangeable (extra-framework) cation sites. Reproduced with permission from Ref.<sup>125</sup> Copyright © 2010, © SAGE Publications.

The distributions of these extra-framework motifs depend mainly on the distribution of lattice anions and, therefore, on the location of framework aluminum species (**Figure 1.9**) <sup>126</sup>. The charge of these EF cations may directly alter the acid strength of BAS and/or affect the adsorptive attitude of the zeolite <sup>127</sup>. Consequently, these EF cations play a significant role in determining the catalytic properties of zeolites <sup>124</sup>. By choosing a particular zeolite topology and exchangeable cations, zeolites with desired properties can be obtained for practical applications. For instance, incorporating  $\text{Ga}^{3+}$  or  $\text{Zn}^{2+}$  in zeolites can generate strong Lewis acid sites active in dehydrogenation and dehydro-aromatization of light alkanes <sup>128</sup>. Recent research has been conducted on basic and rare earth cations and transition metals as exchangeable cations

129-132



**Post-synthetic modifications:** Typically, most zeolites are synthesized in aluminum-rich form. Such as-synthesized low silica zeolites usually exhibit weak Brønsted acidic strength and low hydrothermal stability. Therefore, different post-synthetic treatments are performed on zeolites to reduce aluminum content in the framework and improve zeolite's acidity and hydrothermal stability. Lewis acidity can also stem from post-synthesis treatments, such as high-temperature calcination, acid/base leaching, and steaming, which can result in removing some framework aluminum and forming extra-framework species<sup>133-135</sup>.

Kuhl<sup>136</sup> proposes the formation of Lewis acid sites in two steps (**Figure 1.10**). The first step involves dehydroxylation at adjacent bridging hydroxyl groups. In the second stage, zeolite attains a stable state with the aid of an adjacent framework aluminum center. As the existence of the closest neighboring aluminum atoms turns the under-coordinated atoms to be less stable, this leads to the detachment of aluminum from the zeolite framework. The second step can conveniently occur in zeolites with a low Si/Al ratio, with plenty of adjacent aluminum centers. However, this step seems less preferable in zeolites with a high Si/Al ratio, as they mostly contain isolated BAS<sup>136-138</sup>. Further details on the nature and acidity of such species are discussed in the following sections.

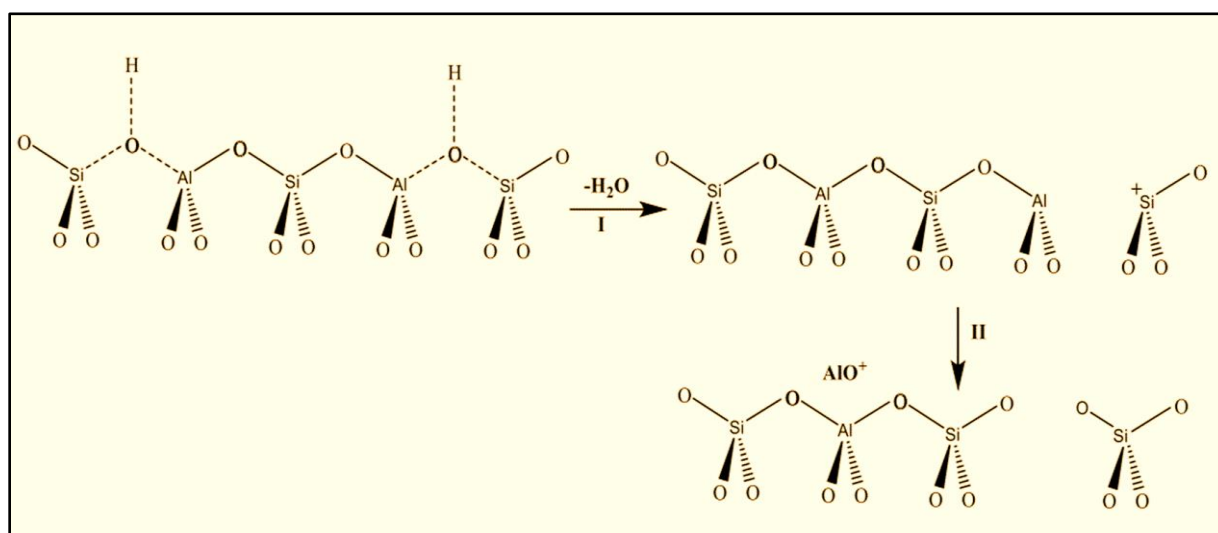


Figure 1.10: A two-step mechanism for the formation of extra-framework Al species: I) dehydroxylation and II) dealumination. Inspired from Ref.<sup>136</sup>

### 1.3. Aluminum Lewis acid sites in zeolites

While the Lewis acidity is usually incorporated in zeolites by non-trivial protocols of incorporating heteroatoms<sup>117-119</sup>, Lewis acidic aluminum in zeolites can be formed without



tedious synthesis procedures and is not restricted to specific zeolite topologies. However, unlike Brønsted acid sites (BAS), which originate from a hydroxyl group bridging framework silicon and aluminum atoms<sup>24</sup>, the structure of Lewis acid sites (LAS) still remains ambiguous. This is due to the multiplicity of aluminum structures responsible for Lewis acidity in zeolites, as presented in **Figure 1.11**<sup>62</sup>. Even though considerable research has been carried out on the Lewis acidity of zeolites, the literature still lacks a sound understanding of the structure and strength of aluminum Lewis acid sites in zeolites<sup>60, 139-141</sup>. Different proposals about the aluminum motifs responsible for Lewis acid sites have been put forward, including framework-associated aluminum (FA-Al), framework aluminum (F-Al), and extra-framework aluminum (EFAI). A recent work by Ravi. M. et al.<sup>62</sup> compiles the available literature about Lewis acidic aluminum species and discuss different proposals in detail, providing the latest field information. The following sections discuss the proposed characteristics of LAS corresponding to different aluminum structures, whereas **Figure 1.12** presents the proposed schematic of these LAS.

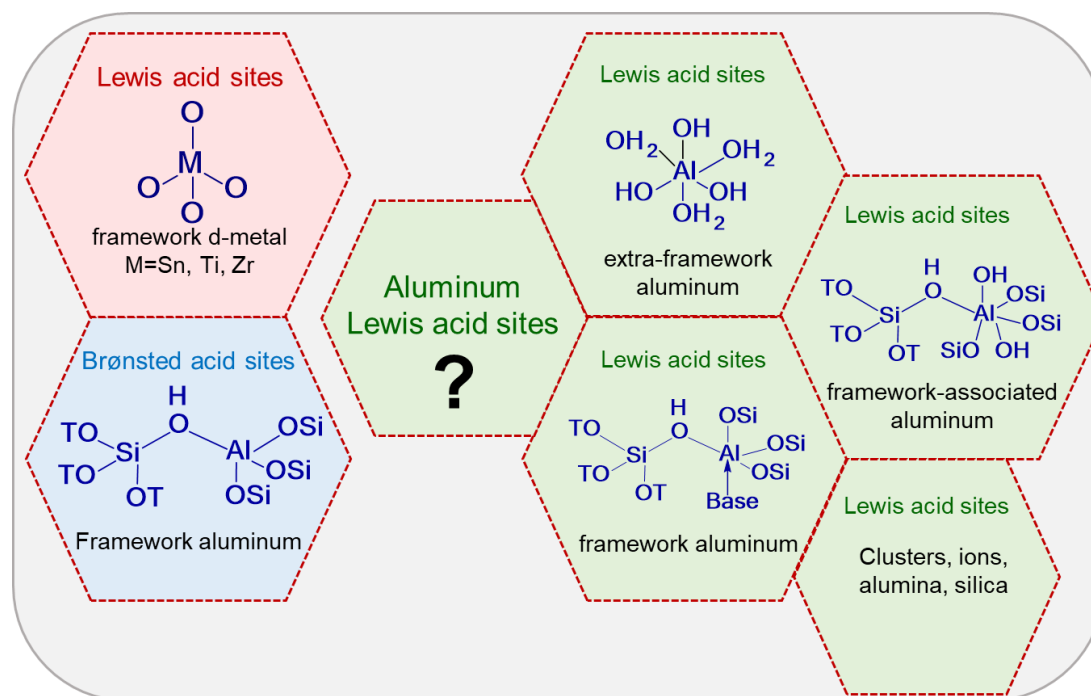


Figure 1.11: Representation of multiplicity of aluminum Lewis acid sites (green hexagons). Brønsted acid site (blue hexagon), Lewis acid site of framework heteroatom (pink hexagon).

### 1.3.1. Framework aluminum Lewis acid sites

Typically, aluminum in the framework, with tetrahedral coordination, is associated with BAS. However, post-synthetic modifications like steaming, high-temperature calcination, and acid

leaching can result in defective aluminum centers in the zeolite framework that can serve as Lewis acid sites (**Figure 1.11, structure L**)<sup>139, 142-144</sup>. The distorted and/or perturbed aluminum in the framework, like that of  $(\text{SiO})_3\text{AlOH}$  species in ferrierite and chabazite zeolites, can dehydroxylate at relatively mild temperatures and act as Lewis acidic centers (**Figure 1.11, structure K**)<sup>139</sup>. Furthermore, another possibility has been put forward for framework Lewis acidity where a framework with tetrahedral coordination, upon exposure to a base molecule under high vacuum conditions, can acquire extra coordination with the base (**Figure 1.12, structure J**)<sup>143</sup>. However, experimental literature is still not available to support this proposal.

### 1.3.2. Extra-framework aluminum Lewis acid sites

Extra-framework aluminum (EFAl) correspond to aluminum species that are not part of zeolite's framework. These species are usually generated in zeolites when they undergo different post-synthesis treatments for desired end applications. As a consequence of these treatments, e.g., high-temperature calcination, acid/base leaching, and/or steaming, some of the aluminum species are entirely dislodged from the framework and exist as extra-framework species<sup>133-135</sup>. A prominent example is zeolite Y, one of the benchmark catalysts for the petrochemical industry<sup>145</sup>. High-temperature steaming on zeolite Y is traditionally performed to improve its hydrothermal stability and catalytic activity, and the resultant zeolite Y is typically termed ultra-stable Y (USY). This treatment leads to a part of lattice Al migrating to the extra-framework positions in zeolite pores. The presence of such extra-framework Al (EFAl) species promoted the acidity and catalytic performance<sup>146-148</sup>.

The enhanced acidity is attributed to the generation of EFAl in USY zeolite. These LAS were attributed to assist the improvement of catalytic performance in two possible ways (1) either these LAS promote the intrinsic acid strength of the vicinal BAS via polarization effect, (2) an alternative promoting effect of EFAl species has been attributed to the decrease of the effective size of the super-cage cavities, resulting in tighter confinement and, accordingly, more efficient dispersive stabilization of the transition states during catalytic reactions<sup>146-148</sup>. Such EFAl species in zeolite Y have been reported to exist in many different forms:  $\text{Al}^{3+}$ ,  $\text{Al}(\text{OH})^{2+}$ ,  $\text{Al}(\text{OH})^{2+}$ ,  $\text{AlOOH}$ ,  $\text{Al}(\text{OH})_3$ , and  $\text{Al}_2\text{O}_3$  (**Figure 1.12, Structure B, C, D, M**).<sup>145, 149-151</sup>

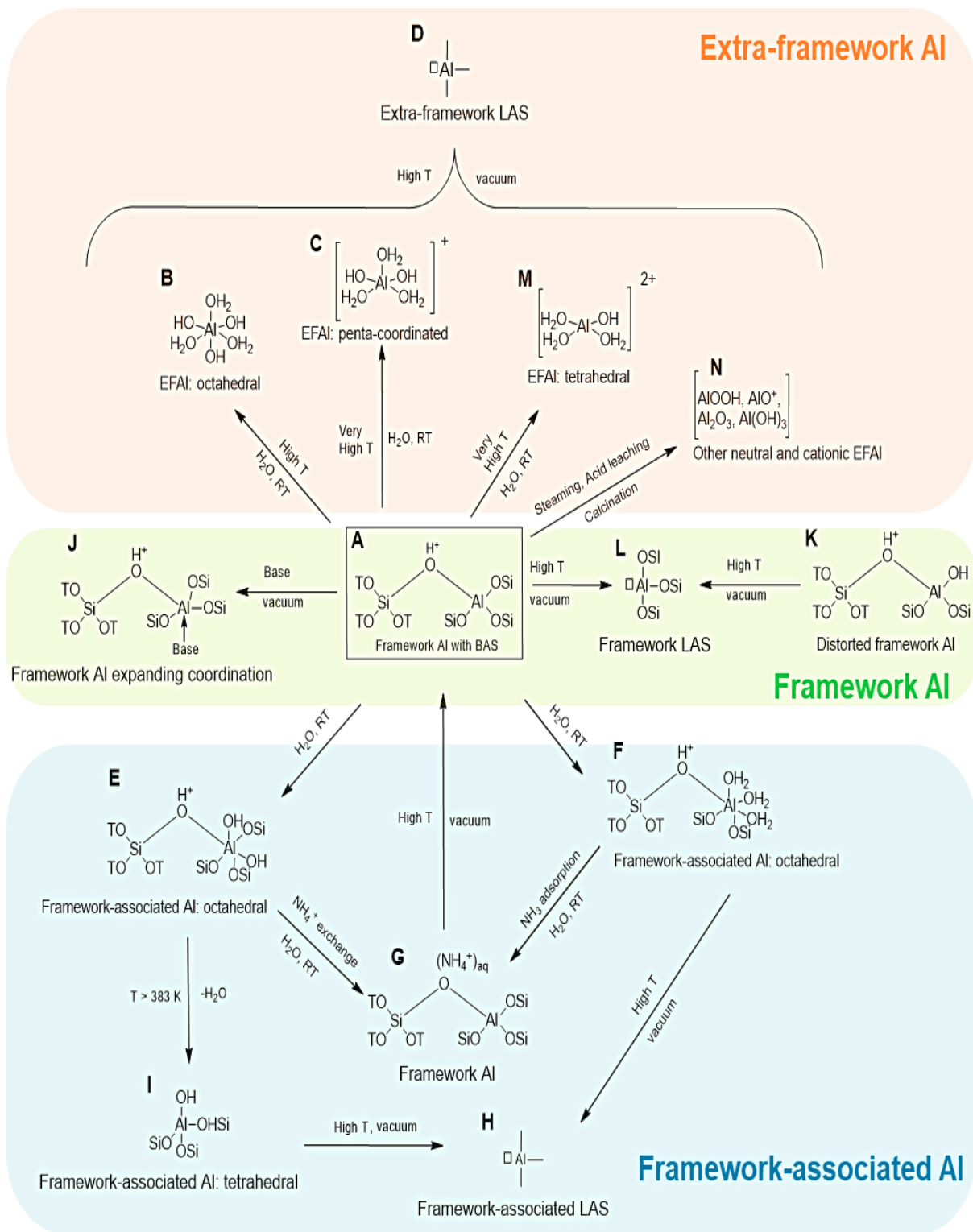


Figure 1.12: A summary of the different proposals of aluminum motifs associated with Lewis acid sites. Pathways showing the changes in aluminum structure with changing conditions and classification of Lewis acidic aluminum as originating from extra-framework,<sup>145, 149-152</sup> framework-associated,<sup>56, 60, 142, 151</sup> and framework aluminum.<sup>139, 142-144</sup> All structures in the figure except for structure K have been reported in FAU. Reproduced with permission from Ref.<sup>62</sup> Copyright © 2020, Springer Nature Limited.

The EFAl aluminum is widely associated in the literature with Lewis acidity. While this is true in most cases, some of the reported literature explains that only some EFAl are Lewis acidic<sup>153-155</sup>. Of all the possible forms, the cationic extra-framework species  $\text{Al}^{3+}$ ,  $\text{Al}(\text{OH})^{2+}$ , and  $\text{Al}(\text{OH})^{2+}$  are regarded as strong LAS capable of hydrocarbon conversion by a hydride transfer mechanism<sup>156, 157</sup>. Moreover, the factors like Si/Al ratio<sup>158-160</sup>, type of co-cation (e.g.,  $\text{Na}^+$ ,  $\text{H}^+$ ,  $\text{NH}_4^+$ , etc.)<sup>66, 142, 161</sup> and the nature and severity of post-synthetic treatment<sup>133, 153, 155, 162-167</sup> significantly affect the Lewis acidity of EFAl.

### 1.3.3. Framework-associated Aluminum Lewis acid sites

Framework-associated aluminum (FA-Al) are octahedrally-coordinated aluminum species that can be re-introduced into a tetrahedrally framework site. The characteristic feature of these species is their ability to adopt tetrahedral or octahedral coordination depending on the conditions applied ).<sup>56, 168</sup>. Additionally, their existence in either coordination can be reversibly transformed to the other as a function of conditions (**Figure 1.12, structure E, F & H**).<sup>56, 66, 168, 169</sup>. In the presence of charge-balancing cations other than a proton, i.e., potassium, sodium, and ammonium, these aluminum species adopt a tetrahedral geometry, characterized by resonance at  $\sim 60$  ppm in  $^{27}\text{Al}$  NMR spectrum of a hydrated zeolite. However, in the presence of protons as charge-compensating cations, these structures acquire octahedral coordination, characterized by a sharp resonance at  $\sim 0$  ppm of  $^{27}\text{Al}$  NMR spectrum of a hydrated zeolite<sup>56, 60, 66, 142, 169</sup>. A study on zeolite MOR, employing  $^{27}\text{Al}$  NMR and FTIR on adsorbed probe molecules, confirms the linear correlation of FA-Al to Lewis acidity<sup>60</sup>. Similarly, SSZ-33 zeolite with FA-Al species also showed a significant concentration of LAS<sup>142</sup>. Apart from FTIR and NMR techniques, X-ray photoelectron spectroscopy (XPS) and in situ, X-ray absorption spectroscopy also demonstrate this reversibility of coordination<sup>56, 170-173</sup>.

The generation and stabilization of these species depend on the zeolite morphology, location of T-sites, and Si/Al ratio<sup>174, 60, 175</sup>. The process of reinsertion of these species again into the framework of zeolite follows (1) an increase in the intensity of tetrahedral resonance at  $\sim 60$  ppm and disappearance of resonance at  $\sim 60$  ppm  $^{27}\text{Al}$  NMR and (2) an increase in the intensity of BAS in IR spectra<sup>176</sup>. This suggests that not only the coordination but the associated acidity of FA-Al is also reversible, implying a Brønsted-Lewis acid site conversion. As FA-Al is a precursor to a LAS formed upon heating; after which it is cannot be converted back to its original structure.

The tetrahedral-octahedral reversibility or an associated BAS-LAS conversion of FA-Al species becomes an ultimate criterion to distinguish FA-Al from EFAl species<sup>66</sup>. Both FA-Al

and EFAl exist in octahedral coordination in protonic zeolite <sup>142</sup>. The species reverting to the zeolite framework are FA-Al upon interaction with ammonia (or wet ammonium ion-exchange). In contrast, the species that retain their octahedral coordination independent of conditions are termed true EFAl species. In a typical example, zeolite Y possesses FA-Al after high-temperature calcination. While still connected via three framework coordination, such species coordinate with three water molecules to acquire octahedral coordination (**Figure 1.12, structure F**). These species are converted to a tetrahedral environment after ammonia adsorption. However, upon an increase in the severity of thermal treatments, the FA-Al species completely dislodge from the framework, resulting in the generation of EFAl, whose coordination cannot be reversed by ammonia exposure <sup>177, 178</sup>.

#### 1.4. Research gaps associated with aluminum Lewis acidic zeolites

Zeolites hold a central place in heterogeneous catalysis because of the combination of unique characteristics: their role as adsorbents <sup>5</sup>, their molecular sieve properties <sup>6-9</sup>, and their widely used ion-exchange properties <sup>4</sup>. The most important role of zeolites as acid catalysts stems from the co-presence of LAS and BAS. However, many open questions are associated with the Lewis acidity of aluminum motifs, highlighted as follows.

- I. Aluminum LAS are usually generated by conventional high-temperature calcination or steaming. The high-temperature calcination results in the dehydroxylation of the BAS. Similarly, LAS obtained by steaming completely dislodges the aluminum from the zeolite framework. Even mild steaming also reduces the number of BAS. Thus, the Lewis acidity is only enhanced at the expense of BAS. Moreover, these approaches usually lead to a substantial heterogeneity of aluminum species and the formation of many lattice defect sites.
- II. The generation of LAS at the expense of BAS is unsuitable for catalytic processes, which entail cooperative catalysis employing both acid sites, e.g., biomass valorization. A typical example is the conversion of glucose to 5-hydroxymethylfurfural (HMF)<sup>179</sup>. This cascade reaction involves two steps (1) isomerization of glucose to fructose and (2) dehydration of fructose to HMF. This reaction occurs on a bi-functional catalyst where aluminum LAS catalyzes the first step and the second employs BAS.
- III. Complications in establishing the sound relation between the structure and performance of aluminum LAS originates from the varying effectiveness of post-synthetic modifications for zeolites of different structure types <sup>50, 75, 80</sup>. Most importantly, the role of EFAl as LAS is hampered by the difficulty to unambiguously identifying their structure, as the conventional methods allow limited control over the fate of FA-Al or EFAl.

- IV. The generation of LAS by introducing heteroatom at framework or extra-framework positions also entails limitations: (1) in the case of the former, the generation of isolated acid sites via heteroatom substitution is not trivial and has been limited to a few zeolite frameworks<sup>117, 118, 121, 122</sup>. Furthermore, by using this approach only limited amount of heteroatom can be introduced ( typical Si/M ratios are 30-100). (2) in the later, heteroatoms usually occupy charge-compensating positions resulting in loss of BAS. Although different ways of generating LAS in zeolites<sup>129-132</sup> are extensively explored, more attention should be paid to the rational design of aluminum LAS to counter the challenges posed by conventional methods (high-temperature calcination, acid treatments, or steaming).
- V. While EFAl is usually associated with Lewis acidity, the literature indicates that the quantitative correlation of the content of EFAl to the concentration of Lewis acid sites and the performance in a catalytic reaction is still missing. This lack of correlation stems from two reasons: (1) most of the literature overlooks the types of aluminum structures that can serve as Lewis acid sites. In this respect, systematic experiments to distinguish EFAl LAS from FA-Al LAS are not usually employed while explaining the Lewis acidity of aluminum zeolites. (2) <sup>27</sup>Al MAS NMR usually assesses the aluminum structure under hydrated conditions, and the Lewis acidity is characterized by FTIR under dehydrated and evacuated conditions. In contrast, catalytic activity is assessed under high-temperature conditions. Therefore, it is very likely that not all aluminum structures might necessarily be present under all conditions.

To address these open questions clearly defined, systematic research is essential that can provide (1) a more profound understanding of the nature and role of aluminum LAS, (2) new prospects for the design of efficient aluminum LAS in zeolites, (3) experimental evidence to distinguish different types of LAS.

## Chapter 2

### Scope of the thesis

Though the Lewis acidity of zeolites remains an extensive area of research and application, the Lewis acidity of aluminum in zeolites remains ambiguous and needs thorough investigation. Many essential questions about the activity and nature of extra-framework species remain open. Therefore, the present work extensively explores the aluminum Lewis acidic in zeolites. Particular emphasis is on the rational design of extra-framework aluminum (EFAl) Lewis acid sites in zeolites. The main goal is understanding the nature of extra-framework aluminum (EFAl) species and their associated Lewis acidity and catalytic performance. **Figure 2.1** presents the central areas of research that are being explored in this thesis.

- A.** As the post-synthetic treatments do have very little control over the generation and heterogeneity of extra framework aluminum, their correlation to Lewis acidity becomes difficult. Even though cation exchange is extensively used to incorporate heteroatom Lewis acid sites in zeolites, aluminum ion-exchange has been rarely employed for this purpose. The work in **Chapter 4** aims to tune the Lewis acid sites in zeolites through a facile aluminum ion-exchange procedure. The introduced aluminum species' structure and nature are thoroughly characterized to correlate their structure to Lewis acidity and catalytic activity.
  
- B.** The generation of LAS by post-synthetic treatments has been established to be affected by different factors, including the nature of treatment conditions, the nature of co-cation, and the Si/Al ratio of a zeolite. In light of this, **Chapter 4** and **Chapter 5** investigate different factors affecting the generation of extra-framework aluminum Lewis acid sites by aluminum ion-exchange protocol, e.g., conditions of aluminum exchange, nature of co-cation, and concentration of aluminum-exchange precursor, etc. A particular question of interest was to evaluate how the protocols used to introduce Lewis acidity in this work affect the intrinsic Brønsted acidity of zeolites.

- C.** The consequences of post-synthetic modifications are not the same for all zeolite structures. This can be because of different reasons, including the framework structure, pore sizes, location of aluminum sites, etc. **Chapter 6** explores the effectiveness of the aluminum-exchange procedure in introducing Lewis acidity in zeolites of different morphologies and pore dimensions.
- D.** As the zeolite is composed of aluminum and silicon, introducing the additional aluminum might affect the structure and acidity of already existing aluminum species. Therefore, it is essential to characterize the newly introduced aluminum species and quantitatively distinguish extra-framework aluminum species from framework-associated aluminum. Additionally, most of the post-synthetic modifications influence the structural integrity, porosity, and Brønsted acidity of zeolite in one way or the other. Thus, **Chapters 4-7** evaluate the structure of aluminum species in different environments and quantify their acidity, whereas the porous crystalline structure of zeolite is also evaluated during aluminum modifications. In particular, **Chapter 8** thoroughly investigates the distribution of extra-framework and framework-associated aluminum motifs in zeolite and their associated acidity in different cationic forms of a zeolite synthesized by different routes. Furthermore, combining (a) FTIR spectroscopy using different probe molecules and (b)  $^{27}\text{Al}$  NMR under hydrated and evacuated conditions provides valuable information on the generation, nature, and strength of acid sites. Consequently, the EFAI LAS are These pieces of evidence were used in **Chapter 9** to revisit the literature assignment about the aluminum species associated with very high-frequency (VHF) hydroxyls of zeolites.
- E.** The introduction of aluminum by ion-exchange generated Lewis acidity, which FTIR confirmed. However, whether or not these aluminum species are active, accessible, and stable under actual reaction conditions is essential. Therefore, the activity of the introduced LAS was tested primarily in the MPV reaction, which is a benchmark reaction to explore LAS (**Chapters 4, 5, 6, and 8**). However, the MPV reactions occur under mild conditions and involve the activation of the C-C bond. Thus, these reactions don't require very strong and/or stable LAS. Therefore, in (**Chapter 7**) the strength and thermal stability of Lewis acid sites have also been evaluated in the alkane dehydrogenation process, which is an energy-intensive reaction involving the activation of the C-H bond.



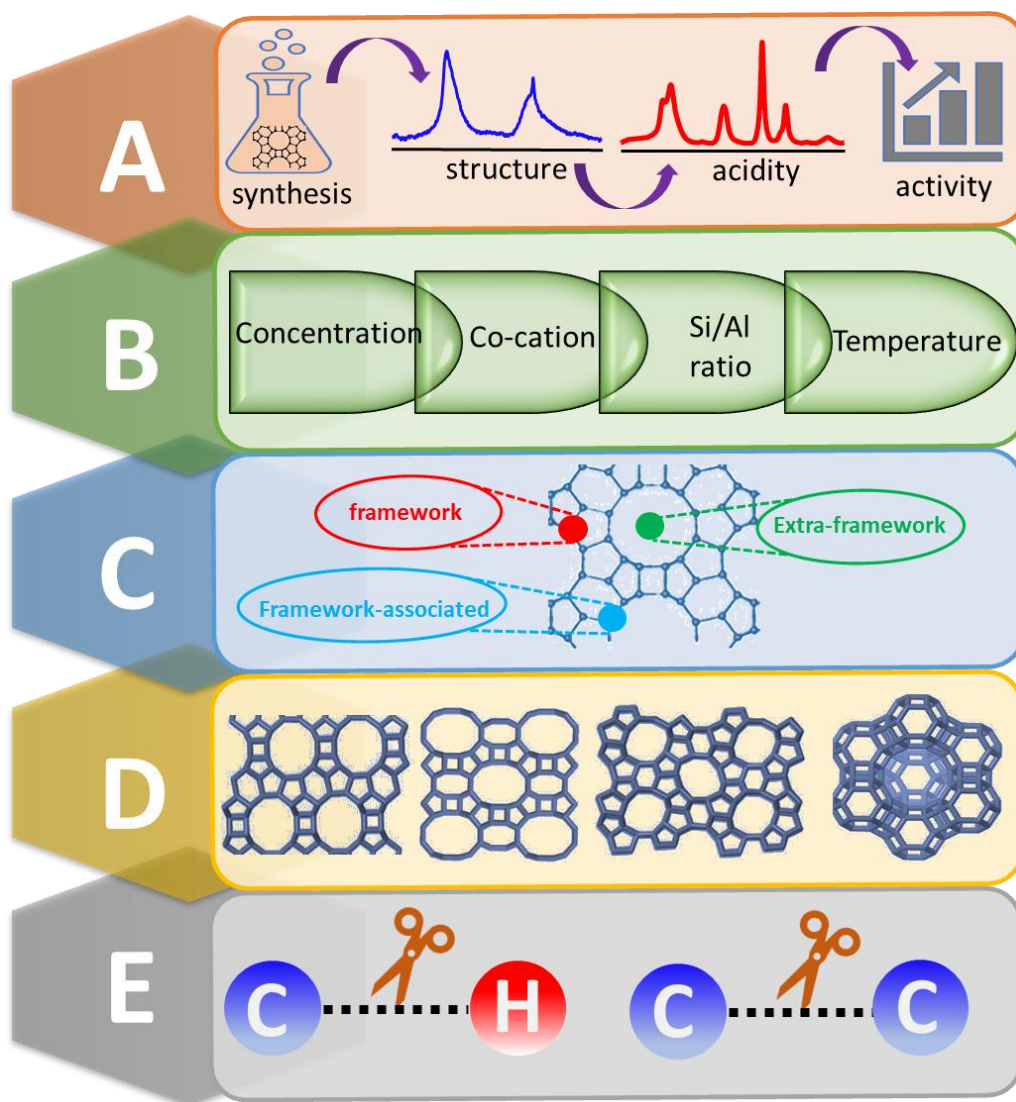


Figure 2.1: Schematic representation of the scope of the thesis. (A) Incorporation of EFAl species in zeolites by ion-exchange and their correlation to Lewis acidity (B) How can zeolite's Si/Al ratio, the presence of co-cation, and the synthesis conditions affect the structure, generation, and activity of EFAl LAS? (C) Distribution of framework, framework-associated and extra-framework aluminum and their associated acidity and activity; how does the generation of LAS affect the inherent BAS of a zeolite? (D) Factors affecting the incorporation of ion-exchanged Lewis acid sites in different zeolite morphologies. (E) Is the strength and thermal stability of ion-exchanged Lewis acid sites capable of activating C-C and C-H bonds?

# Chapter 3

## Materials and Methods

This chapter discusses the details of the material synthesis procedures and characterization methods used to study the zeolite materials in this work. The respective chapters will contain separate "Materials and Methods" sections to specify each chapter's techniques and synthesis procedures.

### 3.1. Synthesis Procedures

This work involves the modifications of zeolite samples through various post-synthetic procedures, including aluminum-exchange, sodium-exchange, ammonium-exchange, and acid treatments. The general details of the synthesis protocols used in the coming chapters are discussed in the following section (unless otherwise specified in the respective chapters).

#### 3.1.1. Aluminum Ion-exchange Procedure

In their proton forms, zeolite powders were aluminum-exchanged using a facile aluminum ion-exchange (Al-IE) procedure<sup>180, 181</sup>. **Figure 3.1** presents the schematic of the Al-IE procedure.

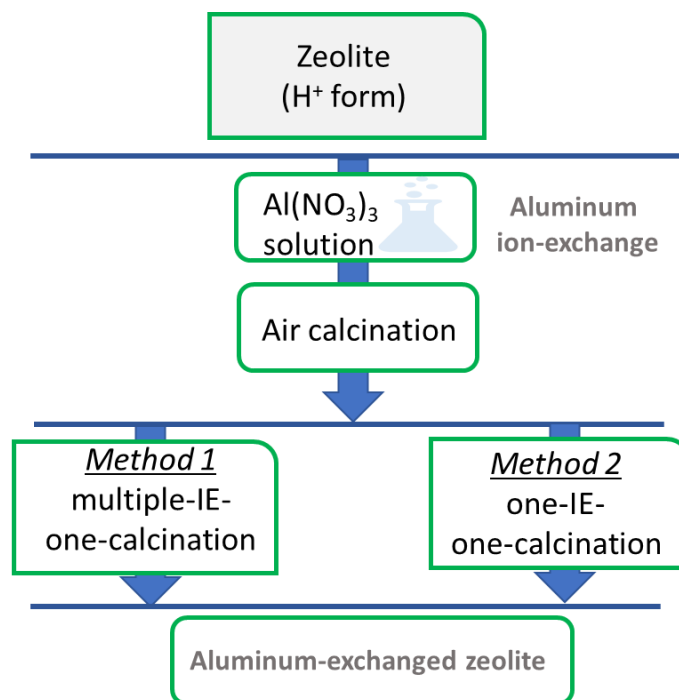


Figure 3.1: Schematic representation of the aluminum-exchange procedure.

Zeolite powder was immersed in  $\text{Al}(\text{NO}_3)_3$  solution ( $72 \text{ mL g}_{\text{zeolite}}^{-1}$ ) at room temperature for 6 hours. The pH of zeolite containing ion-exchange solution was constantly kept around 4 by dropwise addition of 0.2M solution of ammonium acetate. The resultant suspension was filtered and washed with deionized water to remove all the nitrates and dried overnight at about 373K under a high vacuum. The ion-exchanged zeolite powder was calcined at 823K in static air for 6 hours at a 1K/min heating ramp. The zeolite powders were ion-exchanged 1 to 5 times by two methods of ion-exchange: (1) multiple IE followed by single calcination and (2) Multiple IE, with each IE followed by one calcination step.

### **3.1.2. Ammonium Ion-exchange Procedure**

In their proton forms, zeolite powders were converted to ammonium form by ammonium ion-exchange ( $\text{NH}_4^+$ -IE) procedure. Zeolite powder was stirred in 0.2 M solution of ammonium nitrate ( $100 \text{ mL g}_{\text{zeolite}}^{-1}$ ) overnight at 353 K with pH monitoring. The resultant suspension was then filtered at room temperature and rinsed thoroughly with deionized water to remove all nitrates. This procedure was repeated twice to obtain the zeolites in their ammonium form.

### **3.1.3. Sodium Ion-exchange Procedure**

Zeolite powders, in their proton forms, were converted to sodium form by ammonium ion-exchange (Na-IE) procedure. Zeolite powder was allowed to stir in 0.1 M solution of sodium nitrate ( $60 \text{ mL g}_{\text{zeolite}}^{-1}$ ) overnight at room temperature with pH monitoring. The suspension was then filtered and washed thoroughly with deionized water to remove all nitrates. This procedure was repeated twice. The zeolite was dried overnight at 373 K in a drying oven and then calcined in static air at 823K for 6 hours at a 1K/min heating ramp.

### **3.1.4. Dealumination Procedure**

Zeolite powders, in their proton forms, were dealuminated under drastic conditions. Zeolite powder was stirred in a 13M  $\text{HNO}_3$  solution ( $20 \text{ mL g}_{\text{zeolite}}^{-1}$ ) at 373 K for 20 hours. The powder was filtered, washed thoroughly with deionized water, and dried at 373 K overnight, followed by calcination at 823K in static air at a heating ramp rate of 1 K/min to obtain dealuminated zeolites.

## 3.2. Material Characterization

The zeolite materials are studied employing various characterization techniques. To avoid recurrence, the following section discusses the standard details of the working principle and the experimental conditions. Any change in experimental conditions in the respective chapters will be addressed accordingly.

### 3.2.1. Fourier Transform infrared (FTIR) spectroscopy of adsorbed molecules

**Working Principle:** Fourier Transform Infrared (FTIR) Spectroscopy identifies the molecular structures based on the atom vibration and rotation<sup>182</sup>. **Figure 3.2** presents the schematic of the basic principle of the FTIR spectrometer. A polychromatic source directs infrared radiations to a beam splitter, dividing the incident beam into two beams: one beam reflects to a moving mirror and the other to a fixed mirror. The beam recombines after being reflected at each mirror. This generates constructive or destructive interference based on the distance between the movable and the fixed mirror. Two beams are produced from here; one goes back to the source, and the other directs to the samples. The detector measures the latter, followed by the generation of an interferogram and conversion by a Fourier transform to a conventional transmittance or absorbance spectrum.

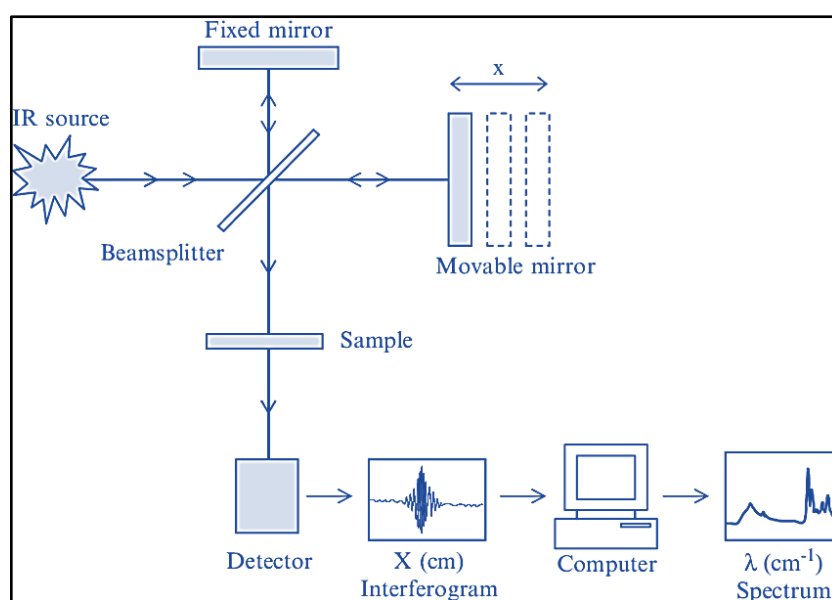


Figure 3.2: Schematic representation of the basic principle of FTIR spectroscopy. To produce a transmittance spectrum, FTIR spectrometers can either be a double beam (where the background is continuously subtracted from the sample) or a single beam (where the background has to be subtracted from the sample). Most systems multiply the transmittance value by 100 to give percent transmittance ( $T$ ). However, the absorbance ( $A$ ) scale,

where  $A = -\ln(T/100)$ , is more frequently used for quantitative analysis, as according to Beer's law, absorbance is linearly related to the sample concentration<sup>183, 184</sup>. Reproduced with permission from ref.<sup>185</sup> Copyright 2012 Springer Science + Business Media, LLC.

**Experimental Conditions:** FTIR spectra of zeolites using probe molecules were measured in an in-situ FTIR setup with a Thermo Nicolet iS50 FTIR spectrometer with a DTGS detector. **Figure 3.3** presents the schematic of this in-situ FTIR setup for measuring FTIR spectra over adsorbed pyridine, ~20 mg of zeolite powders was used to make self-supporting discs. The discs were placed in an IR transmission cell attached to a vacuum line and activated at 723 K for 4 h. The activated zeolites were dosed with pyridine by exposing them to 3 torr of pyridine at about 423 K for 0.5 h and then evacuated for 0.5 h. The FTIR spectra of zeolites before and after pyridine adsorption were acquired at an optical resolution of  $4\text{ cm}^{-1}$  by taking 128 scans.

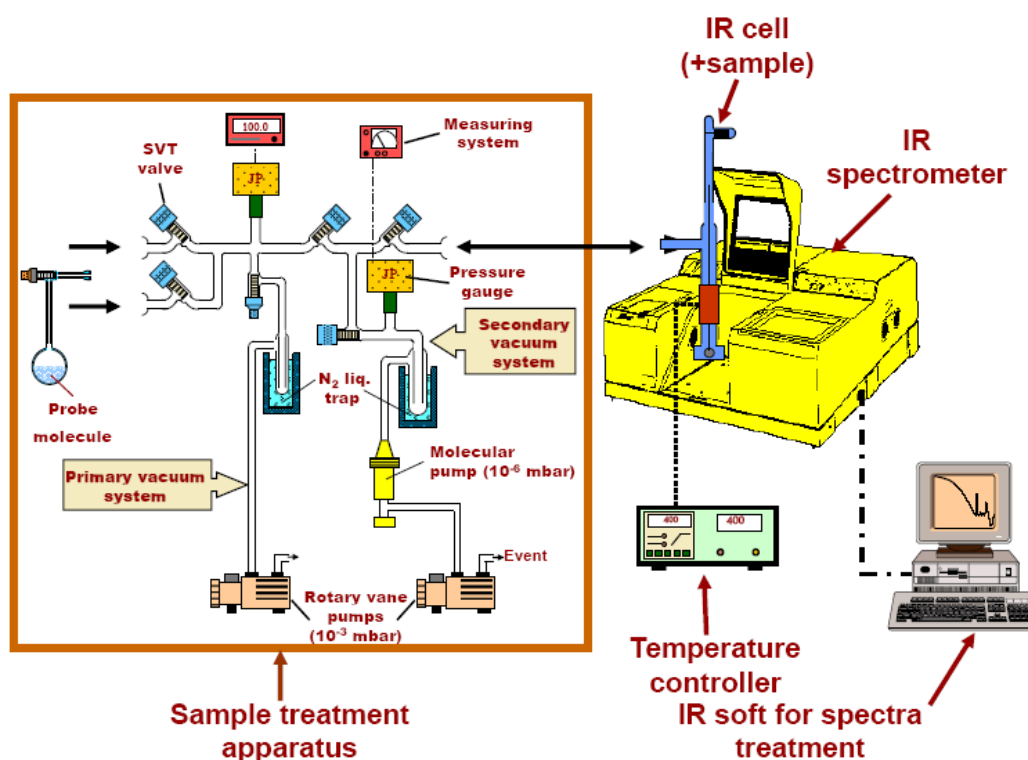


Figure 3.3: Schematic representation of in-situ FTIR setup used to acquire FTIR spectra of samples with adsorbed probe molecules. It consists of a vacuum rig, including a turbomolecular pump and oil pump 1.5 with pressure control, IR spectrometer, and temperature controller. The in-situ IR cell is made of quartz, which enables high-temperature treatment of the sample up to 873K. The electrical furnace uses a 48V AC source for the heating, which is controlled by a temperature-programmed controller. The system of magnets can manipulate the sample inside the cell.

For the measurement of FTIR spectra over adsorbed carbon monoxide, a similar method was followed to activate the samples, as described above, using pyridine as the probe molecule. A low-temperature vacuum cell, cooled with liquid nitrogen, was used for carbon monoxide adsorption. The calibrated aliquots of carbon monoxide were introduced stepwise until complete saturation of the active sites, and the spectra were recorded immediately; a Pfeiffer gauge monitored pressure. The processing software package OMNIC 9.3 was used to obtain the difference spectra by subtracting the spectra of activated samples from the spectra of zeolites with pyridine/carbon monoxide. All the presented FTIR spectra were normalized to the mass of sample discs.

### 3.2.2. Solid-state NMR spectroscopy

**Working Principle:** Nuclear magnetic resonance (NMR) spectroscopy probes the chemical structure, three-dimensional assembly, and motion of molecules and materials. When a nucleus with non-zero spin is placed in an external magnetic field, the degenerate nuclear spin states exhibit dissimilar energies, with a difference  $\Delta E$  according to the following equation.

$$\Delta E = \gamma \hbar (1 - \sigma) B_0 \quad (3.1)$$

where  $\gamma$  is the ratio of a nucleus' magnetic moment to its angular momentum, called gyromagnetic ratio, a characteristic property of each isotope.  $\sigma$  is the chemical shielding around a nucleus, and  $B_0$  is the strength of the external magnetic field (typically 5-28T). Upon electromagnetic radiofrequency irradiation, transitions can be induced between these nuclear spin states, which are sensitive to the electronic distribution of a nucleus. These transitions correspond to nuclear magnetic resonance (NMR)<sup>186, 187</sup>. As the different nuclei of a given isotope in a sample have different chemical shielding ( $\sigma$ ), they exhibit different resonances that identify the chemical structure.

**Figure 3.4** presents the schematics of the working mechanism of solid-state NMR. Among the spectroscopic techniques that can be utilized to characterize solid catalysts, solid-state NMR (SSNMR) spectroscopy has emerged as a powerful technique with atomic-level resolution in the structural investigation of catalysts<sup>188, 189</sup>. Magic-angle spinning (MAS) aids the acquisition of high-resolution SSNMR spectra. In the MAS NMR technique, the powdered samples are allowed to spin at  $\sim 10$  to 100 kHz about an axis oriented at  $54.74^\circ$  with respect to the applied magnetic field (**Figure 3.4b**). This significantly reduces the orientation-dependent anisotropic interactions, substantially narrowing the solid-state NMR spectra<sup>190</sup>.

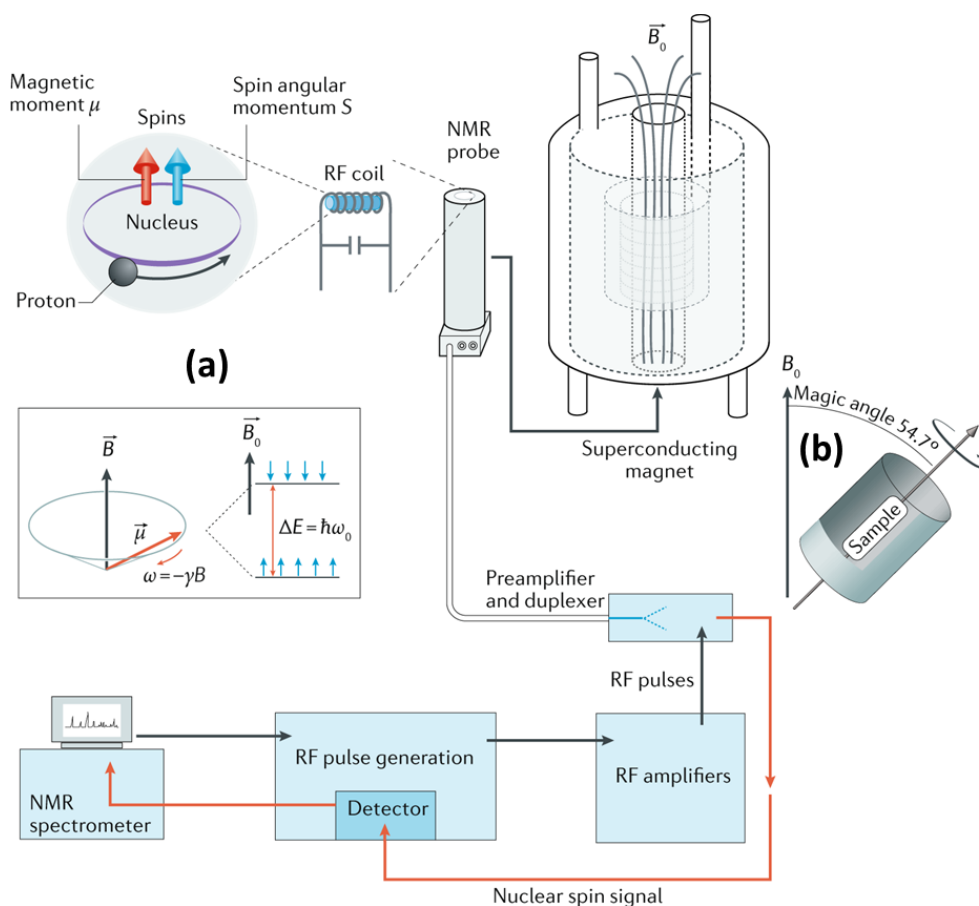


Figure 3.4: Schematic representation of the working mechanism of solid-state NMR. Reproduced with permission from ref.<sup>190</sup> Copyright 2021, Springer Nature Limited. Solid samples, packed in cylindrical rotors, are usually placed in the NMR probe, which is then inserted into the superconducting magnet. The oscillatory signals generated by the nuclear spin are then amplified and converted through Fourier transform to conventional NMR spectra.

**Experimental Conditions:** Solid-state  $^{27}\text{Al}$  MAS NMR spectroscopy was performed at a resonance frequency of 79.5 MHz for aluminum ( $^{27}\text{Al}$ ) nucleus using a Bruker AVANCE III HD spectrometer and Bruker 400 MHz Ultra-Shield magnet. Prior to experiments, 20-50 mg of zeolite sample was packed into 4 mm zirconia rotors at room temperature. The  $^{27}\text{Al}$  MAS NMR spectra were recorded by spinning the packed rotors at a rate of 10 kHz for 3000 scans. The  $^{27}\text{Al}$  chemical shift was referenced to  $\text{AlNH}_4(\text{SO}_4)_2 \cdot 12\text{H}_2\text{O}$ . Similarly, solid-state multiple quantum magic angle spinning nuclear magnetic resonance (MQMAS NMR) spectra were recorded using a Bruker 700MHz Ultra-Shield spectrometer. The 2.5 mm zirconia rotors packed at room temperature, with 2-8 mg of zeolite powders, were allowed to spin in a 2.5 mm MAS probe with 20 kHz spinning speed, and the  $^{27}\text{Al}$  MAS NMR spectra were recorded for 1440 scans. Spectral analysis and deconvolutions were performed using Topspin 4.0.9 software

package (provided by Bruker) and dmfit32 software, respectively <sup>191</sup>. The deconvolution of MQMAS spectra was done using the Czjzek line shape model <sup>192</sup> to determine the quadrupolar coupling constant ( $Q_{cc}$ ) and isotropic chemical shift ( $\delta_{iso}$ ).

### 3.2.1. X-ray diffraction (XRD)

**Working Principle:** X-ray diffraction relies on the elastic scattering of photons from crystalline materials' atomic planes, thus treating them as mirrors. Figure 3.5a presents the schematic of the X-ray diffraction principle. An X-ray wavelength  $\lambda$  strikes the atomic planes of spacing  $d$  at an incident angle  $\theta$ . The beam scatters from the planes at an angle  $\theta$ , equal to the incident angle with respect to the crystalline plane. As the wavelength of X-rays is of the same order of magnitude as the interatomic distances in crystals (0.15 – 0.5 nm), the scattering leads to constructive and destructive interference phenomena <sup>193</sup>. The geometric considerations show that constructive interference will occur for certain angles,  $\theta_B$ , depending on the interplanar spacing  $d$  (**Figure 3.5a**). Bragg's equation relates the angular position of diffracted X-rays to the lattice spacing and determines the structure of crystalline materials. For X-ray powder diffraction, the diffractometers typically use Bragg-Brentano optics (**Figure 3.5b**), where a high-intensity divergent X-ray beam is focused on the fixed sample to obtain strong diffraction signals <sup>194</sup>.

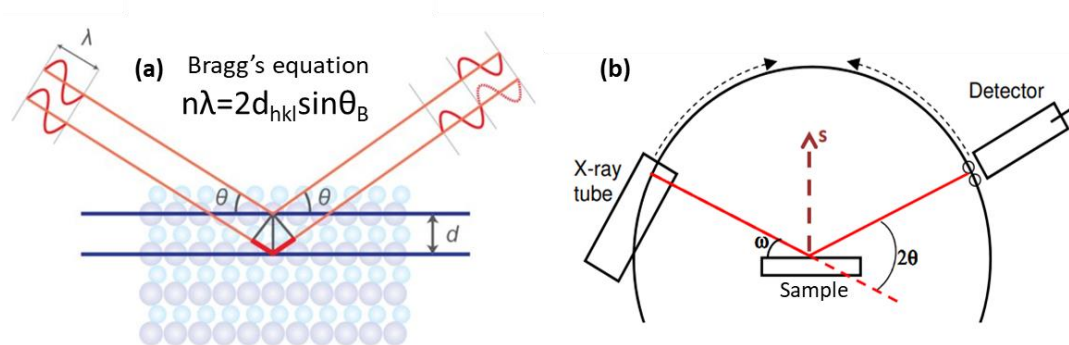


Figure 3.5: (a) Schematic representation of X-ray diffraction principle. The relative phase shifts between X-rays scattered from the first and second planes are due to the red-marked distance. In Bragg's equation, ' $\theta_B$ ' is the Bragg angle, ' $n$ ' is the order of the diffraction maxima, and  $hkl$  are the Miller indices of the crystallographic plane <sup>195</sup>. (b) Bragg-Brentano geometry for powder x-ray diffractometers. In a  $\theta$ : $\theta$  instrument (e.g., PANalytical X'Pert Pro), the sample is fixed, the tube rotates at a rate -  $\theta$  °/min, and the detector rotates at a rate of  $\theta$  °/min. In the Bragg-Brentano geometry, the diffraction vector ( $s$ ) that bisects the angle between the incident and scattered beam is always normal to the sample's surface. It is inspired by ref <sup>193</sup>.

**Experimental Conditions:** The XRD technique characterized the crystalline structure of the zeolites. XRD patterns were obtained at room temperature on a PANalytical X'Pert PRO MPD



diffractometer with Cu K $\alpha$  ( $\lambda = 0.15418$  nm) radiation. The  $2\theta$  scans covered the range 3–60° with a scan rate of 1°/min; the accelerating voltage and applied current were 40 kV and 100 mA, respectively. Before measurement, the samples were pressed into sample holders. Origin software was used to calculate the diffraction parameters using the XRD data.

### 3.2.2. N<sub>2</sub> physisorption

**Working Principle:** The technique used to analyze the specific surface area of materials is based on the Brunauer–Emmett–Teller (BET) theory which explains the physical adsorption of gas molecules on a solid surface. Depending on the available solid surface and the relative pressure, gas molecules fill the sample's surface layer by layer. Filling the first layer enables the measurement of the material's surface area, as the amount of gas adsorbed when the monolayer is saturated is proportional to the sample's entire surface area. The complete adsorption/desorption analysis is called an adsorption isotherm.

As the specific surface area is scale-dependent, with no single true value of specific surface area definable, the BET surface area measurements vary depending on the adsorbate molecule and its adsorption cross section<sup>196</sup>. A BET surface area analyzer usually employs inert gas adsorbates like argon, carbon dioxide, and nitrogen to probe the sample surface area. However, the standard BET analysis is generally carried out with nitrogen gas. **Figure 3.6** presents the schematic of the BET surface area analyzer.

**Experimental Conditions:** Porous characteristics of the samples were analyzed by nitrogen adsorption-desorption on a Micromeritics Tristar instrument at 77 K according to the BET method for the specific surface area and the Barrett-Joyner-Halenda (BJH) method for the pore size distribution. The volume of micropores in zeolites was determined using the t-Plot method. Before each analysis, zeolite powders were thoroughly degassed at 523K overnight.

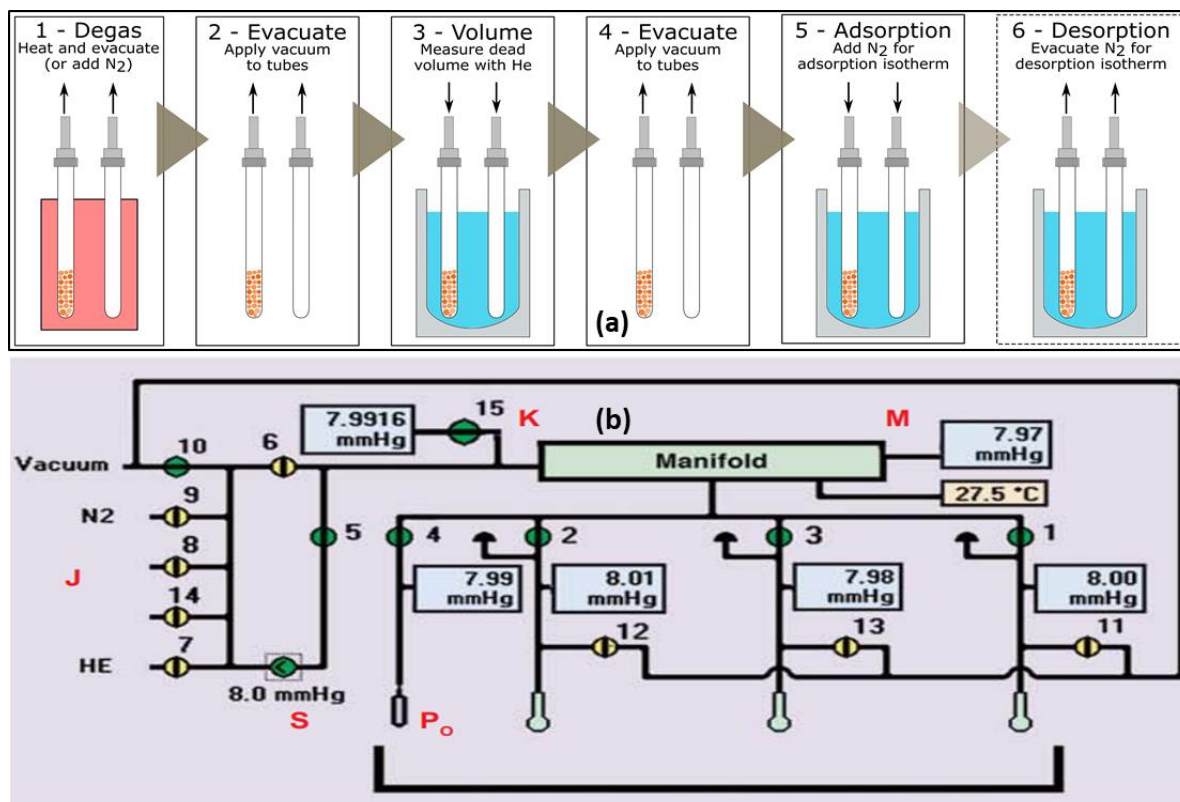


Figure 3.6: (a) Steps involved in nitrogen adsorption-desorption measurement. (b) schematic representation of the BET surface area analyzer. The figure is taken from Micrometrics. The instrument employs static volumetric gas adsorption, introducing consecutive known amounts of *adsorbate* to the sample holder, which is kept at liquid nitrogen temperature (77 K). Adsorption of the injected gas onto the sample causes the pressure to decrease slowly until an equilibrium pressure is established in the manifold. The equilibrium pressure is measured by a transducer chosen according to the pressure range where adsorption is established during the experiment. The static volumetric technique is useful for evaluating surface area and pore size in the region of micro and mesopores<sup>197</sup>.

### 3.2.3. Inductively coupled plasma optical emission spectroscopy

**Working Principle:** The inductively coupled plasma optical emission spectrometry (ICP-OES) technique is a multi-functional analytical technique for analyzing an element in different samples with a wide range of concentrations. This technique uses the spontaneous emission of ions or atoms excited through a radio frequency discharge<sup>198</sup>. The schematic of the working principle (ICP-OES) is presented in **Figure 3.7**.

The liquid samples, via injection system, are introduced into inductively coupled argon plasma where molecules are ionized and atomized in the plasma followed by excitation. When high-energy electrons return to a lower energy level, ions and atoms release photons. These photons are collected on the detector, which separates them depending on their emission wavelengths<sup>199</sup>. The detector measures the signal intensity of respective wavelengths proportional to the element's abundance in the plasma.

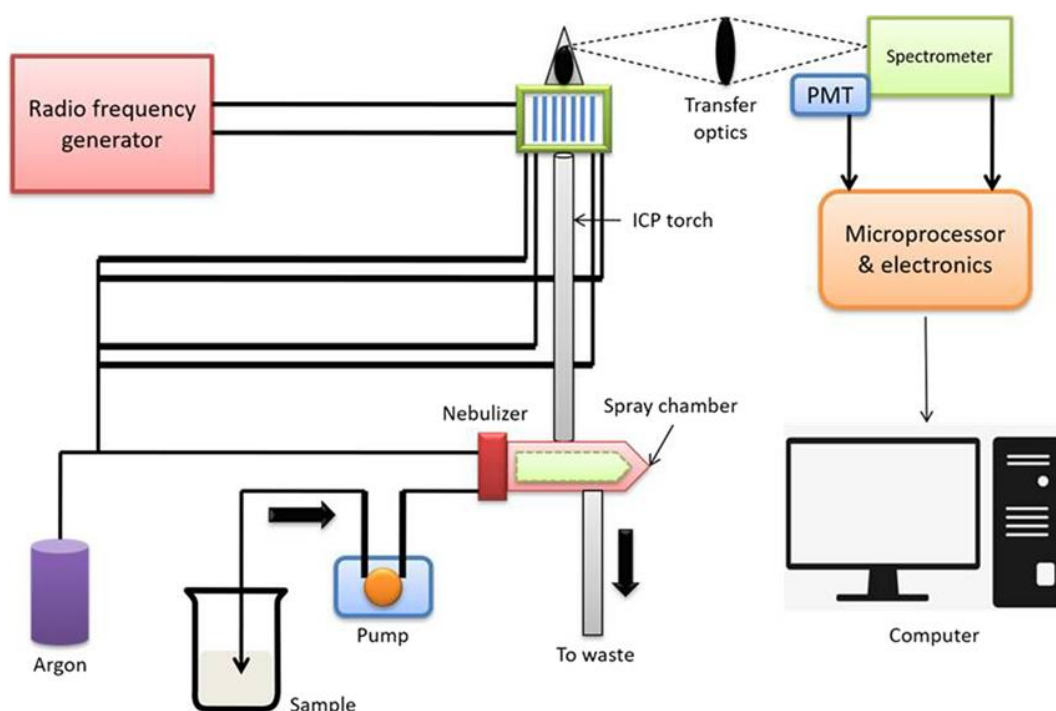


Figure 3.7: Schematic representation of ICP-OES instrument. Reproduced with permission from ref. <sup>199</sup> Copyright 2021, Springer Science Business Media, LLC, part of Springer Nature. The liquid sample transforms into an aerosol via the aerosol nebulization process in the argon plasma channel. Therefore, solid samples require the acid digestion or extraction of the analyte, whereas the gas samples can be directly introduced into the instrument <sup>200, 201</sup>.

**Experimental Conditions:** The metal content of zeolite samples was measured using ICP-OES. Before measurements, 30-50 mg of zeolite powders were dissolved in a mixture containing 60% nitric acid (3–5 mL) and hydrofluoric acid (3–5 mL) and diluted with deionized water (25–40 mL). The mixture was stirred at room temperature to completely digest the zeolite, then diluted to the calibration range. The metal contents of the resulting solutions were determined using a Horiba Ultra 2 ICP-OES instrument equipped with a photo-multiplier tube detector. Si/Al ratio was calculated based on the Al and Si content of the samples determined from ICP-OES.

### 3.3. Catalytic Evaluation by Gas Chromatography-Flame Ionization Detection

**Working Principle:** Gas chromatography is a separation technique providing very high resolution and is well suited for analyzing complex mixtures of substances present in different concentrations <sup>202</sup>. The GC analytes must be volatile enough so that the mobile phase can carry them from the injection port to the detection system. A flame ionization detector (FID) relies on the generation of ions during the combustion of the sample species, assuming that the sample

compounds will ionize inside of a flame, whereas the carrier gas will not. Helium and nitrogen, commonly employed carrier gases with FID sensors, produce negligible ions in the combustion flame. **Figure 3.8** shows the schematic of the working principle of GC-FID. A hydrogen flame, which produces little ions in combustion, ionizes any gas molecules exiting through the chromatograph column except carrier gas. Once the sample molecules interact with the flame, the conductivity of the flame increases compared to the conductivity without the sample molecules. Consequently, the detector circuit detects the increased conductivity with a measurable electrical signal <sup>203</sup>.

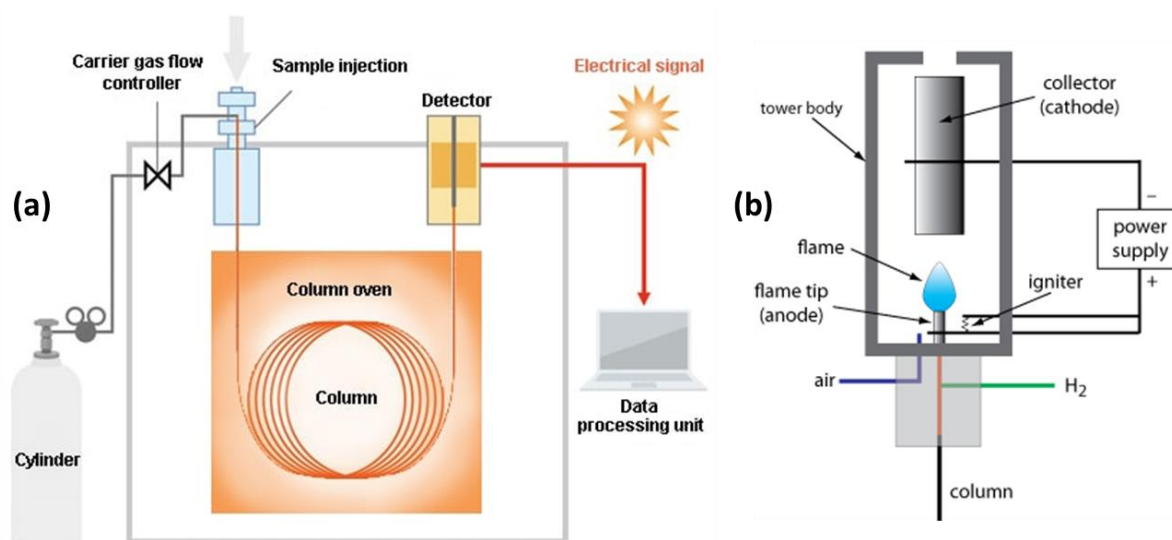


Figure 3.8: Schematic representation of the working principle of (a) GC and (b) FID detector.

**Experimental Conditions:** Zeolite catalysts were activated in an inert atmosphere before testing. For activation, 200 g (unless otherwise specified) of as-synthesized zeolite powder, packed into a ceramic boat and mounted horizontally in a tubular oven, was heated in a nitrogen atmosphere at 723 K for 6 h with a heating ramp rate of 1 K/min. For measuring the catalytic activity of zeolite powders, the Meerwein-Ponndorf-Verely reduction reaction was carried out using a zeolite sample as the catalyst. In a typical experiment, 2.5 mmoles of 4-*tert*-butylcyclohexanone, 50 mL of isopropanol (additionally dried over molecular sieves), and 1 mmole of 1,3,5-tri-*tert*-butylbenzene (internal standard) were added to a 3-necked round-bottom flask. The activated catalyst was added to the reaction mixture, and the reaction was carried out in N<sub>2</sub> atmosphere at 355 K with constant stirring. *Cis*- and *trans*-4-*tert*-butylcyclohexanol were the only products formed. Samples were taken regularly and analyzed by a GC equipped with a CP-52-Carbowax column (50 m and an inner diameter of 0.53 mm) and FID <sup>81</sup>. Based on the concentrations of 4-*tert*-butylcyclohexanone calculated from GC-FID

data, the initial rate of reaction was determined as the slope of the linear regression in the time-concentration plot between zero time and 110 minutes of reaction time.

$$\text{Conc. of 4-tert-butylcyclohexanone} = -\frac{\text{rate of reaction}}{\text{time}} + C \quad (3.2)$$

Where the *conc.* of 4-*tert* butylcyclohexanone is in mmolL<sup>-1</sup>, time is in minutes, and *C* is the concentration at zero time.”

## **Chapter 4**

### **Correlating Lewis acid activity to extra-framework aluminum species in zeolite Y introduced by ion-exchange**

#### **Contributions**

The content of Chapter 1 was published in *Journal of Catalysis* 408 (2022) 24–35. The content is distributed under the terms of the Creative Commons CC-BY-NC-ND license. The synthesis, NMR, XRD, nitrogen physisorption characterization and catalytic evaluation of materials was performed by the author the thesis

## 4.1. Introduction

Zeolite Y with FAU topology is widely employed at refineries<sup>40</sup>. Its three-dimensional pore system, large pore openings, and large micropore volume make it an excellent material for catalytic applications as well as ion-exchange, separation, and gas adsorption<sup>6-8</sup>. Brønsted acidity in zeolite Y originates from a hydroxyl group bridging framework silicon and aluminum atoms<sup>24</sup>. The ultra-stable zeolite Y (USY), prepared by controlled post-synthetic steaming treatment of Y, shows much higher thermal and hydrothermal stability as well as catalytic activity as compared to non-steamed Y zeolites<sup>162, 204, 205</sup>. Consequently, USY is extensively utilized as an efficient catalyst in fluid catalytic cracking reactions<sup>27, 28</sup>. The post-synthetic steaming process results in partial dealumination of the framework, thus forming extra-framework aluminum species<sup>206, 207</sup>. Such extra-framework aluminum species in zeolite Y have been reported to exist in many different forms:  $\text{Al}^{3+}$ ,  $\text{Al}(\text{OH})^{2+}$ ,  $\text{Al}(\text{OH})_2^+$ ,  $\text{AlOOH}$ ,  $\text{Al}(\text{OH})_3$ , and  $\text{Al}_2\text{O}_3$ . Of all the possible forms, the cationic extra-framework species  $\text{Al}^{3+}$ ,  $\text{Al}(\text{OH})^{2+}$ , and  $\text{Al}(\text{OH})_2^+$  are regarded as strong Lewis acid sites capable of hydrocarbon conversion by a hydride transfer mechanism<sup>156, 157</sup>. The generation of framework LAS by isomorphous substitution of heteroatom is a widely used approach. However, this protocol is not effective for zeolite Y as the acid treatments do not entirely dealuminate zeolite Y<sup>123</sup>.

Even though considerable research has been done into the different ways of generating LAS in Y and other zeolites<sup>129-132</sup>, a sound correlation among the structure of the LAS, their amount, and catalytic performance is still missing. The work, described in this chapter, introduces Lewis acidity into zeolites through simple ion-exchange of aluminum species. The aluminum in a proton form of zeolite Y was ion-exchanged by using different concentrations of the aluminum precursor; the resulting catalysts were characterized by means of XRD, nitrogen-physisorption, pyridine and CO-probed FTIR, <sup>27</sup>Al-NMR and catalytic testing in the Meerwein-Ponndorf-Verley (MPV) reduction of 4-*tert* butylcyclohexanone.

This work aims to systematically correlate the structure of newly introduced Lewis acidic species to their concentration and catalytic performance, which is a valuable development toward understanding the nature and role of Lewis acid sites in zeolite catalysis. Ion-exchanged aluminum occupied the non-framework positions without destroying the zeolite skeleton, and these EF species were found to dramatically increase the number of Lewis acid sites. The increase in the concentration of these LAS resulted in a proportional increase in the catalytic activity of the modified zeolite catalysts for the conversion of 4-*tert* butylcyclohexanone to 4-

*tert* butylcyclohexanol. Moreover, these aluminum-exchanged zeolite materials, with pronounced Lewis acidity, can possibly serve as potential catalysts for various LAS catalyzed reactions of industrial significance e.g. FCC reactions and biomass conversion to value-added chemicals<sup>32, 37, 38, 208</sup>.

## 4.2. Materials and Methods

**Chemicals and Materials:** Commercially available zeolite Y (CBV-760, Si/Al=30, proton form) was purchased from Zeolyst International and was used as received. Aluminum nitrate nonahydrate (99.99%) was provided by ABCR and used without further modification and anhydrous Ammonium acetate (NH<sub>4</sub>(CH<sub>3</sub>COO)) (99%) was purchased from Merck.

**Material Preparation:** The parent proton form of CBV-760 is referred to as ‘Y30-H<sup>+</sup>’, where ‘30’ stands for the Si/Al ratio of zeolite. Starting from Y30-H<sup>+</sup> aluminum-exchanged samples were prepared by Al-IE procedure discussed in **Section 3.2.1**. using 0.1M to 0.5M concentration of Al(NO<sub>3</sub>)<sub>3</sub> solution. The zeolite powders were ion-exchanged 1 to 5 times by two methods of ion-exchange: (1) multiple IE followed by single calcination and (2) Multiple IE, with each IE followed by one calcination step. The labels of the ion-exchanged samples were chosen so that the parent code is followed by the total number of ion-exchanges, the concentration of the ion-exchange solution in brackets and the method of ion-exchange (described above), respectively. For example, for Y30-5IE(0.1Al)-1: Y30 is the parent code, 5IE indicates that a total number of 5 ion-exchange treatments, 0.1Al is the molar concentration (0.1 M) of the ion-exchange solution and 1 represents the preparation (ion-exchange) of the sample by the first method of IE treatment, multiple IE followed by single calcination.

**Characterization:** The integrity of the zeolite structure after the ion-exchange treatments was characterized by XRD. Textural characteristics of the samples were analysed by nitrogen adsorption-desorption on a Micromeritics Tristar II 3020 instrument at 77 K. The metal contents of the as-synthesized samples were determined by ICP-OES using a Horiba Ultra 2 instrument equipped with a photo-multiplier tube detector. Solid-state <sup>27</sup>Al MAS NMR spectra were recorded on a Bruker 400 MHz Ultra-Shield magnet and AVANCE III HD spectrometer, at a spinning rate of 10 kHz for 3000 scans. The solid state <sup>27</sup>Al MQMAS spectra were recorded with 2.5 mm probe on a Bruker 700MHz Ultra-Shield spectrometer at 20 kHz for 1440 scans. FTIR spectra of zeolite powders before and after pyridine and carbon monoxide adsorption were acquired on a Thermo Nicolet iS50 FTIR spectrometer equipped with a DTGS detector by taking 128 scans at optical resolution of 4 cm<sup>-1</sup>. The difference spectra were obtained by



subtracting the spectra of activated samples from those of the samples with adsorbed pyridine and carbon monoxide. All the FTIR spectra were normalized to the weight of the sample discs.

**Catalytic testing:** For measuring the catalytic activity of zeolite powders, the Meerwein-Ponndorf-Verely reduction reaction was carried out as discussed in **Section 3.3**. In the catalytic experiment, 200 mg of zeolite catalyst, 2.5 mmol of 4-*tert*-butylcyclohexanone, 50 mL of isopropanol and 1 mmol of 1,3,5-tri-*tert*-butylbenzene (internal standard) was used.

### 4.3. Results and Discussion

**Physical chemical properties:** Figure 4.1(a) shows the XRD patterns of all the aluminum-exchanged FAU-type zeolites and the pristine zeolite. The diffraction peaks, exclusive for the crystal structure of zeolite Y, were observed after ion-exchange, indicating that no crystalline impurities formed during preparation. The absence of reflections related to any alumina types suggests that aluminum species are well-dispersed and do not form larger aluminum oxide agglomerates. Due to this dispersion, the characteristic Y topology of the zeolite materials remains intact after modification. The incorporated aluminum species are most likely homogeneously distributed throughout the zeolite. This is because under the simplistic ion-exchange conditions, it cannot be expected to have zoning of the incorporated Al species upon ion-exchange. The relative crystallinity of the aluminum-exchanged samples was determined by calculating the total area of each of nine strong diffraction peaks in the  $2\theta$  region between  $5^\circ$  and  $35^\circ$  and comparing these with that of the same peaks in the pattern of the pristine zeolite<sup>209</sup>.

Many researchers apply this procedure to calculate the relative crystallinity in zeolite Y and other zeolites, where the parent zeolite is considered to be 100% crystalline and the crystallinity of modified samples is calculated relative to the parent zeolite<sup>210, 211</sup>. Therefore, the pristine Y30-H<sup>+</sup> sample was assumed 100% crystalline. After aluminum ion-exchange, the relative crystallinity of all the modified zeolites decreases only slightly, from 91 to 79% (**Table 4.1**). Y30-1IE(0.1Al)-1, prepared by a single ion-exchange with the lowest concentration of aluminum, retains 91% of its crystalline structure.

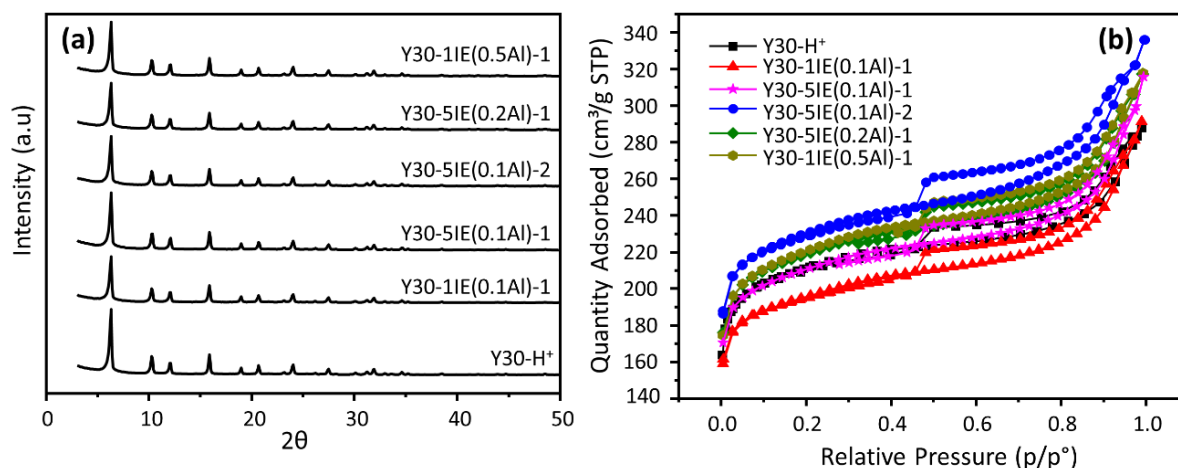


Figure 4.1: (a) PXRD patterns of pristine zeolite and aluminum ion-exchanged samples. (b) N<sub>2</sub> adsorption isotherms (with offset values on Y-axis) of pristine zeolite Y and aluminum ion-exchanged samples.

An increase, in the number of ion-exchange treatments with the same concentration of the Al-source and as well as in the concentration of aluminum-source, causes a decrease in the crystallinity. Y30-5IE(0.1Al)-1 and Y30-5IE(0.1Al)-2, which were synthesized by the same number of ion-exchange treatments as well as the same concentration of aluminum-source showed 82% and 90% crystallinity, respectively. The lattice parameter  $a_0$  of the parent zeolite was 24.85 Å (typical of zeolite Y) and it decreases after the incorporation of aluminum. The lattice parameter of all the exchanged zeolites ranges from 24.64 to 24.55 Å (**Table 4.1**). The  $a_0$  value of Y30-1E(0.1Al)-1 is 24.63 Å.

Increasing the number of ion-exchange treatments with the same concentration of aluminum-source gives the lattice parameter of 24.62 Å. The change in the lattice parameter of ion-exchanged samples as compared to pristine zeolite (24.85 Å) is significant. This may be due to the loss of some of the water molecules during ion-exchange, thus causing a slight compression of the unit cell, and/or it might also be that the incorporated extra-framework species do not occupy the ion-exchange positions<sup>212</sup>. Some of the water molecules attached to the extra-framework/framework-associated aluminum species of the pristine zeolite can be removed upon aluminum ion-exchange followed by calcination. Either the loss of water molecules can be due to certain redistribution of balancing cations in the framework of zeolite or due to the reason that incorporated extra-framework species do not occupy the ion-exchange positions<sup>213</sup>. In order to accommodate the incorporated charge-neutral aluminum species, some water molecules might detach upon calcination, depending upon the concentration of IE solution and Si/Al ratio of ion-exchanged zeolite.

**Figure 4.1b** shows the nitrogen adsorption/desorption isotherms of all the ion-exchanged materials. The nitrogen sorption isotherm of the parent zeolite exhibits Type-IV hysteresis typical of Y zeolite with a Si/Al ratio of about 30. Y30-H<sup>+</sup> is synthesized by post-synthetic steaming and mineral acid leaching of Y2.6 (which exhibits Type-I isotherm particular for microporous crystalline materials) under severe conditions, as suggested by Remy et al.<sup>65</sup> and Zhang et al.<sup>209</sup>.

Table.1: Physical and chemical characterization of pristine and modified Y zeolites

Zeolite	$S_{\text{BET}}$	$V_{\text{total}}$	$V_{\text{micro}}$	$S_{\text{micro}}$	$S_{\text{meso}}$	$a_0$	Crystallinity <sub>rel</sub>
Sample	$\text{m}^2\text{g}^{-1}$	$\text{cm}^3\text{g}^{-1}$	$\text{cm}^3\text{g}^{-1}$	$\text{m}^2\text{g}^{-1}$	$\text{m}^2\text{g}^{-1}$	Å	%
Y30-H <sup>+</sup>	740	0.44	0.33	555	180	24.85	100
Y30-1IE(0.1Al)-1	760	0.49	0.32	600	200	24.63	91
Y30-5IE(0.1Al)-1	749	0.49	0.23	520	231	24.62	82
Y30-5IE(0.1Al)-2	770	0.47	0.31	560	210	24.60	90
Y30-5IE(0.2Al)-1	735	0.46	0.29	550	183	24.55	85
Y30-1IE(0.5Al)-1	745	0.33	0.25	715	180	24.64	79

Owing to the post-synthesis modifications under severe conditions, mesopores are produced (besides the zeolite's intrinsic microporous structure), resulting in hysteresis in the desorption branch of nitrogen physisorption<sup>209</sup>. Initiated by a sharp increase in the amount of nitrogen adsorbed, up to  $P/P_0=0.02$ , the isotherm follows a gradual uptake of nitrogen, which is followed by a steep increase in nitrogen uptake at relative pressures above 0.8 and a hysteresis loop (from  $P/P_0=0.98$  to  $P/P_0=0.5$ ) respectively. After ion-exchange, the ad- and desorption isotherms are very similar to those of the original zeolite. However, after ion-exchange, hysteresis continues from  $P/P_0=0.99$  to  $P/P_0=0.48$ . **Table 4.1** lists the porous characteristics of all zeolites that were extracted from the nitrogen sorption data. Zeolite Y30-H<sup>+</sup> has a micropore volume of  $0.33 \text{ cm}^3\text{g}^{-1}$  and a BET surface area of  $740 \text{ m}^2\text{g}^{-1}$ . All aluminum-exchanged zeolites have a similar micropore volume, ranging from  $0.25$  to  $0.33 \text{ cm}^3\text{g}^{-1}$  and a BET surface area between  $735$  and  $770 \text{ m}^2\text{g}^{-1}$ . These features indicate that the zeolites retain their porous structure after Al-IE.

**Solid-state NMR spectroscopy:** **Figure 4.2** shows the  $^{27}\text{Al}$  MAS NMR spectra of the zeolites recorded under ambient conditions. **Figure A2** presents the  $^{27}\text{Al}$  MQMAS spectra of all the samples; the Czjzek line shape model <sup>192</sup> was applied to these spectra to calculate the isotropic chemical shift ( $\delta_{\text{iso}}$ ) and quadrupolar coupling constant ( $Q_{\text{cc}}$ ) (**Table 4.3**).

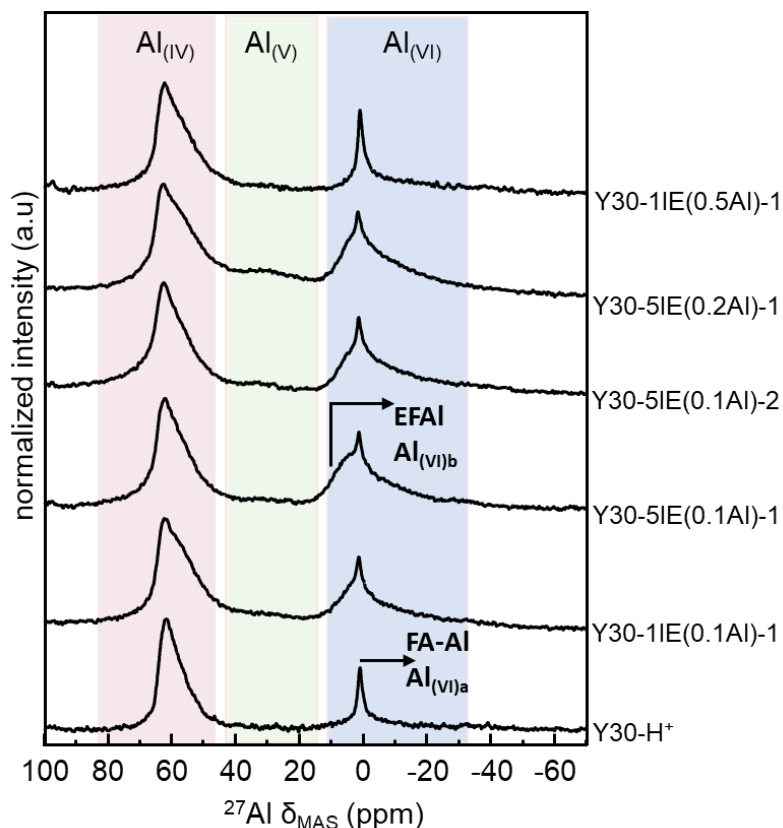


Figure 4.2:  $^{27}\text{Al}$  MAS NMR spectra of zeolite Y before and after aluminum ion-exchange

The  $^{27}\text{Al}$  MAS NMR spectrum for pristine zeolite in its proton form (Figure 4.2) clearly exhibits two resonances, one at 61 ppm ( $\text{IV}_a$ ), relates to the four-coordinated framework aluminum, and one at 0 ppm ( $\text{VI}_a$ ), due to aluminum entities with octahedral coordination <sup>61, 62</sup>. The resonance at 0 ppm for the H-form of the zeolite is explained as the framework-associated aluminum species, because the reinsertion of these species into a crystalline framework position is possible after conversion to the  $\text{NH}_4^+$ -form (**Figure A1**) <sup>66</sup>. Apart from these two resonances, there is a slight broadening of the tetrahedral peak towards high field. The  $^{27}\text{Al}$  MQMAS spectrum (Figure A2a) of this sample reveals that this broadening is due to another tetrahedrally coordinated aluminum species at  $\delta_{\text{iso}} = 59$  ppm ( $\text{IV}_b$ ), appearing on the diagonal, with a small  $Q_{\text{cc}}$  of 1 MHz.

After ion-exchange, the  $^{27}\text{Al}$  MAS NMR spectra show some interesting features. First, apart from the sharp resonance at 0 ppm, a broad asymmetric resonance at  $\sim 3$  ppm ( $\text{VI}_b$ ) emerges in

all the modified samples. The MQMAS spectra (**Figure A2b-d**) of aluminum-exchanged samples reveal that this peak is associated with an isotropic broadening along the diagonal with a little horizontal expansion and a  $Q_{cc}$  of about 2.7 MHz. With an increase in the amount of exchanged aluminum (**Table 4.2**), the intensity of this resonance increases. Therefore, the broad and asymmetric resonance at  $\sim 3$  ppm ( $VI_b$ ) correlates to the incorporated aluminum species, which have mainly octahedral coordination. The broad resonance is apparent in all the modified samples with the lowest intensity in Y30-1IE(0.5Al)-1. Second, the spectra show further broadening of the tetrahedral resonance upon sample modification, the maximum being observed for the samples with the highest degree of aluminum exchange (**Figure 4.2** and **Table 4.2**).

Table 4.2 Concentration of aluminum obtained from ICP and quantitative analysis of aluminum concentration (mmoles  $g^{-1}$ ) in different coordination obtained by deconvolution of  $^{27}Al$  MAS NMR spectra using NMR parameters from  $^{27}Al$  MQMAS NMR;  $Al(IV)_a$ ,  $Al(IV)_b$ ,  $Al(IV)_c$ ,  $Al(V)$ ,  $Al(VI)_b$ , and  $Al(VI)_a$  correspond to aluminum with isotropic chemical shifts at 61, 59, 62, 37, 3, and 0 ppm respectively.

Zeolite Sample	$Al_{ICP}$	$Al(IV)_a$	$Al(IV)_b$	$Al(IV)_c$	$Al(V)$	$Al(VI)_a$	$Al(VI)_b$
Y30- $H^+$ form	1.13	0.54	0.37	-	-	0.24	-
Y30-1IE(0.1Al)-1	2.2	0.50	0.3	0.41	-	0.16	0.83
Y30-5IE(0.1Al)-1	3.04	0.67	0.41	0.74	-	0.25	0.97
Y30-5IE(0.1Al)-2	3.25	0.59	0.38	0.68	0.1	0.17	1.12
Y30-5IE(0.2Al)-1	2.8	0.54	0.26	0.7	-	0.21	1.08
Y30-1IE(0.5Al)-1	2.06	0.67	0.52	0.3	-	0.37	0.20

The MQMAS spectra illustrate that this enhanced quadrupolar broadening is due to the distorted tetrahedral species  $Al(IV)_c$  at  $\sim 62$  ppm. **Table 4.3** shows the quantitative distributions of aluminum species in different coordination, calculated from spectral deconvolution utilizing the MQMAS NMR parameters. The results suggest a clear increase in EFAl  $Al(VI)_b$  species due to ion-exchange with an accompanying increase in the concentration of the distorted tetrahedral species. Moreover, Y30-5IE(0.1Al)-1 and Y30-5IE(0.1Al)-2 bear more octahedrally coordinated aluminum compared to the sample that was ion-exchanged only once with a higher concentration of the ion-exchange solution.

The extra-framework aluminum species in zeolite Y have been reported to exist in various cationic forms and as neutral complexes, e.g.  $\text{Al}^{3+}$ ,  $[\text{AlO}]^+$ ,  $[\text{Al}(\text{OH})]^{2+}$ ,  $[\text{Al}(\text{OH})_2]^+$ ,  $\text{AlOOH}$ ,  $\text{Al}(\text{OH})_3$ , and  $\text{Al}(\text{OH})_3(\text{H}_2\text{O})_3$ <sup>214</sup>. The solid-state aluminum NMR investigations and DFT calculations, carried out for dealuminated zeolite Y, may suggest the existence of cationic  $[\text{Al}(\text{OH})]^{2+}$  entities and neutral  $\text{Al}(\text{OH})_3$  complexes in sodalite cages and the super cage of faujasite skeleton<sup>215, 216</sup>. The Lewis acidic nature of these species has also been discussed in these studies. Mota et al.<sup>150, 217</sup>, while comparing the stability of six different extra-framework aluminum species by DFT, suggested that the  $[\text{Al}(\text{OH})]^{2+}$  species have the most favorable structure. Li. et al.<sup>218</sup> identified the octahedral  $[\text{Al}(\text{OH})_2(\text{H}_2\text{O})_4]^+$  structure with rigid and mobile  $\text{H}_2\text{O}$  ligands as the preferred intra-zeolite aluminum structure in hydrated and dealuminated zeolite Y.

A detailed DFT study and ab initio thermodynamic analysis on the extra-framework aluminum species in faujasite zeolite, mainly the neutral  $\text{Al}(\text{OH})_3(\text{H}_2\text{O})_3$ ,  $\text{Al}(\text{OH})_3$ , and  $\text{AlOOH}$  complexes and the cationic  $[\text{Al}(\text{OH})_2]^+$ ,  $[\text{AlO}]^+$ ,  $[\text{Al}(\text{OH})]^{2+}$ , and  $\text{Al}^{3+}$  complexes was performed by Liu. C et al.<sup>219</sup>. The cationic clusters with high a formal charge ( $\text{Al}^{3+}$  and  $[\text{Al}(\text{OH})]^{2+}$ ), were suggested to occupy the SII site of the zeolite framework. Furthermore, it appears that of all the mononuclear extra-framework aluminum species, only  $\text{Al}(\text{OH})_3(\text{H}_2\text{O})_3$  species exist in an octahedral coordination. Other mononuclear aluminum centers (neutral and monovalent) exhibit tetrahedral coordination. Based on these previous studies, we assume that, in aluminum-exchanged zeolite Y, the extra-framework species responsible for the octahedral resonance at ~3 ppm ( $\text{VI}_b$ ) are present either as neutral  $\text{Al}(\text{H}_2\text{O})_3(\text{OH})$  species or  $\text{Al}_2\text{O}_3$  nano clusters or as  $\text{Al}^{3+}$  or  $[\text{Al}(\text{OH})]^{2+}$  cations. Similarly, we also propose that the distorted tetrahedral species  $\text{Al}(\text{IV}_c)$  responsible for the resonance at ~59 ppm are part of the extra-framework aluminum species (EFAI) and are probably present as  $\text{Al}_2\text{O}_3$  nano clusters. Such cationic mononuclear EFAI species self-organize during high-temperature activation into di-, tri-, and tetrameric species. The dimeric species can stabilize equally well at SII, SIII (super cage) and SI' (sodalite cage) of the faujasite framework bearing distorted tetrahedral or trigonal-bipyramidal coordination<sup>219</sup>. The tri- and tetra nuclear complexes, however, are preferentially stabilized inside the small sodalite cages.

**Lewis Acidity:** For the characterization of acidic sites by FTIR, we utilized pyridine and carbon monoxide as the probe molecules. Owing to their different size and basicity, detailed information can be obtained about the strength and/or nature of acid sites probed by these molecules. Pyridine is one of the desirable probe molecules, because known molar extinction

coefficients of pyridine vibrations in the IR region enable the quantitative analysis of acid sites of a solid catalyst<sup>49, 220</sup>. The dotted-line spectra in **Figure 4.3a** illustrate the FTIR spectra of the samples before adsorption of pyridine in the hydroxyl-stretching region. In the spectrum of Y30-H<sup>+</sup>, the band at 3747 cm<sup>-1</sup> appears to be due to terminal silanol groups whereas the features at 3630 cm<sup>-1</sup> (HF) and 3565 cm<sup>-1</sup> (LF) correspond to the BAS, the bridging Si-OH-Al, in the super cage and sodalite cage, respectively<sup>77</sup>. In aluminum ion-exchanged zeolites prior to pyridine adsorption, apart from the three typical bands mentioned above a band also appears at a lower frequency of 3597 cm<sup>-1</sup>, which corresponds to the hydroxyl groups on the extra-framework entities and the interaction of the silanols with the extra-framework material<sup>78, 79</sup>.

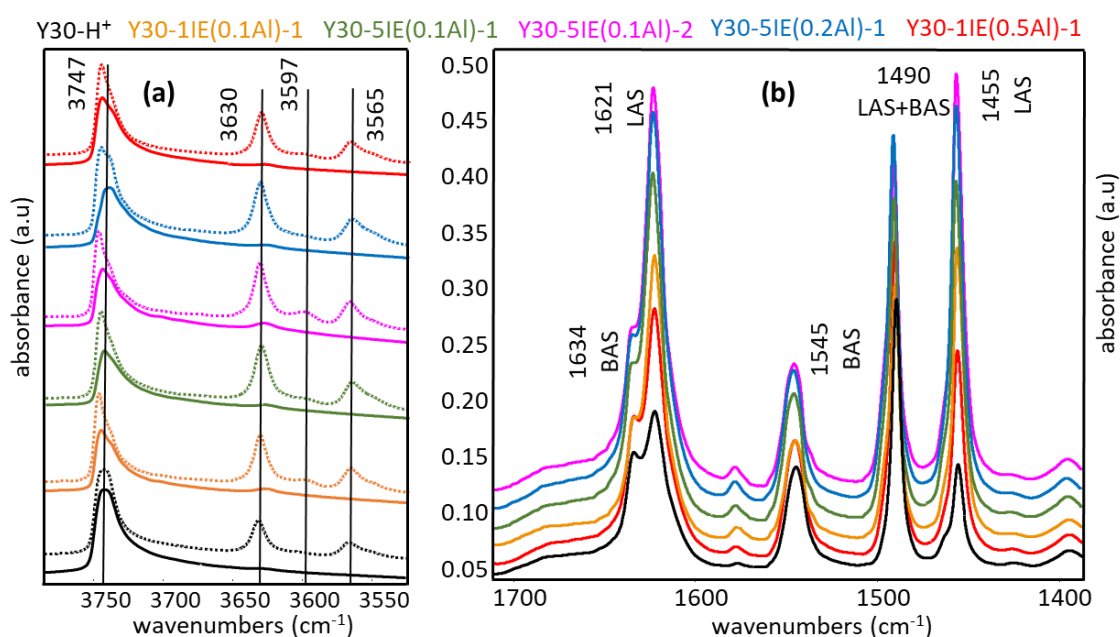


Figure 4.3 Pyridine-FTIR difference spectra in (a) OH stretching region; dotted lines represent spectra of evacuated samples at 723K and solid lines represent spectra after pyridine adsorption at 423K followed by evacuation at 423K. (b) Pyridine stretching region obtained by subtraction of spectra after activation at 723K from spectra after pyridine adsorption at 423K followed by evacuation at 423K.

**Figure 4.3b** illustrates FTIR spectra after pyridine adsorption over zeolite catalysts in the region of pyridine vibrations. The bands at 1455 cm<sup>-1</sup> and 1621 cm<sup>-1</sup> are due to the interaction of pyridine with LAS and the bands at 1545 cm<sup>-1</sup> and 1634 cm<sup>-1</sup> correspond to BAS. The band at 1500 cm<sup>-1</sup> is a superposition of LAS and BAS; it can be termed as structure insensitive and cannot be used for quantification. There is strong variation in the intensity of the bands corresponding to LAS i.e. 1455 cm<sup>-1</sup> and 1621 cm<sup>-1</sup> in the spectra of the samples after ion-exchange. The spectrum of the parent zeolite shows the lowest intensity; the intensity of these peaks increases

in all the ion-exchanged samples in the order Y30-1IE(0.5Al)-1<Y30-1IE(0.1Al)-1<Y30-5IE(0.1Al)-1<Y30-5IE(0.2Al)-1<Y30-5IE(0.1Al)-2. There is no significant variation in the intensity of peaks of the BAS-bound pyridine ( $1545\text{ cm}^{-1}$  and  $1634\text{ cm}^{-1}$ ).

Typical of zeolite Y, after pyridine adsorption, the HF and LF bands of the parent zeolite shift to lower frequencies because the BAS responsible for these features are being probed by pyridine. In aluminum ion-exchanged zeolites, following interaction with pyridine, the LF band and the new band at  $3597\text{ cm}^{-1}$  entirely disappear, whereas the HF band shows a sharp decrease in intensity (**Figure 4.3a**). An in-depth analysis of the silanol band in the FTIR difference spectra of the OH stretching region (**Figure A3**), shows that silanols decrease slightly in intensity along with the appearance of a band at the lower frequency of  $3597\text{ cm}^{-1}$ . It might be that the incorporated aluminum might generate weak BAS in the vicinity of the silanols, which, after the pyridine interaction, tend to perturb the silanols, resulting in a decrease in the intensity of the Si-OH band<sup>77</sup>. The remaining band intensity of the HF bridging hydroxyls after pyridine adsorption suggests that some of the BAS are not probed by pyridine possibly due to a blockage of some of the BAS species in the super cages due to the inserted aluminum.

**Table 4.3** lists the quantification of LAS and BAS of zeolite catalysts, considering the area under the peaks, at  $1450\text{ cm}^{-1}$  and  $1540\text{ cm}^{-1}$ , and employing the available molar extinction coefficients of these peaks<sup>221</sup>. The concentration of LAS of pristine zeolite is  $0.07\text{ mmol g}^{-1}$  and there is a large increase in the Lewis acid content after incorporation of aluminum. The content of Lewis acid sites after ion-exchange ranges between  $0.11$  and  $0.23\text{ mmol g}^{-1}$ , with Y30-5IE(0.1Al)-2 reaching the maximum LAS content. It is evident from the quantitative data that the BAS content of ion-exchanged samples ( $0.12$  to  $0.14\text{ mmol g}^{-1}$ ) is almost the same as that of the parent zeolite ( $0.14\text{ mmol g}^{-1}$ ). A careful comparison of Y30-5IE(0.1Al)-2 and Y30-5IE(0.1Al)-1 shows that the former zeolite contains more LAS than the latter, thus suggesting that the 2<sup>nd</sup> ion-exchange is better for introducing extra-framework Lewis acidity into zeolite Y, while retaining the crystallinity of the sample to a greater extent.



Table 4.3 (a) Concentrations of Na, Si, and Al (mmoles g<sup>-1</sup>) measured by ICP and calculated Si/Al ratio based on the elemental concentrations obtained from ICP. (b) LAS and BAS content from pyridine-FTIR (mmoles g<sup>-1</sup>). (a) Carbon monoxide-FTIR analysis; the relative content of acidic sites was obtained from the sum of the areas of deconvoluted peaks at 2230 cm<sup>-1</sup> and 2195 cm<sup>-1</sup> for LAS and at 2180 cm<sup>-1</sup> for BAS respectively at carbon monoxide dosage of 10 torr.

Zeolite Sample	Elemental analysis <sup>a</sup>				Pyridine <sup>b</sup>		Carbon monoxide <sup>c</sup>	
	Na	Si	Al	Si/Al ratio	LAS	BAS	LAS	BAS
Y30-H <sup>+</sup>	0.1	34.5	1.13	30.5	0.07	0.14	0.13	1.44
Y30-1IE(0.1Al)-1	0.1	33.5	2.2	15.2	0.15	0.13	1.10	1.52
Y30-5IE(0.1Al)-1	1.5	31.2	3.04	9.6	0.16	0.13	1.11	1.61
Y30-5IE(0.1Al)-2	0.26	32.5	3.25	10.6	0.23	0.12	1.25	1.65
Y30-5IE(0.2Al)-1	0.1	32.9	2.7	12.2	0.19	0.14	1.16	1.36
Y30-1IE(0.5Al)-1	1.17	32.3	2.45	13.2	0.11	0.14	0.67	1.31

Being a strong base, pyridine probes the majority of all the accessible acid sites without differentiating between the probed acid sites in terms of their strength. Some of the sites are sterically inaccessible. Therefore, the use of carbon monoxide as a probe molecule has the additional advantages of differentiating among the acid sites, depending on their strength, because carbon monoxide has acidic strength weaker than pyridine <sup>72</sup>. **Figure 4.4** shows the FTIR spectra of absorbed carbon monoxide over acidic zeolites at low temperature (100 K).

Uptake of carbon monoxide by acidic catalysts at low temperature causes the bonding of carbon monoxide to the LAS and the formation of H bonds with hydroxyl groups. The carbon monoxide-FTIR spectrum of Y30-H form illustrates three characteristic bands at 2230, 2195, and 2180 cm<sup>-1</sup> in the carbon monoxide stretching region (**Figure 4a**) due to three-coordinate LAS, five-coordinate LAS, and surface hydroxyl groups (BAS), respectively <sup>77</sup>. All the bands below 2180 cm<sup>-1</sup> are due to physisorbed carbon monoxide. The band at 2157 cm<sup>-1</sup> corresponds to carbon monoxide interacting with the silanols <sup>80</sup>. The initial doses of carbon monoxide result in its coordination with LAS, resulting in the band at 2230 cm<sup>-1</sup>, and successively, the band at

2195  $\text{cm}^{-1}$ , thus differentiating between them based on their strength. Further doses of carbon monoxide probe the BAS and yield the band at 2180  $\text{cm}^{-1}$ .

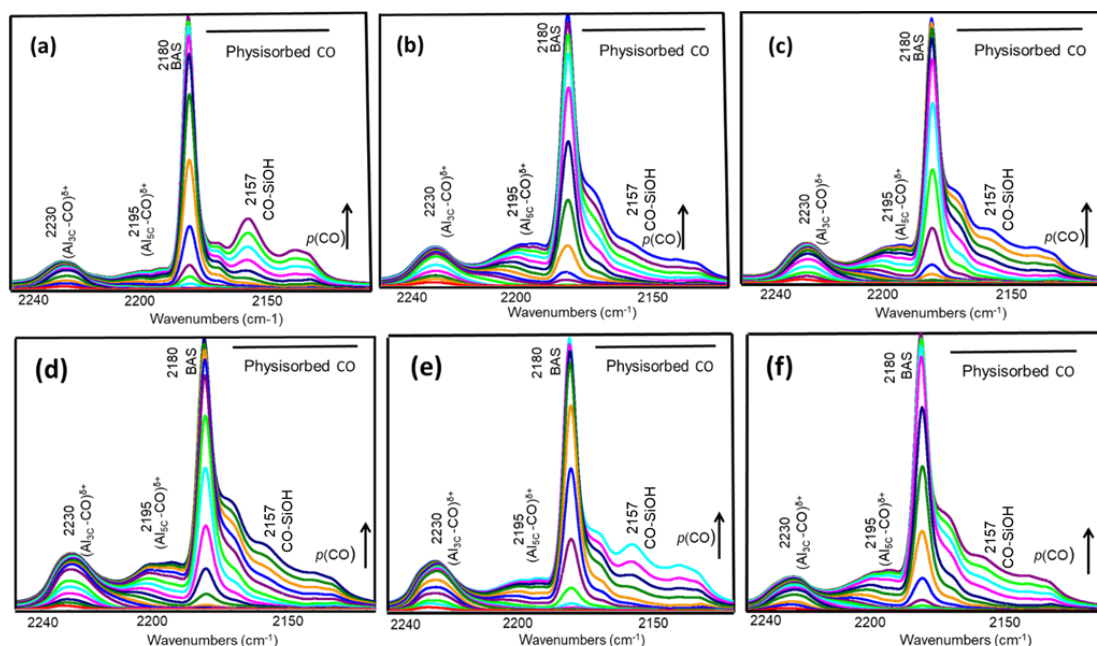


Figure 4.4 FTIR difference spectra over adsorbed carbon monoxide in the carbon monoxide stretching region obtained by subtraction of spectra of cold wafers at 70 K from spectra after CO adsorption at 70K. (a) Y30- $\text{H}^+$  (b) Y30-1IE(0.1Al)-1 (c) Y30-5IE(0.1Al)-1 (d) Y30-5IE(0.1Al)-2 (e) Y30-5IE(0.2Al)-1 (f) Y30-1IE(0.5Al)-1.

FTIR difference spectra in the hydroxyl-stretching region display ( $\nu'(\text{OH})$ ) bands, at 3749  $\text{cm}^{-1}$ , due to Si-OH species, and at 3630  $\text{cm}^{-1}$  (HF) and 3570  $\text{cm}^{-1}$  (LF), due to BAS, respectively, thus giving the fingerprint information (**Figure A4**). Carbon monoxide adsorption leads to perturbation of the HF-OH stretching vibrations with the appearance of the perturbed ( $\nu'(\text{OH})$ ) band at about 3280  $\text{cm}^{-1}$  (OH stretching region) and a CO ( $\nu(\text{CO})$ ) stretching vibration at around 2170  $\text{cm}^{-1}$  (CO stretching region). Moreover, the spectra reveal that the BAS, responsible for the LF band at 3570  $\text{cm}^{-1}$ , are not being fully probed by carbon monoxide.

Almutairi et al. suggest different reasons that carbon monoxide does not or hardly influence(s) the LF ( $\nu'(\text{OH})$ ) of zeolite Y<sup>181</sup>. The reasons given include solvent effects, the much less acidic nature of the LF-OH groups compared to the HF-OH groups, steric effects, and the presence of the probe molecules in the large cavities. Apart from these, the electrostatic interactions of the (LF)OH hydroxyl groups with the framework oxygen atoms in the sodalite cages can interfere with the proton mobility<sup>181, 222</sup>. Another considerable feature, which prevails after carbon monoxide adsorption, is the negative-positive absorbance of the Si-OH band in the difference spectra (**Figure A4b-f**), owing to a slight shift in the silanol band. This might be due to a slight

decrease in temperature of the sample due to improved contact, induced by carbon monoxide <sup>223-225</sup>. After ion-exchange, the spectra mainly demonstrate bands, similar to those of pristine zeolite in the spectral regions of carbon monoxide and the corresponding hydroxyl stretching vibrations (**Figure 4b-f**).

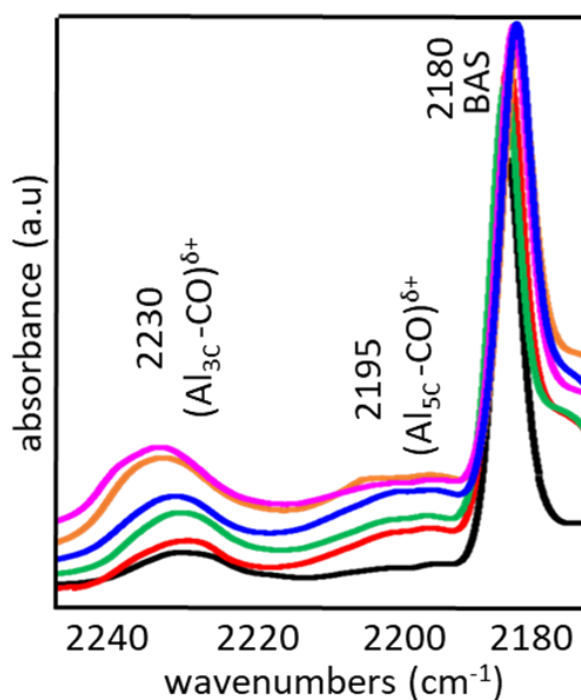
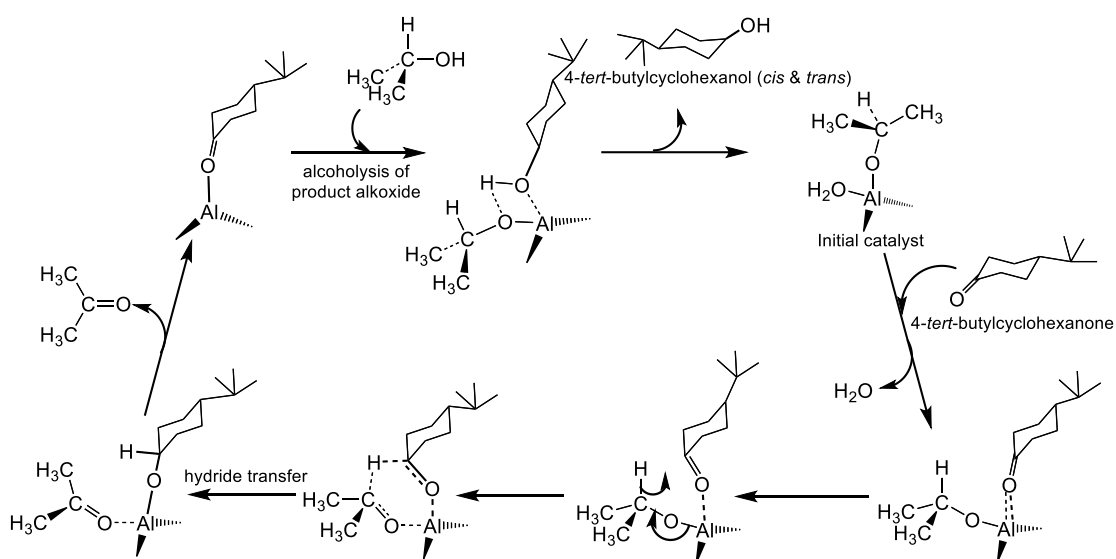


Figure 4.5 Carbon monoxide probed FTIR difference spectra at a carbon monoxide dosage of 10 torr in the carbon monoxide stretching region: Y30-H<sup>+</sup> (black), Y30-1IE(0.1Al)-1 (green), Y30-5IE(0.1Al)-1 (blue), Y30-5IE(0.1Al)-2 (pink), Y30-5IE(0.2Al)-1 (orange) and Y30-1IE(0.5Al)-1 (red).

**Figure 4.5** shows the carbon monoxide-FTIR spectra of the original zeolite and those of ion-exchanged zeolites compared at a similar dosage of 10 torr and gives the variations in the intensity of the LAS bands before and after ion exchange. The three-coordinate LAS at band 2230 cm<sup>-1</sup> is more intense than the five-coordinate LAS one 2195 cm<sup>-1</sup> in the spectrum of the parent zeolite. Aluminum ion-exchange gives rise to a sharp increase in the intensity of both LAS bands. The integrated peak area values of these bands, calculated for all the samples at this particular CO dosage of 10 torr (Table 4.2), reveal the pronounced increase in LAS, which is in line with the trends observed for pyridine-probed FTIR. However, there is no considerable variation in BAS in exchanged zeolites, compared to the parent zeolite (Figure 4.5 and Table 4.3). The fact, that the concentration of BAS in exchanged zeolites does not change, proposes

that the incorporated aluminum species, responsible for increasing LAS concentration, are not occupying the charge-balancing positions of zeolite.

**Lewis acid catalytic activity:** The catalytic activity of the acid was determined by performing Meerwein-Ponndorf-Verley reduction of 4-*tert* butylcyclohexanone (**Scheme 4.1**). **Figure 4.6a** illustrates the catalytic conversion of 4-*tert* butylcyclohexanone versus time on stream. *Cis*- and *trans*-4-*tert* butylcyclohexanol are the two products of the reaction with a greater proportion of *trans*-ol during the course of reaction (**Figure 4.6b**). **Table 4.4** gives the initial catalytic rate and selectivity to *cis* and *trans* products.



Scheme 4.1 Proposed reaction schematic for Meerwein-Ponndorf-Verely reduction of 4-*tert* butylcyclohexanone over Lewis acid zeolite catalyst <sup>81</sup>

In line with FTIR analysis, the pristine zeolite, due to its low intrinsic Lewis acidity, reached only 23% conversion of ketone after 24 h at a very low initial reaction rate of about  $0.02 \text{ mmolL}^{-1}\text{min}^{-1}$ . Cumulative *cis* and *trans* alcohols were produced at a ratio of about 25:75. The rates of reaction increase sharply (from  $0.17$  to  $0.45 \text{ mmolL}^{-1}\text{min}^{-1}$ ) after aluminum ion-exchange, with the catalysts reaching very high conversion (90-100%). Y30-5IE(0.1Al)-2 shows the highest initial rate of reaction of  $0.45 \text{ mmolL}^{-1}\text{min}^{-1}$ , whereas Y30-1IE(0.5Al)-1 has the lowest one ( $0.17 \text{ mmolL}^{-1}\text{min}^{-1}$ ) and the lowest maximum conversion among the ion-exchanged zeolites. The rates of reaction follow the amounts of LAS determined by carbon monoxide-FTIR and pyridine-FTIR (**Table 4.4**). Apart from the increase in the initial rate of reaction using aluminum-exchanged catalysts, there is an observable difference in the cumulative ratio of *cis* and *trans* 4-*tert* butylcyclohexanol during time on stream. As evident in **Figure A5**, the initial *cis*-alcohol formation is followed by exclusive formation of *trans*-alcohol with time on stream

for all catalysts. The increase in the reaction rates results in a steady increase in *trans*-alcohol; this gives the impression that there is an increase in the selectivity of the *trans* product and a decrease in the selectivity of *cis*-ol.

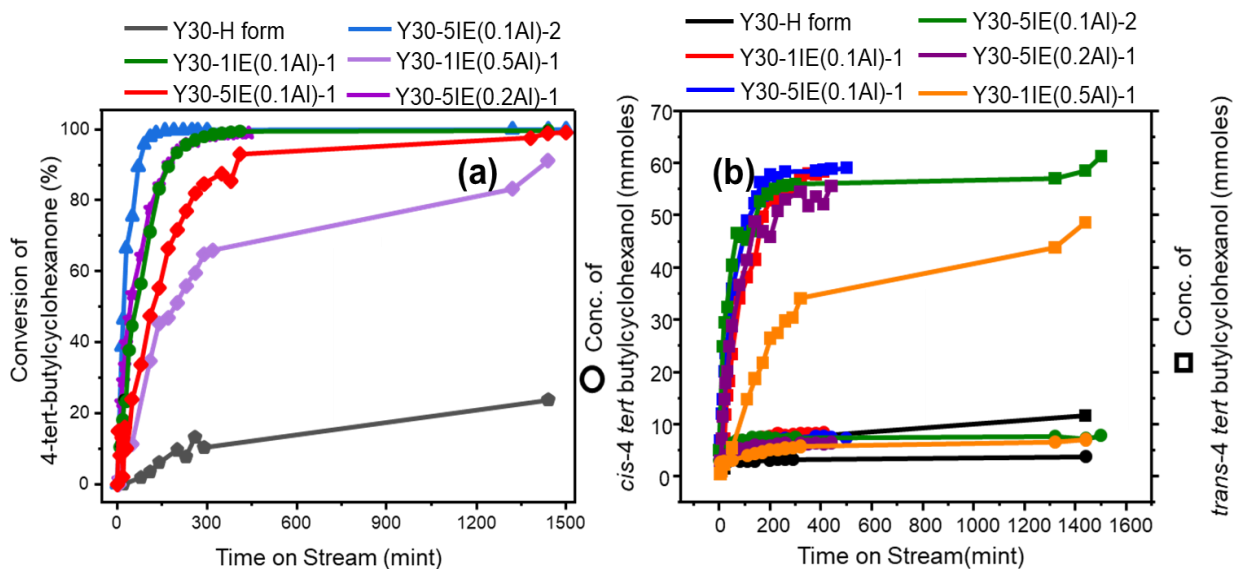


Figure 4.6 Catalytic conversion (%) of 4-*tert* butyl cyclohexanone with respect to time on stream over modified zeolite Y catalysts (a). Concentration of *cis* (circles) and *trans* (squares) 4-*tert* butylcyclohexanol formed during reaction (b).

Table 4.4 Catalytic data of MPV reduction of 4-*tert* butylcyclohexanone over 200 mg of zeolite catalysts ( $\pm 5\%$ ); (a) conversion (%) of 4-*tert* butylcyclohexanone after 7.4 h; (b) initial rate of reaction in  $\text{mmoles L}^{-1}\text{min}^{-1}$ ; (c) cumulative selectivity (%) after 7.4 h to *cis* and *trans* 4-*tert* butylcyclohexanol.

Zeolite Sample	Conversion	Initial Rate	<i>cis:trans</i>
Y30-H form	23.7	0.02	25:75
Y30-1IE(0.1Al)-1	99.4	0.34	10:90
Y30-5IE(0.1Al)-1	99.2	0.37	11:89
Y30-5IE(0.1Al)-2	99.9	0.45	12:87
Y30-5IE(0.2Al)-1	99.7	0.38	10:90
Y30-1IE(0.5Al)-1	91.2	0.17	13:87

To confirm the heterogeneous nature of this reaction, we performed a hot filtration test (Figure A6). After starting the experiment, the catalyst was removed by filtration after 110 minutes and the filtrate was allowed to run on its own for the rest of the time on stream. There was no conversion of the 4-*tert* butylcyclohexanone after the removal of the solid catalyst from the reaction mixture, which confirms that the reaction is catalyzed by the solid Lewis-acid zeolite.

**Correlations among aluminum coordination, Lewis acidity, and activity:** A quantitative comparison of  $^{27}\text{Al}$  MAS NMR, Lewis acidity obtained by FTIR analysis and the catalytic activity indicates clear relationships among them. In pristine zeolite Y, the sharp peak at 0 ppm of Al NMR, as discussed above, is ascribed to framework-associated aluminum Al(VI<sub>a</sub>) species in octahedral coordination. This feature is present in acidic zeolites and the corresponding species forms during hydration of the acidic form of the zeolite. As Y30-H<sup>+</sup> is converted into the H<sup>+</sup>-form, some aluminum species are at least partially dislodged from the framework and acquire octahedral coordination with a sharp resonance at 0 ppm (**Figure A1**)<sup>62</sup>. The Lewis acidic nature of these aluminum species is well established in literature<sup>133-135</sup>. Owing to its Lewis acidic character, the sharp peak at 0 ppm due to framework associated aluminum Al(VI<sub>a</sub>) can be ascribed to the Lewis acidic signatures at 2230 cm<sup>-1</sup> and 2195 cm<sup>-1</sup> in carbon monoxide-probed FTIR spectra (**Figure 4a**) and at 1455 cm<sup>-1</sup> and 1621 cm<sup>-1</sup> in pyridine-FTIR spectra (**Figure 3a**), respectively.

Quantitative  $^{27}\text{Al}$  MAS NMR and pyridine-FTIR data shows that such aluminum species have a small concentration for both pristine and aluminum exchanged samples (**Tables 4.2 and 4.3**). Therefore, it can be inferred that the low catalytic conversion and minimal reaction rate originate from the low intrinsic Lewis acidity of the pristine zeolite due to framework-associated aluminum Al(VI<sub>a</sub>) species. As expected, after aluminum ion-exchange, the total aluminum content of zeolites increases (**Table 4.2**). The incorporated aluminum species reside in extra-framework positions and mainly in octahedral coordination Al(VI<sub>b</sub>) and are responsible for the broad asymmetric resonance at ~3 ppm together with existence of framework-associated aluminum Al(VI<sub>a</sub>) species.

Considering the pyridine and the carbon monoxide probed FTIR spectra, there is a sharp increase in the intensity of the bands characteristic of LAS, correlating to the extra-framework Al(VI<sub>b</sub>) species (**Figures 4.3 and 4.4**). This leads to the deduction that the higher rates of Lewis-acid catalyzed MPV reduction and the associated greater conversion compared to pristine zeolite correspond to the introduction of extra-framework Al(VI<sub>b</sub>) species, which are

responsible for increasing the number of the catalytically active Lewis acidic aluminum sites. Such sites have octahedral coordination under the conditions of NMR measurement. However, after incorporation of aluminum, the intensity of the band responsible for BAS in Py-FTIR does not vary. Consequently, the concentrations of BAS, calculated from Py-FTIR, remain in the same range as that of the parent zeolite. This suggests that the introduced aluminum species are not charge-balanced by the framework and, hence, are not present at extra-framework cationic sites of the zeolite. We propose that these octahedral aluminum Al(VI<sub>b</sub>) species in extra-framework positions are probably present in the form of charge-neutral Al(H<sub>2</sub>O)<sub>3</sub>(OH)<sub>3</sub> clusters and/or Al<sub>2</sub>O<sub>3</sub> clusters, thus ruling out the possibility of the existence of such extra-framework aluminum species in the form of charge balancing Al<sup>3+</sup> or [Al(OH)]<sup>2+</sup> cations, (described in NMR section). Likewise, Liu et al. suggested that distorted tetrahedral aluminum Al(IV<sub>c</sub>) species with a resonance at ~59 ppm are probably the binuclear species and are the part of the extra-framework as nano-sized Al<sub>2</sub>O<sub>3</sub> species <sup>219</sup>.

**Figure 4.7** shows a quantitative correlation of the MPV reduction rate with the total Lewis acid sites from pyridine-probed FTIR and the concentration of extra-framework Al(VI<sub>b</sub>) species obtained by <sup>27</sup>Al MAS NMR. A direct correlation exists between concentration of extra-framework species, probed by different characterization techniques, and catalytic reactivity. These results show that the pyridine probes both the zeolite's intrinsic LAS and the extra-framework LAS, correlating well with the elemental analysis and NMR results. Consequently, the concentration of LAS probed by pyridine does not start at zero (**Figure 4.7**), which means that pyridine also probes the intrinsic Lewis-acid sites of the parent zeolite thus giving the non-zero value of the LAS concentration being probed by pyridine in the parent form.

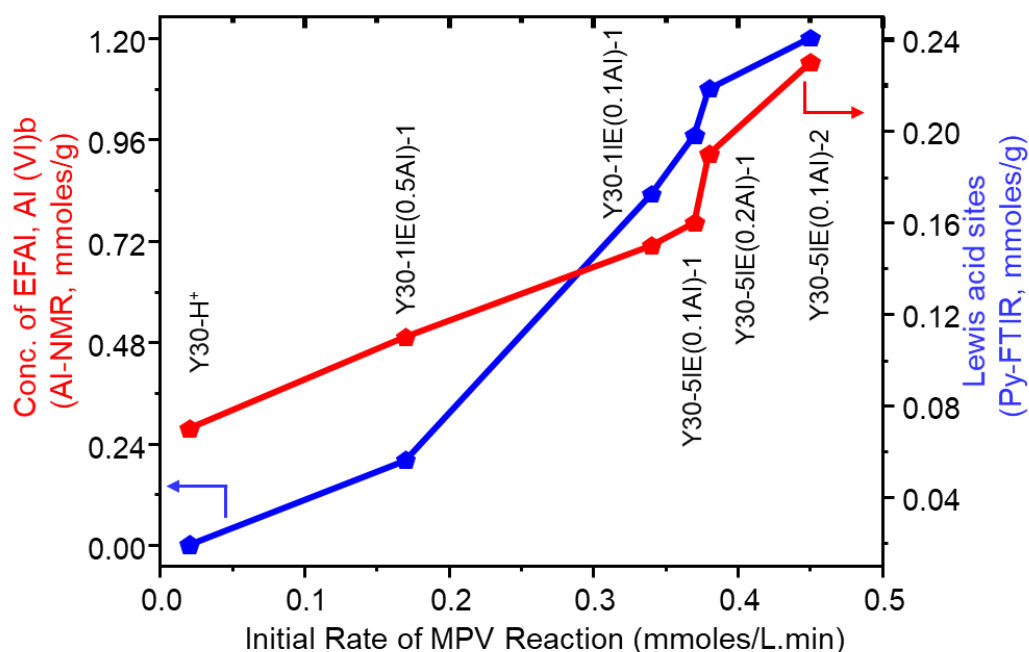


Figure 4.7 Correlating the concentration of extra-framework Al(VI)<sub>b</sub> species to catalytic rate of reaction and total content of LAS obtained from pyridine-probed FTIR quantitative analysis.

However, carbon monoxide does not probe all of the extra-framework aluminum, which is incorporated by ion-exchange. This may be because carbon monoxide does not interact with non-charged moieties. The nature of its interaction is usually electrostatic, which is why it does not respond to most of the incorporated extra-framework aluminum species that are present as charge-neutral species. Therefore, the increase in the intensity of the LAS bands after aluminum-exchange is about ~20-30%, which does not account for all the introduced aluminum. This may be because of two reasons; (1) as carbon monoxide is a weak base so it does not probe the LAS acid sites, which are weak, and (2) some of the LAS, which are inaccessible to carbon monoxide, are present in sodalite cages.

Employing a 2<sup>nd</sup> ion-exchange method is more suitable to enhance the concentration of extra-framework Al(VI)<sub>b</sub> species. Consequently, the number of LAS from pyridine-FTIR, the sum of LAS peak areas from carbon monoxide probed FTIR and the rate of reaction, were higher compared to first ion-exchange method. Likewise, the Y30-1IE(0.5Al)-1 has the lowest values of all the above parameters. This corresponds to a higher concentration of the aluminum-source, thus, an increase in the severity of ion-exchange environment may reduce the zeolite crystallinity (**Table 4.1**). Due to greater concentration of aluminum species, either some of the extra-framework positions are blocked (possibly sodalite cages) or there might be certain redistribution of exchangeable cations preventing the formation of desired aluminum species. Therefore, multiple IE with lower concentration of IE solution gave far better catalysts (in terms



of crystallinity, Lewis acidity and reaction rate) than the single IE with higher concentration of IE solution.

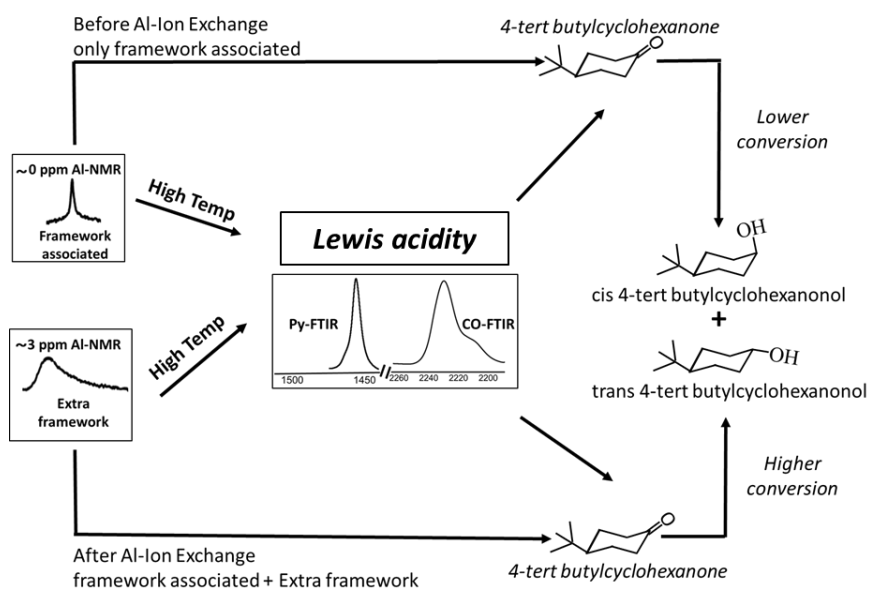


Figure 4.8 Summary of results illustrating aluminum species in different coordination responsible for Lewis acidity before and after aluminum ion-exchange.

Altogether, we summarize these results in **Figure 4.8**, which shows that before ion-exchange, framework-associated aluminum centers of a Lewis acidic nature act as the active sites for the hydride transfer reaction and are responsible for Lewis acidic signatures in pyridine- and carbon monoxide- probed FTIR spectra. With the extent of incorporated aluminum dependent on the synthesis conditions, after ion-exchange, the extra-framework aluminum Al(VI<sub>b</sub>) entities serve as the dominant active centers for hydride transfer to form alcohol and are the reason for the enhancement of the LAS vibrations as shown by FTIR analysis. These extra-framework aluminum species are probably neutral aluminum oxide /hydroxide species.

#### 4.4. Conclusions

Lewis acidity was introduced into zeolite Y through simple ion-exchange using aluminum nitrate aqueous solution. The number of Lewis acid sites, determined by FTIR of adsorbed pyridine and carbon monoxide, quantitatively correlated to the rate of reaction for MPV reduction of 4-*tert* butyl cyclohexanone and to the octahedrally coordinated extra-framework aluminum determined by <sup>27</sup>Al MAS NMR. The results lead to the conclusion that ion-exchange of extra-framework cations is a feasible way to introduce and/or enhance the Lewis acidity of pristine zeolite. These species, however, do not result in charge-compensating aluminum ions;

rather form neutral extra-framework clusters. Thus, the Lewis acid sites are likely present as charge-neutral  $\text{Al}(\text{OH})_3$  and/or nano-sized  $\text{Al}_2\text{O}_3$  clusters. Furthermore, further ion-exchange after calcination on a previously exchanged sample maximizes the Lewis acidity.

## **Chapter 5**

### **Role of Si/Al ratio, co-cation and experimental conditions on the generation of extra-framework aluminum Lewis acid sites**

#### **Contributions**

The synthesis, XRD, nitrogen physisorption, FTIR and NMR characterization and catalytic evaluation of materials was performed by the author the thesis.

## 5.1 Introduction

The Lewis acid sites are generally generated in zeolites by steam calcination, which extracts aluminum from the framework location to generate extra-framework aluminum motifs. Some of the aluminum species also exist as EF-Al, whose coordination depends on the nature of the charge-balancing cation as well as the temperature and the conditions under which zeolite exists<sup>158-160</sup>. Alternatively, Lewis acid sites are generated by incorporating heteroatom at the framework and extra-framework positions by hydrothermal or post-synthetic modifications. The extent of the generation of Lewis acid sites employing these routes varies, depending on different factors. These include the nature and severity of conditions in the hydrothermal synthesis or post-synthetic treatments, the Si/Al ratio of the zeolite, and the type of charge-balancing cations<sup>50, 75, 80</sup>. The work described in the previous chapter illustrated that facile aluminum-exchange is also an efficient way to increase the number of Lewis acid sites in zeolite Y without affecting the zeolite's intrinsic Brønsted acidity<sup>180</sup>. The content of these sites quantitatively correlated with the EFAl species determined by NMR and the catalytic activity in the MPV reaction. The work also showed that the multiple aluminum-exchange treatments with low concentrations of aluminum precursor and performing calcination after each aluminum-exchange treatment favors the maximum incorporation of catalytically active EFAl LAS.

The work presented in this chapter explores the effect of the Si/Al ratio of the parent zeolite, the severity of aluminum-exchange conditions, and the nature of co-cation on the generation of EFAl LAS. For this, we systematically study the generation of aluminum-exchanged EF LAS in zeolite Y employing (1) different Si/Al ratios ranging from 2.5-40, (2) aluminum-exchange treatment accompanied with and without the heating or stirring conditions, (3) parent zeolites of different cationic forms, i.e., sodium, proton, and ammonium. Furthermore, the focus is also given to highlight the conditions that favor the maximum incorporation of catalytically active EFAl LAS by Al-IE procedure without significantly affecting the zeolite's framework and inherent porous characteristics. The work demonstrates that, like other routes, the Si/Al ratio, the severity of conditions, and the nature of co-cation significantly affect the efficiency of the aluminum-exchange procedure to introduce EFAl LAS in zeolite Y as follows. Starting with relatively dealuminated parent zeolites, i.e., high Si/Al ratios, increases the extent of generation of catalytically active EFAl LAS. Similarly, a constant stirring of the zeolite in Al-IE solution

at room temperature favors the maximum incorporation of EFAl LAS and maximum preservation of the zeolite's structure. Furthermore, the presence of sodium as co-cation not only hampers the incorporation of acid sites but also negatively affects the zeolite's framework and pore structure. These findings provide optimization of parameters to introduce EFAl LAS and generate Lewis-acid catalytic activity into zeolites.

## 5.2. Materials and Methods

**Chemicals and Materials:** Commercially available zeolite Y samples were purchased from Zeolyst International with Si/Al ratios as follows; CBV300 (ammonium form, Si/Al = 2.5), CBV714 (ammonium form, Si/Al = 6), CBV720 (proton form, Si/Al = 15), CBV760 (proton form, Si/Al = 30), and CBV780 (proton form, Si/Al = 40). Aluminum nitrate nonahydrate (99.99%, ABCR), sodium nitrate (>99%, Sigma-Aldrich), ammonium nitrate (>99%, Sigma-Aldrich), and ammonium acetate ( $\text{NH}_4(\text{CH}_3\text{COO})$ ) (99%, Merck) were used as received.

**Material Preparation:** Ammonium forms of zeolites were converted to their respective proton forms by calcination at 823 K in static air at a heating ramp rate of 1K/min for 6 h. The parent proton forms of Y zeolites were labeled as Y2.5-H<sup>+</sup>, Y6-H<sup>+</sup>, Y15-H<sup>+</sup>, Y30-H<sup>+</sup> and Y40-H<sup>+</sup>, respectively, where integers give the Si/Al ratio of parent zeolites. The proton forms of zeolites were aluminated according to the Al-IE procedure described in **Section 3.1.1** using 0.1M  $\text{Al}(\text{NO}_3)_3$  solution. The samples were one-fold and five-fold aluminum-exchanged without heating or stirring. The samples obtained by one-fold Al-IE were labelled as Y2.5-1IE(0.1Al), Y6-1IE(0.1Al), Y15-1IE(0.1Al), Y30-1IE(0.1Al), and Y40-1IE(0.1Al). Five-fold aluminum-exchanged samples were labelled as Y2.5-5IE(0.1Al), Y6-5IE(0.1Al), Y15-5IE(0.1Al), Y30-5IE(0.1Al) and Y40-5IE(0.1Al). The samples Y30-H<sup>+</sup> and Y30-1IE(0.1Al) were sodium-exchanged using the Na-IE procedure described in **Section 3.1.3**, and the resultant samples were labeled as Y30-Na and Y30-1IE(0.1Al)-Na, respectively. The sample Y30-Na-IE(0.1Al) was prepared by one-fold aluminum-exchange on Y30-Na using the Al-IE procedure as stated above. Similarly, the sample Y30-NH<sub>4</sub><sup>+</sup>-IE(0.1Al) was prepared by ammonium-exchange of Y30-H<sup>+</sup> (using NH<sub>4</sub><sup>+</sup>-IE procedure described in **Section 3.1.2**), followed by a one-fold alumination using Al-IE procedure. Zeolite Y30-H<sup>+</sup> was also aluminated under different Al-IE conditions as follows. The one-fold Al-IE of Y30-H<sup>+</sup> was performed at 373K, and the resultant sample was labeled as Y30-1IE(0.1Al)-H, whereas the sample Y30-1IE(0.1Al)-S was prepared by one-fold Al-IE while constantly stirring the zeolite containing solution at 1000rpm. The

sample Y30-1IE(0.1Al)-H+S was prepared by one-fold Al-IE at 373K and stirring the zeolite-containing solution at 1000rpm.

**Material Characterization:** The X-ray diffraction patterns of zeolite powders were recorded at room temperature on a PANalytical X'Pert PRO MPD diffractometer. The specific surface areas of zeolites were determined by collecting nitrogen adsorption-desorption isotherms at 77 K with Micromeritics Tristar II 3020 gas adsorption analyzer. ICP-OES determined the aluminum and silicon content of zeolite samples. Si/Al ratio was calculated based on the Al and Si content of the samples determined from ICP-OES. The  $^{27}\text{Al}$  MAS NMR spectra were recorded using a Bruker AVANCE III HD spectrometer and Bruker 400 MHz Ultra-Shield magnet at a rate of 10 kHz for 3000 scans. The  $^{27}\text{Al}$  MQMAS NMR spectra were recorded using a Bruker 700MHz Ultra-Shield spectrometer at 20 kHz for 1440 scans. The FTIR spectra of zeolite samples using pyridine as a probe molecule were recorded using a Thermo Nicolet iS50 FTIR spectrometer with a DTGS detector.

**Catalytic Evaluation:** The Meerwein-Ponndorf-Verley (MPV) reduction reaction was performed to estimate zeolites' catalytic activity. The catalytic experiment involved zeolite catalyst (0.2 g), isopropanol (50 mL), 4-*tert*-butylcyclohexanone (2.5 mmol), and 1,3,5-tri-*tert*-butylbenzene as an internal standard (1 mmol).

### 5.3. Results and Discussion

**Effect of Si/Al ratio:** The Si/Al ratios of the parent Y-H<sup>+</sup> zeolites with different Si/Al ratios and the respective aluminum-exchanged samples are presented in **Table 5.1**. After Al-IE, Si/Al ratios decrease in all samples due to the uptake of aluminum during Al-IE treatment. The results manifest that the decrease in Si/Al ratio after Al-IE becomes more significant while increasing the Si/Al of the parent zeolite, i.e., the Si/Al ratios after 5-fold Al-IE of Y2.5-H<sup>+</sup> and Y40-H<sup>+</sup> decrease from 2.7 to 2.2 and from 40.02 to 8.68, respectively. Thus, starting with a parent zeolite with less aluminum content results in higher uptake of aluminum than that starting with greater aluminum content. The X-ray diffraction patterns of the parent Y-H<sup>+</sup> zeolites with different Si/Al ratios and the respective aluminum-exchanged samples are presented in **Figures 5.1a, 5.1b, and 5.1c**, respectively. The nitrogen adsorption/desorption isotherms of these samples are shown in **Figures 5.1d, 5.1e, and 5.1f**, respectively, whereas **Table 5.1** summarizes the quantitative characteristics.

Table 5.1: Physicochemical characterization of parent Y-H<sup>+</sup> zeolites with different Si/Al ratios and the respective aluminum-exchanged samples

Zeolite	<sup>a</sup> S <sub>BET</sub> m <sup>2</sup> g <sup>-1</sup>	<sup>b</sup> V <sub>total</sub> cm <sup>3</sup> g <sup>-1</sup>	<sup>c</sup> V <sub>micro</sub> cm <sup>3</sup> g <sup>-1</sup>	<sup>c</sup> S <sub>micro</sub> m <sup>2</sup> g <sup>-1</sup>	<sup>c</sup> S <sub>meso</sub> m <sup>2</sup> g <sup>-1</sup>	<sup>d</sup> Crystallinity <sub>rel</sub> <sup>e</sup> Si/Al (%)	ratio
Y2.5-H <sup>+</sup>	500	0.21	0.23	305	29	100	2.71
Y2.5-1IE(0.1Al)	210	0.23	0.21	200	20	62	2.50
Y2.5-5IE(0.1Al)	120	0.24	0.18	180	18	5	2.21
Y6-H <sup>+</sup>	630	0.26	0.27	532	45	100	5.60
Y6-1IE(0.1Al)	570	0.29	0.27	522	41	89	5.32
Y6-5IE(0.1Al)	565	0.3	0.3	596	46	84	4.93
Y15-H <sup>+</sup>	700	0.39	0.32	610	190	100	15.00
Y15-1IE(0.1Al)	680	0.36	0.3	610	180	90	9.12
Y15-5IE(0.1Al)	635	0.28	0.29	565	69	87	7.49
Y30-H <sup>+</sup>	740	0.44	0.33	555	180	100	30.53
Y30-1IE(0.1Al)	760	0.49	0.32	600	200	91	15.23
Y30-5IE(0.1Al)	770	0.47	0.31	560	210	90	10.00
Y(40)-H <sup>+</sup>	740	0.49	0.34	655	210	100	40.02
Y40-1IE(0.1Al)	725	0.45	0.32	610	205	93	13.12
Y40-5IE(0.1Al)	755	0.44	0.32	640	195	90	8.68

<sup>a</sup>calculated from the BET method, <sup>b</sup>based on single point adsorption at p/po = 0.97, <sup>c</sup>calculated from the t-plot method, <sup>d</sup>calculated by a previously described method <sup>180</sup>, assuming the crystallinity of parent zeolites as 100%, <sup>e</sup>calculated from ICP

The samples after 1-fold and 5-fold Al-IE of Y6-H<sup>+</sup>, Y15-H<sup>+</sup>, Y30-H<sup>+</sup>, and Y40-H<sup>+</sup> show all characteristic diffraction peaks comparable to those in the respective parent zeolites <sup>50</sup>. The relative crystallinity <sup>180</sup> of these aluminum-modified zeolites (where the crystallinity of parent zeolites is assumed to be 100%) ranges from 84 to 93%, only indicating a minor change (**Table 5.1**). Likewise, the nitrogen physisorption isotherms after Al-IE on Y6-H<sup>+</sup>, Y15-H<sup>+</sup>, Y30-H<sup>+</sup>, and Y40-H<sup>+</sup> look identical to those of their corresponding parent zeolites <sup>209, 226-228</sup>. The BET

surface areas and micropore volume of these zeolites before and after treatment remain almost unchanged, staying within the error limits (**Table 5.1**).

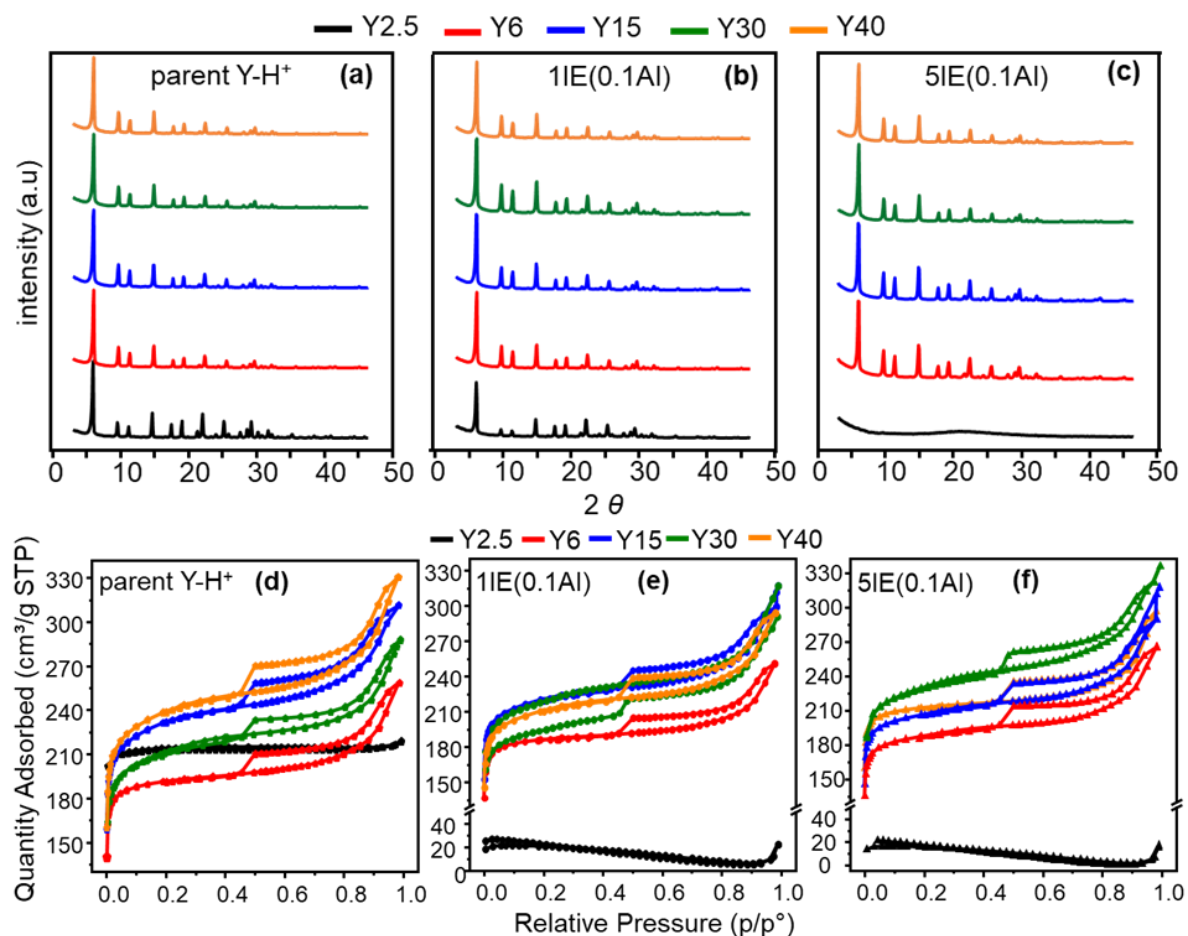


Figure 5.1: PXR D patterns normalized to the weight of the samples (a) parent Y-H<sup>+</sup> (b) 1IE(0.1Al) and (c) 5IE(0.1Al). The nitrogen adsorption isotherms of (a) parent Y-H<sup>+</sup> (b) 1IE(0.1Al) and (c) 5IE(0.1Al).

However, Al-IE on Y2.5-H<sup>+</sup> results in drastic changes in the crystallinity and porosity of parent zeolite. After the first Al-IE, the PXR D pattern of Y2.5-IE(0.1Al) shows a significant decrease in the intensity of diffraction peaks, possessing 62% crystallinity relative to Y2.5-H<sup>+</sup>. Upon 5-fold Al-IE, all the diffraction intensities disappear with 5% remaining crystallinity. Similarly, there is a significant decrease in the BET surface areas and micropore volumes of these samples which shows that the zeolite structure of Y2.5 collapses after Al-IE treatments.

The <sup>27</sup>Al MAS and MQMAS spectra of the zeolites recorded under ambient conditions are presented in **Figures 5.2** and **B.1**, respectively. As discussed in **Section 4.3**, the spectra of parent Y-H<sup>+</sup> zeolites show two tetrahedral peaks at  $\sim 61$  ppm (IV<sub>a</sub>), and  $\sim 59$ -56 ppm (IV<sub>b</sub>), the former being sharp and the latter slightly broader. The sharp peak at  $\sim 0$  ppm (VI<sub>a</sub>) is due to FA-Al, which adopts octahedral coordination in the proton form of zeolites<sup>61, 62, 66</sup>. Apart from



these resonances, Y2.5-H<sup>+</sup>, Y6-H<sup>+</sup>, and Y15-H<sup>+</sup> also show a broad resonance at ~62-64 ppm (IV<sub>a</sub>) with large Q<sub>cc</sub> (3.2-3.8 MHz) due to distorted tetrahedral aluminum.

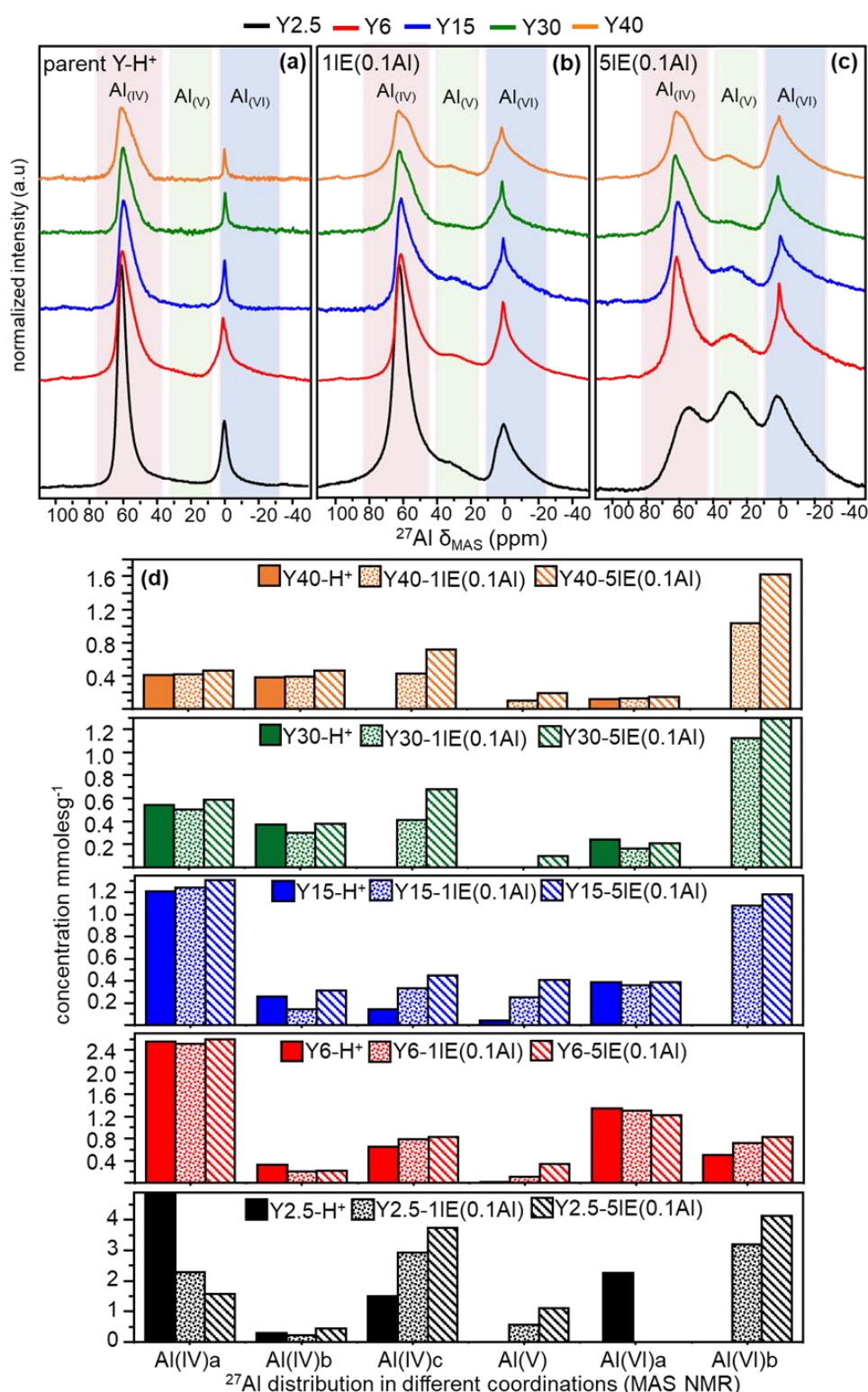


Figure 5.2: <sup>27</sup>Al MAS NMR spectra of zeolites (a) parent Y-H<sup>+</sup> (b) 1IE(0.1Al) and (c) 5IE(0.1Al). Colored regions are added to guide the eye. The spectra are normalized by the weight of the sample used; (d) Quantitative distribution (in mmol g<sup>-1</sup>, ± 10 %) of aluminum

species in different coordinations obtained from  $^{27}\text{Al}$  MAS and MQMAS NMR spectra. Solid bars: parent- $\text{H}^+$  forms, dotted bars: 1IE(0.1Al) and diagonal strip bars: 5IE(0.1Al).

Furthermore,  $\text{Y6-H}^+$  also exhibits a resonance at  $\sim 30\text{-}37$  ppm (V) pentahedral aluminum and a broad asymmetric resonance at  $\sim 3$  ppm ( $\text{VI}_b$ ) due to EFAl, respectively<sup>65</sup>.  $\text{Y6-H}^+$  is commercially synthesized by post-synthetic steaming and mineral acid leaching of  $\text{Y2.5-H}^+$ <sup>65, 209</sup> which can extract the framework aluminum and FA-Al to form EFAl but also leach out aluminum thus increasing the bulk Si/Al ratio. However, the EFAl generated during steam calcinations is not completely leached out during acid treatments, due to which  $\text{Y6-H}^+$  possesses EFAl. All aluminum-exchanged samples show an increase in the intensity of resonance at  $\sim 3$  ppm due EFAl and at 30-37 ppm due to Al(V) species. Furthermore, the tetrahedral region shows enhanced quadrupolar broadening due to distorted tetrahedral species Al( $\text{IV}_c$ ) at  $\sim 62\text{-}64$  ppm (**Figure B.1**). The spectrum of  $\text{Y2.5-5IE}(0.1\text{Al})$  shows drastic changes with a significant increase in intensity in penta- and octahedral region, where the tetrahedral feature also becomes significantly broad. **Figure 5.2d** shows the quantitative distribution of aluminum species in different coordination, calculated from spectral deconvolution utilizing the MQMAS NMR parameters. The results suggest that EFAl Al( $\text{VI}_b$ ) species increase due to ion-exchange with an accompanying increase in the concentration of the distorted tetrahedral and penta-coordinated species. The increase in the concentration of EFAl Al( $\text{VI}_b$ ) is more prominent after 5-fold, which agrees with the results explained in **Section 4.3**.

In parent zeolites, the concentration of FA-Al decreases with an increasing Si/Al ratio, i.e., maximum in  $\text{Y2.5-H}^+$  and minimum for  $\text{Y40-H}^+$ , whereas EFAl are only present in  $\text{Y6-H}^+$ . The concentration of FA-Al does not vary much after Al-IE treatment except for  $\text{Y2.5-IE}(0.1\text{Al})$  and  $\text{Y2.5-5E}(0.1\text{Al})$  samples where FA-Al species are no more present. With an increase in the Si/Al ratio of parent zeolites, the concentration of EFAl after Al-IE treatments tends to increase. However, this is not the case for Si/Al=2.5 of parent zeolite, as aluminum-exchanged samples of  $\text{Y2.5}$  show the maximum concentration of EFAl. The slight decrease in Si/Al ratio and the maximum concentration of EFAl after Al-IE treatments of  $\text{Y2.5-H}^+$  suggest that all the FA-Al are entirely dislodged from the framework and exist as EFAl. Some of the framework Al( $\text{IV}_a$ ) in these samples are also removed from the framework as EFAl.

These results suggest that the increase in the concentration of EFAl after Al-IE treatments of  $\text{Y2.5-H}^+$  is not mainly due to aluminum uptake during Al-IE. After the Si/Al ratio=2.5 of parent zeolites, the increase in the concentration of EFAl nicely correlates with a decrease in Si/Al ratio, suggesting that the incorporated aluminum exists mainly as EFAl (**Table 5.1** and **Figure**

**5.2d**). The maximum concentration of EFAl with an associated maximum decrease in Si/Al ratio is observed for Y40-5IE(0.1Al). These results corroborate that the higher Si/Al ratios of parent zeolites favor the maximum incorporation of EFAl species by Al-IE without significantly affecting the FA-Al or framework aluminum species. Although a 5-fold Al-IE results in a higher concentration of EFAl, the effect of Al-IE treatment on the generation of EFAl is more prominent after 1-fold Al-IE. However, this does not hold for Y6-H<sup>+</sup> as it contains a significant concentration of EFAl species in its pristine form, which increases almost equally after 1-fold and 5-fold Al-IE.

The FTIR difference spectra of samples in the pyridine aromatic ring stretching region are presented in **Figures 5.3a to 5.3c**. The spectra of all samples show five distinct bands. The bands at 1455 cm<sup>-1</sup> and 1621 cm<sup>-1</sup> correspond to pyridine bound to LAS, and the bands at 1545 cm<sup>-1</sup> and 1634 cm<sup>-1</sup> correspond to pyridine interacting with BAS<sup>49, 220</sup>. The 1490 cm<sup>-1</sup> band is structure-insensitive. The bands at 1445 and 1545 cm<sup>-1</sup> are used to quantify LAS and BAS, respectively<sup>70</sup> (**Figure 5.3d and Table B.2**). Before Al-IE, the maximum concentration of LAS and BAS is present in Y2.5-H<sup>+</sup> and the minimum in Y40-H<sup>+</sup> which is due to maximum aluminum content in the former and minimum in the latter. After Al-IE treatments on Y2.5-H<sup>+</sup>, the concentration of LAS increases significantly with Y2.5-5IE(0.1Al), giving the maximum concentration of LAS among all the aluminum-exchanged zeolites. However, this increase in the number of LAS after Al-IE of Y2.5-H<sup>+</sup> is also followed by a significant decrease in the concentration of BAS, i.e., 0.75 mmolg<sup>-1</sup> in Y2.5-H<sup>+</sup> to 0.01 mmolg<sup>-1</sup> in Y2.5-5IE(0.1Al)).

The disappearance of bands at 3643 and 3570 cm<sup>-1</sup> (due to external and internal bridging Si-OH-Al) in the hydroxyl region of pyridine-FTIR difference spectra after Al-IE of Y2.5-H<sup>+</sup> further confirms this observation (**Figure B.2a**). It can be that either the concentration of BAS drastically decreases or the BAS is not accessed by pyridine as the structure of Y2.5-H<sup>+</sup> collapses after Al-IE treatments. The FTIR difference spectra in the carbon monoxide stretching region after Al-IE treatments of Y2.5-H<sup>+</sup> show the significant intensity of the band at 2180cm<sup>-1</sup> due to BAS (**Figure B.2b**). This suggests that not all the BAS are lost during Al-IE. Instead, they cannot be accessed by pyridine due to the collapse of the zeolite framework and associated pore blockage. This also suggests that the LAS accessed by pyridine are not likely to present in the micropores but are located on the external surface.

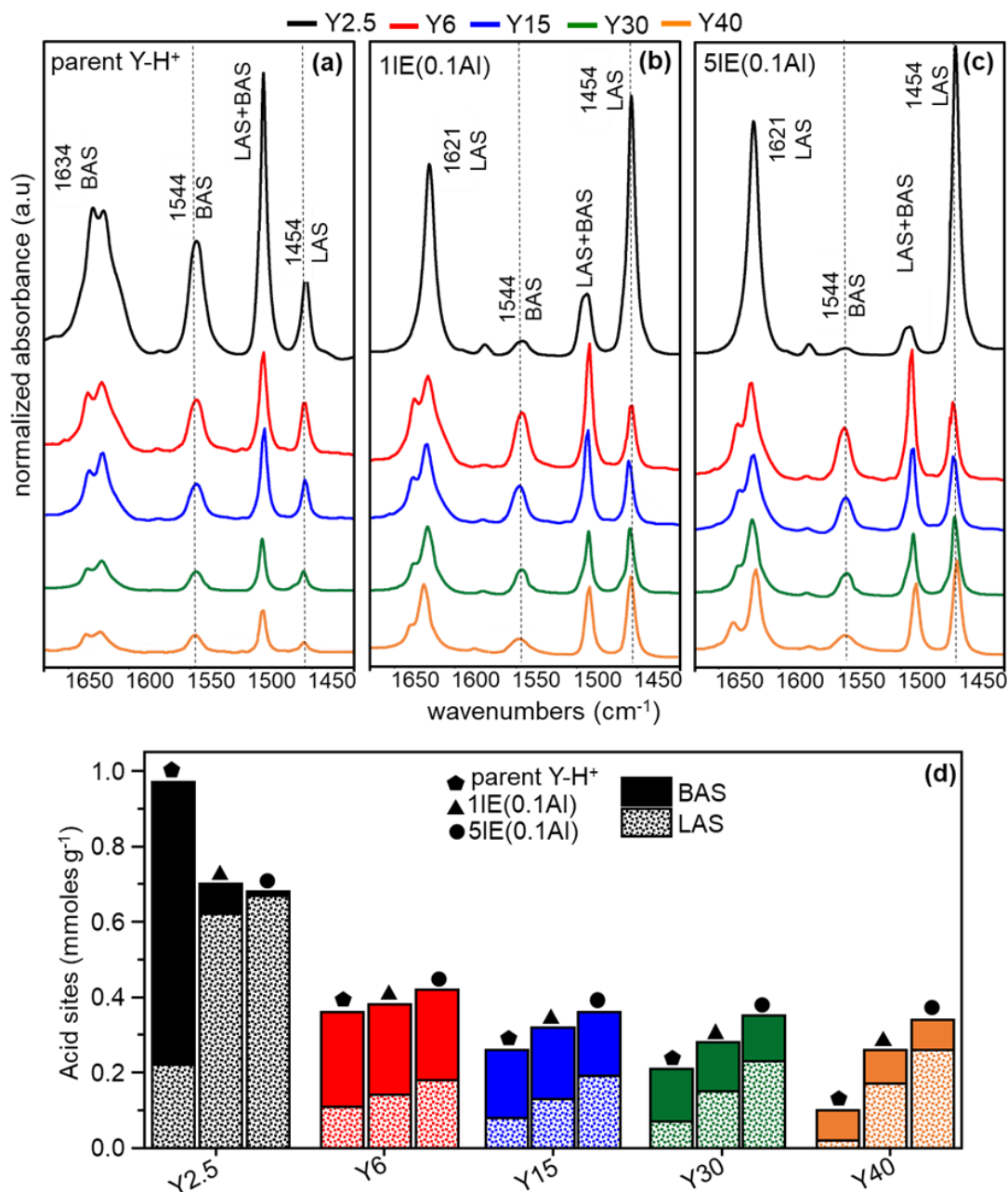


Figure 5.3: FTIR difference spectra in pyridine stretching region obtained by subtraction of spectra after activation at 723K from spectra after pyridine adsorption at 423K followed by evacuation at 423K. (a) parent Y-H<sup>+</sup> (b) 1IE(0.1Al) and (c) 5IE(0.1Al). Colored regions are added to guide the eye, and the spectra are normalized by the weight of the sample used; (d) Quantitative distribution of acid sites accessed by pyridine (mmoles g<sup>-1</sup>,  $\pm 10\%$ ); ( $\blacklozenge$ ) parent Y-H<sup>+</sup> ( $\blacktriangle$ ) 1IE(0.1Al) ( $\bullet$ ) 5IE(0.1Al). Solid bars represent BAS, and dotted bars show LAS.

In comparison, the Al-IE treatments of Y6-H<sup>+</sup>, Y15-H<sup>+</sup>, Y30-H<sup>+</sup>, and Y40-H<sup>+</sup> increase the concentration of LAS without any significant decrease in the content of BAS, suggesting that the incorporated LAS are neutral species. In these samples, the concentration of LAS after Al-IE increases with an increase in the Si/Al ratio of parent zeolites, which is in line with <sup>27</sup>Al MAS NMR and elemental analysis. Similarly, 5-fold Al-IE on these samples maximizes the

concentration of LAS. However, the effect of Al-IE on LAS is more prominent after 1-fold Al-IE. However, the concentration of LAS and BAS of all samples accessed by pyridine is orders of magnitudes lower than the concentration of EFAl and framework aluminum quantified by  $^{27}\text{Al}$  MAS NMR. This is because the amount of acid sites a probe molecule measures depends on the strength of acid sites and  $\text{pK}_b$  of the used base as well as the size of the molecule. Despite this difference, the increase in the concentration of LAS accessed by pyridine after Al-IE of  $\text{Y6-H}^+$ ,  $\text{Y15-H}^+$ ,  $\text{Y30-H}^+$ , and  $\text{Y40-H}^+$  quantitatively correlates with the increase in the concentration of EFAl calculated from  $^{27}\text{Al}$  MAS NMR. Thus, among aluminum-exchanged samples (except the ones with Y2.5 as the parent zeolites), the sample Y40-5IE(0.1Al) has the maximum concentration of EFAl ( $1.62 \text{ mmoleg}^{-1}$ ) as well as the maximum concentration of LAS ( $0.26 \text{ mmoleg}^{-1}$ ).

The Lewis acid catalytic MPV reduction of 4-*tert* butylcyclohexanone was performed to compare the catalytic performance of zeolites. **Figure 5.4a** illustrates the catalytic conversion of 4-*tert* butylcyclohexanone versus time on stream, whereas the initial rate of reaction and selectivity to *cis* and *trans* products are presented in **Figure 5.4b** and **Table B.2**. The conversion of ketone in all the parent zeolites remains very low, reaching only 15-24% conversion after 7.4 h at very low initial reaction rate ranging  $0.02\text{-}0.08 \text{ mmolL}^{-1}\text{min}^{-1}$ . The cumulative *cis* and *trans* alcohols were produced at a ratio of about 25:75 with  $\text{Y6-H}^+$ ,  $\text{Y15-H}^+$ ,  $\text{Y30-H}^+$ , and  $\text{Y40-H}^+$  samples, whereas  $\text{Y2.5-H}^+$  is highly selective towards *cis*-alcohol (*cis:trans* selectivity is 96:04). The rate of reaction in  $\text{Y15-H}^+$ ,  $\text{Y30-H}^+$  and  $\text{Y40-H}^+$  linearly correlates with the amount of LAS and the concentration of FA-Al species. However, this does not hold well for  $\text{Y2.5-H}^+$  and  $\text{Y6-H}^+$  as in the case of the former, the concentration of LAS and FA-Al is maximum among all parent zeolites, and the latter also possesses a relatively large concentration of LAS (as compared to parent zeolites with higher Si/Al ratios) and has both FA-Al and EFAl species. In  $\text{Y2.5-H}^+$ , this can be explained in terms of its hydrothermal stability and small micropore volumes so that the bulky reactant molecules cannot travel through. As  $\text{Y6-H}^+$  is synthesized by post-synthetic steaming and mineral acid leaching of  $\text{Y2.5-H}^+$ <sup>65, 209</sup> and these treatments have very little control on the fate of aluminum species extracted. Thus, it is very likely that the EFAl generated by steam calcinations is not completely leached out during acid treatment and results in pore blockage. Therefore, the catalytic activity of  $\text{Y6-H}^+$  does not quantitatively correlate with the amount of FA-Al and EFAl and with the concentration of LAS.

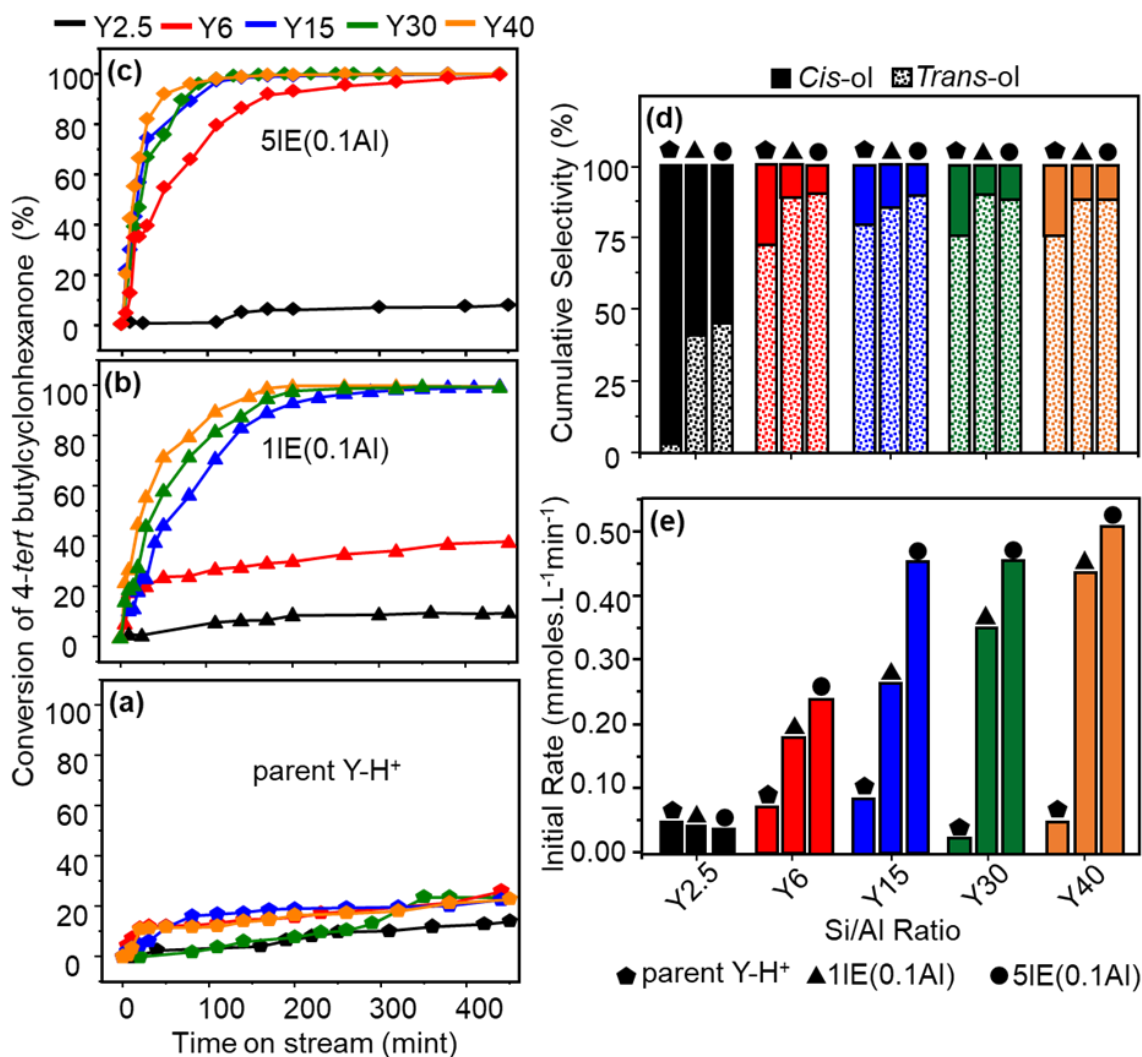


Figure 5.4: Catalytic data of MPV reduction of 4-*tert* butylcyclohexanone ( $\pm 5\%$ ). Conversion (%) of 4-*tert* butylcyclohexanone as a function of time on stream (a) parent Y-H<sup>+</sup> (b) 1IE(0.1Al) and (c) 5IE(0.1Al). (d) Cumulative selectivity towards *cis* (solid bars) and *trans* (dotted bars) 4-*tert* butylcyclohexanol; (e) Initial rate of reaction of determined as the slope of the linear regression in the time-concentration plot between zero and 110 min; (◆) parent Y-H<sup>+</sup> (▲) 1IE(0.1Al) (●) 5IE(0.1Al).

After Al-IE treatments of Y15-H<sup>+</sup>, Y30-H<sup>+</sup>, and Y40-H<sup>+</sup>, the conversion and rate of reaction increases sharply (ranging from 0.26 to 0.51 mmol.L<sup>-1</sup>.min<sup>-1</sup>) with the in aluminum exchanged catalysts reaching very high conversion (96-100%). The conversion and respective reaction rate increase with increasing the Si/Al ratio of the parent zeolites and the number of ion-exchanges, which agrees with the findings from FTIR and NMR. The increase in catalytic activity after the first ion-exchange is more prominent than 5-fold Al-IE as the conversions reach > 96% after 1-fold Al-IE of Y15-H<sup>+</sup>, Y30-H<sup>+</sup>, and Y40-H<sup>+</sup>. Further Al-IE treatments predominantly increase the rates of reaction, and Y40-5IE(0.1Al)-2 shows the highest rate of reaction (51 mmol.L<sup>-1</sup>.min<sup>-1</sup>) amongst all aluminum-exchanged samples. After Al-IE treatments on Y2.5-H<sup>+</sup>, the catalytic

activity decreases with the conversion of ketone decreasing from 15 to 8 %, whereas the reaction rate only slightly decreases from 0.05 to 0.04 mmolL<sup>-1</sup>min<sup>-1</sup>. The *cis:trans* selectivity shows a drastic change after Al-IE treatments of Y2.5-H<sup>+</sup> (from 96:04 to 44:55). As the MPV reaction occurs within the micropores of zeolite Y, the poor catalytic performance of Y2.5-H<sup>+</sup> after Al-IE corresponds to the collapse of the zeolite framework. Consequently, the pore structure is either destroyed or heavily blocked. In the case of Y6-1IE(0.1Al) and Y6-5IE(0.1Al), the catalytic activity increases, but this increase is not as significant as in the case of aluminum-exchanged samples of Y15-H<sup>+</sup>, Y30-H<sup>+</sup>, and Y40-H<sup>+</sup>, which agrees with the FTIR and NMR results. (**Figure 5.3** and **Table B.1**). However, the significant increase in activity of Y6-1IE(0.1Al) and Y6-5IE(0.1Al) as compared to the parent Y6-H<sup>+</sup>, despite a slight rise in LAS and EFAl, points out that Al-IE treatments result in opening the blocked pores. This facilitates the MPV reactants to penetrate through them, and the EFAl and FA-Al, which were not active in the parent zeolite due to pore blockage, also significantly contribute to enhanced activity after Al-IE.

**Effect of aluminum-exchange conditions:** To evaluate the effect of conditions of Al-IE treatment, conditions Y30-H<sup>+</sup> were taken as a starting material. As the effects of Al-IE treatment appear to be more prominent after 1-fold Al-IE, Y30-1IE(0.1Al) prepared without heating and stirring will be compared with the samples prepared under varying conditions of heating (Y30-1IE(0.1Al)-H), stirring (Y30-1IE(0.1Al)-S), and combined heating and stirring (Y30-1IE(0.1Al)-H+S). The Si/Al ratios of these samples are presented in **Table 5.2**. The decrease in Si/Al ratio of parent Y30-H<sup>+</sup>, due to the uptake of aluminum during Al-IE treatments, is highest in Y30-1IE(0.1Al)-H+S, i.e., 12.89 and lowest in the case of Y30-1IE(0.1Al)-H, i.e., 16.93. The samples Y30-1IE(0.1Al) and Y30-1IE(0.1Al)-H give values of 15.23 and 13.26, respectively. This suggests that the uptake of mere aluminum after 1-fold Al-IE is most efficient under combined heating and stirring, whereas Al-IE under heating reduces the uptake compared to the Al-IE without heating and stirring. The X-ray diffraction patterns and nitrogen adsorption/desorption isotherms of these samples are presented in **Figures 5.5a** and **5.5b**, respectively, whereas the values of relative crystallinity and porous characteristics are listed in **Table 5.2**.

Table 5.2: Physicochemical characterization of parent Y30-H<sup>+</sup> and aluminum-exchanged zeolites under different Al-IE conditions

Zeolite	<sup>a</sup> S <sub>BET</sub>	<sup>b</sup> V <sub>total</sub>	<sup>c</sup> V <sub>micro</sub>	<sup>c</sup> S <sub>micro</sub>	<sup>c</sup> S <sub>meso</sub>	<sup>d</sup> Crystallinity <sub>rel</sub> <sup>e</sup> Si/Al	ratio
	m <sup>2</sup> g <sup>-1</sup>	cm <sup>3</sup> g <sup>-1</sup>	cm <sup>3</sup> g <sup>-1</sup>	m <sup>2</sup> g <sup>-1</sup>	m <sup>2</sup> g <sup>-1</sup>	(%)	
Y30-H <sup>+</sup>	740	0.44	0.33	555	180	100	30.53
Y30-1IE(0.1Al)	760	0.49	0.32	600	200	91	15.23
Y30-1IE(0.1Al)-H	710	0.41	0.29	525	170	86	16.93
Y30-1IE(0.1Al)-S	750	0.46	0.32	520	220	90	13.26
Y30-1IE(0.1Al)-H+S	580	0.39	0.27	470	150	77	12.89

<sup>a</sup>calculated from the BET method, <sup>b</sup>based on single point adsorption at p/po = 0.97, <sup>c</sup>calculated from the t-plot method, <sup>d</sup>calculated by a previously described method <sup>180</sup>, assuming the crystallinity of parent zeolites as 100%, <sup>e</sup>calculated from ICP

All the samples after Al-IE under different conditions exhibit all the characteristic diffraction peaks comparable to the parent Y30-H<sup>+</sup> sample, with the relative crystallinity of these samples ranging from 77 to 91% <sup>50, 180</sup>. The sample Y30-1IE(0.1Al)-H+S shows the least crystallinity (77%), whereas the samples Y30-1IE(0.1Al) and Y30-1IE(0.1Al)-S have maximum crystallinity, i.e., ~91% relative to Y30-H<sup>+</sup>. Likewise, the nitrogen physisorption isotherms after Al-IE look comparable to parent Y30-H<sup>+</sup> sample <sup>209, 226-228</sup>, except for the sample Y30-1IE(0.1Al)-H+S, where the amount of adsorbed nitrogen significantly decreases as compared to other aluminum-exchanged samples and Y30-H<sup>+</sup>. The BET surface area and micropore volume of this sample are also considerably lower than other samples (**Table 5.2**). Thus, the highest uptake of aluminum in Y30-1IE(0.1Al)-H+S is also associated with reduced crystallinity and porous structure. However, the retention of the crystallinity and porous structure is maximum in the case of Y30-1IE(0.1Al)-S, which shows the second-highest aluminum content. The BET surface areas and micropore volume of these zeolites before and after treatment remain almost unchanged, staying within the error limits.

The <sup>27</sup>Al MAS and MQMAS spectra of the zeolites recorded under ambient conditions are presented in **Figures 5.5c** and **B.3**, respectively. All aluminum-exchanged samples show an increase in the resonances at ~3 ppm, 30-37 ppm, and ~62-64 ppm due EFAl, pentahedral aluminum, and distorted tetrahedral aluminum species, respectively.



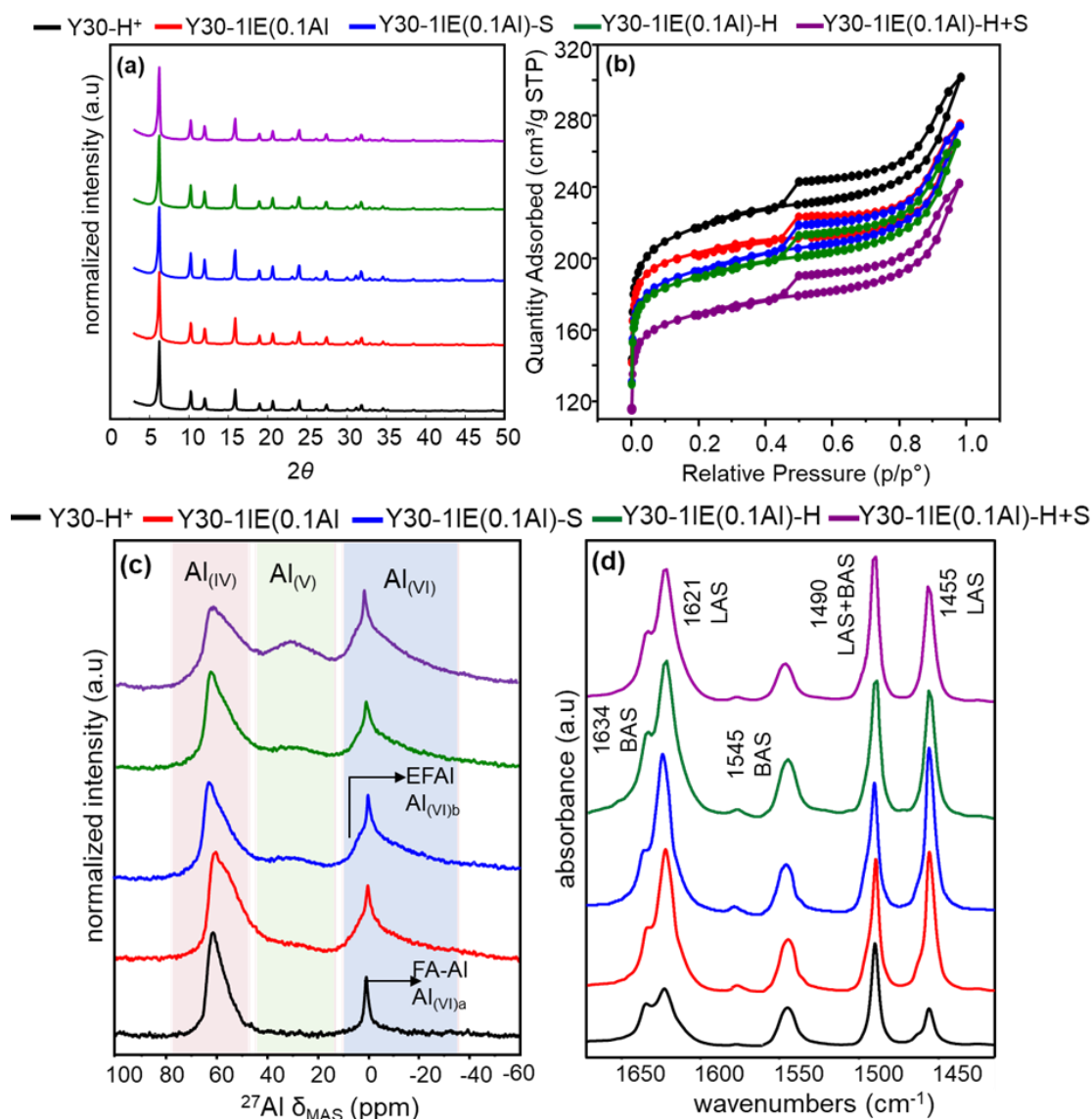


Figure 5.4: Parent Y30-H<sup>+</sup> and aluminum-exchanged samples under different Al-IE conditions; (a) PXRD patterns normalized to the weight of the sample used (b) nitrogen adsorption isotherms (c) <sup>27</sup>Al MAS NMR spectra normalized to the weight of the sample used; colored regions are added to guide the eye (d) FTIR difference spectra in pyridine stretching region normalized by the weight of the sample used. The difference spectra are obtained by subtraction of spectra after activation at 723K from spectra after pyridine adsorption at 423K followed by evacuation at 423K.

Of all the aluminum-exchanged samples, the broad resonance at ~3 ppm appears to be most intense in the spectra of samples Y30-1IE(0.1Al)-S and Y30-1IE(0.1Al)-H+S and least intense in the spectrum of Y30-1IE(0.1Al)-H. Furthermore, the sample Y30-1IE(0.1Al)-H+S also shows maximum intensity in the pentahedral region and a significant decrease in intensity in the tetrahedral region. In comparison, the spectrum of Y30-1IE(0.1Al)-S shows the tetrahedral intensity comparable to that of Y30-1IE(0.1Al), with the former having slightly intense

pentahedral resonance. The quantitative distribution of aluminum species in different coordination, presented in **Figure 5.6a**, shows that the concentration of EFAl is maximum for Y30-1IE(0.1Al)-H+S, i.e.,  $1.03 \text{ mmoleg}^{-1}$  and minimum for Y30-1IE(0.1Al)-H, i.e.,  $0.61 \text{ mmoleg}^{-1}$ . For sample Y30-1IE(0.1Al)-S, EFAl concentration is only slightly lower than that of Y30-1IE(0.1Al)-H+S, i.e.,  $0.97 \text{ mmoleg}^{-1}$  (**Figure 5.6a** and **Table B.1**). Similarly, the concentration of Al(V) and Al(IV<sub>c</sub>) is maximum for Y30-1IE(0.1Al)-H+S, whereas that of Al(IV<sub>a</sub>) and Al(IV<sub>b</sub>) species is minimum in this sample. This suggests that the combined heating and stirring not only incorporates the maximum concentration of EFAl but also produces the maximum number of penta-coordinated species and extract some of Al(IV<sub>a</sub>) and Al(IV<sub>b</sub>) species. However, the stirring generates a very high concentration of EFAl, but that of Al(IV<sub>a</sub>) and Al(IV<sub>b</sub>) remains comparable to parent zeolite samples.

The FTIR difference spectra of samples in the pyridine aromatic ring stretching region are presented in **Figure 5.5d**, whereas the quantitative distribution of BAS and LAS is presented in **Figure 5.6b**. The results show that the concentration of BAS in all samples ranges from  $0.14\text{-}0.12 \text{ mmoleg}^{-1}$ . The concentration of BAS is maximum for Y30-H<sup>+</sup> and Y30-1IE(0.1Al)-S, whereas the sample Y30-1IE(0.1Al)-H+S shows the minimum content of BAS. After Al-IE, the concentration of LAS increases in all the samples. The sample Y30-1IE(0.1Al)-S shows the maximum concentration of LAS, i.e.,  $0.20 \text{ mmoleg}^{-1}$ , whereas the sample Y30-1IE(0.1Al)-H+S has a minimum concentration, i.e.,  $0.11 \text{ mmoleg}^{-1}$ . The concentration of LAS in Y30-1IE(0.1Al)-H and Y30-1IE(0.1Al) is  $0.13 \text{ mmoleg}^{-1}$  and  $0.15 \text{ mmoleg}^{-1}$ , respectively. The amounts of LAS accessed by pyridine do not quantitatively correlate with the concentration of EFAl calculated by NMR, which can be explained as follows. The combined heating and stirring during Al-IE cause maximum loss of crystallinity and micropore volume resulting in obstruction of some zeolite micropores. The pore blockage might also be due to the maximum concentration of distorted tetrahedral aluminum species in this sample. Consequently, all the EFAl responsible for Lewis acidity cannot be accessed by pyridine due to steric limitations. In comparison, Y30-1IE(0.1Al)-S shows the maximum concentration of LAS because the Al-IE with stirring retains the crystalline structure and porous characteristics. As Y30-1IE(0.1Al)-S contains the highest concentration of incorporated EFAl after Y30-1IE(0.1Al)-H+S, therefore, the concentration of LAS accessed by pyridine is maximum in this sample. Lastly, the second lowest LAS content of Y30-1IE(0.1Al)-H nicely correlates with elemental analysis and the NMR results.

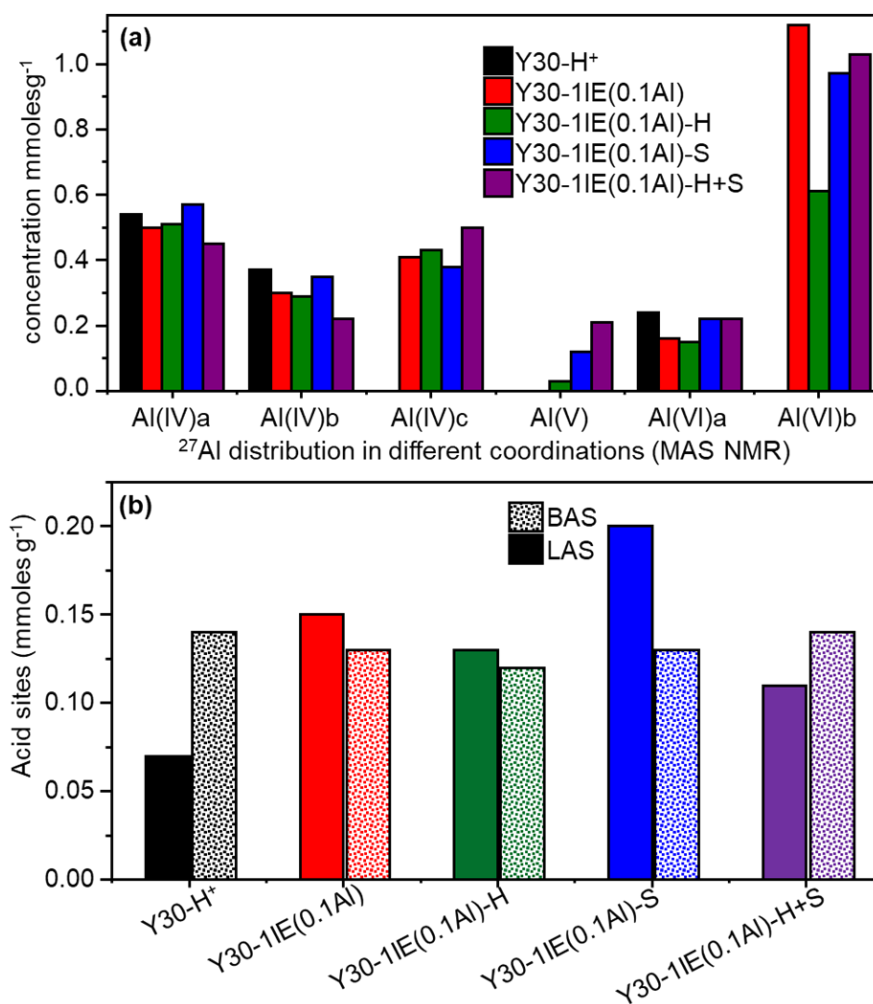


Figure 5.5: Parent Y30- $\text{H}^+$  and aluminum-exchanged samples under different Al-IE conditions; (a) Quantitative distribution (in mmol  $\text{g}^{-1}$ ,  $\pm 10\%$ ) of aluminum species in different coordinations obtained from  $^{27}\text{Al}$  MAS and MQMAS NMR spectra. (b) Quantitative distribution of acid sites accessed by pyridine (mmol  $\text{g}^{-1}$ ,  $\pm 10\%$ ); solid bars: LAS and dotted bars: BAS.

The catalytic conversion of 4-*tert* butylcyclohexanone, the corresponding selectivity to *cis* and *trans* products, and the initial rates of reaction are presented in **Figures 5.7a** and **5.7b**, respectively. The catalytic conversion after 7.4 h. and the rate of reactions of all the aluminum-exchanged samples increase, whereas no significant differences appear in aluminum-exchanged samples in terms of selectivity to *cis* and *trans* products. The catalytic activity of the samples increases in the following order: Y30- $\text{H}^+$  > Y30-1IE(0.1Al)-S > Y30-1IE(0.1Al) > Y30-1IE(0.1Al)-H > Y30-1IE(0.1Al)-H+S. This order does not correlate with the concentration of EFAl from NMR, however, this order of activity can be easily explained by combining the results of NMR with XRD, nitrogen physisorption, and FTIR results as follows. Due to reduced crystallinity and porosity, the sample Y30-1IE(0.1Al)-H+S, despite having maximum incorporated EFAl, does not show maximum LAS as well as maximum catalytic activity. In comparison, Y30-1IE(0.1Al)-H+S has

slightly lower incorporated EFAI. But it exhibits a maximum concentration of LAS and catalytic activity because the maximum retention of zeolite structure and porosity facilitates most of the EFAI LAS to be accessible to pyridine and 4-*tert* butylcyclohexanone.

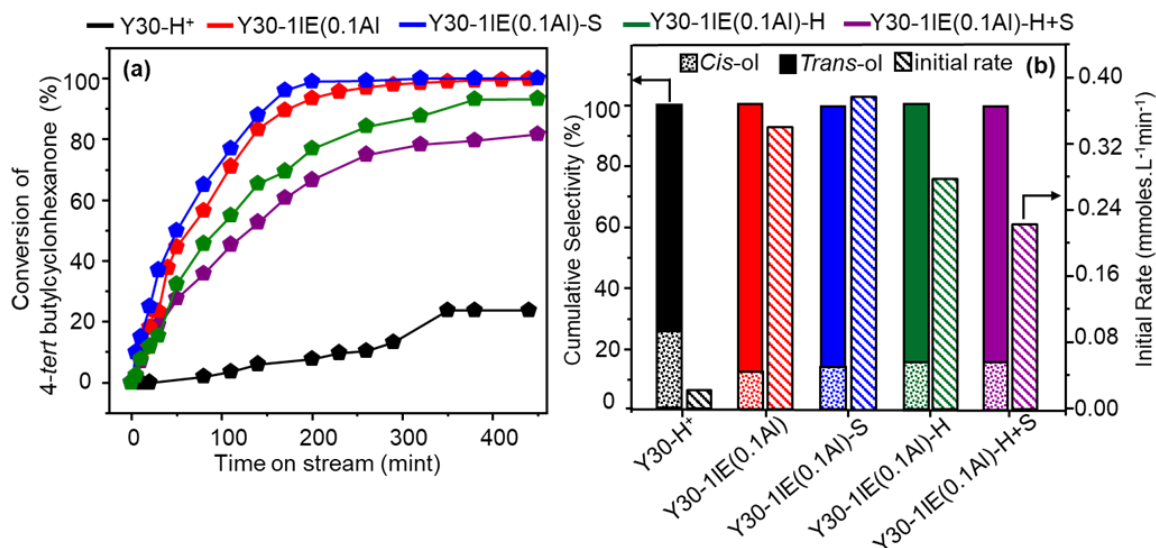


Figure 5.6. Catalytic data of MPV reduction of 4-*tert* butylcyclohexanone in Y30-H<sup>+</sup> and aluminum-exchanged samples under different Al-IE conditions; (a) conversion (%) of 4-*tert* butyl cyclohexanone as a function of time on stream. (b) cumulative selectivity towards *cis* (dotted bars) and *trans* (solid bars) 4-*tert* butylcyclohexanol and initial rate of reaction of parent (diagonal stripes bars) determined as the slope of the linear regression, in the time-concentration plot between zero and 110 min. of reaction time.

**Effect of Co-cation:** To evaluate the effect of co-cation on the generation of EFAI, Y30-H<sup>+</sup> was taken as a starting material. The sodium-exchange (Na-IE) treatment was performed before and after Al-IE treatment of Y30-H<sup>+</sup> which yields the samples as follows Y30-Na, Y30-1IE(0.1Al)-Na, and Y30-Na-1IE(0.1Al) of Al-IE. The Si/Al ratios and sodium content of these samples are presented in **Table 5.3**. After Na-IE of Y30-H<sup>+</sup>, the Si/Al ratio remains comparable to Y30-H<sup>+</sup>, whereas the sodium content is from 0.1 mmolesg<sup>-1</sup> to 0.98 mmolesg<sup>-1</sup>. Upon one-fold Al-IE of Y30-Na, the Si/Al decreases due to the uptake of aluminum due to Al-IE, whereas the Na content decreases to 0.20 mmolesg<sup>-1</sup>. Furthermore, the decrease in Si/Al ratio in Y30-Na-1IE(0.1Al) is lower than the decrease in Y30-1IE(0.1Al), suggesting that the presence of sodium reduces the efficiency of Al-IE treatment to incorporate aluminum. The Na-IE of sample Y30-1IE(0.1Al) incorporates sodium, whose concentration is lesser as compared to the sodium content obtained after Na-IE of Y30-H<sup>+</sup>. This suggests that the presence of aluminum (generated by Al-IE) lowers the incorporation of sodium after Na-IE. Furthermore, results also confirm that the Al-IE treatment of the Y30-Na sample leaches out sodium from the zeolite.

This was further confirmed by the determination of sodium content in aluminum nitrate solution after Al-IE treatment ( $0.71 \text{ mmoleg}^{-1}$ ). This leaching corresponds to the acidic nature of aluminum nitrate solution as the Al-IE treatment is performed while keeping the pH of about 4.

Table 5.3: Physicochemical characterization of parent Y30-H<sup>+</sup> and aluminum-exchanged zeolites with and without sodium co-cation

Zeolite	<sup>a</sup> S <sub>BET</sub>	<sup>b</sup> V <sub>total</sub>	<sup>c</sup> V <sub>micro</sub>	<sup>c</sup> S <sub>micro</sub>	<sup>c</sup> S <sub>meso</sub>	<sup>d</sup> Crystallinity <sub>rel</sub>	<sup>e</sup> Si/Al	<sup>f</sup> Na
	m <sup>2</sup> g <sup>-1</sup>	cm <sup>3</sup> g <sup>-1</sup>	cm <sup>3</sup> g <sup>-1</sup>	m <sup>2</sup> g <sup>-1</sup>	m <sup>2</sup> g <sup>-1</sup>	(%)	ratio	content
Y30-H <sup>+</sup>	740	0.44	0.33	555	180	100	30.53	0.10
Y30-1IE(0.1Al)	760	0.49	0.32	600	200	91	15.23	0.10
Y30-Na	750	0.45	0.32	560	120	88	30.46	0.98
Y30-Na-1IE(0.1Al)	650	0.41	0.29	520	140	87	17.42	0.20
Y30-1IE(0.1Al)-Na	565	0.33	0.26	410	130	79	14.96	0.66
<sup>e</sup> Al-IE solution	-	-	-	-	-	-	-	0.71

<sup>a</sup>calculated from the BET method, <sup>b</sup>based on single point adsorption at p/po = 0.97, <sup>c</sup>calculated from the t-plot method, <sup>d</sup>calculated by a previously described method <sup>180</sup>, assuming the crystallinity of parent zeolites as 100%, <sup>e</sup>calculated from ICP, <sup>f</sup>calculated from ICP (mmoleg<sup>-1</sup>)

The X-ray diffraction patterns and nitrogen adsorption/desorption isotherms of these samples are presented in **Figures 5.8a** and **5.5b**, respectively, whereas the values of relative crystallinity and porous characteristics are listed in **Table 5.3**. All the samples with and without the presence of sodium exhibit all the characteristic diffraction peaks comparable to the parent Y30-H<sup>+</sup> sample, whereas the relative crystallinity of these samples ranges from 79 to 91% <sup>50, 180</sup>. The samples containing sodium show lower relative crystallinity compared to those that have not undergone Na-IE treatment. The crystallinity of Y30-Na, Y30-Na-1IE(0.1Al), and Y30-1IE(0.1Al)-Na ranges from 88-79%. The nitrogen physisorption isotherms after Al-IE look comparable to comparable to parent Y30-H<sup>+</sup> sample <sup>209, 226-228</sup>, except for the sample Y30-1IE(0.1Al)-Na, where the amount of adsorbed nitrogen significantly decreases as compared to other aluminum-exchanged samples and Y30-H<sup>+</sup>. The BET surface area and micropore volume of this sample are also considerably lower than other samples (**Table 5.3**).

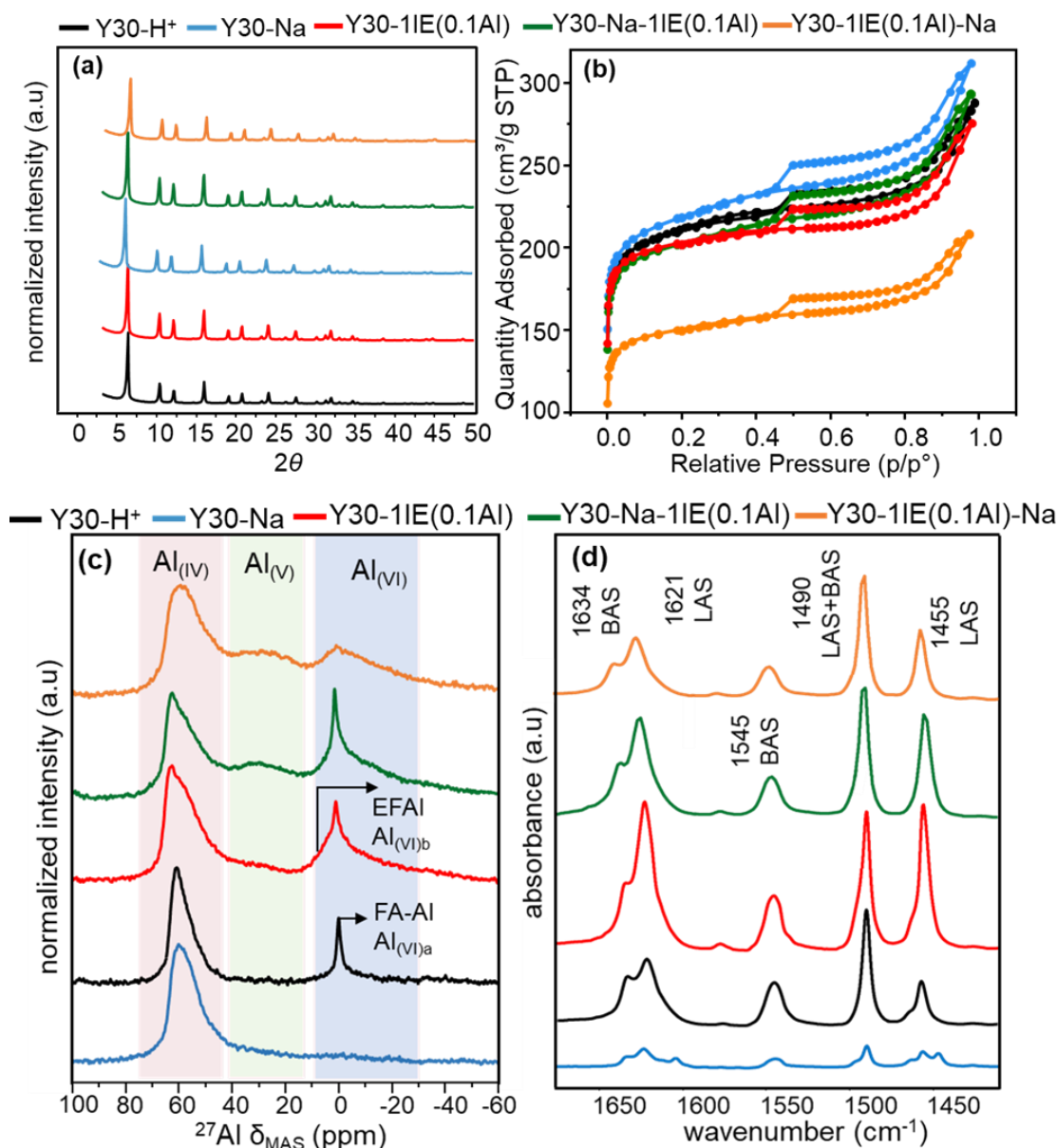


Figure 5.8: Parent Y30-H<sup>+</sup> and aluminum-exchanged samples with and without sodium cations; (a) PXRD patterns normalized to the weight of the sample used (b) nitrogen adsorption isotherms (c) <sup>27</sup>Al MAS NMR spectra normalized to the weight of the sample used; colored regions are added to guide the eye (d) FTIR difference spectra in pyridine stretching region normalized by the weight of the sample used. The difference spectra are obtained by subtraction of spectra after activation at 723K from spectra after pyridine adsorption at 423K followed by evacuation at 423K.

The <sup>27</sup>Al MAS spectra of the samples with and without the presence of sodium cations are presented in **Figure 5.8c**. After Na-IE of parent Y30-H<sup>+</sup>, the sharp feature at ~0 ppm due to FA-Al disappears, and the intensity of tetrahedral resonance increases. This is because the presence of any cation other than proton results in the reinsertion of FA-Al, the framework where it adopts tetrahedral coordination. This has also been discussed in **Chapter 4**, where the

$\text{NH}_4^+$ -IE of Y30- $\text{H}^+$  also results in the disappearance of the peak due to FA-Al with an associated increase in tetrahedral intensity (**Figure A.1**). However, the presence of sodium as co-cation results in tetrahedral feature significantly broader than Y30- $\text{H}^+$  and Y30- $\text{NH}_4^+$ , which corresponds to increase in quadrupolar interaction due to the large size sodium cations. Upon Al-IE of Y30-Na, the FA-Al feature reappears in Y30-Na-1IE(0.1Al), which is more intense than that in Y30-1IE(0.1Al), whereas the broad resonance due to EFAl species in the former is less intense. The former sample also has a significant intensity in the pentahedral region, whereas the intensity in the tetrahedral also decreases. After Na-IE of Y30-Na-1IE(0.1Al), FA-Al again disappears with a consequent increase in broadness and intensity in the tetrahedral region.

The quantitative distribution of aluminum species in different coordination is presented in **Figure 5.9a**, which shows that the concentration of EFAl is maximum in Y30-1IE(0.1Al), i.e.,  $1.12 \text{ mmol}\cdot\text{g}^{-1}$  and minimum in Y30-Na-1IE(0.1Al), i.e.,  $0.56 \text{ mmol}\cdot\text{g}^{-1}$ . Similarly, the concentration of FA-Al is maximum in Y30-Na-1IE(0.1Al), i.e.,  $0.29 \text{ mmol}\cdot\text{g}^{-1}$ , and minimum in Y30-1IE(0.1Al), i.e.,  $0.16 \text{ mmol}\cdot\text{g}^{-1}$ . These results suggest that the incorporation of EFAl due to Al-IE hampers by the presence of sodium. Furthermore, the Na-IE before and after Al-IE also favors the formation of pentacoordinate aluminum species, which is also true for the sample obtained after Al-IE of Y30- $\text{NH}_4^+$  (**Figure B.4**). However, the incorporation of aluminum by Al-IE is not significantly affected due the presence of ammonium cation and the profile of the spectrum of Y30- $\text{NH}_4^+$ -1IE(0.1Al) in the octa- and tetrahedral region looks similar to the that in the spectrum of Y30-1IE(0.1Al).

The FTIR difference spectra of samples in the pyridine aromatic ring stretching region are presented in **Figure 5.8d**, and the quantitative distribution of acid sites accessed by pyridine<sup>49, 70, 220</sup> is presented in **Figure 5.9a**. The spectrum of Y30-Na shows a drastic decrease in the intensities of all the bands. In line with NMR results, the concentration of LAS is maximum in Y30-1IE(0.1Al), i.e.,  $0.15 \text{ mmol}\cdot\text{g}^{-1}$ , and minimum in Y30-Na, i.e.,  $0.02 \text{ mmol}\cdot\text{g}^{-1}$ . The Y30-Na-1IE(0.1Al) and Y30-1IE(0.1Al)-Na consist of  $0.11 \text{ mmol}\cdot\text{g}^{-1}$  and  $0.09 \text{ mmol}\cdot\text{g}^{-1}$  of LAS, respectively, and these concentrations are higher than the content of LAS in parent Y30- $\text{H}^+$  but lower than in Y30-1IE(0.1Al). The concentration of BAS in Y30- $\text{H}^+$  and Y30-1IE(0.1Al) i.e.,  $0.14 \text{ mmol}\cdot\text{g}^{-1}$  and  $0.13 \text{ mmol}\cdot\text{g}^{-1}$ , respectively whereas it is fairly decreased in Y30-Na-1IE(0.1Al) and Y30-1IE(0.1Al)-Na i.e.,  $0.09 \text{ mmol}\cdot\text{g}^{-1}$  and  $0.06 \text{ mmol}\cdot\text{g}^{-1}$ . The presence of Na as co-cation kills almost all the BAS in Y30-Na ( $0.02 \text{ mmol}\cdot\text{g}^{-1}$ ). The higher concentration of BAS in Y30-Na-1IE(0.1Al) compared to Y30-Na agrees with the elemental analysis and

NMR results, suggesting that Al-IE leaches out more than 60%, resulting in regain of some BAS in the former sample.

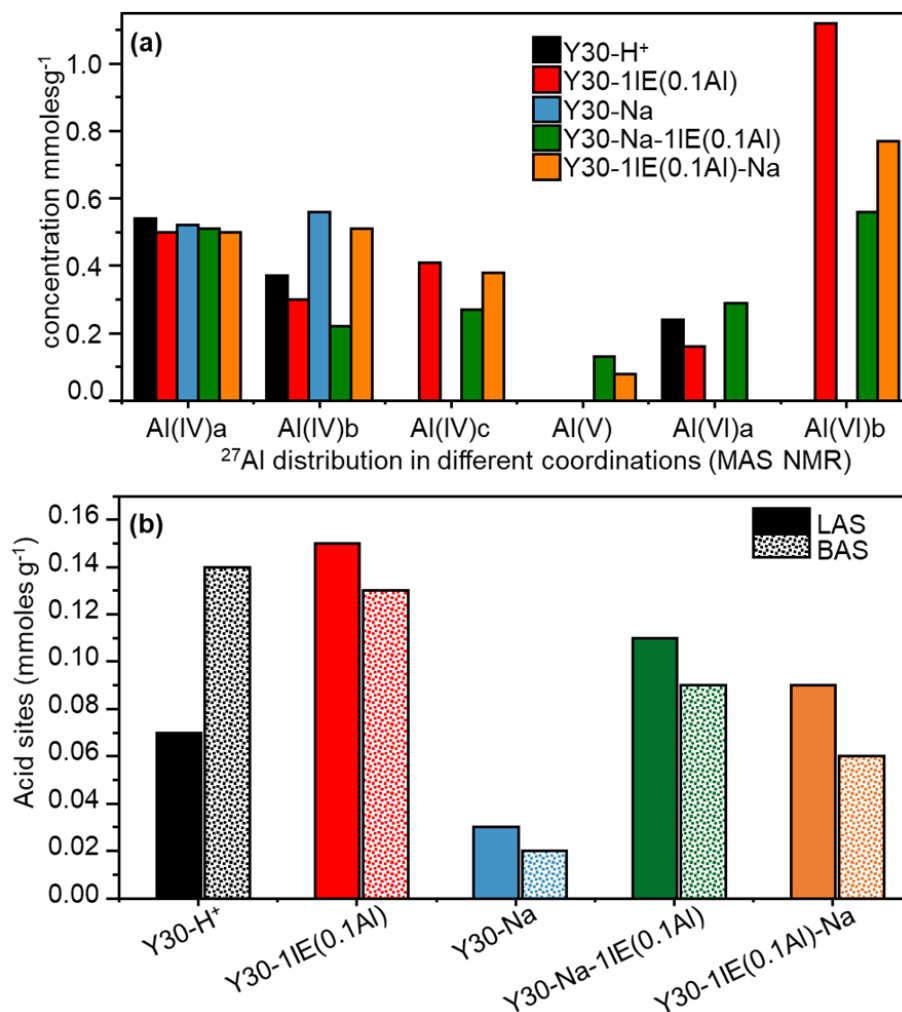


Figure 5.9: Parent Y30-H<sup>+</sup> and aluminum-exchanged samples with and without sodium cations; (a) Quantitative distribution (mmoles g<sup>-1</sup>,  $\pm 10\%$ ) of aluminum species in different coordinations obtained from <sup>27</sup>Al MAS and MQMAS NMR spectra. (b) Quantitative distribution of acid sites accessed by pyridine (mmoles g<sup>-1</sup>,  $\pm 10\%$ ); solid bars: BAS and dotted bars: LAS.

As NMR results suggested, the presence of sodium as a charge-balancing cation in Y30-1IE(0.1Al)-Na does not allow FA-Al to gain octahedral coordination. Consequently, the concentration of LAS in this sample is higher than Y30-Na-1IE(0.1Al) as the sum of the concentration of FA-Al and EFAI is higher in the later sample. Additionally, the crystallinity and porous characteristics are lowest in Y30-1IE(0.1Al)-Na, which can cause accessibility limitations. Thus, the presence of sodium after Al-IE has a negative impact not only on the generation of EFAI LAS by Al-IE but also on the accessibility of acid sites. In comparison, Al-IE of Y30-Na not only preserves the crystalline structure and porosity of zeolite but also



generates a higher concentration of EFAI LAS. However, this concentration remains lower than the sample Y30-1IE(0.1Al), which does not undergo any Na-IE treatment.

The catalytic conversions of 4-*tert* butylcyclohexanone of the samples are shown in **Figure 5.10a**, whereas the respective selectivity of *cis* and *trans* alcohols and the reaction rates are compared in **Figure 5.10b**. Y30-Na shows the least activity among all the samples, with a conversion of 10.3% and a reaction rate of 0.01 mmolL<sup>-1</sup>min<sup>-1</sup>. In comparison, the catalyst Y30-1IE(0.1Al), which does not undergo any Na-IE treatment, exhibits maximum conversion and reaction rate, i.e., 99.4% and 0.34 mmolL<sup>-1</sup>min<sup>-1</sup>, respectively. The samples Y30-Na-1IE(0.1Al) and Y30-1IE(0.1Al)-Na, with the conversion reaching 80% at a rate of 0.27 mmolL<sup>-1</sup>min<sup>-1</sup>, have catalytic activity lower than Y30-1IE(0.1Al) but higher than that of Y30-1IE(0.1Al)-Na (conversion = 36% and rate of reaction = 0.27 mmolL<sup>-1</sup>min<sup>-1</sup>). The selectivity of all the samples towards *cis* and *trans* alcohols remains comparable in all samples except Y30-Na, which shows maximum selectivity towards *trans*-4-*tert* butylcyclohexanol. The results suggest that the presence of sodium lowers the catalytic activity of parent Y30-H<sup>+</sup> and aluminum-exchanged samples. In aluminum-exchanged samples, this effect of sodium is more significant when Na-IE is performed after Al-IE. Thus, the catalytic performance of zeolites agrees well with the explanations discussed in the FTIR results of these samples.

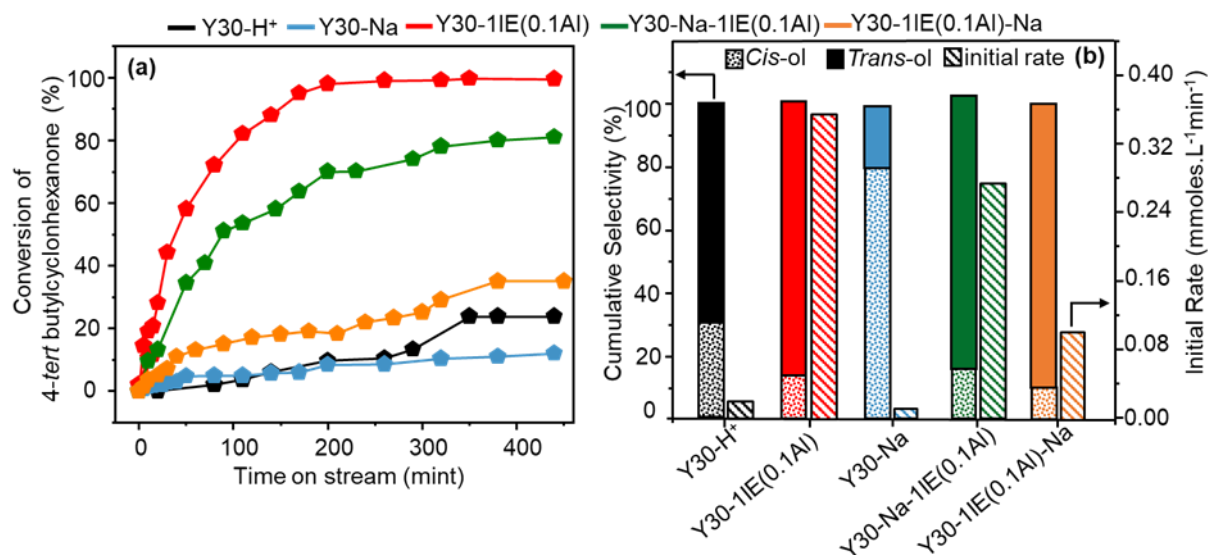


Figure 5.10. Catalytic data of MPV reduction of 4-*tert* butylcyclohexanone ( $\pm 5\%$ ) in parent Y30-H<sup>+</sup> and aluminum-exchanged samples with and without sodium cations; (a) conversion (%) of 4-*tert* butyl cyclohexanone as a function of time on stream. (b) cumulative selectivity towards *cis* (dotted bars) and *trans* (solid bars) 4-*tert* butylcyclohexanol and initial rate of reaction of parent (diagonal stripes bars) determined as the slope of the linear regression, in the time-concentration plot between zero and 110 min. of reaction time.

**Summarizing the role of Si/Al ratio, ion-exchange conditions and co-cation:** The outcomes on the generation of EFAl LAS in zeolite Y as a function of Si/Al ratio of parent zeolites, presence of co-cation and experimental conditions of Al-IE treatment are summarized in **Table 5.4**. The parent zeolites in their protonic forms have FA-Al, which is responsible for LAS; Y6 additionally possesses EFAl formed during steam calcinations of Y2.5. The catalytic activity of parent zeolites correlates with the amount of FA-Al and EFAl as well as the concentration of LAS except the ones with Si/Al ratios of 2.5 and 6, which is explained in terms of poor hydrothermal stability and porous characteristics of these samples. Thus, an increase in Si/Al ratio results in an enhancement of these features. In the parent zeolites with Si/Al ratios ranging from 6-40, the catalytic activity increases after Al-IE with an increasing Si/Al ratio of parent zeolites. This quantitatively correlates with the concentration of LAS from FTIR and EFAl from NMR. The catalytic activity and the EFAl LAS maximize after 5-fold Al-IE irrespective of the Si/Al ratio of parent zeolite, but the effect of Al-IE is more significant after one-fold Al-IE, which agrees with the findings of **Chapter 4**. However, Al-IE treatments of Y2.5, despite generating large concentrations of EFAl LAS, show poor catalytic performance due to the collapse of the zeolitic framework and pore structure.

Furthermore, the Al-IE with combined heating and stirring conditions generates a maximum concentration of EFAl. However, the corresponding catalytic activity and concentration of LAS are lower due to reduced crystallinity and pore volumes. The incorporation of EFAl by Al-IE is always accompanied by increased pentahedral and distorted tetrahedral species, whose content varies as a function of Al-IE conditions. The samples with lower content of these species show better catalytic activity and higher content of LAS accessed by pyridine. The Al-IE treatment under stirring is most favorable to retaining the intrinsic crystallinity and pore structure of zeolite while generating a maximum concentration of accessible EFAl LAS. The presence of sodium as co-cation lowers the Lewis acidity and catalytic activity of parent and aluminum-exchanged zeolites. The Na-IE treatment before and after Al-IE reduces the generation of EFAl. The FA-Al species, after IE with sodium or ammonium cations, no more adopt octahedral coordination but exist as tetrahedral species. The zeolite is usually not calcined after  $\text{NH}_4^+$ -IE as the calcination removes ammonia and converts the zeolite to a protonic form, resulting in octahedral coordination of FA-Al species. In comparison, Na-IE is always followed by a calcination treatment. Even if the aluminum-exchanged sample after Na-IE is followed by calcination, our results show that the EFAl no more acquires octahedral coordination. Most of the EFAl LAS generated by Al-IE possess octahedral coordination under NMR conditions and do not

affect the total BAS content of zeolites; these neutral species may exist in the form of nano-sized oxide and/or hydroxide clusters, as explained in **Chapter 4**<sup>180</sup>.

Table 5.4: Summary of the optimized strategies for the generation and activity of extra-framework Lewis acid sites in zeolite Y

<b>Al-IE conditions</b>	without heating and stirring	✓
	with heating	X
	with Stirring	✓
	with heating + stirring	X
<b>Concentration of IE precursor, type of IE treatment, no. of IE's</b>	single IE with high conc. of IE precursor	✓
	multiple IE's with high conc. of IE precursor	X
	multiple IE's with low conc. of IE precursor	✓
	multiple IE's followed by single calcination	X
	multiple IE's, with each IE, followed by a calcination	✓
<b>Presence of co-cation</b>	H <sup>+</sup>	✓
	Na	X
	NH <sub>4</sub> <sup>+</sup>	✓
<b>Si/Al ratio</b>	2.5	X
	6	X
	15	✓
	30	✓
	40	✓

## 5.4. Conclusions

The role of aluminum-exchange conditions, the Si/Al ratio of parent zeolite, and nature of co-cation in the generation of EFAl LAS by aluminum-exchange were studied. The results indicate that higher Si/Al ratios of parent zeolite favor maximum incorporation of EFAl due to Al-IE in this procedure while retaining the intrinsic pore structure and framework of zeolite. The LAS incorporated in zeolites of higher Si/Al ratios quantitatively correlate with the aluminum content determined by ICP, the octahedrally coordinated EFAl determined by NMR, and the

catalytic activity for MPV reduction of 4-*tert* butyl cyclohexanone. Aluminum-exchange performed under combined heating and stirring conditions yielded zeolites with lower catalytic activity and lower content of LA, despite the maximum concentration of EFAl. However, the Al-IE under stirring conditions is most favorable to incorporate large amounts EFAl with the maximum catalytic activity and the concentration of LAS. The presence of sodium as co-cation negatively affects the generation of EFAl LAS and the catalytic activity. The Al-IE procedure incorporates EFAl LAS, which exist as neutral aluminum oxide/hydroxide nanoclusters because they are not incorporated at the expense of BAS.

## **Chapter 6**

### **Factors affecting the generation and catalytic activity of extra-framework aluminum Lewis acid sites in aluminum-exchanged zeolites**

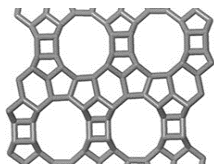
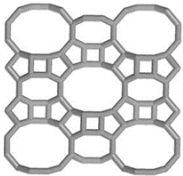
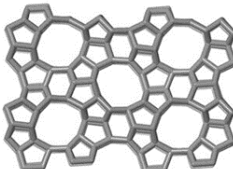
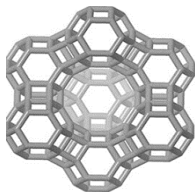
#### **Contributions**

The synthesis, XRD, nitrogen physisorption, FTIR and NMR characterization and catalytic evaluation of materials was performed by the author the thesis

## 6.1 Introduction

The consequences of post-synthetic modifications are not the same for all zeolite structures. This can be because of different reasons, including the framework structure, pore sizes, location of aluminum sites, etc.<sup>158-160</sup>. Consequently, these factors significantly affect the Lewis acidity of EFAl. A complication in establishing the relation between structure and performance originates from the varying effectiveness of post-synthetic modifications for zeolites of different structure types<sup>50, 75, 80</sup>. In previous chapters, combining the catalytic tests in the MPV reaction with FTIR and NMR spectroscopies, we quantitatively correlated the Lewis acidity to the EFAl species introduced by Al-IE. This chapter explores the factors that affect the incorporation of aluminum-exchanged LAS in zeolites of different framework types and their associated catalytic performance. For this, we systematically study the generation of aluminum-exchanged EF LAS in different zeolites of similar Si/Al ratios. We highlight which parameters play a decisive role while tuning the number of Lewis acid sites of different zeolites by Al-IE. We choose zeolite Y, beta, ZSM5, and mordenite structures for aluminum exchange treatments, as presented in **Table 6.1**.

Table 6.2: Selected zeolite structures with distinct features of their respective frameworks\*.

	BEA (Beta)	MOR (Mordenite)	MFI (ZSM5)	FAU (Faujasite Y)
				
Pore Size (Å)	6.7	6.5	5.3	7.4
Cage diameter (Å)	12.5	-	7.8	12.8
Pore dimensions	3	2	3	3

\*Data obtained from the Database of Zeolite Structures, Structure Commission of the International Zeolite Association<sup>22</sup>.

Zeolite BEA is a disordered/distorted/defective framework type due to local defects. These defects arise when a tertiary building unit experiences a right-angle rotation along the c-dimension concerning its neighbors of the same layer, resulting in an obstructed connection of this building unit to adjacent layers. Some T-atoms get partially or entirely dislodged from the framework to relieve these local strains<sup>103, 105, 229</sup>. It has been established that the Lewis acidic aluminum species in BEA reside exclusively in the micropores and not on the external surface.

The fact that the MPV reaction in zeolite BEA occurs solely within the micropores was evidenced using bulky 1-(3,5-di-tert-butylphenoxy)propan-2-one, which, due to its size, is unable to enter the micropores and shows no reactivity in MPV reduction primarily due to the absence of any Lewis acidic aluminum on the external surface<sup>105</sup>.

Zeolite MOR is a large pore and a semi-two-dimensional channel system (Table 1). Apart from 12-MR, it has intersecting 8-MR channels with a window spanning 5.7 x 2.6 Å. The strongly compressed 8-MR rings, with no/very little flexibility, are termed “side pockets” of zeolite MOR<sup>230-232</sup>. Ravi *et al.*<sup>65</sup> have proposed that a significant proportion of FA-Al species of MOR zeolite are located inside these 8-MR “side pockets.” In the case of MFI (ZSM5), although the channels of this zeolite are relatively small<sup>22, 64</sup>, it was shown that naphthalene molecules with a diameter of even 0.74 nm can adsorb in the pores. This is because a molecule can diffuse in the c-dimension by alternatively navigating along the first two dimensions, which explains the flexibility of 10-MR structures<sup>105</sup>. Zeolite FAU (zeolite Y), however, is a large pore zeolite consisting of a three-dimensional structure of pores made of large super-cages (1.2 nm) and small sodalite cages (0.74 nm) connecting them<sup>22</sup>.

We demonstrate that aluminum-exchange is an effective way to enhance the LAS of a zeolite, by generating likely neutral aluminum oxide/hydroxide clusters, without introducing any damage to the intrinsic structure of the zeolite. The incorporation and activity of EF LAS depend on the type of zeolite, pore size, and aluminum precursor used to access them. These findings provide guidelines to introduce LAS and generate Lewis-acid catalytic activity into zeolites.

## 6.2. Materials and Methods

**Chemicals and Materials:** Commercially available zeolite mordenite (CBV21A, ammonium form, Si/Al = 11), zeolite Y (CBV720, proton form, Si/Al = 15), zeolite ZSM5 (CBV 3024E, ammonium form, Si/Al = 15) and zeolite Beta (CP814E\*, ammonium form, Si/Al=12.5) were purchased from Zeolyst International. Aluminum nitrate nonahydrate (99.99%, ABCR) and Ammonium acetate (NH<sub>4</sub>(CH<sub>3</sub>COO)) (99%, Merck) were used as received.

**Material Preparation:** Ammonium forms of zeolites were converted to their respective proton forms by calcination at 823 K in static air at a heating ramp rate of 1K/min for 6 h. The parent proton forms of zeolites were labeled as BEA(12.5), MOR(11), MFI(15), and FAU(15), respectively, where integers in brackets give the Si/Al ratio of parent zeolites. The parent proton

forms of zeolites were aluminated according to the Al-IE procedure described in **Section 3.1.1**. The resultant aluminum-exchanged zeolites were labelled as BEA(12.5)-IE(Al), MOR(11)-IE(Al), MFI(15)-IE(Al) and FAU(15)-IE(Al) respectively. The parent proton forms of zeolites were converted to ammonium forms by the  $\text{NH}_4^+$ -IE procedure described in **Section 3.1.2**.

**Material Characterization:** The X-ray diffraction patterns of zeolite powders were recorded at room temperature on a PANalytical X'Pert PRO MPD diffractometer. The specific surface areas of zeolites were determined by collecting nitrogen adsorption-desorption isotherms at 77 K with Micromeritics Tristar II 3020 gas adsorption analyzer. ICP-OES determined the aluminum and silicon content of zeolite samples. Si/Al ratio was calculated based on the Al and Si content of the samples determined from ICP-OES. The  $^{27}\text{Al}$  MAS NMR spectra were recorded using a Bruker AVANCE III HD spectrometer and Bruker 400 MHz Ultra-Shield magnet at a rate of 10 kHz for 3000 scans. The  $^{27}\text{Al}$  MQMAS NMR spectra were recorded using a Bruker 700MHz Ultra-Shield spectrometer at 20 kHz for 1440 scans. The FTIR spectra of zeolite samples using pyridine as a probe molecule were recorded using a Thermo Nicolet iS50 FTIR spectrometer with a DTGS detector.

**Catalytic Evaluation:** The Meerwein-Ponndorf-Verley (MPV) reduction reaction was performed to estimate zeolites' catalytic activity. The catalytic experiment involved zeolite catalyst (0.2 g), isopropanol (50 mL), 4-*tert*-butylcyclohexanone (2.5 mmoles), and 1,3,5-tri-*tert*-butylbenzene as an internal standard (1 mmole).

### 6.3. Results and Discussion

**Physical Chemical Characterization:** The X-ray diffraction patterns of the parent and aluminum-exchanged zeolites are presented in **Figure 6.1a**. The samples BEA(12.5)-IE(Al), MOR(11)-IE(Al), MFI(15)-IE(Al), and FAU(15)-IE(Al) show all the characteristic diffraction peaks, comparable to those in the parent BEA(12.5), MOR(11), MFI(15) and FAU(15), respectively<sup>50, 233</sup>. The relative crystallinity<sup>180</sup> of the aluminum-modified zeolites (where the crystallinity of parent zeolites is assumed to be 100%) ranges from 89 to 96%, only indicating a minor change. The comparable intensities of diffraction peaks and relative crystallinity in all samples show that the structure of zeolites remains preserved after Al-IE treatment. These results rule out the collapse of the zeolite structure due to the development of any amorphous or crystalline impurities, such as aluminum oxide agglomerations formed during Al-IE or calcination.



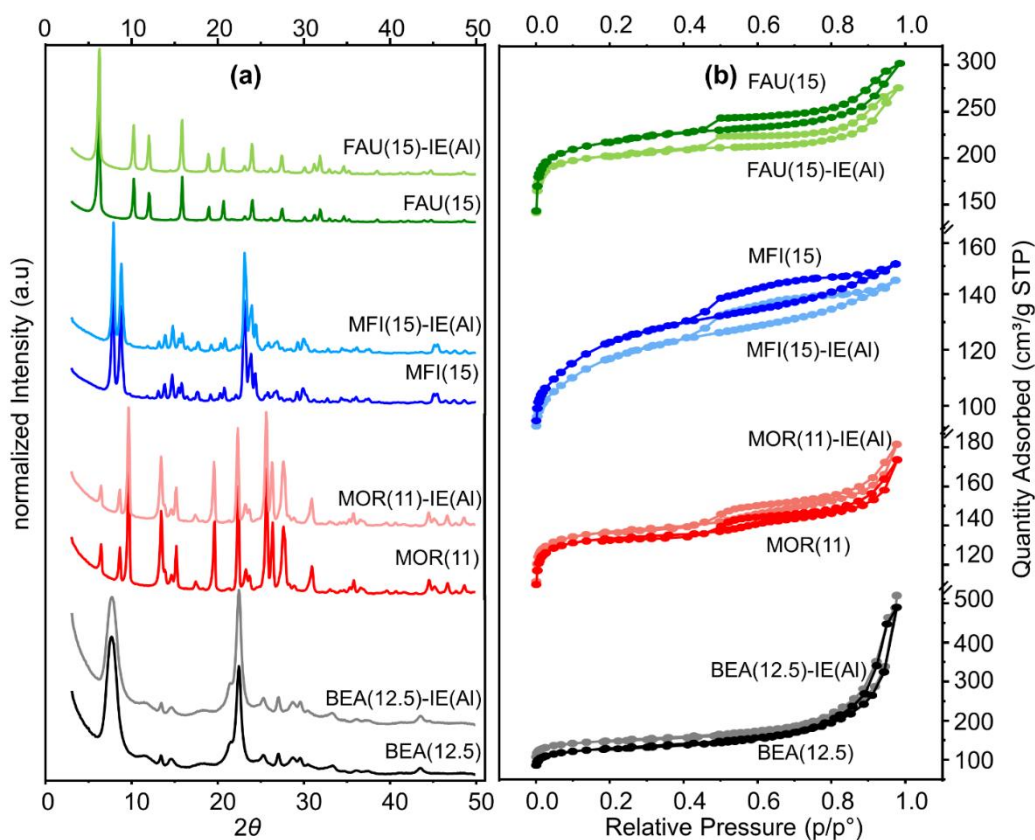


Figure 6.7: PXRD patterns (a) and nitrogen adsorption isotherms (b) of parent zeolite and aluminum-exchanged samples. All the spectra are normalized to the weight of the sample.

The nitrogen adsorption/desorption isotherms of all samples are presented in **Figure 6.1(b)**, whereas **Table 6.2** summarizes the quantitative characteristics. The parent BEA(12.5) and FAU(15) samples exhibit typical type IV isotherms<sup>209, 226, 227</sup>, whereas MFI(15) and MOR(11) show a characteristic type I isotherm<sup>228</sup>. The nitrogen physisorption isotherms of all aluminum-exchanged samples, i.e., BEA(12.5)-IE(Al), MFI(15)-IE(Al), MOR(11)-IE(Al) and FAU(15)-IE(Al), look identical to those of their corresponding parent zeolites. Likewise, BET surface areas and micropore volume of zeolites before and after treatment remain almost unchanged, staying within the error limits (**Table 6.2**). Thus, not only is the crystallinity virtually unchanged by ion exchange, but the intrinsic porosity and adsorption behavior are unaffected. To compare the varying degree of aluminum incorporation in different zeolites due to the Al-IE treatment, the bulk Si/Al ratios of zeolites before and after Al-IE, determined by ICP, are presented in Table 6.2. The Si/Al ratio values determined for BEA(12.5), MFI(15), MOR(11) and FAU(15) are 12.5, 15, 11 and 15 respectively. The Si/Al ratios for MOR(11)-IE(Al) and MFI(15)-IE(Al) are 10.6 and 13.9, showing only a little decrease as compared to those of parent zeolites. However, in the case of BEA(12.5)-IE(Al) and FAU(15)-IE(Al), the Si/Al ratios of 10.4 and 9.1, respectively, are substantially lower than those of their parent zeolites, indicating

an ample uptake of aluminum species by these zeolites during Al-IE treatment. Hence, the increase in total aluminum content after Al-IE with respect to the parent zeolites decreases in the following order: FAU(15)-IE(Al) > BEA(12.5)-IE(Al) > MFI(15)-IE(Al) > MOR(11)-IE(Al).

Table 6.2: Physicochemical characterization of parent and aluminum-exchanged zeolites

Zeolite	<sup>a</sup> S <sub>BET</sub> m <sup>2</sup> g <sup>-1</sup>	<sup>b</sup> V <sub>total</sub> cm <sup>3</sup> g <sup>-1</sup>	<sup>c</sup> V <sub>micro</sub> cm <sup>3</sup> g <sup>-1</sup>	<sup>c</sup> S <sub>micro</sub> m <sup>2</sup> g <sup>-1</sup>	<sup>c</sup> S <sub>meso</sub> m <sup>2</sup> g <sup>-1</sup>	<sup>f</sup> Crystallinity <sub>rel</sub> <sup>g</sup> Si/Al (%)	ratio
BEA(12.5)	480	0.20	0.20	340	150	100	12.5
BEA(12.5)-IE(Al)	450	0.24	0.21	320	130	89	10.4
MOR(11)	390	0.28	0.18	350	40	100	11.0
MOR(11)-IE(Al)	400	0.29	0.19	360	50	95	10.6
MFI(15)	310	0.14	0.15	280	30	100	15.0
MFI(15)-IE(Al)	310	0.15	0.14	270	40	96	13.9
FAU(15)	700	0.39	0.32	610	190	100	15.0
FAU(15)-IE(Al)	680	0.36	0.3	610	180	90	9.1

<sup>a</sup>calculated from the BET method, <sup>b</sup>based on single point adsorption at p/p<sub>0</sub> = 0.97, <sup>c</sup>calculated from the t-plot method, <sup>d</sup>calculated by a previously described method<sup>180</sup>, assuming the crystallinity of parent zeolites as 100%, <sup>e</sup>calculated from ICP

**Solid-state NMR spectroscopy:** The <sup>27</sup>Al MAS and <sup>27</sup>Al MQMAS NMR spectra of the zeolites recorded under ambient conditions are presented in **Figures 6.2** and **6.3**, respectively. **Figure 6.2** shows the sharp resonances at 54, 57, 57, and 61 ppm in the spectra of BEA(12.5), MOR(11), MFI(25), and FAU(15), respectively, due to tetrahedral aluminum species (Al(IV<sub>a</sub>)) in the framework of zeolite<sup>61, 62</sup>. The <sup>27</sup>Al MQMAS NMR spectra (**Figure 6.3a-d**) reveal the Al(IV<sub>a</sub>) resonance on the diagonal (where F1=F2), thus having a very small Q<sub>cc</sub> = 1.4-1.9 MHz (**Table 6.3**). The broadening and asymmetric shape of the tetrahedral signal in MAS NMR spectra of some parent zeolites is due to features other than Al(IV<sub>a</sub>) species. Firstly, a broad resonance, with small Q<sub>cc</sub> (1.3 - 1.9 MHz) but slightly greater isotropic broadening, is present at 58.5 and 56.0 ppm in the spectra of BEA(12.5) and FAU(15), respectively, labeled as Al(IV<sub>b</sub>) species. These Al(IV<sub>b</sub>) species, in FAU(15), are due to framework aluminum that are still in

tetrahedral coordination but facing a slightly different environment <sup>180</sup>. In the case of zeolite BEA(12.5), however, two sets of T sites that differ based on their T-O-T angles. Thus, aluminum on these two T sites are fairly symmetrical yet appear at slightly different chemical shifts in MAS NMR <sup>227, 234</sup>. Secondly, a broad resonance is present in the spectra of BEA(12.5), MOR(11), MFI(15), and FAU(15), at 60.0, 61.5, 62.4, and 63.2 ppm, respectively, that exhibits very large  $Q_{cc}$  (3.8 - 4.5 MHz) and is labeled as Al(IV<sub>c</sub>) species (**Figure 6.3 and Table 6.3**). These Al(IV<sub>c</sub>) species are assigned to distorted-tetrahedral aluminum, whose fraction varies as a function of calcination temperature, as discussed by Ravi *et al.* <sup>50</sup>. The spectra of BEA(12.5) and FAU(15) also show a small peak in the region 30-35 ppm due to penta-coordinated aluminum species <sup>63-65</sup>, labeled as Al(V) species.

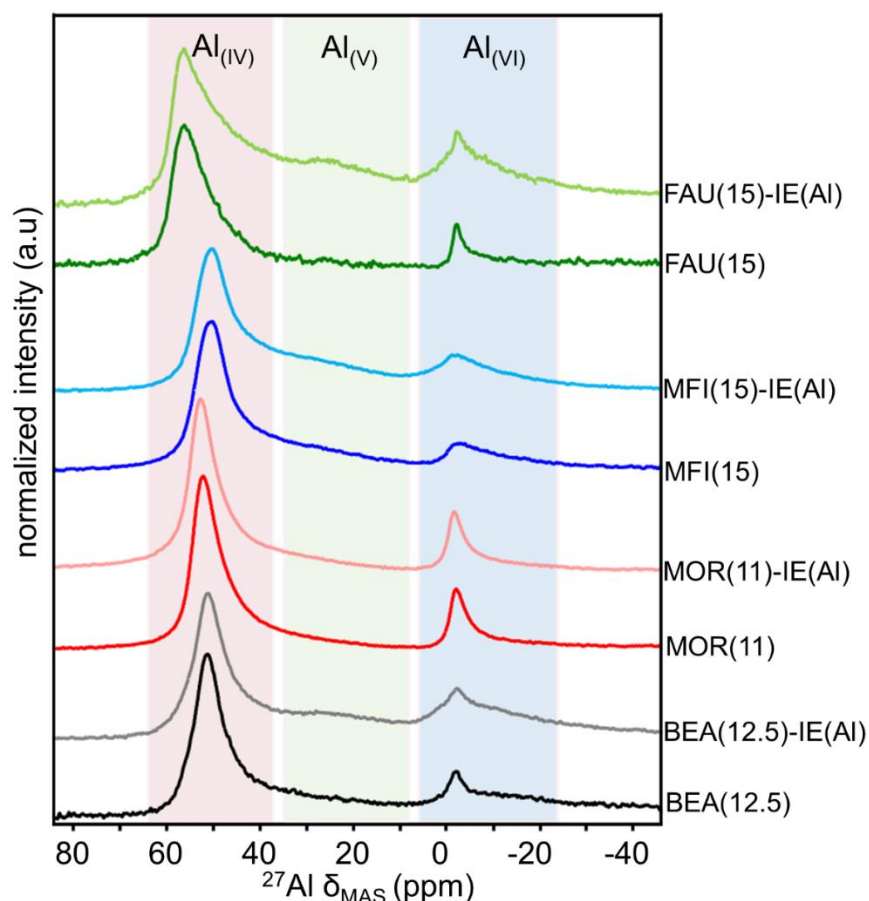


Figure 6.8: <sup>27</sup>Al MAS NMR spectra of parent and aluminum-exchanged zeolites. Colored regions are added to guide the eye. All the spectra are normalized by the weight of the sample used.

Octahedral aluminum, in the proton form of zeolites, can be characterized as (at least) two different types of species. The aluminum species that can be reinserted back into the framework of the zeolite after ammonium ion-exchange (disappearance of resonance in the octahedral

region and increase of intensity in the tetrahedral one) are framework-associated aluminum (FA-Al). Those retaining their octahedral coordination in proton and  $\text{NH}_4^+$  forms of the zeolite are assigned to EFAI<sup>50, 62, 180</sup>. The spectra of parent zeolites show a sharp resonance in the octahedral region at 0.1-1 ppm (**Figure 6.2**). The spectra of the  $\text{NH}_4^+$ -form of parent zeolites (**Figure C1**) do not show any peak at 0.1-1 ppm, with a corresponding increasing intensity in the tetrahedral region. Thus, these octahedral aluminum, corresponding to the 0.1-1 ppm resonance in proton form of zeolites, which appear as the framework tetrahedral species in  $\text{NH}_4^+$ -form of these zeolites, are FA-Al (denoted as  $\text{Al}(\text{VI}_a)$ )<sup>66</sup>. This resonance is narrow in the spectra of BEA(12.5), MOR(11), and FAU(15) samples ( $Q_{\text{cc}}=1.1-1.4$  MHz), whereas, in the spectrum of MFI(15), this peak experiences isotropic broadening, thus having slightly greater  $Q_{\text{cc}}$  (1.8 MHz) as compared to other parent zeolites (**Table 6.3** and **Figure 6.3(a-d)**).

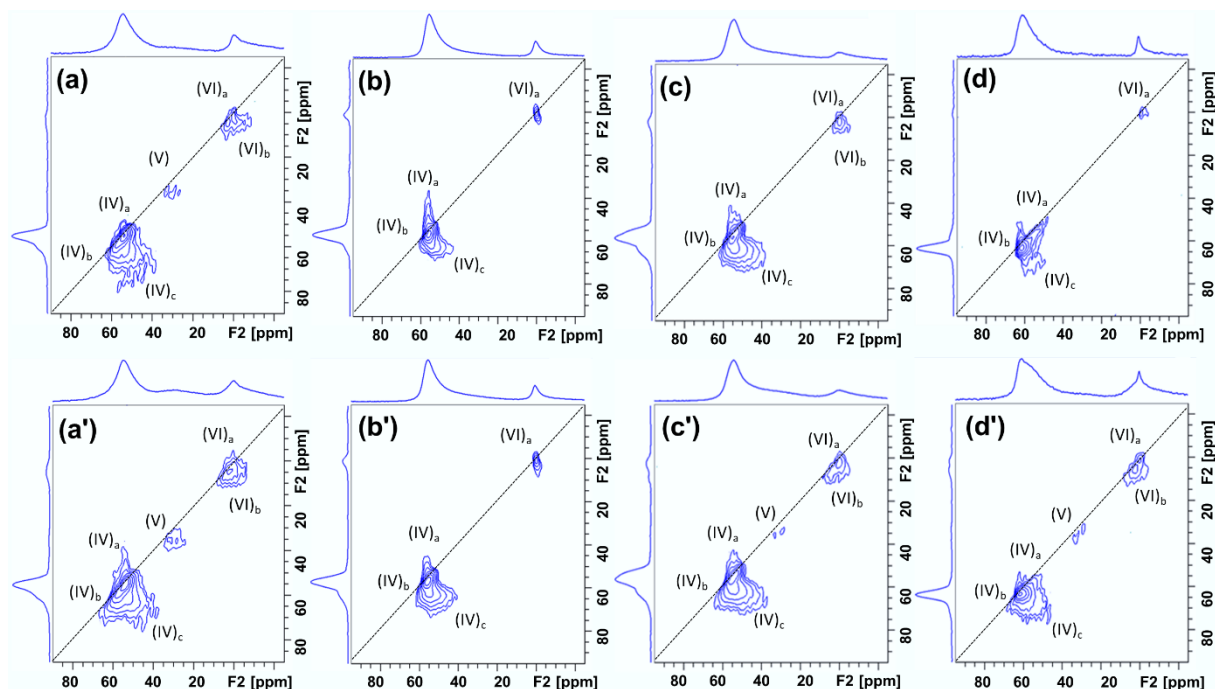


Figure 6.9:  $^{27}\text{Al}$  MQMAS spectra of parent and aluminum-exchanged zeolite BEA (a and a'), MOR (b and b'), MFI (c and c') and FAU (d and d') where a: BEA(12.5), a': BEA(12.5)-IE(Al), b: MOR(11), b': MOR(11)-IE(Al), c: MFI(15), ca: MFI(15)-IE(Al), d: FAU(15) and d' FAU(15)-IE(Al) respectively.

The spectra of BEA(12.5) and MFI(15) also show an additional broad asymmetric resonance at  $\sim 2.8$  ppm, whose intensity does not change in the spectra of respective  $\text{NH}_4^+$ -forms (**Figure C1**). This resonance, irreversible upon  $\text{NH}_4^+$  exchange, has significantly large  $Q_{\text{cc}} \sim 2.7$  MHz and a relatively narrow isotropic broadening ( **Table 6.3**, **Figure 6.3a** and **6.3c**). This broad asymmetric resonance at  $\sim 2.8$  ppm, labeled  $\text{Al}(\text{VI}_b)$ , can correlate to EFAI species. After Al-IE, no significant changes appear in the intensity of any resonances in the spectrum of

MOR(11)-IE(Al). However, the intensity of resonance due to EFAl species increases in the spectrum of BEA(12.5)-IE(Al), thus making the feature due to FA-Al species less prominent (**Figures 6.2 and 6.3a'**). A broad resonance with significant intensity also appears at ~3 ppm, in the spectrum of FAU(15)-IE(Al), which is similar in shape and quadrupolar interaction ( $Q_{cc}=2.8$  MHz) to EFAl species of the BEA(12.5) and BEA(12.5)-IE(Al) (**Figure 6.3 and Table 3**). The absence of this resonance in parent FAU(15) shows that the Al-IE in FAU(15)-IE(Al) results in the generation of EFAl species. In the case of MFI(15)-IE(Al), only a slight intensity increase in the octahedral region is visible, primarily due to FA-Al species (**Figures 2 and 3c'**). For BEA(12.5)-IE(Al), MFI(15)-IE(Al), and FAU(125)-IE(Al), the intensity of the peak due to Al(V) species also slightly increases. Lastly, as evident from MQMAS spectra, all aluminum-exchanged samples undergo a slight increase in the intensity of Al(IV<sub>c</sub>) species.

Table 6.3: NMR parameters including isotropic chemical shift in ppm ( $\delta_{iso}$ ,  $\pm 0.5$ ) and quadrupolar coupling constant in MHz ( $C_Q$ ,  $\pm 0.3$ ) obtained from deconvolution <sup>27</sup>Al MQMAS NMR spectra using the Czjzek line shape model <sup>192</sup>.

		Al(IV) <sub>a</sub>	Al(IV) <sub>b</sub>	Al(IV) <sub>c</sub>	Al(V)	Al(VI) <sub>a</sub>	Al(VI) <sub>b</sub>
BEA(12.5)	$\delta_{iso}$	54	58.5	60	30	0.1	2.7
	$C_Q$	1.7	1.9	4.5	2.5	1.1	2.5
MOR(11)	$\delta_{iso}$	57	-	61.5	-	0.5	-
	$C_Q$	1.7	-	3.1	-	1.4	-
MFI(15)	$\delta_{iso}$	56.8	-	62.4	32	0.9	2.8
	$C_Q$	1.9	-	4.2	2.3	2.8	2.4
FAU(15)	$\delta_{iso}$	61	56	63.2	35	1.0	2.9
	$C_Q$	1.4	1.3	3.8	1.7	1.2	2.8

The quantitative distribution of aluminum species in different coordinations obtained from MAS NMR spectra using the NMR fitting parameters determined from MQMAS spectra is

presented in **Figure 6.4(a-d)**. The quantitative information on the distribution of aluminum species is (with minor discrepancies) in line with the qualitative observations discussed above.

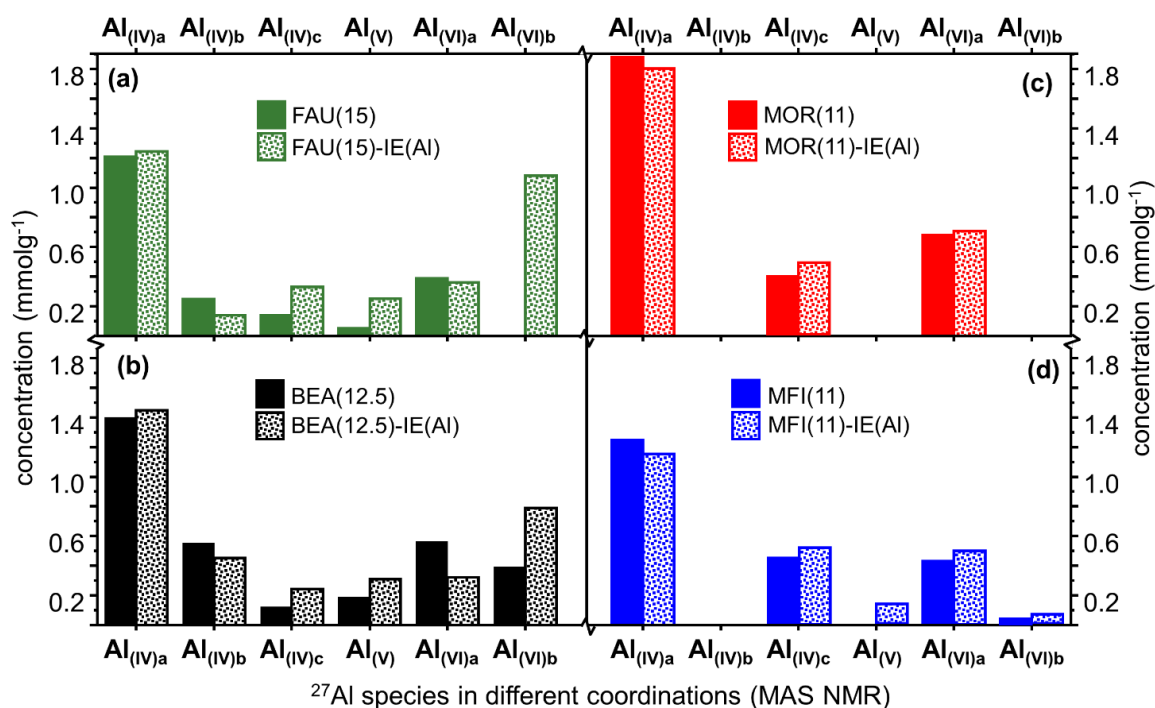


Figure 6.10: Quantitative distribution (in mmol g<sup>-1</sup>,  $\pm 10\%$ ) of aluminum species, i.e. Al(IV<sub>a</sub>), Al(IV<sub>b</sub>), Al(IV<sub>c</sub>), Al(V), Al(VI<sub>a</sub>), Al(VI<sub>b</sub>) species obtained from <sup>27</sup>Al MAS and MQMAS NMR spectra of parent (solid bars) and aluminum-exchanged (dotted bars) samples of FAU(a), BEA(b), MOR(c) and ZSM5(d) zeolites.

After Al-IE, the concentration of Al(IV<sub>c</sub>) species is slightly increased in all aluminum-treated samples, followed by a similar decrease in the concentration of Al(IV<sub>a</sub>) species in MOR(11)-IE(Al) and MFI(15)-IE(Al) and Al(IV<sub>b</sub>) species in FAU(15)-IE(Al) and BEA(12.5)-IE(Al) respectively (**Figure 6.4(a-d)**). The most prominent effect of Al-IE on the aluminum distribution can be observed in zeolite FAU and BEA. The concentration of Al(VI<sub>b</sub>) species (EFAl) in BEA(12.5)-IE(Al) increases from 0.39 to 0.79 mmol g<sup>-1</sup> after Al-IE, whereas that of Al(VI<sub>a</sub>) species (FA-Al) slightly decreases from 0.56 to 0.34 mmol g<sup>-1</sup>. In the case of FAU(15)-IE(Al), Al-IE incorporates 1.08 mmol g<sup>-1</sup> of EFAl Al(VI<sub>a</sub>) species, while the content of Al(VI<sub>a</sub>) species remains comparable to that of FAU(15). There is also a small (but similar) increase in the concentration of both Al(VI<sub>a</sub>) and Al(VI<sub>b</sub>) in MFI(15)-IE(Al). The increase in the octahedral aluminum content is also followed by a slight increase in Al(V) species content in aluminum-exchanged BEA, FAU, and MFI samples. From these results, the collective concentration of EFAl, after Al-IE, increases in the following order: MOR(11)-IE(Al) < MFI(11)-IE(Al) < FAU(15)-IE(Al) < BEA(12.5)-IE(Al) whereas the EFAl content incorporated after Al-IE

increases as follows: MOR(11)-IE(Al) < MFI(11)-IE(Al) << BEA(12.5)-IE(Al) < FAU(15)-IE(Al). The total aluminum content in zeolites plays important in enabling zeolites the stabilization of different structures of different coordination within the pores. Therefore, it is necessary to rule out respectively accepting the possibility that any change in the Si/Al ratio of MOR and MFI zeolites would affect the incorporation of EFAl species after Al-IE. Therefore, the  $^{27}\text{Al}$  MAS NMR of MFI(40) and MOR(45) (with relatively high Si/Al ratios) and their respective aluminum-exchanged samples were recorded (**Figure C2b**). However, Al-IE, yet again, fails to incorporate any EFAl species in MFI(40)-IE(Al) and MOR(45)-IE(Al) samples. Only a slight increase in FA-Al species was visible for MOR(45)-IE(Al) sample (**Figure C2b**).

**FTIR spectroscopy and quantification of Lewis acidity:** The FTIR spectra in the hydroxyl stretching region of parent and aluminum-exchanged zeolites, recorded before (solid spectra) and after pyridine adsorption (dotted spectra), are presented in **Figure 6.5a** and **6.5b**. Before pyridine adsorption, a sharp band at  $\sim 3745\text{ cm}^{-1}$  is present in the spectra of all parent zeolites, ascribed to external silanol groups<sup>235</sup>. The shoulder at  $\sim 3736\text{ cm}^{-1}$  corresponds to internal silanol groups. The band at  $3610\text{ cm}^{-1}$  in the spectra of BEA(12.5), MOR(11), and MFI(15) corresponds to bridging Si(OH)Al groups (BAS). The spectrum of FAU(15) shows two bands at  $3630$  and  $3565\text{ cm}^{-1}$ , corresponding to high and low-frequency bridging OH groups in super/sodalite cages (**Figure 6.5a**). A relatively broad band at  $\sim 3660\text{ cm}^{-1}$  in the spectra of BEA(12.5), MOR(11), and MFI(15) corresponds to framework Al-OH species<sup>50, 236-238</sup>. The spectrum of FAU(15) shows two bands at  $\sim 3660\text{ cm}^{-1}$  and  $\sim 3597\text{ cm}^{-1}$  due to AlOH species in a super cage and sodalite cage of zeolite, respectively<sup>239,240</sup>. A band at  $\sim 3780\text{ cm}^{-1}$  in the spectra of BEA(12.5) and MFI(15) is previously assigned to extra-lattice aluminum species, agglomerated in the form of  $\text{Al}_2\text{O}_3$  microparticles in ZSM-5<sup>241</sup>, EFAl in appearing in an octahedral environment in  $^{27}\text{Al}$  NMR of BEA zeolite<sup>242</sup> or tri-coordinated aluminum connected to the BEA framework<sup>243</sup>. The exact assignment of this band, however, remains ambiguous and is discussed in **Chapter 9**.

After pyridine adsorption, the  $3745\text{ cm}^{-1}$  band slightly lowers its intensity in the FAU(15) and MOR(11) spectra. The bands at  $3780\text{ cm}^{-1}$  and  $3610\text{ cm}^{-1}$  disappear entirely in the spectra of BEA(12.5) and MFI(15), whereas the later band decreases in intensity in MOR(11). The low-frequency OH band of FAU (15) also disappears, and the intensity of high frequency bridging OH band strongly decreases (**Figure 6.5a**). The remaining intensity of BAS bands in MOR(11) and FAU(15) indicates that some of the BAS in these samples are not probed by pyridine due to accessibility hindered by the zeolite pores. Furthermore, the hydroxyl bands due to Al-OH



species undergo complete disappearance in BEA(12.5) and (FAU(15)) and very little decrease in the intensity for MFI(15). In contrast, no significant difference appears in the Al-OH band of MOR(11).

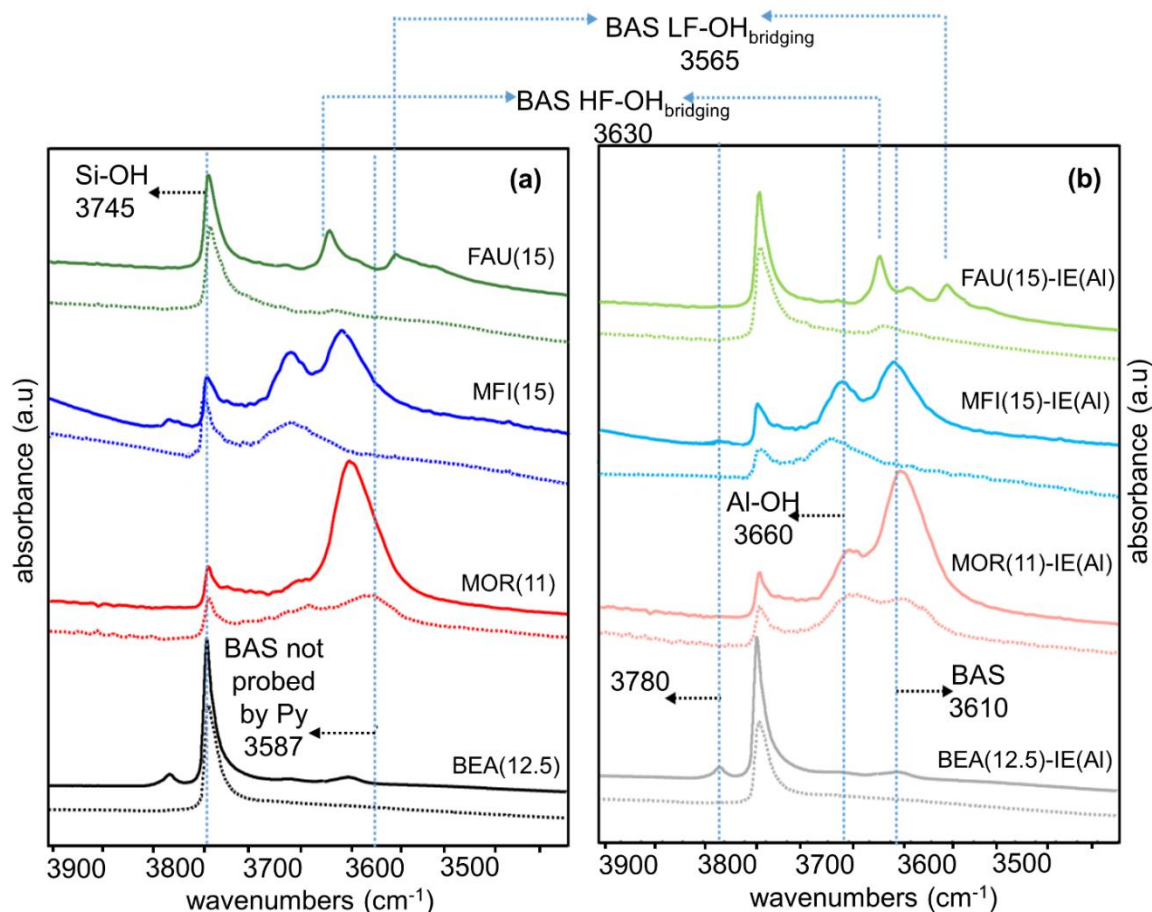


Figure 6.11: FTIR spectra in hydroxyl stretching region of parent (a) and aluminum-exchanged zeolites (b); solid lines represent spectra of evacuated samples at 723K, and dotted lines represent spectra after pyridine adsorption at 423K followed by evacuation at 423K. All the spectra are normalized by the weight of the sample used.

After aluminum incorporation, the FTIR spectra (before and after pyridine adsorption) of BEA(12.5)-IE(Al) and MFI(15)-IE(Al) do not reveal any substantial differences in the position or intensity of bands as compared to the parent zeolites (**Figure 6.5b**). However, the intensity of the bands due to AlOH species, in the case of MOR(11)-IE(Al) and FAU(15)-IE(Al), increases in intensity (at  $3660\text{ cm}^{-1}$  and  $3597\text{ cm}^{-1}$ , respectively). The intensity of the  $3660\text{ cm}^{-1}$  band in MOR has been established to be directly proportional to the amount of highly distorted-tetrahedral aluminum<sup>50</sup>. We also correlate this band to (Al(VI<sub>a</sub>)) species, as in our experiments, Al-IE treatment was always followed by calcination at temperatures similar to those utilized in Ref. 14.



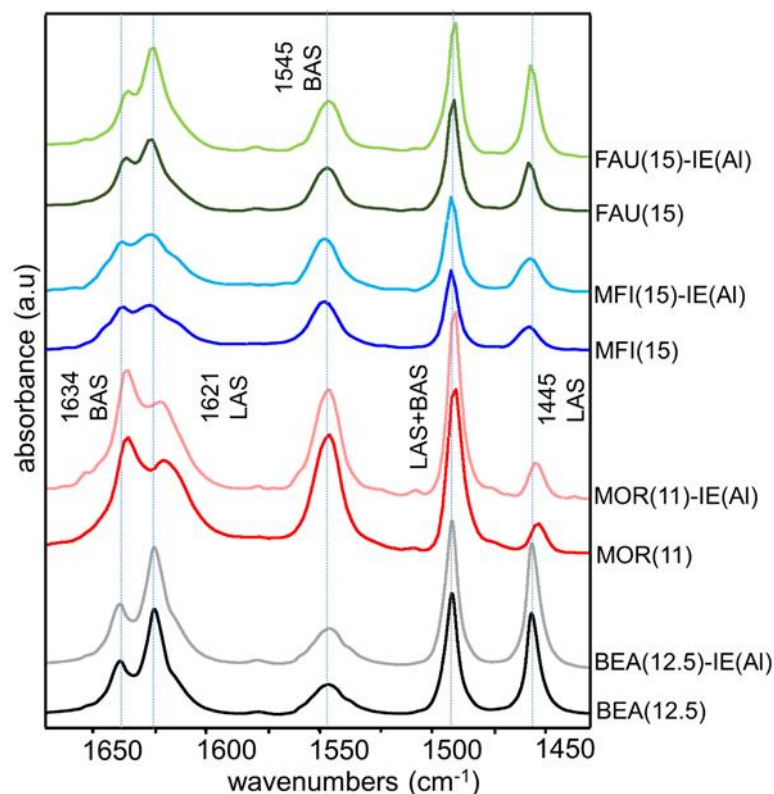


Figure 6.12: Pyridine-FTIR difference spectra in pyridine stretching region obtained by subtraction of spectra after activation at 723K from spectra after pyridine adsorption at 423K followed by evacuation at 423K. All the spectra are normalized by the weight of the sample used.

**Figure 6.6** presents the FTIR difference spectra of samples, before and after Al-IE, in the pyridine aromatic ring stretching region. The spectra of all samples exhibit five distinct bands at  $1455\text{ cm}^{-1}$ ,  $1490\text{ cm}^{-1}$ ,  $1545\text{ cm}^{-1}$ ,  $1621\text{ cm}^{-1}$ , and  $1634\text{ cm}^{-1}$ . The bands at  $1455\text{ cm}^{-1}$  and  $1621\text{ cm}^{-1}$  correspond to pyridine bound to LAS, and the bands at  $1545\text{ cm}^{-1}$  and  $1634\text{ cm}^{-1}$  correspond to vibrations of pyridine interacting with BAS<sup>49, 220</sup>. The  $1490\text{ cm}^{-1}$  band is structure-insensitive. The bands at  $1445$  and  $1545\text{ cm}^{-1}$  are utilized for quantification of LAS and BAS, respectively<sup>70</sup> (**Table 6.4**). Before Al-IE, the spectrum of BEA(12.5) has the maximum intensity of LAS bands, whereas the spectra of MOR(11), MFI(15) and FAU(15) have similar intensities (but lower than BEA(12.5)) of these LAS bands (**Figure 6.6**). The intensity of bands due to BAS is maximum in the spectrum of MOR(11), which, together with a maximum intensity of  $3610\text{ cm}^{-1}$  (**Figure 6.5b**), can be explained in terms of the lowest Si/Al ratio of MOR(11) as compared to the other parent zeolites. The BAS bands in the spectra of BEA(12.5), MFI(15), and FAU(15) show intensities comparable to each other but lower than MOR(11). As presented in **Table 6.4**, BEA(12.5) has the maximum concentration of LAS, i.e.,  $0.17\text{ mmol g}^{-1}$ , whereas LAS content of MOR(11), MFI(15), and FAU(15) is very low, i.e., in the range of

0.06 to 0.08 mmolg<sup>-1</sup>. The concentration of BAS is 0.16, 0.29, 0.20, and 0.18 mmolg<sup>-1</sup> for BEA(12.5), MOR(11), MFI(15), and FAU(15), respectively, the maximum being for MOR(11) zeolite.

Table 6.4: LAS and BAS concentration in mmoles g<sup>-1</sup> ( $\pm 10\%$ ) obtained from pyridine-FTIR spectroscopy (a); catalytic data of MPV reduction of 4-tert butylcyclohexanone ( $\pm 5\%$ ); conversion of 4-tert butylcyclohexanone over after 7.4 h (b); initial Rate of reaction in mmolesL<sup>-1</sup>min<sup>-1</sup>(c); cumulative selectivity after 7.4 h to cis and trans 4-tert butylcyclohexanol (d).

<b>Zeolite</b>	<b>Py-LAS<sup>a</sup></b>	<b>Py-BAS<sup>a</sup></b>	<b>Conversion<sup>b</sup></b>	<b>Initial Rate<sup>c</sup></b>	<b><i>cis:trans</i><sup>d</sup></b>
BEA(12.5)	0.17	0.16	96	1.67	94:06
BEA(12.5)-IE(Al)	0.20	0.15	100	1.9	88:12
MOR(11)	0.06	0.29	10	0.03	45:55
MOR(11)-IE(Al)	0.07	0.27	9	0.04	39:61
MFI(15)	0.07	0.20	9	0.04	37:63
MFI(15)-IE(Al)	0.08	0.21	10	0.05	34:66
FAU(15)	0.06	0.18	24	0.08	25:75
FAU(15)-IE(Al)	0.15	0.19	99	0.26	10:90

After Al-IE, LAS bands do not encounter any significant change in the spectra of MOR(11)-IE(Al) and MFI(15)-IE(Al) as compared to those of the respective parent zeolites. Therefore, the LAS content in MOR(11)-IE(Al) and MFI(15)-IE(Al) samples (0.07 and 0.08 mmolg<sup>-1</sup>, respectively) is also comparable to that of the parent zeolites. Nevertheless, the intensity of the LAS bands increases in the spectra of FAU(15)-IE(Al) and BEA(12.5)-IE(Al), with the spectrum of FAU(15)-IE(Al) showing the maximum increase. Likewise, there is a moderate increase in the LAS content of BEA(12.5)-IE(Al), i.e., 0.20 mmolg<sup>-1</sup>; however, FAU(15)-IE(Al) shows LAS content of 0.15 mmolg<sup>-1</sup> which is relatively large as compared to FAU(15). Thus, the LAS content after Al-IE decreases in the following order: BEA(12.5)-IE(Al) > FAU(15)-IE(Al) > MOR(11)-IE(Al)  $\approx$  MFI(15)-IE(Al). No prominent increase/decrease in the intensity of bands of BAS arises due to Al-IE in any of the spectra of aluminum-exchanged samples. As a result, the concentration of BAS after Al-IE is comparable to parent zeolites, even for FAU(15)-IE(Al), which shows a maximum increase in Lewis acidity.

**Lewis acid catalytic activity:** The catalytic Meerwein-Ponndorf-Verley reduction of 4-*tert* butylcyclohexanone, using isopropanol as the reducing agent, was performed to compare the catalytic performance of parent and aluminum-exchanged zeolites (**Figure 6.7a-d**, and **Table 6.4**). In the case of FAU(15), the reaction rate is 0.08 mmolL<sup>-1</sup>min<sup>-1</sup>, and the conversion increases with time on stream, reaching 24%. BEA(12.5) outperforms all parent zeolites, showing a very steep increase in conversion within 2 h of reaction time and gets the maximum conversion of 96% at a very high initial rate of 1.67 mmolL<sup>-1</sup>min<sup>-1</sup> (**Figure 6.7d** and **Table 6.4**). As *cis*- and *trans*-4-*tert* butylcyclohexanol are the two reaction products, there is a significant difference in the ratio of *cis* to *trans*-ol cumulative selectivity in parent zeolites (**Figure 6.7c** and **Table 6.4**). It appears that BEA(12.5) is most selective towards *cis*-ol (*cis:trans* selectivity of 94:06), whereas FAU(15) exhibits the greatest selectivity to the *trans* product (*cis:trans* ratio of 25:75 respectively).

The most prominent variation upon Al-IE in catalytic performance (as compared to parent zeolites) occurred in the case of FAU(15)-IE(Al), where the conversion increases sharply during the time on stream and reaches a very high value of 99 %, at a very high reaction rate of 0.26 mmolL<sup>-1</sup>min<sup>-1</sup> (**Figure 6.7b**, **6.6d** and **Table 6.4**). The increase in catalytic activity is also followed by a 15% increase in the *trans*-ol selectivity, with *cis:trans* selectivity reaching 10:90 % (**Figure 6.7c** and **Table 6.4**). Similarly, in BEA(12.5)-IE(Al), Al-IE increases the conversion to 100% within the reaction time studied, with a higher rate of reaction of 1.90 mmolL<sup>-1</sup>min<sup>-1</sup>, whereas *cis:trans* selectivity remains comparable to that of parent zeolite (**Figure 6.7d** and **Table 6.4**). The catalytic data of MOR and MFI zeolites are discussed in detail in SI (**section C2**). Thus, the catalytic activity of parent zeolites follows the order: BEA(12.5) > FAU(15) > MOR(11) ≈ MFI(15). However, the increase in the catalytic activity of aluminum-exchanged samples, when compared with their respective parent zeolites, decreases in the following order: FAU(15)-IE(Al) > BEA(12.5)-IE(Al) > MOR(11)-IE(Al) ≈ MFI(15)-IE(Al). Thus, BEA(12.5)-IE(Al) has the highest catalytic activity among all the parent and aluminum-exchanged zeolites.

Since parent BEA(12.5) inherits a large concentration of LAS (**Table 6.4**), and it already shows 96% conversion, it is rather challenging to observe the potential effect of EFAl LAS incorporated by Al-IE (only a 4% increase). Therefore, BEA(150) zeolite with a very low concentration of LAS and comparatively lower conversion (42%) and its respective aluminum-exchanged sample, i.e., BEA(12.5)-IE(Al), were also tested (**Table C3**). After Al-IE, the conversion reaches 100%, with a significant change in the rate of reaction (0.3 to 1.59 mmolL<sup>-1</sup>

$^1\text{min}^{-1}$ ), whereas *cis:trans* selectivity does not vary much when compared to BEA(150) sample (Table C3).

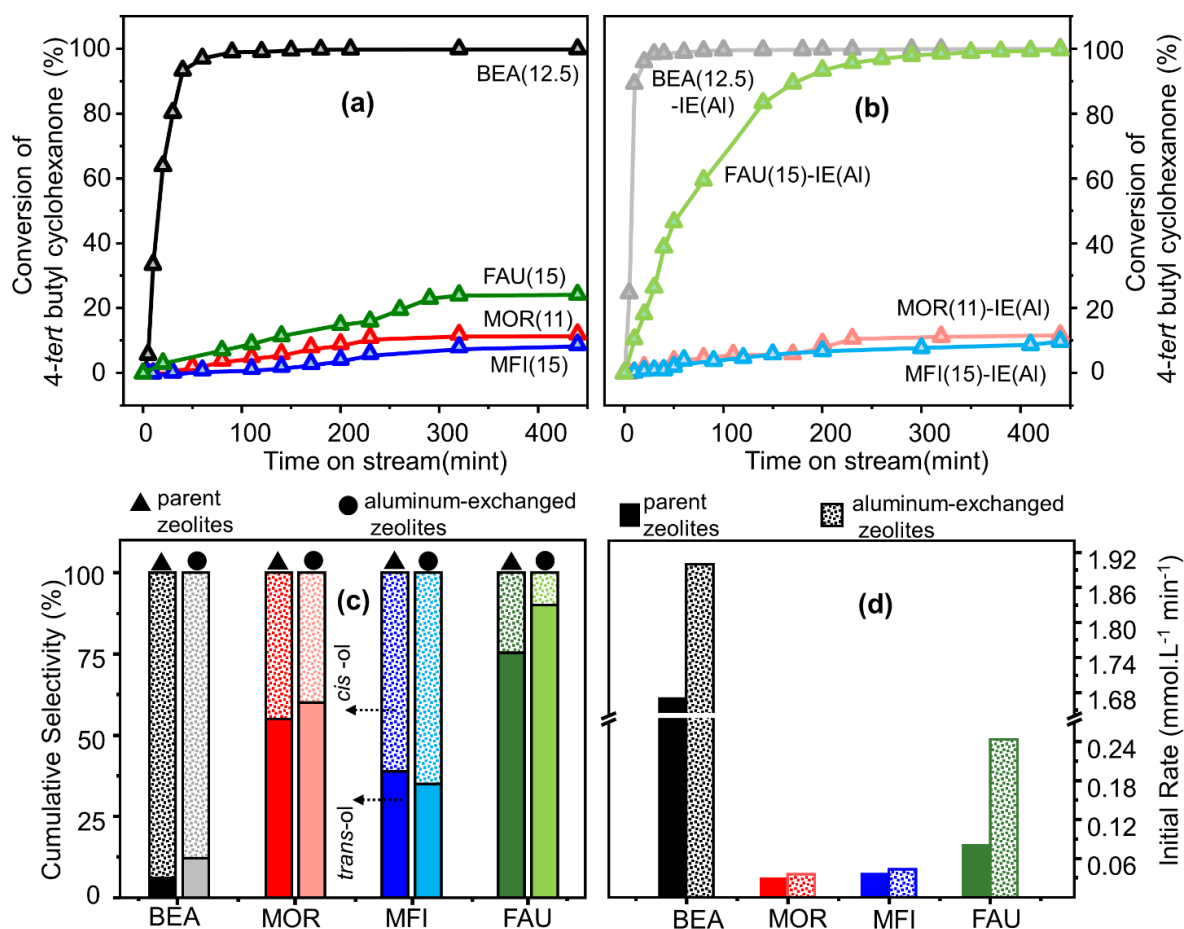


Figure 6.13. Catalytic conversion (%) of 4-tert butyl cyclohexanone as a function of time on stream over parent (a) and aluminum-exchanged (b) zeolites. Cumulative selectivity (c) towards *cis* (dotted bars) and *trans* (solid bars) 4-tert butylcyclohexanol for parent (▲) and aluminum-exchanged zeolites (●). Initial rate of reaction (d) of parent (solid bars) and aluminum-exchanged zeolites (dotted bars), determined as the slope of the linear regression, in the time-concentration plot between zero and 110 min. of reaction time.

**Factors affecting the generation and activity of extra-framework Lewis acid sites in different zeolites:** A comprehensive comparison of LAS from Py-FTIR and concentration of FA-Al and EFAl species as a function of MPV catalytic activity and pore size is presented in **Figures 6.8a** and **6.8b**. The Lewis acidic aluminum in parent proton forms of zeolites is formed due to the post-synthetic modifications. In the course of post-synthetic modification, some framework Si–O–Al bonds can hydrolyze, either completely, leaching the aluminum out of framework in a form of EFAl, or partially, generating FA-Al with reversible coordination<sup>50, 75, 80</sup>. However, the possibility of these Lewis acidic aluminum to act as catalytically active sites and their accessibility by the methods used to probe the Lewis acidity, depends on many factors.

These factors include the structure of acid site and its position in zeolite framework, the conditions under which they are being tested, type of zeolite framework and the size and shape of zeolite pores openings (**Section C3**)<sup>65, 234, 239</sup>. Both FA-Al and EFAl species contribute to Lewis acidity, as the inherent Lewis acidity of FAU(15) and MOR(11) is solely due to FA-Al. That of BEA(12.5) and MFI(15) is due to both FA-Al and EFAl species, respectively (**Figures 6.8a** and **6.8b**).

The highest catalytic activity and Lewis acidity of BEA(12.5) among all parent zeolites (**Figures 6.8a** and **6.8b**) are governed by the framework type, which in the case of BEA(12.5) is defective and can possess a substantial concentration of Lewis acid sites in the form of defect sites. Moreover, the Lewis acidic aluminum species located exclusively in the walls of micropores further account for the high activity of BEA(12.5) in MPV reaction and its higher stereoselectivity towards *cis*-4 *tert* butyl cyclohexanol product. Due to these reasons, an appreciable increase of EFAl LAS was possible after Al-IE with an associated increase in catalytic activity.

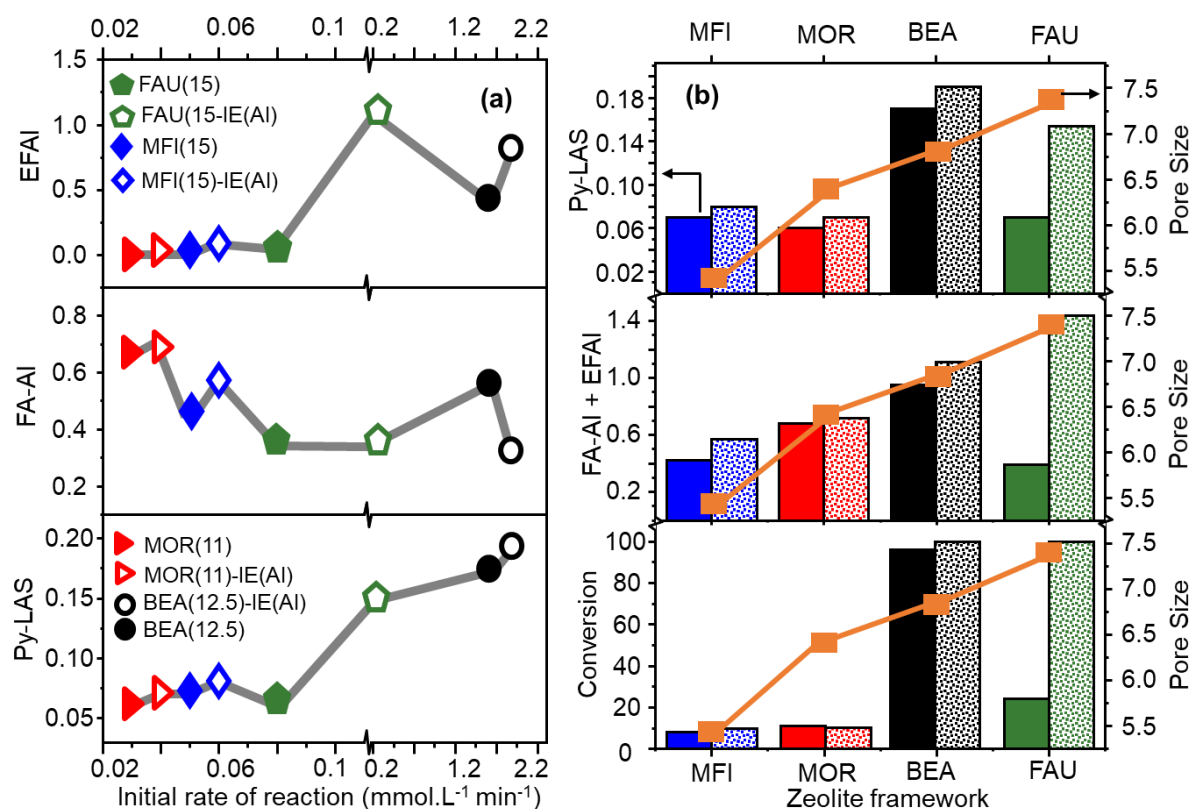


Figure 6.14: Total LAS content (mmolg<sup>-1</sup>) determined by Py-FTIR and concentration of FA-Al and EFAl species (mmolg<sup>-1</sup>) determined by NMR plotted as a function of the initial rate of reaction (a); Total MPV conversion (%) after 7.4 h, sum of the concentration of FA-Al and EFAl species (mmolg<sup>-1</sup>) and total LAS content ((mmolg<sup>-1</sup>) in parent and aluminum-exchanged

zeolites (b); Orange curves with squares in (b) represent the pore size of MFI, BEA, MOR, and FAU zeolites.

In the case of FAU(15), the concentration of FA-Al species nicely correlates with the inherent Lewis acid content measured by FTIR of adsorbed pyridine (**Figure 6.8a**). The activity of zeolite FAU(15), greater than MFI(15) and MOR(11), can be explained by the fact that it has the widest pores openings among all zeolites studied. Because the MPV reaction in FAU also takes place within micropores, FAU shows the highest selectivity towards the *trans*-alcohol. The lower activity of FAU(15) as compared to BEA(12.5) can be explained by the presence of a four times greater content of octahedral Al(VI<sub>a</sub>) and Al(VI<sub>b</sub>) species aluminum species and at least two times greater content of LAS. After Al-IE, the largest pore size of FAU(15) facilitates the maximum incorporation and stabilization of Lewis acidic EFAl and the associated maximum increase in the catalytic performance.

Table 6.5: Summary of factors affecting the generation and activity of extra-framework Lewis acid sites in zeolites studied in this work

	Lewis acidic Al species	<i>cis/trans</i> selectivity	product in	Accessibility Limitation (pyridine, MPV ketone/alcohol)	Steric hindrance for EFAl	Lewis acid activity of pristine zeolite	Increase in Lewis acid activity after Al-IE
<u>BEA(12.5)</u>	FA-Al+EFAl	<i>Cis</i> (small pore size, LAS present in micropores)		X (size+distorted framework)	X	very high	-
<u>BEA(12.5)-IE(Al)</u>	FA-Al+EFAl				X	-	considerable
<u>MOR(11)</u>	FA-Al	<i>Trans</i> (large pore size)		✓ (due to 8 MR)	✓	negligible	-
<u>MOR(11)-IE(Al)</u>	FA-Al				✓	-	negligible
<u>MFI(15)</u>	FA-Al+ EFAl	<i>Cis</i> (small pore size)		✓ (small pore size)	✓	negligible	-
<u>MFI(15)-IE(Al)</u>	FA-Al+ EFAl				✓	-	negligible
<u>FAU(15)</u>	FA-Al	<i>Trans</i> (large pore size)		X (large pore size)	X	small	-
<u>FAU(15)-IE(Al)</u>	FA-Al+ FAI				X	-	very high

The low Lewis acidity (accessed by pyridine) and the very low activity in MPV reaction in the case of MOR(11), yet with a very high concentration of FA-Al and wide pore openings, is due to the accessibility limitations offered by 8-MR “side pockets” and the position of FA-Al species (**Section C3**). The same factors account for the lowest incorporation of EFAl after Al-IE (**Section C3**). There is also a second possibility that EFAl species could not be formed/stabilized in the side pockets of zeolite due to the FA-Al already sitting in there (**Section C3**). In the case of MFI(15) zeolite, the low Lewis acidity accessed by pyridine and the low catalytic activity (**Figure 6.8a and 6.8b**) can be explained in terms of its small pore size

(Section C3). Furthermore, the large size of aluminum precursor and small pore size of zeolite also administrates the ineffectiveness of the Al-IE procedure to introduce EFAl LAS.

**Table 6.5** summarizes the factors affecting extra-framework Lewis acid site generation and their activity in MPV reaction. The information obtained from this work clearly demonstrates that Al-IE is an efficient method to increase Lewis acidity without affecting a zeolite's porous structure and crystallinity. As most of the EF aluminum Lewis acid sites generated by Al-IE possess octahedral coordination under NMR conditions and do not affect the total BAS content of zeolites (**Figures 8a and b**), these neutral species may exist in the form of nano-sized oxide and/or hydroxide clusters, as suggested in our previous work<sup>180</sup>. However, the catalytic activity of parent zeolites and the efficiency of Al-IE to introduce Lewis acidic moieties depends on different factors which are relevant in different ways, i.e., type of zeolite framework, pore size, accessibility, size of aluminum precursor, location of Lewis acidic aluminum, transition state stability and the symmetry of the reactant (**Table 6.5**). The relative selectivity towards *cis/trans* 4-*tert* butyl cyclohexanol before and after Al-IE is governed by the zeolite pore size and the location of LAS species and not by the nature of Lewis acidic aluminum they have (**Table 6.5**).

Another important factor that can facilitate the accommodation of EFAl in zeolites is the presence of defect sites in the parent zeolites, which are usually associated with post-synthetic treatments. The formation of no/very little EFAl LAS in MOR(11) and MFI(15) after Al-IE is in line with the fact that these zeolites are highly crystalline and contain few defect sites. FAU(15) and BEA (12.5) hold large amounts of defect sites as the commercial synthesis protocol of the former is realized by steaming and acid-leaching treatments<sup>209</sup>, whereas that of the latter employs alkalies as mineralizing agents (that cannot form defect-free BEA)<sup>244</sup>, respectively. Therefore, the positive effect of the presence of defect sites also holds well for FAU(15) and BEA(12.5). This is further supported by the fact that BEA(150), prepared by post-synthetic treatments and likely to have substantial amounts of defect sites, shows a greater concentration of EFAl after Al-IE compared with BEA(12.5) zeolite. However, MOR(45) and MFI(40) do not show significant increase in EFAl after Al-IE (**Figure C2a, C2b, and Table C3**).

## 6.4. Conclusions

The aluminum-exchange procedure was employed to compare the generation and activity of Lewis acidity in zeolites with BEA, MOR, MFI, and FAU topologies. The results indicate that this procedure efficiently incorporates a significant amount of LAS in BEA and FAU zeolites, as determined by FTIR of adsorbed pyridine. The incorporated LAS in these zeolites and the framework ones have a quantitative correlation with the aluminum content determined by ICP, the octahedrally coordinated EFAI determined by  $^{27}\text{Al}$  MAS NMR, and the catalytic activity for MPV reduction of 4-*tert* butyl cyclohexanone. The LAS in BEA and FAU are not incorporated at the expense of BAS, therefore, likely exist as neutral aluminum oxide/hydroxide nanoclusters. These LAS could not be generated in MFI zeolite due to its small pore size and in MOR zeolite due to accessibility limitations caused by side pockets and potential positions of these EFAI LAS in MOR, respectively. Consequently, no significant change in the content of EFAI and MPV catalytic activity was observable in these zeolites. The respective selectivity, determined by the zeolite pore size of all zeolite catalysts, towards *cis* to *trans* 4-*tert* butylcyclohexanol does not vary after Al-IE treatments.



## **Chapter 7**

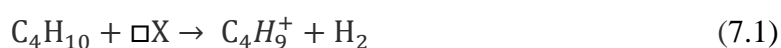
### **Butane dehydrogenation over aluminum-exchanged Lewis acidic zeolites**

#### **Contributions**

The synthesis, XRD, nitrogen physisorption, FTIR and NMR characterization and evaluation of catalytic data of materials was performed by the author the thesis

## 7.1 Introduction

The dehydrogenation of light alkanes, especially propane, and butane, is widely exploited for the large-scale production of corresponding olefins<sup>107</sup>. This process is of prime significance as lower alkanes are readily available feedstocks from petroleum and gas resources and can serve as precursors to many value-added chemicals. This reaction involves the activation of C-H bonds; thus, this is an energy-intensive process. Specifically, the non-oxidative heterogeneous dehydrogenation of butane has an activation energy of ~121–143 kJ/mol. As presented in **Eqs. 7.1** and **7.2**, dehydrogenation generally proceeds via the protolysis of alkane on LAS, followed by the release of hydrogen and the formation of a carbenium ion/alkoxy group<sup>114, 115</sup>.



After the formation of carbenium ion via dehydrogenation, it may (i) desorb as olefins from the catalyst, (ii) undergo double-bond-, cis/trans-, and skeletal isomerization, (iii) di- and/or oligomerize. Thus, this is an energy-intensive process as it involves the activation of C-H bonds. The dehydrogenation reactions of light alkanes are reversible, thermodynamically limited, strongly endothermic, and prone to volume expansion<sup>111, 112</sup>. Consequently, a high reaction temperature (850–1000K) and/or low alkane partial pressure are usually required<sup>108</sup>. At high temperatures and lower partial pressures of reactant, the unimolecular dehydrogenation mechanism is favorable. In contrast, low temperatures and high partial pressures favor the bimolecular mechanism for the dehydrogenation of alkanes. Activating C-H bonds of light alkanes over zeolites involves cooperative catalysis of LAS and BAS of zeolites<sup>111, 112</sup>. The later sites usually aid the activation of C-C bonds by the insertion of proton to C-C results. Consequently, carbonium ion intermediates are formed, which eventually result in cracking products<sup>109</sup>. As the C-H bonds of alkanes are stronger than C-C bonds, a suitable catalyst for alkane dehydrogenation is the one that enhances the C-H bond cleavage over C-C bond activation to avoid side reactions. Literature suggests that extra-framework cations can serve as LAS for C-H activation. In zeolites, the isolated framework heteroatom LAS<sup>245-248</sup>, as well as heteroatom extra-framework LAS species<sup>249, 250</sup>, are explored as catalysts for alkane dehydrogenation. However, the literature lacks the exploration of EFAl LAS for this purpose.

The work presented in previous chapters describes that Lewis acidic EFAl can be incorporated in zeolites by facile aluminum-exchange procedure. As discussed in **Chapter 1**, EFAl species may exist in many different forms:  $\text{Al}^{3+}$ ,  $\text{Al}(\text{OH})^{2+}$ ,  $\text{Al}(\text{OH})_2^+$ ,  $\text{AlOOH}$ ,  $\text{Al}(\text{OH})_3$ , and  $\text{Al}_2\text{O}_3$ <sup>206, 207</sup>. Of all the possible forms, the cationic extra-framework species  $\text{Al}^{3+}$ ,  $\text{Al}(\text{OH})^{2+}$ , and  $\text{Al}(\text{OH})_2^+$  are regarded as strong Lewis acid sites capable of hydrocarbon conversion by a hydride transfer mechanism<sup>156, 157</sup>. In the previous chapters, FTIR and NMR analysis confirmed that EFAl LAS species incorporated by Al-IE don't reduce the number of BAS; thus, they are neutral species<sup>180</sup>. Despite being neutral, these LAS appear strong enough to significantly improve the activity in the MPV reduction reaction over zeolite Y and BEA. As the MPV reduction of ketones to respective alcohols involves a hydride transfer mechanism from an easily oxidizable secondary alcohol, e.g., isopropanol, this reaction is not termed as highly energy intensive<sup>100, 103</sup>. This suggests that the LAS of medium and weak strength can also catalyze this reaction, provided the suitable pore size of zeolite<sup>158-160</sup>. Furthermore, as MPV reduction involve mild reaction conditions, this is very likely that the structure of LAS and the zeolite may not suffer from any significant destruction. In comparison, butane dehydrogenation requires strong LAS and operates under severe reaction conditions.

As the aluminum-exchange selectively introduces LAS without affecting the number of BAS, n-butane dehydrogenation is a suitable probe reaction to assess the performance of ion-exchanged EFAl LAS. Therefore, the work presented in this chapter explores the catalytic activity of zeolites with higher contents of LAS due to the generation of neutral EFAl species. For this, the aluminum-exchanged zeolites prepared for the work presented in **Chapter 4** and **Chapter 5** are employed for the catalytic dehydrogenation of n-butane. The strength of aluminum LAS of these samples to activate the C-H bonds is evaluated, focusing on the strength and thermal stability of EFAl LAS generated by Al-IE. The work demonstrates that the ammonium forms of parent zeolites of low Si/Al content show higher n-butane conversion than proton forms but are more selective to cracking pathway. At Si/Al ratios above 15, the protonic zeolites are more active, but the ammonium forms are more selective to dehydrogenation. The aluminum-exchange treatment significantly increases the conversion with enhanced selectivity to dehydrogenation products. No significant change in selectivity occurs by lowering the BAS content of aluminum-exchanged samples by Na-IE. Furthermore, the structure of EFAl species and their Lewis acidic nature remains preserved in the zeolites after regeneration of the spent catalysts, which proposes that dehydrogenation occurs on EFAl LAS. The preservation of EFAl

LAS in regenerated catalysts confirms that the thermal stability and strength of neutral EFAl LAS, produced by Al-IE, are capable of cleaving the C-H bonds of alkanes.

## 7.2. Materials and Methods

**Chemicals and Materials:** Commercially available zeolite Y samples were purchased from Zeolyst International with Si/Al ratios as follows; CBV300 (ammonium form, Si/Al = 2.5), CBV714 (ammonium form, Si/Al = 6), CBV720 (proton form, Si/Al = 15), CBV760 (proton form, Si/Al = 30), and CBV780 (proton form, Si/Al = 40). Aluminum nitrate nonahydrate (99.99%, ABCR), sodium nitrate (>99%, Sigma-Aldrich), ammonium nitrate (>99%, Sigma-Aldrich), and ammonium acetate ( $\text{NH}_4(\text{CH}_3\text{COO})$ ) (99%, Merck) were used as received.

**Material Preparation:** Ammonium forms of zeolites were converted to their respective proton forms by calcination at 823 K in static air at a heating ramp rate of 1K/min for 6 h. The parent proton forms of Y zeolites were labeled as Y2.5-H<sup>+</sup>, Y6-H<sup>+</sup>, Y15-H<sup>+</sup>, Y30-H<sup>+</sup>, and Y40-H<sup>+</sup>, respectively, where integers give the Si/Al ratio of parent zeolites. **Table 7.1** presents the codes of all samples used in this work with the respective treatment conditions. The proton forms of zeolites were aluminated according to the Al-IE procedure described in **Section 3.1.1** using 0.1M  $\text{Al}(\text{NO}_3)_3$  solution. The samples were one-fold and five-fold aluminum-exchanged without heating or stirring. Y30-H<sup>+</sup> and Y30-1IE(0.1Al)-H<sup>+</sup> were sodium-exchanged using the Na-IE procedure described in **Section 3.1.3**. The sample Y30-Na-IE(0.1Al)-H<sup>+</sup> was prepared by one-fold Al-IE on Y30-Na-H<sup>+</sup> using the Al-IE procedure as stated above. The proton forms of all parent zeolites were converted to their respective ammonium forms using the  $\text{NH}_4^+$ -IE procedure described in **Section 3.1.2**. The aluminum-exchanged samples were converted to their respective ammonium forms by a partial gaseous ammonification procedure. In this procedure, gaseous ammonia was adsorbed for an hour from a flow of 10%  $\text{NH}_3$  in He on protonic zeolites at 423K. The ammonium zeolites prepared by  $\text{NH}_4^+$ -IE contain are labeled with ' $\text{NH}_4^+$ ', whereas those prepared by gaseous ammonification are labeled with ' $\text{NH}_3$ '.

**Material Characterization:** The X-ray diffraction patterns of zeolite powders were recorded at room temperature on a PANalytical X'Pert PRO MPD diffractometer. The specific surface areas of zeolites were determined by collecting nitrogen adsorption-desorption isotherms at 77 K with Micromeritics Tristar II 3020 gas adsorption analyzer. ICP-OES determined the aluminum and silicon content of zeolite samples. Si/Al ratio was calculated based on the Al and Si content of the samples determined from ICP-OES. The  $^{27}\text{Al}$  MAS NMR spectra were recorded using a Bruker AVANCE III HD spectrometer and Bruker 400 MHz Ultra-Shield

magnet at a rate of 10 kHz for 3000 scans. The  $^{27}\text{Al}$  MQMAS NMR spectra were recorded using a Bruker 700MHz Ultra-Shield spectrometer at 20 kHz for 1440 scans. The FTIR spectra of zeolite samples using pyridine as a probe molecule were recorded using a Thermo Nicolet iS50 FTIR spectrometer with a DTGS detector. The weight loss on the spent catalysts was determined by thermogravimetric analysis (TGA, NETZSCH STA 409 PC/PG) from room temperature to 1073K (10K /min) in a high-purity oxygen atmosphere. Prior to the FTIR and NMR measurements on the spent catalysts, the samples were calcined at 823K in a high-purity oxygen atmosphere at 1K/min for 4 h. to remove carbon contents.

Table 7.1: Sample codes used in this work with the respective treatment conditions

Sr. No.	Zeolite	Treatment Conditions
1	Y2.5-H <sup>+</sup>	
2	Y15-H <sup>+</sup>	air calcination of as-received zeolites
3	Y30-H <sup>+</sup>	
4	Y40-H <sup>+</sup>	
5	Y2.5-NH <sub>4</sub> <sup>+</sup>	
6	Y6-NH <sub>4</sub> <sup>+</sup>	3x ammonium-exchange of parent protonic zeolites
7	Y15-NH <sub>4</sub> <sup>+</sup>	
8	Y30-NH <sub>4</sub> <sup>+</sup>	
9	Y40-NH <sub>4</sub> <sup>+</sup>	
10	Y15-1IE(0.1Al)-H <sup>+</sup>	1x aluminum-exchange on Y15-H <sup>+</sup>
11	Y15-5IE(0.1Al)-H <sup>+</sup>	5x aluminum-exchange on Y15-H <sup>+</sup>
12	Y30-1IE(0.1Al)-H <sup>+</sup>	1x aluminum-exchange on Y30-H <sup>+</sup>
13	Y30-5IE(0.1Al)-H <sup>+</sup>	5x aluminum-exchange on Y30-H <sup>+</sup>
14	Y15-1IE(0.1Al)-NH <sub>3</sub>	gaseous ammonification of Y15-1IE(0.1Al)-H <sup>+</sup>
15	Y15-5IE(0.1Al)-NH <sub>3</sub>	gaseous ammonification of Y15-5IE(0.1Al)-H <sup>+</sup>
16	Y30-1IE(0.1Al)-NH <sub>3</sub>	gaseous ammonification of Y30-1IE(0.1Al)-H <sup>+</sup>
17	Y30-5IE(0.1Al)-NH <sub>3</sub>	gaseous ammonification of Y30-5IE(0.1Al)-H <sup>+</sup>
18	Y30-Na-H <sup>+</sup>	2x sodium-exchange of Y30-H <sup>+</sup>
19	Y30-Na-1IE(0.1Al)-H <sup>+</sup>	2x sodium-exchange of Y30-H <sup>+</sup> followed by 1x Al-IE
20	Y30-Na-1IE(0.1Al)-NH <sub>3</sub>	gaseous ammonification of Y30-Na-1IE(0.1Al)-H <sup>+</sup>
21	Y30-1IE(0.1Al)-Na-H <sup>+</sup>	2x sodium-exchange of Y30-1IE(0.1Al)-H <sup>+</sup>
22	Y30-1IE(0.1Al)-Na-NH <sub>3</sub>	gaseous ammonification of Y30-1IE(0.1Al)-Na-H <sup>+</sup>

**Catalytic Evaluation:** The catalytic n-butane dehydrogenation reaction was performed on a homemade continuous flow set-up hosting a quartz reactor (internal diameter = 6 mm) loaded with a fixed catalyst bed. Silicon carbide ( $WC = 0.720$  g) particles were mixed well with the catalysts (weight of catalyst  $W_{cat} = 0.3$  g) and placed in the reactor as a catalyst bed. The reactor was put into a tubular electric oven, and the reaction temperature was regulated by a Type K thermocouple, whose tip was positioned in the center of the catalyst bed. Prior to the reaction, the catalyst bed was heated up to 823 K under argon flow ( $F_{Ar} = 300$  cm<sup>3</sup> STP min<sup>-1</sup>) at a heating rate of 10 K min<sup>-1</sup> and held at this temperature for 1 h to remove potential impurities from the zeolite. After that, the reactor was cooled down to a temperature at which the reaction was performed. The reaction mixture, i.e., 25% C<sub>4</sub>H<sub>10</sub> using argon (Ar) as a diluent, pre-stabilized through a bypass line, was then admitted through the reactor. The n-butane dehydrogenation reaction was carried out at temperatures  $T = 750$  to 850 K and  $P = 1.1$  bar by feeding  $F_{C_4H_{10}} = 20$  cm<sup>3</sup> STP min<sup>-1</sup> of C<sub>4</sub>H<sub>10</sub> diluted with  $F_{Ar} = 95$  cm<sup>3</sup> STP min<sup>-1</sup> of argon. The effluent contents in the outlet reactor feed were analyzed online by a gas chromatograph equipped with a flame ionization detector (GC-FID) and HP PLOT-Q column. The conversion (X) and the selectivity of hydrocarbon products were calculated according to the following equations.

$$\text{Conversion}(X) = \frac{\dot{n}_{C_4H_4,in} - \dot{n}_{C_4H_4,out}}{\dot{n}_{C_4H_4,in}} \quad (7.3)$$

$$\text{Selectivity}(S) = \frac{\dot{n}_{C_xH_y,out}}{\dot{n}_{C_4H_4,in} - \dot{n}_{C_4H_4,out}} \quad (7.4)$$

In these equations,  $\dot{n}_{C_4H_4, in}$  and  $\dot{n}_{C_4H_4, out}$  denote the inlet and outlet molar flows of n-C<sub>4</sub>H<sub>4</sub>, respectively, and x and y represent the number of carbon and hydrogen atoms in hydrocarbon product C<sub>x</sub>H<sub>y</sub>.

### 7.3. Results and Discussion

The results of the characterization (X-ray diffraction, nitrogen physisorption, elemental analysis, and surface areas) of fresh samples are discussed in **Chapter 5** and **Chapter 6**. This chapter discusses the catalytic performance of the samples for the dehydrogenation of n-butane. It has been reported that the proton form of zeolite Y undergo hydrolysis on exposure to air and breaks some fraction of Al-O and Si-O bonds<sup>176</sup>. This leads to a partially amorphous structure

and a loss of long-range order and micropore volume, whereas a large part of the network of the Si-O-T bonds remains intact. This collapse of some Al-O and Si-O bonds results in the loss of some of the acid sites of zeolite. The heat treatment of the protonic zeolite causes further structural collapse, with a consequent loss of catalytic activity at elevated temperatures. This structural collapse can be avoided by converting the protonic zeolites to their ammonium counterparts before high-temperature treatment, where the ammonium forms of zeolites show comparatively higher performance at high temperatures<sup>66, 176, 251, 252</sup>. In this work, the butane dehydrogenation is performed under high-temperature conditions, i.e., 750 to 850 K, prior to which activation is performed at 823K. To minimize the effect of structural collapse during these conditions, parent protonic zeolites were converted to ammonium forms by NH<sub>4</sub><sup>+</sup>-IE procedure. However, to avoid any change in the structure of newly introduced EFAl in aluminum-exchanged samples during NH<sub>4</sub><sup>+</sup>-IE, these samples were converted to ammonium forms by gaseous adsorption of NH<sub>3</sub> instead of NH<sub>4</sub><sup>+</sup>-IE.

**n-butane dehydrogenation over parent Y zeolites:** The non-oxidative conversion of butane as a function of reaction temperature over parent zeolites with Si/Al ratios ranging from 2.5-40 is presented in **Figure 7.1**. The results show that the conversion in all samples increases with an increase in temperature. Y2.5-H<sup>+</sup>, which contains the maximum concentration of BAS and LAS (**Section 5.3**), shows only 4.6% conversion, whereas the sample Y15-H<sup>+</sup> reaches 22% conversion. However, a further increase in Si/Al ratio significantly lowers the conversion in Y30-H<sup>+</sup> and Y40-H<sup>+</sup>, reaching 5.3% and 3.5%, respectively. Thus, an increase in Si/Al ratio increases the conversion up to Si/Al ratio = 15, after which the conversion decreases. Changing the cationic form of the parent zeolite shows some prominent differences in the performance as the conversion reaches 9.8% and 17.3% in Y6-NH<sub>4</sub><sup>+</sup> and Y6-NH<sub>4</sub><sup>+</sup>, respectively. This agrees well with the literature, suggesting that NH<sub>4</sub><sup>+</sup>-IE of Y2.5-H<sup>+</sup> and Y6-NH<sub>4</sub><sup>+</sup> prevents the collapse of Al-O and Si-O bonds, resulting in enhanced catalytic activity<sup>66, 176, 251, 252</sup>.

In sample Y15-NH<sub>4</sub><sup>+</sup>, the conversion at lower temperatures increases compared to Y15-H<sup>+</sup> (from 6.2% in Y15-H<sup>+</sup> to 9.6% in Y15-NH<sub>4</sub><sup>+</sup>). However, at higher temperatures, the conversion of Y15-NH<sub>4</sub><sup>+</sup> is not higher than Y15-H<sup>+</sup>, instead is slightly lowered from 22% in Y15-H<sup>+</sup> to 20% in Y15-NH<sub>4</sub><sup>+</sup> (**Figure 7.1a** and **Table D.1**). Thus, the increase in conversion upon NH<sub>4</sub><sup>+</sup>-IE is 5.2% and 3.4% at Si/Al ratio of 2.5 and 15, respectively. Similarly, ammonium forms of Y30 and Y40 are also accompanied by a decrease in conversion ( 5% and 2.1%, respectively) compared to respective proton forms. These results suggest that the protonic zeolites at lower Si/Al ratios (higher aluminum) content are more vulnerable to hydrolysis of Al-O and Si-O

bonds than those at higher Si/Al ratios. Consequently, the role of  $\text{NH}_4^+$  cations in reverting the structural collapse and increasing the catalytic activity is dominant at lower Si/Al ratios. In comparison, increasing the Si/Al lowers this effect, and after Si/Al=15,  $\text{NH}_4^+$ -IE decreases the activity.

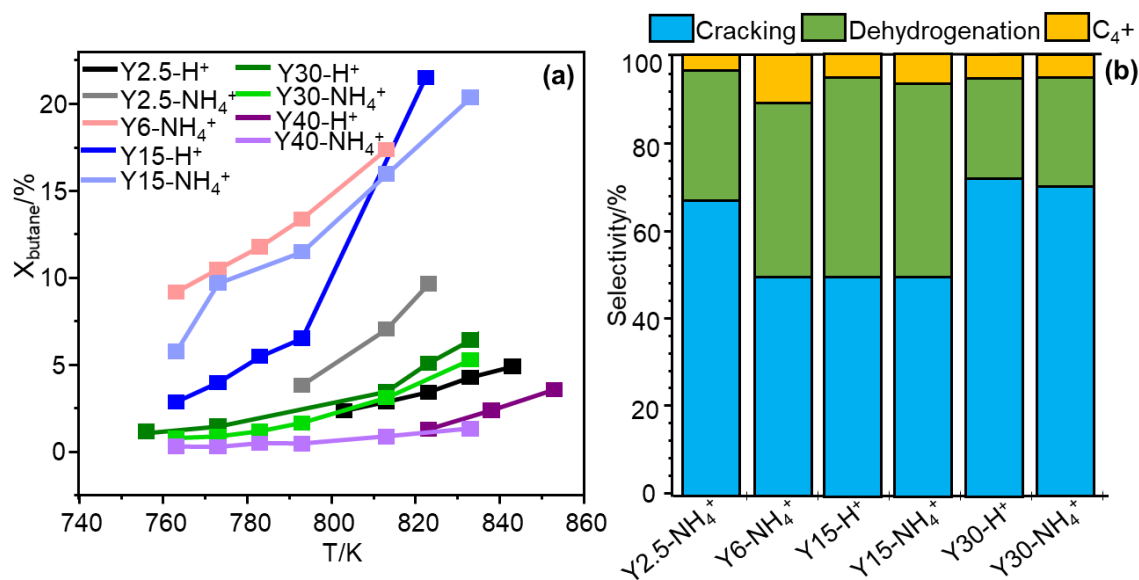


Figure 7.15: (a) Conversion (X) (%) of n-butane over parent Y zeolites in proton and ammonium forms (b) Selectivity (%) of cracking ( $\text{CH}_4$ ,  $\text{C}_2\text{H}_4$ ,  $\text{C}_2\text{H}_6$ ,  $\text{C}_3\text{H}_6$ , and  $\text{C}_3\text{H}_8$ ), dehydrogenation ( $i\text{-C}_4\text{H}_{10}$ ,  $i\text{-C}_4\text{H}_8$ ,  $1\text{-C}_4\text{H}_8$ , and  $2\text{-C}_4\text{H}_8$ ) and  $\text{C}_4^+$  products at 5% n-butane conversion, calculated from the individual product distributions presented in Figure 7.2. The samples Y2.5-H<sup>+</sup>, Y40-H<sup>+</sup>, and Y40-NH<sub>4</sub><sup>+</sup> are not shown in (b) as they do not show a 5% conversion.

The distribution of products formed by n-butane conversion is plotted in **Figure 7.2**, and the overall selectivity to cracking ( $\text{CH}_4$ ,  $\text{C}_2\text{H}_4$ ,  $\text{C}_2\text{H}_6$ ,  $\text{C}_3\text{H}_6$ , and  $\text{C}_3\text{H}_8$ ), dehydrogenation ( $i\text{-C}_4\text{H}_{10}$ ,  $i\text{-C}_4\text{H}_8$ ,  $1\text{-C}_4\text{H}_8$ , and  $2\text{-C}_4\text{H}_8$ ) and  $\text{C}_4^+$  products at 5% conversion is presented in **Figure 7.1b**. The samples Y2.5-H<sup>+</sup>, Y40-H<sup>+</sup>, and Y40-NH<sub>4</sub><sup>+</sup> are not shown in **Figure 7.1b** as the conversion is lower than 5% in these samples. The results illustrate that the product distribution changes with increasing conversion at higher temperatures; therefore, the overall selectivity to cracking, dehydrogenation, and  $\text{C}_4^+$  products at two different temperatures is presented in **Figure D.1**. At lower conversions, the sample Y2.5-H<sup>+</sup> shows very high selectivity towards most of the cracking products including  $\text{CH}_4$ ,  $\text{C}_2\text{H}_4$ ,  $\text{C}_2\text{H}_6$ ,  $\text{C}_3\text{H}_6$ , reaching an overall cracking selectivity of 56%. The selectivity to dehydrogenation is 42% (mainly due to  $i\text{-C}_4\text{H}_{10}$  and  $i\text{-C}_4\text{H}_8$ ), whereas that to  $\text{C}_4^+$  products is less than 5%. At higher conversions, the selectivity of cracking products



decreases by 7% with an increase in dehydrogenation products (due to the formation of 1-C<sub>4</sub>H<sub>8</sub>) (Figure D.1).

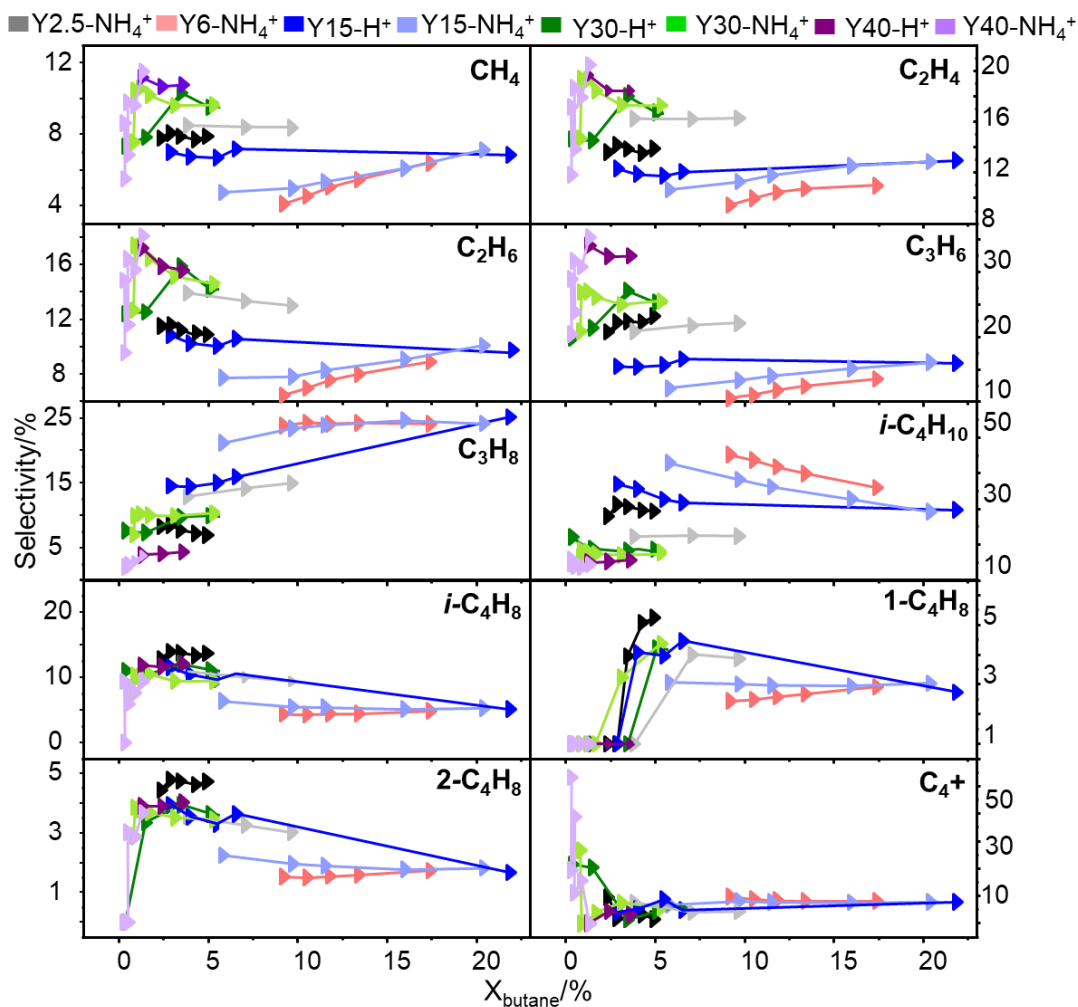


Figure 7.2: The selectivity distribution of products as a function of n-butane conversion over parent Y zeolites in proton and ammonium forms

Increasing the Si/Al ratio of parent zeolites up to 15 results in lower selectivity to CH<sub>4</sub>, C<sub>2</sub>H<sub>4</sub>, C<sub>2</sub>H<sub>6</sub>, C<sub>3</sub>H<sub>6</sub> products followed by an increase to that of C<sub>3</sub>H<sub>8</sub>. Therefore, the overall selectivity to cracking products is only slightly lowered as compared to Y2.5-H<sup>+</sup>. Furthermore, the selectivity of dehydrogenation products also increases as isobutane (*i*-C<sub>4</sub>H<sub>10</sub>) becomes more selective among all dehydrogenation products. The selectivity to C<sub>4</sub><sup>+</sup> products also slightly increases. Higher conversions in these samples result in a decrease in dehydrogenation products with an increase in cracking<sup>111, 112</sup>. This agrees well with the literature, as elevated temperatures favor cracking yields. However, the samples with Si/Al ratios above 15 become more selective towards cracking. The cracking products further increase in selectivity on samples Y2.5-NH<sub>4</sub><sup>+</sup>, Y15-NH<sub>4</sub><sup>+</sup>, and Y30-NH<sub>4</sub><sup>+</sup>, with Y2.5-NH<sub>4</sub><sup>+</sup> showing a maximum increase of 10% followed by

a similar decrease in that of dehydrogenation products. As BAS favors the cracking reactions, the results demonstrate that the role of ammonification is most significant at a Si/Al ratio of 2.5. This is due to hydrothermal instability, Y zeolite at lower Si/Al ratios is more vulnerable to structural collapse, and ammonification treatment recovers a good fraction of BAS, resulting in an increased rate of cracking reactions which agrees with the highest increase in conversion of  $\text{NH}_4^+$  form of Y2.5 as compared to the respective parent zeolites.

**n-butane dehydrogenation over Y15 and aluminum-exchanged zeolites: Figure 7.3a.** presents the conversion (%) of butane as a function of reaction temperature over Y15 and the respective aluminum-exchanged zeolites. At lower temperatures, the one- and 5-fold aluminum-exchanged samples in their proton forms show 15% and 17% conversion, which is higher than  $\text{Y15-H}^+$ . However, at higher temperatures, the conversion of  $\text{Y15-H}^+$  is maximum. As a result of ammonification treatment, the samples' conversion at low-temperatures further increases to 16.8 and 17.5 in one- and five-fold aluminum-exchanged samples. As the aluminum-exchanged samples were not tested at temperatures at which parent  $\text{Y15-H}^+$  and  $\text{Y15-NH}_4^+$  show maximum conversion, an increase in conversion with increasing temperature proposes that these samples can also show higher conversion at higher temperatures. It is important to note that the increase in activity after ammonification is not as significant as when  $\text{Y15-H}^+$  was converted to  $\text{Y15-NH}_4^+$ . This can well be because the content of LAS increases after Al-IE, and this Al-IE procedure generates neutral EFAl species. Apart from increasing the activity, this species also stabilizes the structure to some extent.

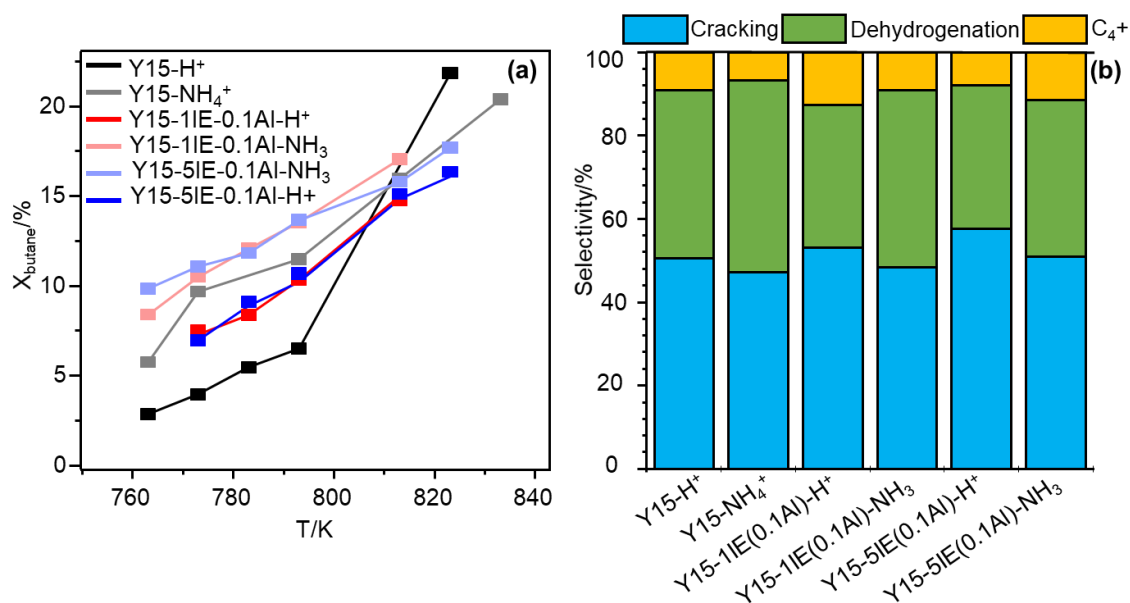


Figure 7.3: Catalytic activity of parent Y15 and aluminum-exchanged zeolites in proton and ammonium forms; (a) Conversion (X) (%) and (b) Selectivity (%) of cracking ( $\text{CH}_4$ ,  $\text{C}_2\text{H}_4$ ,  $\text{C}_2\text{H}_6$ ,  $\text{C}_3\text{H}_6$ , and  $\text{C}_3\text{H}_8$ ), dehydrogenation ( $i\text{-C}_4\text{H}_{10}$ ,  $i\text{-C}_4\text{H}_8$ ,  $1\text{-C}_4\text{H}_8$ , and  $2\text{-C}_4\text{H}_8$ ) and  $\text{C}_4^+$

products at 5% n-butane conversion, calculated from the individual product distributions presented in Figure 7.4.

The detailed distribution of n-butane conversion products and the overall selectivity to cracking, dehydrogenation, and  $C_4^+$  products at 5% conversion are presented in **Figure 7.4**. **Figure 7.3b**. Even though Al-IE results in an increase in the conversion, an overall selectivity of dehydrogenation products at 6% conversion does not significantly vary after Al-IE treatment.

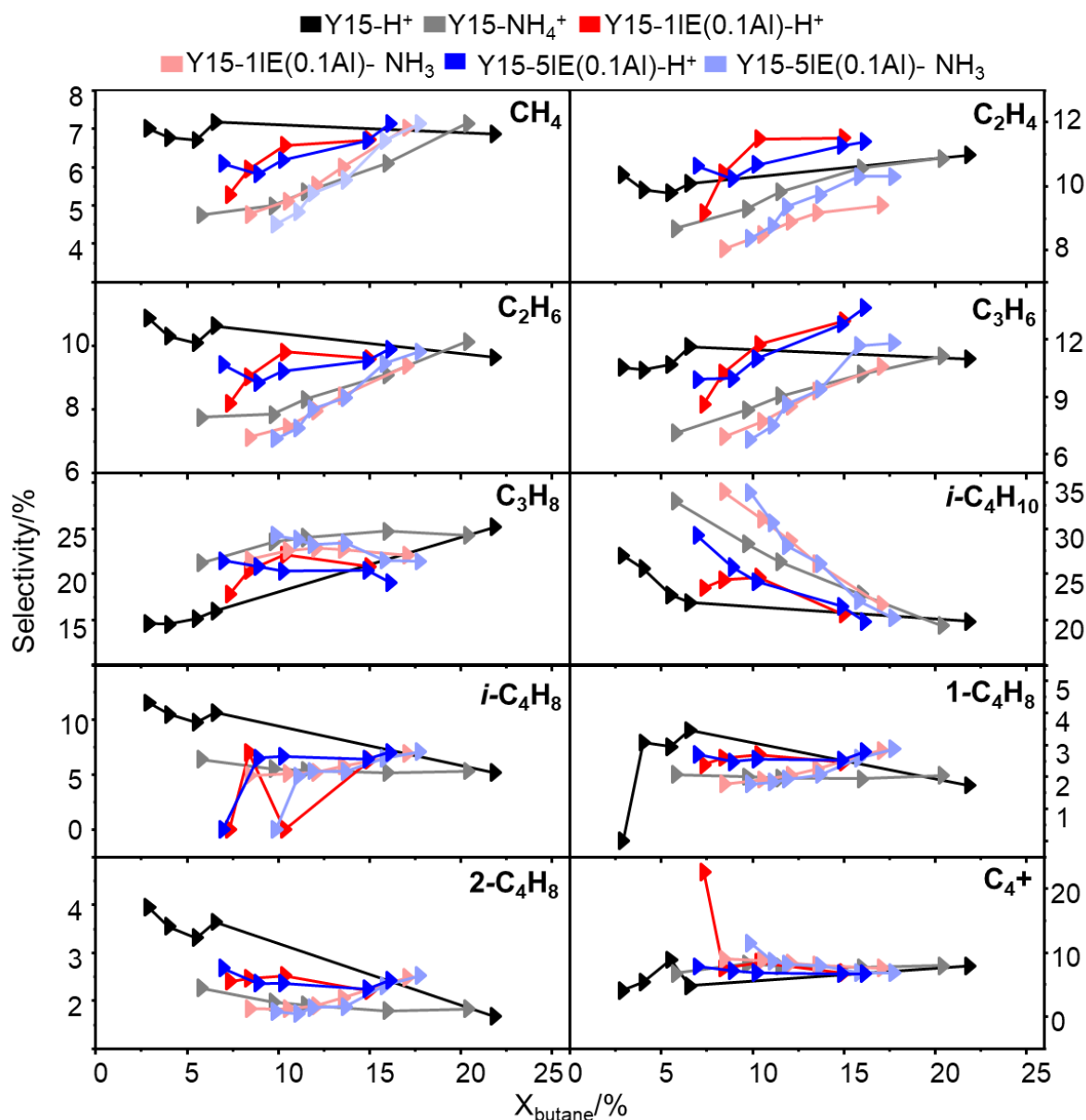


Figure 7.4: The selectivity distribution of products as a function of n-butane conversion over Y15 and aluminum-exchanged zeolites in proton and ammonium forms

However, **Figure 7.4** shows that the aluminum-exchanged samples in their proton and ammonium form become more selective to isobutane ( $i-C_4H_{10}$ ) compared to Y15- $H^+$  and Y15- $NH_4^+$  samples, respectively. This increase in selectivity for isobutane is more significant after 5-fold Al-IE, i.e. the sample Y15-5IE(0.1Al)- $H^+$  shows a 10% increase from 20% to 30% with

respect to Y15-H<sup>+</sup>. After the ammonification of these samples this selectivity further increases to 37%. Most of the cracking products (mainly CH<sub>4</sub>, C<sub>2</sub>H<sub>4</sub>, C<sub>2</sub>H<sub>6</sub>, C<sub>3</sub>H<sub>6</sub>) also decrease selectivity in aluminum-exchanged samples. But the overall similar ratios of dehydrogenation to cracking products are because there is an increase in selectivity of C<sub>3</sub>H<sub>6</sub>.

**n-butane dehydrogenation over Y30 and aluminum-exchanged zeolites:** It has been discussed in the previous chapters that the efficiency of AL-IE treatment to incorporate EFAl while retaining the zeolite framework and pore structure increases with an increase in the Si/Al ratio of parent zeolites. Therefore we also evaluate the catalytic performance of aluminum-exchange performed on zeolite Y of Si/Al of 30. As discussed above, the catalytic performance of parent Y30 in ammonium and proton forms is significantly low compared to Y15. Furthermore, the former has a very low content of BAS as compared to the later (**Figure 5.3**). This suggests that the effect of LAS incorporated by Al-IE is expected to be more prominent. **Figure 7.5a** presents the conversion as a function of temperature for Y30 and respective aluminum-exchanged zeolites in ammonium and proton forms.

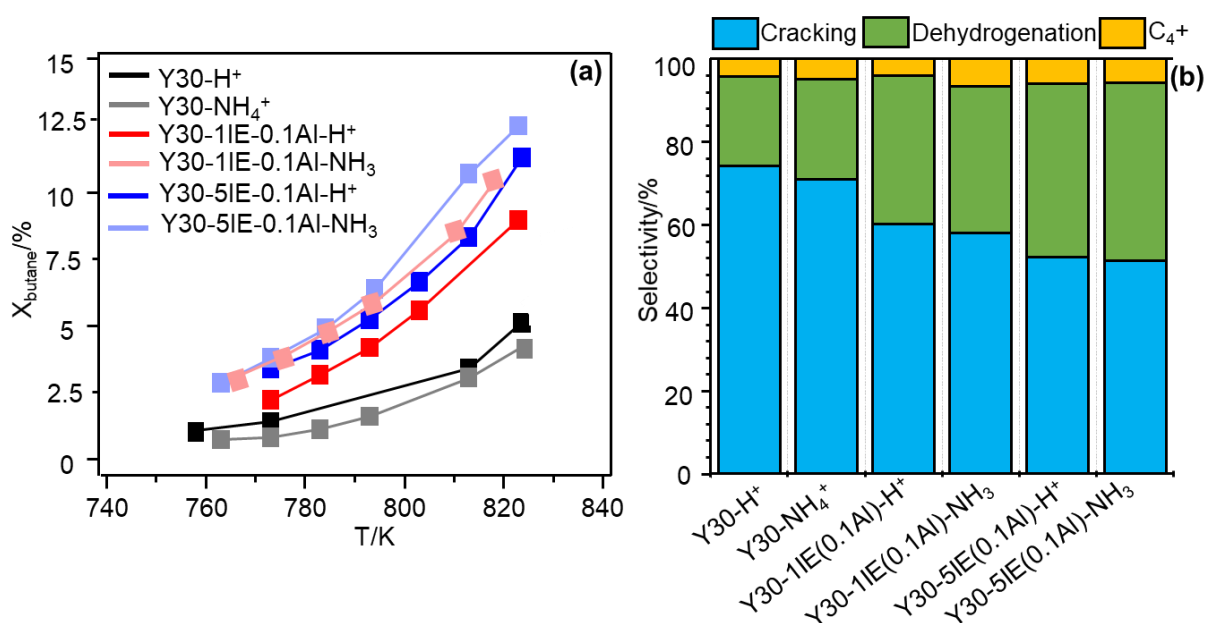


Figure 7.5: Catalytic activity of parent Y30 and aluminum-exchanged zeolites in proton and ammonium forms; (a) Conversion (X) (%) and (b) Selectivity (%) of cracking (CH<sub>4</sub>, C<sub>2</sub>H<sub>4</sub>, C<sub>2</sub>H<sub>6</sub>, C<sub>3</sub>H<sub>6</sub>, and C<sub>3</sub>H<sub>8</sub>), dehydrogenation (*i*-C<sub>4</sub>H<sub>10</sub>, *i*-C<sub>4</sub>H<sub>8</sub>, 1-C<sub>4</sub>H<sub>8</sub>, and 2-C<sub>4</sub>H<sub>8</sub>) and C<sub>4</sub><sup>+</sup> products at 5% n-butane conversion calculated from the individual product distributions presented in Figure 7.6.

The sample Y30-H<sup>+</sup> exhibits 5.3% conversion, which decreases only slightly to 5% in Y30-NH<sub>4</sub><sup>+</sup>. One-fold aluminum-exchange increases the conversion to 9.1% in sample Y30-

1IE(0.1Al)-H<sup>+</sup>. The conversion increases to 12% in sample Y30-5IE(0.1Al)-H<sup>+</sup>. The ammonification of these samples only slightly increases the conversion to 10.4 and 12.5%. Even at higher temperatures, the aluminum-exchanged samples of Y30, in protonic and ammonium forms, show higher conversions with respect to Y30-NH<sub>4</sub><sup>+</sup> and Y30-H<sup>+</sup>. This trend is contrary to the that observed for aluminum-exchanged samples of Y15, where at higher conversions, parent proton and ammonium forms show higher conversions. Furthermore, the differences in conversion among protonic and ammonium forms of aluminum-exchanged Y30 samples are also less significant than those of Y15.

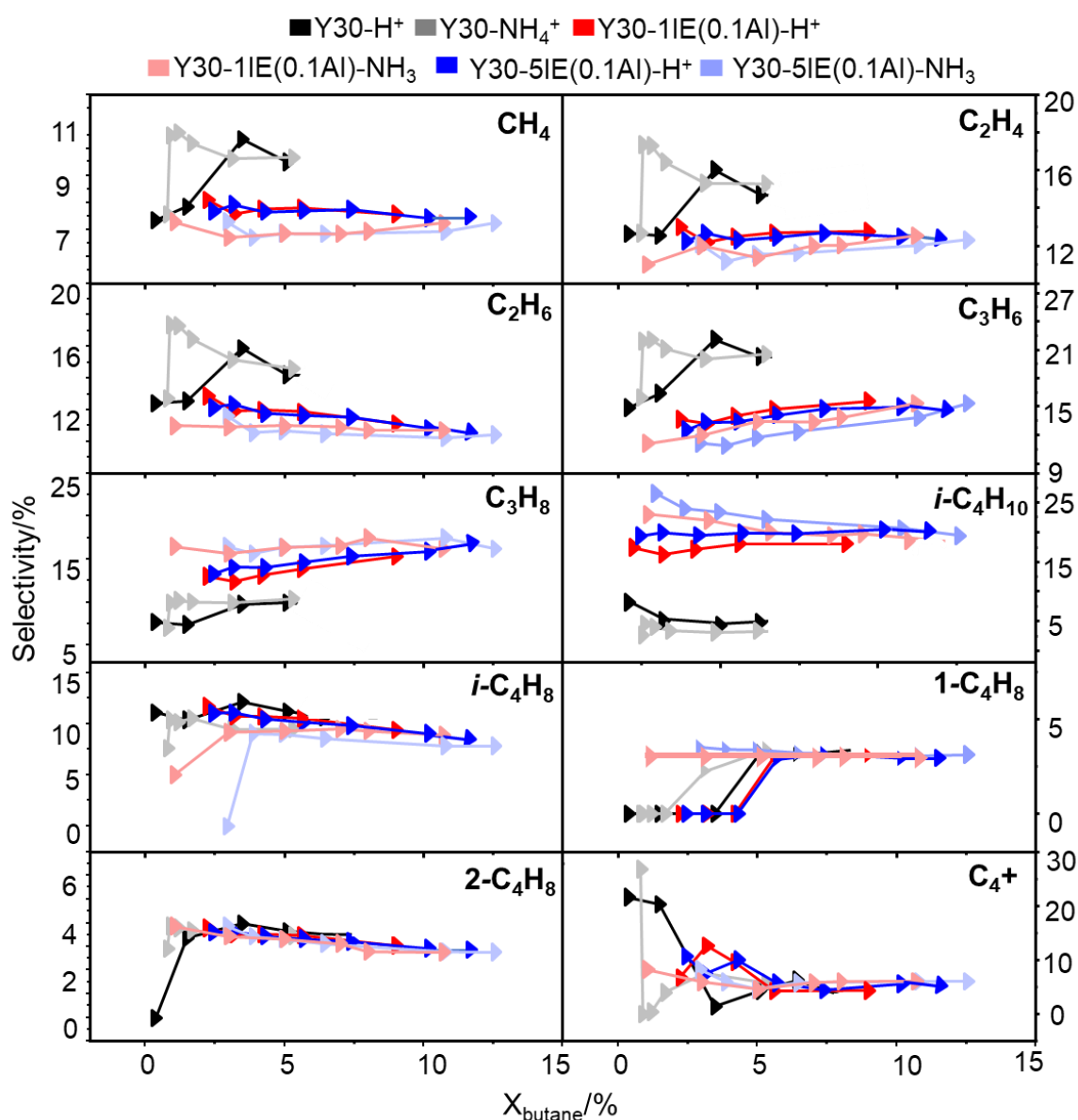


Figure 7.6: The selectivity distribution of products as a function of n-butane conversion over Y30 and aluminum-exchanged zeolites in proton and ammonium forms

The detailed distribution of n-butane conversion products and the overall selectivity to cracking, dehydrogenation, and  $C_4^+$  products at 5% conversion are presented in **Figure 7.6**. **Figure 7.5b**. The results illustrate that ratio of cracking to dehydrogenation products significantly changes in aluminum exchanged samples. Parent Y30- $H^+$  exhibits 74% selectivity to cracking and 22% to dehydrogenation, whereas that of  $C_4^+$  products is less than 5%. These values do not vary significantly in the sample Y30- $NH_4^+$  (71%, 24% and 5%, respectively). After the first Al-IE, Y30-1IE(0.1Al)- $H^+$ , the selectivity to dehydrogenation reaction increases significantly from 22% to 35%, thereby decreasing the cracking products' selectivity to 61%. No significant change occurs for  $C_4^+$  products. **Figure 7.6** shows that the increase in dehydrogenation occurs predominantly due to an enhanced formation of isobutane ( $i-C_4H_{10}$ ), which increases in selectivity from 5% into Y30- $H^+$  to 18% in Y30-1IE(0.1Al)- $H^+$ . This is also followed by a decrease in the conversion of cracking products. The selectivity distribution further shifts towards dehydrogenation, reaching 39% in Y30-5IE(0.1Al)- $H^+$ , followed by an increase in isobutane selectivity to 22%. Upon ammonification, the overall change in the ratio of dehydrogenation to cracking reactions does not vary significantly. However, selectivity to isobutane further increases by 27%. A prominent difference in the catalytic performance of aluminum-exchanged samples of Y30 with other samples is that the selectivity to isobutane remains constant with the increasing conversion or temperature. In comparison, parent zeolites and aluminum-exchanged samples of Y15 show a significant decrease in isobutane at elevated temperatures, followed by an increase in cracking reactions.

**Effect of sodium cation:** The work presented in **Chapter 5** shows that the presence of Na as co-cation before and after Al-IE has a negative effect on the extent of generation of EFAl LAS. However, the sodium-treated aluminum-exchanged samples can be promising candidates for the evaluation of the strength of EFAl LAS generated by Al-IE. This is because the Na-IE before and after Al-IE results in a significant loss of BAS, the effect being stronger in the later case. Lower content of BAS compared to parent zeolite but higher content of LAS is an efficient combination to get insight into the catalytic role of EFAl LAS in alkane dehydrogenation. **Figure 7.7a** shows the catalytic data of Y30-Na and aluminum-exchanged samples of Y30, which have gone through Na-IE treatment before and after Al-IE. The sample Y30-Na shows the least catalytic conversion (1.3%) among all the samples used in this work. The incorporation of aluminum on Y30-Na by Al-IE results in an increase in conversion; thus, sample Y30-Na-1IE(0.1Al)- $H^+$  shows 7.1% conversion in n-butane dehydrogenation, which is also greater than that of Y30- $H^+$ . The ammonification treatment further increases the conversion to 8.2%. The

lower conversion of Y30-Na-1IE(0.1Al)-H<sup>+</sup> compared to Y30-1IE(0.1Al)-H<sup>+</sup> is in line with the fact that the former has a lower content of LAS and BAS than the latter (**Section 5.3**). As the concentration of BAS of Y30-Na-1IE(0.1Al)-H<sup>+</sup> is lower than Y30-H<sup>+</sup>, the increase in conversion in the former is mainly due to a higher concentration of LAS. This trend of catalytic performance is comparable to the activity of these samples in the MPV reduction of 4-*tert* butyl cyclohexanone presented in **Chapter 5**. Furthermore, the sample Y30-1IE(0.1Al)-Na-H<sup>+</sup> decreases significantly, reaching 2.1%, which only increases by 0.3% in Y30-1IE(0.1Al)-Na-NH<sub>4</sub><sup>+</sup>.

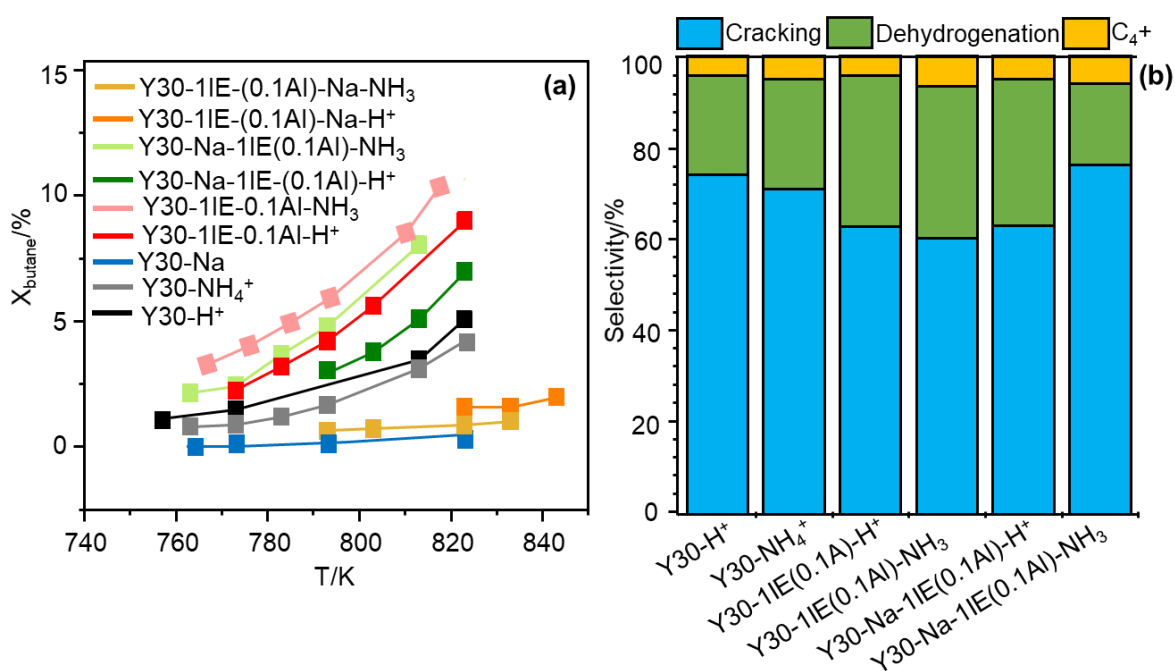


Figure 7.7: Catalytic activity of proton and ammonium forms of parent and aluminum-exchanged Y30 samples with and without sodium cations; (a) Conversion (X) (%) and (b) Selectivity (%) of cracking (CH<sub>4</sub>, C<sub>2</sub>H<sub>4</sub>, C<sub>2</sub>H<sub>6</sub>, C<sub>3</sub>H<sub>6</sub>, and C<sub>3</sub>H<sub>8</sub>), dehydrogenation (*i*-C<sub>4</sub>H<sub>10</sub>, *i*-C<sub>4</sub>H<sub>8</sub>, 1-C<sub>4</sub>H<sub>8</sub>, and 2-C<sub>4</sub>H<sub>8</sub>) and C<sub>4</sub><sup>+</sup> products at 5% n-butane conversion, calculated from the individual product distributions presented in Figure 7.8.

In the case of the MPV reduction reaction, the performance of this sample is only slightly greater than parent Y30-H<sup>+</sup>. The smaller conversion of this sample in butane dehydrogenation can be explained by a significantly low concentration of BAS and the massive loss of porous characteristics. Similarly, the concentration of LAS is also lower than the samples Y30-Na-1IE(0.1Al)-H<sup>+</sup> and Y30-1IE(0.1Al)-H<sup>+</sup>. **Figure 7.7b** demonstrates that selectivity to C<sub>4</sub><sup>+</sup> products is comparable in all samples in their protonic forms, whereas a slight increase appears in the respective ammonium forms. The sample Y30-Na-1IE(0.1Al)-H<sup>+</sup> shows 32% overall selectivity to dehydrogenation products and 61% to cracking products. These values are comparable with those of Y30-1IE(0.1Al)-H<sup>+</sup>. As shown in **Figure 7.8**, Y30-Na-1IE(0.1Al)-H<sup>+</sup>

exhibits 14% selectivity to isobutane, which is 5% lower than Y30-1IE(0.1Al)-H<sup>+</sup>, in addition to the presence of sodium favors slightly higher formation of other dehydrogenation products, i.e., *i*-C<sub>4</sub>H<sub>8</sub>, 1-C<sub>4</sub>H<sub>8</sub>, and 2-C<sub>4</sub>H<sub>8</sub>.

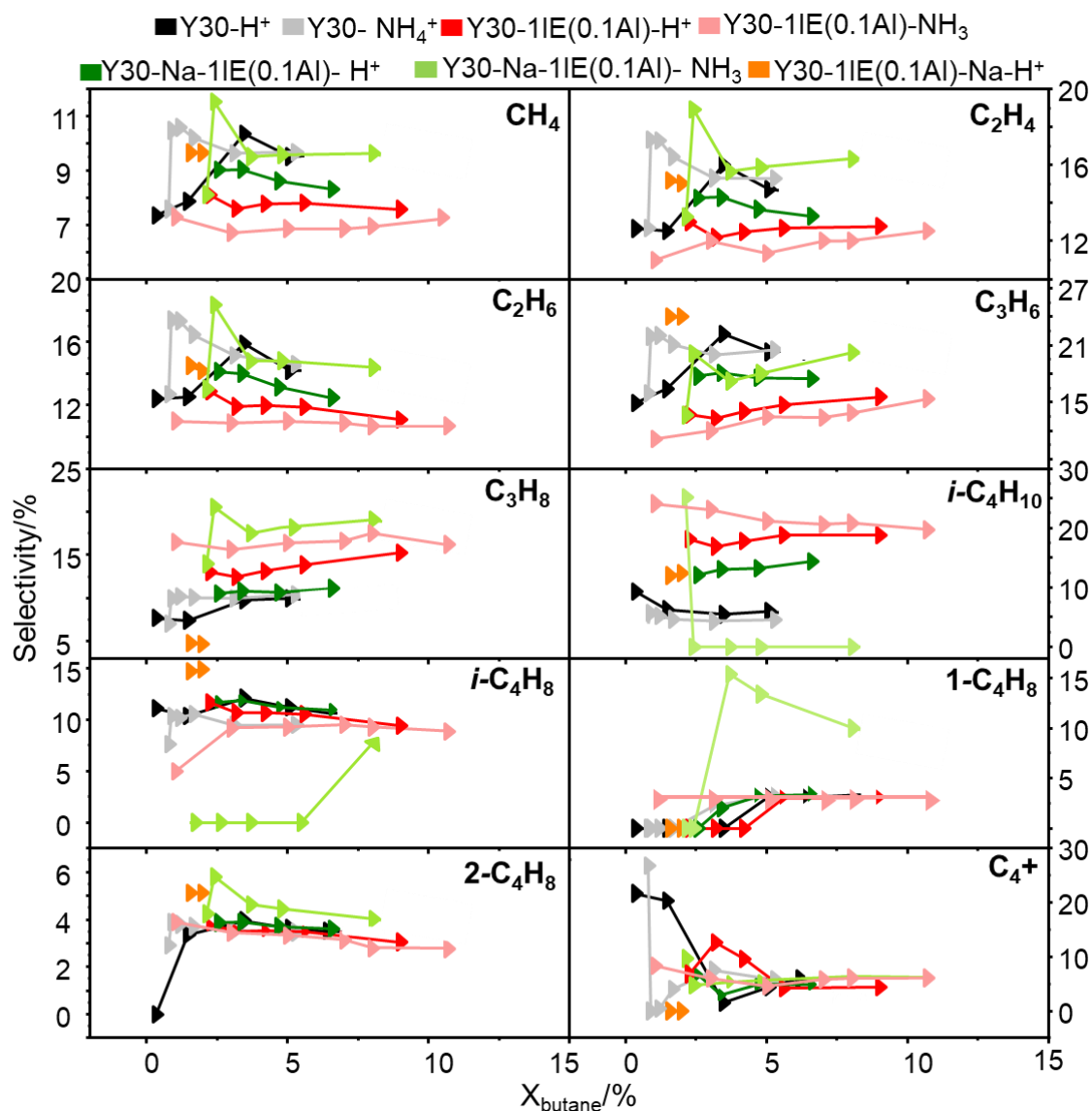


Figure 7.8: The selectivity distribution of products as a function of n-butane conversion over Y30 and aluminum-exchanged zeolites in proton and ammonium forms. The sample Y30-Na is not included as it shows less than 1.5% conversion.

However, due to ammonification, the selectivity to dehydrogenation decreases significantly to 20%, comparable to Y30-H<sup>+</sup>. The isobutane selectivity drops down to less than 5%, and the dehydrogenation products are dominated by the formation of 1-C<sub>4</sub>H<sub>8</sub>, i.e., the selectivity increases from 0% to 15%. Nevertheless, the sample Y30-1IE(0.1Al)-Na-H<sup>+</sup> despite having a lower conversion, shows dehydrogenation selectivity (i.e., 32% dehydrogenation, 68% cracking, and 0% C<sub>4</sub><sup>+</sup> products) comparable to Y30-1IE(0.1Al)-H<sup>+</sup> at 2% conversion (**Table**



**D.1).** The product distribution in **Figure 7.8** illustrates that the dehydrogenation products are dominated by 12% selectivity to  $i\text{-C}_4\text{H}_{10}$ , 15% to  $i\text{-C}_4\text{H}_8$  and 5% to  $2\text{-C}_4\text{H}_8$ . Thus, the presence of sodium shifts the selectivity from isobutane to other dehydrogenation products.

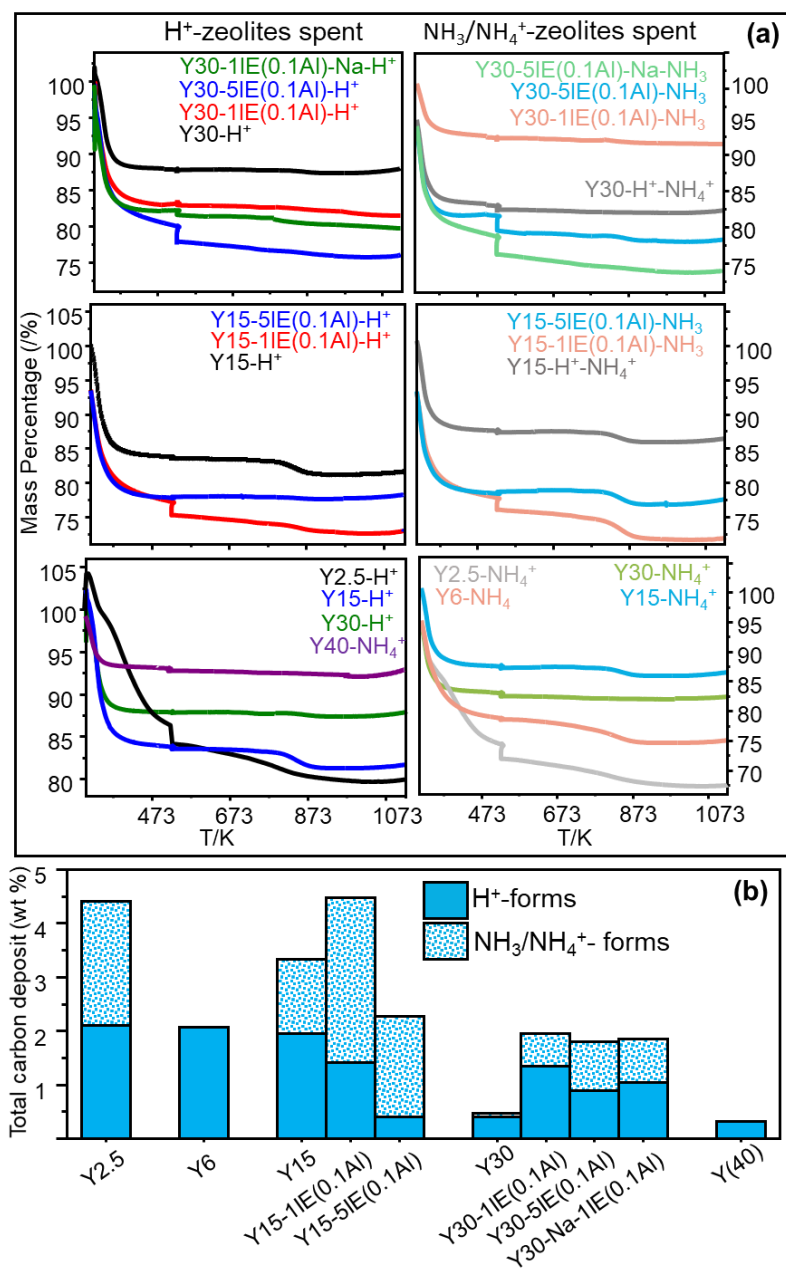


Figure 7.9. (a) TGA profiles of the selective spent Y zeolite catalysts (b) total carbon deposits on spent catalysts calculated from TGA profiles.

**Deposit on spent catalysts:** The TGA profiles of the spent catalysts are presented in **Figure 7.9a**. The weight loss in the temperature range of 723K -1073K is correlated with the combustion of carbon or hydrocarbon deposits entrapped in these zeolites due to a dehydrogenation reaction. In comparison, the mass loss at temperatures below 723K

corresponds to removing water contents trapped in zeolites. The total carbon deposits of the samples calculated from weight loss in the temperature range of 723K -1073K are presented in **Figure 7.9b**. The deposit amounts of parent protonic and ammonium forms of zeolites globally decrease with increasing the Si/Al ratio, i.e., the amounts are 2.4%, 1.95%, 0.4, and 0.33% in samples Y2.5-H<sup>+</sup>, Y15-H<sup>+</sup>, Y30-H<sup>+</sup>, and Y40-H<sup>+</sup>, respectively. Similarly, the samples Y2.5-NH<sub>4</sub><sup>+</sup>, Y6-NH<sub>4</sub><sup>+</sup>, Y15-NH<sub>4</sub><sup>+</sup>, and Y30-NH<sub>4</sub><sup>+</sup> have 2.3% 2.07%, 1.38%, 0.08% carbon contents, respectively. The carbon wt% in a one-fold protonic aluminum-exchanged sample of Y15 is 1.41% which is higher than that of Y30 (1.35%). In comparison, Y15-5IE(0.1Al)-H<sup>+</sup> contains lower carbon deposits as compared to Y30-H<sup>+</sup> (0.4% and 0.9%, respectively). Upon ammonification, the deposits significantly increase in an aluminum-exchanged sample of Y15, reaching 3.05% in Y15-1IE(0.1Al)-NH<sub>3</sub> and 1.87% in Y15-5IE(0.1Al)-NH<sub>3</sub>. In comparison, the deposits decrease in Y30-1IE(0.1Al)-NH<sub>3</sub> to 0.6, whereas no change in total carbon wt% of Y30-5IE(0.1Al)-NH<sub>3</sub> compared to the protonic form.

**Regeneration of active sites in spent catalysts:** Some selected spent catalysts in n-butane dehydrogenation were calcined under an oxygen environment to eliminate carbon deposits; the calcination converts the catalysts to proton forms. The regenerated catalysts were characterized via <sup>27</sup>Al MAS NMR and FTIR spectroscopy, and the spectra were compared with the respective fresh catalysts. **Figures 7.10a** and **7.10b** present the <sup>27</sup>Al MAS NMR spectra of the regenerated and fresh catalysts, whereas the difference FTIR spectra in the pyridine stretching region are presented in the present in **Figures 7.10c** and **7.10d**. The results show that the regenerated Y15-H<sup>+</sup> shows an increase in the intensity at 0 ppm ( corresponding to FA-Al<sup>61, 62, 66</sup>) in the NMR spectra, with a respective decrease in intensity in the tetrahedral region. This suggests that some aluminum species partially dislodge from the framework by gaining extra coordination with hydroxyls. Similarly, the regenerated Y15-NH<sub>4</sub><sup>+</sup> also shows an increase in intensity at ~0 ppm due to FA-Al species. In addition to that, EFAl is also generated in Y15-NH<sub>4</sub><sup>+</sup>, as the spectrum shows the broad octahedral resonance at ~3 ppm<sup>65, 209</sup>. The increase in intensity of features due to LAS bands (1455 cm<sup>-1</sup> and 1621 cm<sup>-1</sup><sup>49, 220</sup>) further confirms this behavior.

The regenerated Y2.5-NH<sub>4</sub><sup>+</sup> shows a drastic change in the profile of the <sup>27</sup>Al NMR spectrum as compared to the fresh Y2.5-H<sup>+</sup> and Y2.5-NH<sub>4</sub><sup>+</sup> samples (**Figure D.4**), as the intensity dramatically increases in the octahedral region (broad resonance due to EFAl) and pentahedral region. This suggests that the zeolite at Si/Al of 2.5 is more prone to structural damage as compared to higher Si/Al ratios. These results are in line with the catalytic conversion of zeolites. After regeneration, the 5-fold aluminum-exchanged samples of Y15 also show a slight

increase in the octahedral intensity (due to EFAl) and a decrease in the intensity of pentahedral resonance. This is also followed by a slight increase in LAS band intensity at  $1545\text{ cm}^{-1}$ . No significant changes appear in the NMR spectra of aluminum exchanged samples of Y30. However, the sample Y30-5IE(0.1Al)-NH<sub>3</sub>, after regeneration, exhibits a slight lowering in the intensity of LAS and BAS band <sup>70</sup>.

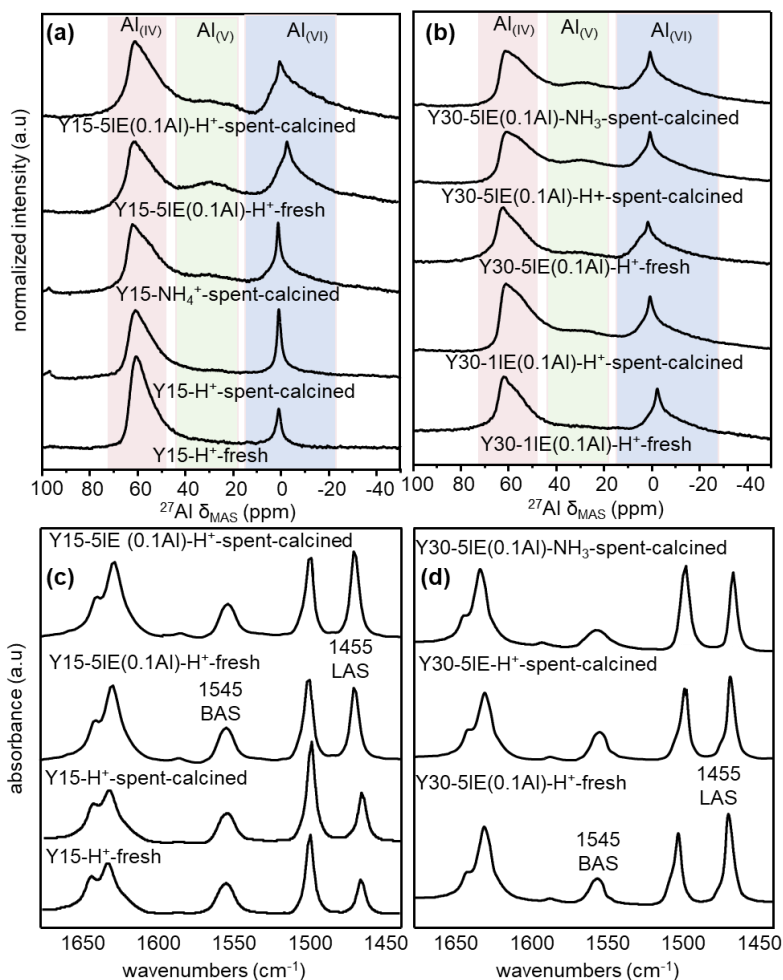


Figure 7.10: <sup>27</sup>Al MAS NMR spectra of selective fresh and regenerated catalysts (a) Y15 and aluminum-exchanged samples (b) Y30 and aluminum-exchanged samples. The presented spectra are normalized to the weight of the sample used. Colored regions are added to guide the eye. FTIR difference spectra in pyridine stretching region of selective fresh and regenerated catalysts (c) Y15 and aluminum-exchanged samples (d) Y30 and aluminum-exchanged samples. The difference spectra are obtained by subtraction of spectra after activation at 723K from spectra after pyridine adsorption at 423K followed by evacuation at 423K.

**Summarizing the performance of Y zeolites in n-butane conversion:** The catalytic conversion of alkanes involves the cooperative catalysis of LAS and BAS. Therefore, the performance of the catalysts Y zeolites in n-butane dehydrogenation may not likely correlate to their performance in MPV reduction, as the latter reaction only probes the LAS of zeolites.

Furthermore, the size of the reactants and the severity of operating conditions also vary in these reactions. However, some essential parallels in the catalytic activity of LAS can be established. The content of LAS and BAS in parent zeolites vary while decreasing with the increase in Si/Al ratio. Another important factor is hydrothermal stability, which increases with the Si/Al ratio. The protonic forms of zeolites, at low Si/Al ratio, are highly vulnerable to structural collapse in the presence of water or at higher temperatures. The presence of ammonium cations stabilizes the structure and enhances the activity of acid sites. The role of ammonium cations in the improvement of catalytic activity is more significant at lower Si/Al ratios. Therefore, the conversion of Y2.5-H<sup>+</sup> significantly increases after NH<sub>4</sub><sup>+</sup>-IE. This difference in activity of proton and ammonium forms of zeolite decreases in Y15, after which NH<sub>4</sub><sup>+</sup>-IE lowers the conversion compared to protonic zeolite. The catalytic activity of aluminum-exchanged samples of Y15 shows a significant increase in conversion at lower temperatures, but at higher temperatures, activity is lower than the parent zeolites. Similarly, the difference in activity of proton and ammonium forms of these zeolites is lower as compared to parent Y15. These samples show become more selective 10% more selective to isobutane. However, this does not significantly increase overall dehydrogenation selectivity compared to parent zeolite, as the production of other dehydrogenation products, i.e., *i*-C<sub>4</sub>H<sub>8</sub>, 1-C<sub>4</sub>H<sub>8</sub>, and 2-C<sub>4</sub>H<sub>8</sub>, decreases.

The increase in catalytic performance is more significant and consistent in aluminum-exchanged samples of Y30, resulting in a 7% increase in conversion compared to Y30-H<sup>+</sup>. The conversion is maximum after 5-fold Al-IE, whereas the increase in conversion after 1-fold is more significant, which is in line with catalytic performance in MPV reduction (**Chapter 5**); in addition to that, the increase in conversion due to ammonification is significantly lower as compared to that observed in samples of Y15. A prominent increase in the overall selectivity of dehydrogenation occurs after Al-IE, reaching from 22% in parent Y30 to 40% in a 5-fold aluminum-exchanged sample. Among the dehydrogenation products, isobutane becomes the most selectivity with a ~15-20% increase compared to parent Y30. Furthermore, unlike parent zeolites and aluminum-exchanged samples of Y15, the selectivity to isobutane does not decrease at elevated temperatures. The sample prepared with a Na-IE followed by Al-IE also shows higher conversion than parent Y30, with dehydrogenation selectivity comparable to aluminum-exchanged samples prepared without Na-IE. This sample possesses lower content of BAS as compared to parent Y30 and a significantly higher content of LAS. However, the content of later sites is lower than the aluminum-exchange sample without sodium. The higher conversion with an associated increased dehydrogenation selectivity in this sample confirms that the dehydrogenation of n-butane predominantly occurs with the aid of a Lewis acid site. In

comparison, the Na-IE, after Al-IE results in conversions even lower than parent Y30, is explained as follows (1) the Na-IE after Al-IE makes a sample with reduced framework crystallinity and pore structure (2) the contents of BAS and LAS are less as compared to samples prepared by Na-IE before Al-IE treatment.

Despite the lower conversions, the selectivity to dehydrogenation remains comparable to other aluminum-exchanged samples of Y30. Furthermore, the evaluation of the carbon deposits shows that the coking decreases with an increase in the Si/Al ratio of parent zeolites and aluminum-exchanged zeolites. The comparison of the regenerated catalysts with the fresh ones shows that the parent Y zeolites undergo structural deformation while completely dislodging aluminum from the framework. However, this collapse is less severe at higher Si/Al ratios, where the increase in the content of FA-Al is more significant. However, the aluminum-exchanged zeolites show no significant change in the distribution of EFAl and FA-Al species. Similarly, the concentration of LAS is also comparable to fresh samples. The results suggest that the EFAl LAS generated by Al-IE are strong enough to catalyze the activation of the C-H bond in n-butane conversion. The higher selectivity to isobutane indicates that the reaction proceeds by activating the C-H bond on Lewis acid sites, resulting in the formation of a carbenium ion. This is followed by the skeletal isomerization to isobutane<sup>111, 112, 253</sup>. The evaluation of regenerated catalysts confirmed that the parent Y zeolites undergo structural collapse up to the Si/Al ratio of 15. However, this is not the case for aluminum-exchanged samples, as the structure and acid sites remain preserved, even though the Si/Al ratios of aluminum-exchanged samples range from 7-15. This proposes that the EFAl LAS species generated by Al-IE aid in preventing structural damage.

#### **7.4. Conclusions**

The catalytic performance of zeolite Y with different Si/Al ratios and the respective aluminum-exchanged samples was evaluated for n-butane dehydrogenation, and catalysts in their proton and ammonium forms were tested. The parent protonic zeolites at low Si/Al ratios, despite having maximum content of both LAS and BAS, show minimal conversion i.e. < 5%. The activity increases significantly in the respective ammonium zeolite, reaching 10%, whereas the selectivity to the dehydrogenation pathway decreases by 15%. Increasing the Si/Al ratio increases the conversion of protonic zeolites to 22% and decreases the activity improvement due to the presence of ammonium cations. After Si/Al of 15, the activity of protonic zeolites lowers to 3.5 with a further increase in Si/Al ratio; the presence of ammonium cations further lowers the conversion. Aluminum-exchange results in a ~8-10% increase in the conversion of

parent zeolites, and the effect is more prominent and consistent with Al-IE treatments on Y30 zeolite. Al-IE on Y15 results in a 10% increase in isobutane selectivity, however, the overall selectivity to dehydrogenation remains comparable to parent zeolites. In comparison, Al-IE on Y30 results in a 22% increase in dehydrogenation selectivity, making isobutane 15-20% more selective. Despite lowering BAS due to Na-IE before and after Al-IE, the dehydrogenation selectivity of aluminum-exchanged samples does not change. Furthermore, the structure of EFAl species and their Lewis acidic nature remains preserved in the zeolites after regeneration of the spent catalysts. The results suggest that the neutral EFAl Lewis acid sites incorporated by Al-IE are thermally stable and strong enough to activate C-H bonds. Higher selectivities of isobutane propose that the protolysis of n-butane to form carbenium ion occurs on LAS, followed by the skeletal isomerization to isobutane.

## **Chapter 8**

### **Distribution of aluminum Lewis acid sites during aluminations and dealuminations-realuminations of BEA**

#### **Contributions**

The synthesis, XRD, nitrogen physisorption, FTIR and NMR characterization and catalytic evaluation of materials was performed by the author the thesis

## 8.1. Introduction

Zeolite BEA, a 12-MR three-dimensional structure with a channel size of  $7.6 \times 6.4 \text{ \AA}$  (**Figure 8.1**), is very active in various industrially important BAS-catalyzed reactions<sup>254-256</sup>. In addition, zeolite BEA demonstrates high activity in the Lewis acid-catalyzed Meerwein–Ponndorf–Verley reduction<sup>81, 100, 103</sup>. The reduction of 4-*tert*-butylcyclohexanone, one of the most widely studied ketone reactants, generally produces a mixture of isomeric *cis*- and *trans*-4-*tert*-butylcyclohexanols<sup>103</sup>. All the homogeneous and most heterogeneous Lewis catalysts selectively produce *trans*-alcohol, a thermodynamically favorable product. However, the size and geometry of the free void volume of beta zeolite provide optimum conditions for stereoselective production of commercially relevant *cis*-alcohol, with selectivity  $\geq$  of 90%<sup>106, 257, 258</sup>.

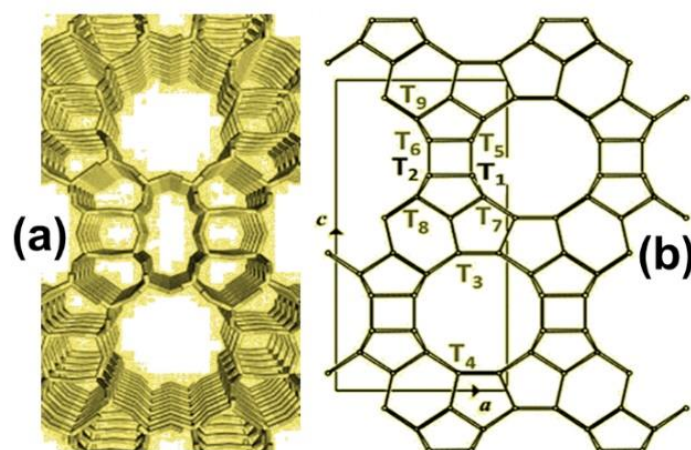


Figure 8.5: The framework structure of zeolite BEA (a) Unit cell of zeolite BEA showing different crystallographic T-sites in the framework (b)

The protonic form of steamed BEA zeolite contains both FA-Al and EFAl species. Zeolite beta experiences substantial distortions due to its less stable framework, which initiates, after post-synthetic treatments, the opening of the framework Al–O linkages. This results in a considerable amount of FA-Al species<sup>66, 259</sup>, whereas severe steaming treatments of beta zeolites lead to the preferential formation of EFAl species<sup>81</sup>. However, the FA-Al species (coordinated to three framework oxygens and an OH group) have widely been proposed as the active site in the selective MPV reduction of ketones and reverse Oppenauer oxidation<sup>66, 106, 257, 258</sup>.

In this chapter, we evaluate the nature and type of aluminum LAS active in MPV reaction by quantitative analysis of the distribution of catalytically active aluminum LAS during



alumination and dealumination-realumination of zeolite BEA. We demonstrate that Al-IE enhances the MPV activity of zeolite BEA by primarily generating EFAl LAS species, which retain their octahedral coordination upon ammonium-exchange ( $\text{NH}_4^+$ -IE), and that both FA-Al and EFAl can serve as the MPV active sites. This work also shows that the VHF-OH band of BEA, at  $\sim 3780 \text{ cm}^{-1}$  of IR region, is correlated neither to the strongly acidic FA-Al species nor to the EFAl species generated by aluminum-exchange.

## 8.2. Materials and Methods

**Chemicals and materials:** Commercially available zeolite Beta (CP814E\*, ammonium form, Si/Al=12.5) was purchased from Zeolyst International. Aluminum nitrate nonahydrate (99.99%, ABCR), Ammonium acetate ( $\text{NH}_4(\text{CH}_3\text{COO})$ ) (99%, Merck), Nitric acid (>65%, Sigma-Aldrich), and Ammonium nitrate (>99%, Sigma-Aldrich) were used as received.

Table 8.1: List of parent and modified BEA samples with the respective treatment conditions

Sample ID	Treatment conditions
BEA- $\text{H}^+$	1x calcination of zeolite Beta (CP814E*) in static air
BEA- $\text{NH}_4^+$	2x ammonium-exchange of BEA- $\text{H}^+$
BEA-1IE(Al)- $\text{H}^+$	1x Al-IE of BEA- $\text{H}^+$ followed by calcination in static air
BEA-1IE(Al)- $\text{NH}_4^+$	2x ammonium-exchange of BEA-1IE(Al)- $\text{H}^+$
BEA(deAl)- $\text{H}^+$	1x dealumination of BEA- $\text{H}^+$ , followed by calcination in static air
BEA(deAl)-1IE(Al)- $\text{H}^+$	1x Al-IE of BEA(deAl)- $\text{H}^+$ followed by calcination in static air
BEA(deAl)-1IE(Al)- $\text{NH}_4^+$	2x ammonium-exchange of BEA(deAl)-1IE(Al)- $\text{H}^+$
BEA(deAl)-5IE(Al)- $\text{H}^+$	5x Al-IE of BEA(deAl)- $\text{H}^+$ followed by calcination in static air
BEA(deAl)-5IE(Al)- $\text{NH}_4^+$	2x ammonium-exchange of BEA(deAl)-5IE(Al)- $\text{H}^+$

**Material Preparation:** Zeolite Beta (ammonium form) was calcined at 823 K in static air at a heating ramp rate of 1K/min for 6 hours to obtain proton form zeolite. The BEA- $\text{H}^+$  was aluminated using the ion-exchange procedure described in **Section 3.1.1**. The dealuminated-realuminated BEA was prepared by a two-step procedure which consisted of the dealumination of parent BEA- $\text{H}^+$  followed by aluminated dealuminated BEA via ion-exchange. To prepare dealuminated BEA, dealumination procedure described in **Section 3.1.5** was followed. Realumination was done using the aluminum-exchange procedure. Likewise, to increase the

extent of realumination, the dealuminated BEA was five-fold aluminum exchanged, with each ion exchange followed by calcination. The samples were converted to ammonium forms by the  $\text{NH}_4^+$ -IE procedure described in **Section 3.1.2**. **Table 8.1** lists the nomenclature of the samples used in this work.

**Material Characterization:** The X-ray diffraction patterns of zeolite powders were recorded on a PANalytical X'Pert PRO MPD diffractometer using  $\text{Cu K}\alpha$  radiation ( $\lambda = 0.15418$  nm). The specific surface areas of zeolites were determined by collecting nitrogen adsorption-desorption isotherms at 77 K with Micromeritics Tristar II 3020 gas adsorption analyzer. Inductively coupled plasma optical emission spectroscopy (ICP-OES) determined zeolite samples' aluminum and silicon content.  $^{27}\text{Al}$  MAS NMR spectra were acquired by spinning the sample rotors at 10 kHz at a resonance frequency of 79.5 MHz for the  $^{27}\text{Al}$  nucleus using a Bruker AVANCE III HD spectrometer and Bruker 400 MHz Ultra-Shield magnet. Similarly,  $^{27}\text{Al}$  MQMAS NMR spectra were recorded using a Bruker 700MHz Ultra-Shield spectrometer using a 2.5 mm MAS probe at a 20 kHz spinning speed. Fourier Transform infrared (FTIR) spectra of zeolite samples using pyridine and carbon monoxide as probe molecules were recorded using a Thermo Nicolet iS50 FTIR spectrometer having a DTGS detector (**Section 3.2.1**). All the FTIR spectra presented here were normalized to the weight and area of the sample discs.

**Catalytic Evaluation:** The Meerwein-Ponndorf-Verley reduction reaction was carried out to measure zeolite powders' catalytic activity, as discussed in **Section 3.3**. In the catalytic experiment, 200 mg of a zeolite catalyst, 2.5 mmoles of 4-*tert*-butylcyclohexanone, 50 mL of isopropanol, and 1 mmole of 1,3,5-tri-*tert*-butylbenzene (internal standard) was used. The catalytic experiments were performed under similar conditions using 20 mg of zeolite powders.

### 8.3. Results and Discussion

**Lewis acid catalytic activity:** **Figures 8.2a** and **8.2b** present the catalytic reduction of 4-*tert*-butylcyclohexanone to *cis/trans* 4-*tert*-butylcyclohexanol over 200 mg of zeolites in  $\text{H}^+$  forms. The respective conversion after 7.4 h, an initial rate of reaction, and the selectivity to *cis* and *trans* products, using 200 mg of catalyst, are given in Table 2. The pristine BEA- $\text{H}^+$ , due to its very high inherent Lewis acidity, reaches 96% conversion within 2 h of reaction time at a very high initial rate of  $1.67 \text{ mmolL}^{-1}\text{min}^{-1}$  (Figure 2 and Table 2). The conversion increases only by 4% after Al-IE reaching to 100% in BEA-1IE(Al)- $\text{H}^+$  at a relatively higher rate of  $1.90 \text{ mmolL}^{-1}$

$^1\text{min}^{-1}$  increasing the ketone conversion to 100% within the reaction time studied, with a higher rate of reaction of  $1.90 \text{ mmolL}^{-1}\text{min}^{-1}$ . The dealuminated  $\text{BEA}(\text{deAl})\text{-H}^+$  appears inactive compared to  $\text{BEA}\text{-H}^+$ , exhibiting 16% conversion and a reaction rate of  $0.04 \text{ mmolL}^{-1}\text{min}^{-1}$ , respectively. After realumination, a prominent increase in activity has been observed, with the sample  $\text{BEA}(\text{deAl})\text{-5IE}(\text{Al})\text{-H}^+$  appearing to be the best-performing catalyst reaching 100% conversion at a rate of  $2.11 \text{ mmolL}^{-1}\text{min}^{-1}$ .

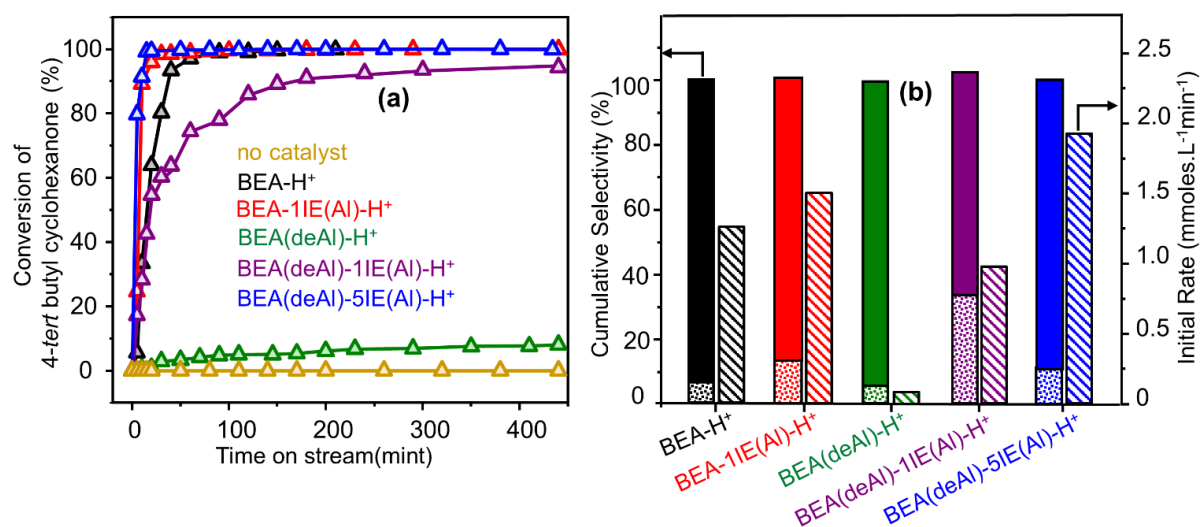


Figure 8.2. (a) Catalytic conversion (%) of 4-*tert* butyl cyclohexanone as a function of time on stream over 200 mg of BEA zeolites. (b) Cumulative selectivity towards *cis* (solid bars) and *trans* (dotted bars) 4-*tert* butylcyclohexanol after 7.4 h and initial rate of reaction (bars with diagonal stripes). The initial reaction rate is determined as the linear regression slope in the time-concentration plot between zero time and 110 minutes of reaction time.

Due to the very high inherent catalytic activity of  $\text{BEA}\text{-H}^+$ , the difference in activity between  $\text{BEA}\text{-H}^+$ ,  $\text{BEA}\text{-1IE}(\text{Al})\text{-H}^+$  and  $\text{BEA}(\text{deAl})\text{-5IE}(\text{Al})\text{-H}^+$  is ambiguous. Although the reaction rates are relatively different in these samples, the conversion remains in the 96-100% range. Therefore the catalytic tests using a 10 times lesser amount of catalyst were performed (**Figure E1 and Table 2**). The results demonstrate that  $\text{BEA}\text{-H}^+$  (26% conversion and a rate of  $0.14 \text{ mmolL}^{-1}\text{min}^{-1}$ ) shows a substantial increase in the activity after alumination, i.e., the conversion and reaction rate in  $\text{BEA}\text{-1IE}(\text{Al})\text{-H}^+$  is 38% and  $0.17 \text{ mmolL}^{-1}\text{min}^{-1}$ , respectively. Likewise, the sample  $\text{BEA}(\text{deAl})\text{-5IE}(\text{Al})\text{-H}^+$  outperforms in all BEA samples (44% conversion and a rate of  $0.14 \text{ mmolL}^{-1}\text{min}^{-1}$ ).

Table 8.2: Catalytic data of MPV reduction of 4-*tert* butylcyclohexanone over 200 mg of zeolite catalysts ( $\pm 5\%$ ); (a) conversion (%) of 4-*tert* butylcyclohexanone after 7.4 h; (b) initial rate of reaction in  $\text{mmolesL}^{-1}\text{min}^{-1}$ ; (c) cumulative selectivity (%) after 7.4 h to *cis* and *trans* 4-*tert* butylcyclohexanol; \*values given in brackets show the results of catalytic tests using 20 mg of BEA catalysts.

Zeolite	Conversion <sup>a</sup>	Initial Rate <sup>b</sup>	<i>cis:trans</i> <sup>c</sup>
BEA-H <sup>+</sup>	96 (26*)	1.67 (0.11*)	94:06 (85:15*)
BEA-1IE(Al)-H <sup>+</sup>	100 (38)	1.9 (0.15)	88:12 (80:20)
BEA(deAl)-H <sup>+</sup>	16 (0.7)	0.04 (0.003)	94:06 (88:12)
BEA(deAl)-1IE(Al)-H <sup>+</sup>	95 (9)	1.29 (0.08)	76:24 (59:41)
BEA(deAl)-5IE(Al)-H <sup>+</sup>	100 (44)	2.11 (0.21)	90:10 (79:21)

As the LAS in BEA are present in the micropores and not on the external surface, the MPV reaction in zeolite BEA occurs exclusively within the micropores<sup>103, 105, 229</sup>. Therefore, BEA-H<sup>+</sup> produces cumulative *cis* and *trans* alcohols with a ratio of about 94:06. The respective *cis:trans* selectivity does not change much after alumination, dealumination-realumination treatments. Only the sample BEA(deAl)-1IE(Al)-H<sup>+</sup> produces *trans*-alcohol with slightly lower *cis:trans* selectivity of 76:24, which further changes to 59:41 by using a 10 times lesser amount of catalyst.

**Physical chemical properties:** The elemental analysis of all the samples, presented in **Table 8.3**, shows a significant change in the bulk aluminum content of the zeolites during alumination and dealumination-realumination treatments. The Si/Al ratio of BEA-H<sup>+</sup> decreases from 12.5 to 10.4 in BEA-1IE(Al)-H<sup>+</sup>, indicating uptake of aluminum by the zeolite during alumination. A substantial increase of Si/Al ratio to 1460 in BEA(deAl)-H<sup>+</sup> illustrates the extraction of large amounts of aluminum from the zeolite framework due to the severity of nitric acid treatment, as previously discussed by many investigations acids<sup>227, 234</sup>. After the first realumination of the dealuminated sample, the Si/Al ratio decreases from 1460 to 14.1 in BEA(deAl)-1IE(Al)-H<sup>+</sup>. The Si/Al ratio after 5-fold realumination becomes 9.7 in BEA(deAl)-5IE(Al)-H<sup>+</sup>, which is even lower than BEA-H<sup>+</sup> and BEA-1IE(Al)-H<sup>+</sup>. These results corroborate that the maximum uptake of aluminum has been achieved after multiple realumination of a dealuminated sample in the case of BEA(deAl)-5IE(Al)-H<sup>+</sup> (Table 3). No significant changes in these samples' Si/Al ratio were observed in their respective NH<sub>4</sub><sup>+</sup> forms (**Table E2**).

Table 8.3: Physicochemical characterization of parent and aluminum-exchanged zeolites

Zeolite	<sup>a</sup> 2 $\theta$	<sup>a</sup> d <sub>302</sub>	<sup>b</sup> Crystallinity <sub>rel</sub> (%)	<sup>c</sup> Si/Al ratio	<sup>d</sup> S <sub>BET</sub> m <sup>2</sup> g <sup>-1</sup>	<sup>e</sup> V <sub>total</sub> cm <sup>3</sup> g <sup>-1</sup>	<sup>f</sup> V <sub>micro</sub> cm <sup>3</sup> g <sup>-1</sup>
BEA-H <sup>+</sup>	22.44	3.96	100	12.5	480	0.20	0.20
BEA-1IE(Al)-H <sup>+</sup>	22.44	3.96	89	10.4	450	0.24	0.21
BEA(deAl)-H <sup>+</sup>	22.53	3.94	90	1460	460	0.23	0.19
BEA(deAl)-1IE(Al)-H <sup>+</sup>	22.44	3.96	88	14.1	470	0.22	0.20
BEA(deAl)-5IE(Al)-H <sup>+</sup>	22.44	3.96	86	9.7	460	0.23	0.19

<sup>a</sup>calculated from XRD patterns, <sup>b</sup>calculated by a previously described method<sup>180</sup>, assuming the crystallinity of parent zeolites as 100%, <sup>c</sup>calculated from ICP, <sup>d</sup>calculated from BET method <sup>e</sup>based on single point adsorption at p/po = 0.97, <sup>f</sup>calculated from t-plot method

The X-ray diffraction patterns of the parent BEA-H<sup>+</sup> and the samples prepared by alumination and dealumination-redealumination procedures are presented in **Figure 8.3a**. The modified zeolite samples prepared by alumination (BEA-1IE(Al)-H<sup>+</sup>), dealumination (BEA(deAl)-H<sup>+</sup>), and dealumination-redealumination (BEA(deAl)-1IE(Al)-H<sup>+</sup> and BEA(deAl)-5IE(Al)-H<sup>+</sup>) show all the characteristic diffractions peaks, comparable to those in the parent BEA-H<sup>+</sup><sup>233</sup>. No reflections related to any alumina types are visible, suggesting that aluminum species are well-dispersed and do not form larger aluminum oxide agglomerates (**Figure 8.3a**).

The 2 $\theta$  values for the diffraction near 22–23°, due to (302) reflection, and the corresponding d-spacing values are given in **Table 8.3**. Any changes in this diffraction peak indicate possible contraction/expansion of the BEA framework due to post-synthetic treatments<sup>260</sup>. As shown in Figure S2 and Table 3, the alumination of BEA-H<sup>+</sup> does not affect the 2 $\theta$  position (22.44°) and the consequent d<sub>302</sub> spacing value (3.96 Å) in BEA-1IE(Al)-H<sup>+</sup>. However, after the dealumination of BEA-H<sup>+</sup>, the 2 $\theta$  position shifts towards a higher angle, from 22.44° to 22.53° in BEA(deAl)-H<sup>+</sup>. Consequently, the d<sub>302</sub> value also decreases from 3.96 Å to 3.94 Å. After dealumination treatments of BEA(deAl)-H<sup>+</sup>, 2 $\theta$  position shifts back to the original position (22.44°) in BEA(deAl)-1IE(Al)-H<sup>+</sup> and BEA(deAl)-5IE(Al)-H<sup>+</sup> samples and the d<sub>302</sub> value increases from 3.94 Å to 3.96 Å (**Figure E2 and Table 8.3**).

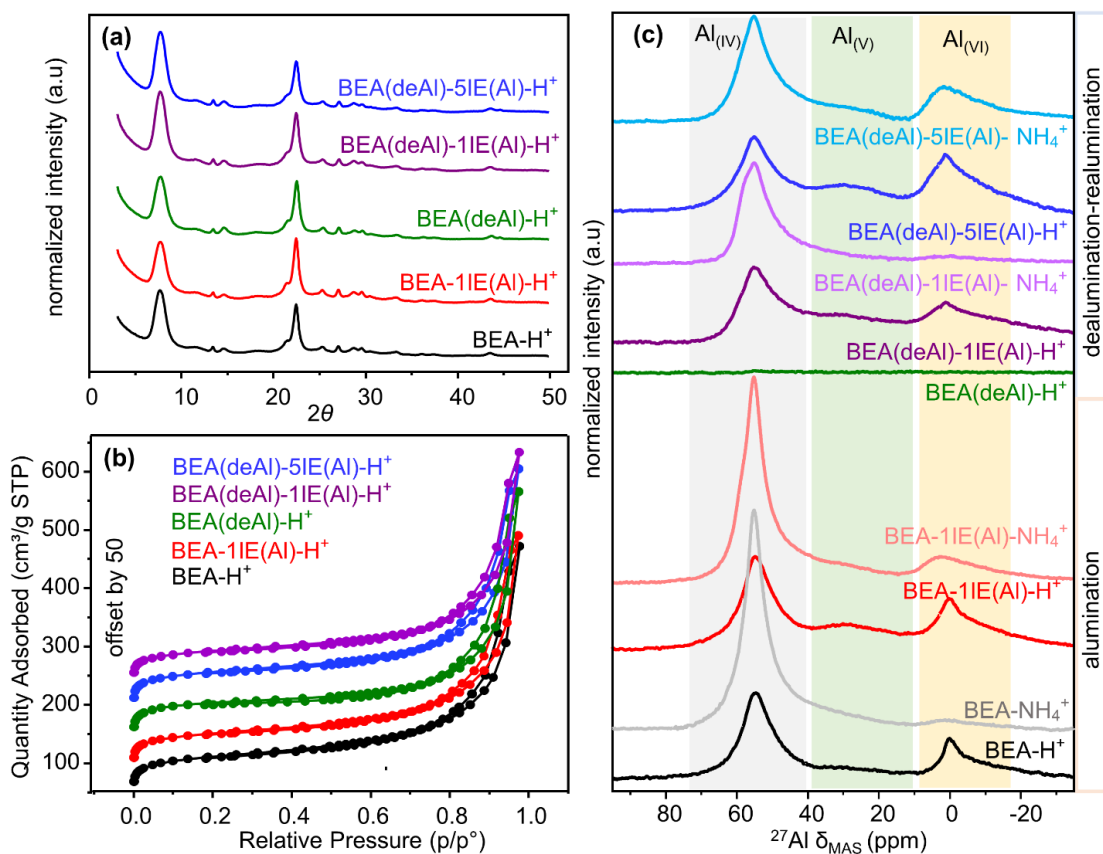


Figure 8.3. (a) PXRD patterns, (b) nitrogen adsorption/desorption isotherms, and (c) <sup>27</sup>Al MAS NMR spectra of parent, aluminated, and dealuminated-realuminated BEA samples. Colored regions in (c) are added to guide the eye.

These results can be explained in terms of the addition or removal of aluminum species to or from the zeolite framework, respectively. Upon dealumination, aluminum was removed from the framework without any structural collapse. Most (if not all) of aluminum can be reinserted into the framework by the realumination of a Si-BEA. In contrast, the alumination of parent BEA increases the total aluminum content of the zeolite without incorporating aluminum into framework sites. Assuming the crystallinity of parent BEA-H<sup>+</sup> to be 100%<sup>180</sup>, the relative crystallinity of the aluminum-modified zeolites indicates only a minor change, ranging from 86 to 90% (**Table 8.3**). These results illustrate that the crystalline structure of BEA zeolite remains intact after these treatments, even after performing severe acid-dealumination<sup>92, 233</sup>.

The nitrogen adsorption/desorption isotherms of all samples are presented in **Figure 8.3(b)**, whereas **Table 8.3** summarizes the quantitative characteristics. The parent BEA-H<sup>+</sup> zeolite exhibits typical type IV isotherms with hysteresis loop<sup>227</sup>. The nitrogen physisorption isotherms of all the modified samples look very similar to the one of the parent BEA-H<sup>+</sup> zeolite. Likewise, BET surface area (450-480 m<sup>2</sup>g<sup>-1</sup>), micropore volume (0.19-0.21 cm<sup>3</sup>g<sup>-1</sup>), and total pore volume (0.22-0.24 cm<sup>3</sup>g<sup>-1</sup>) of zeolites before and after treatments remain almost unchanged, staying

within the error limits (**Table 8.3**). These results confirm the preservation of the microporous structure of BEA zeolites after all post-synthetic alumination and dealumination-realumination events. Slight changes in the total pore volumes of the  $\text{NH}_4^+$  forms of dealuminated-realuminated BEA samples have been observed (**Table E2**).

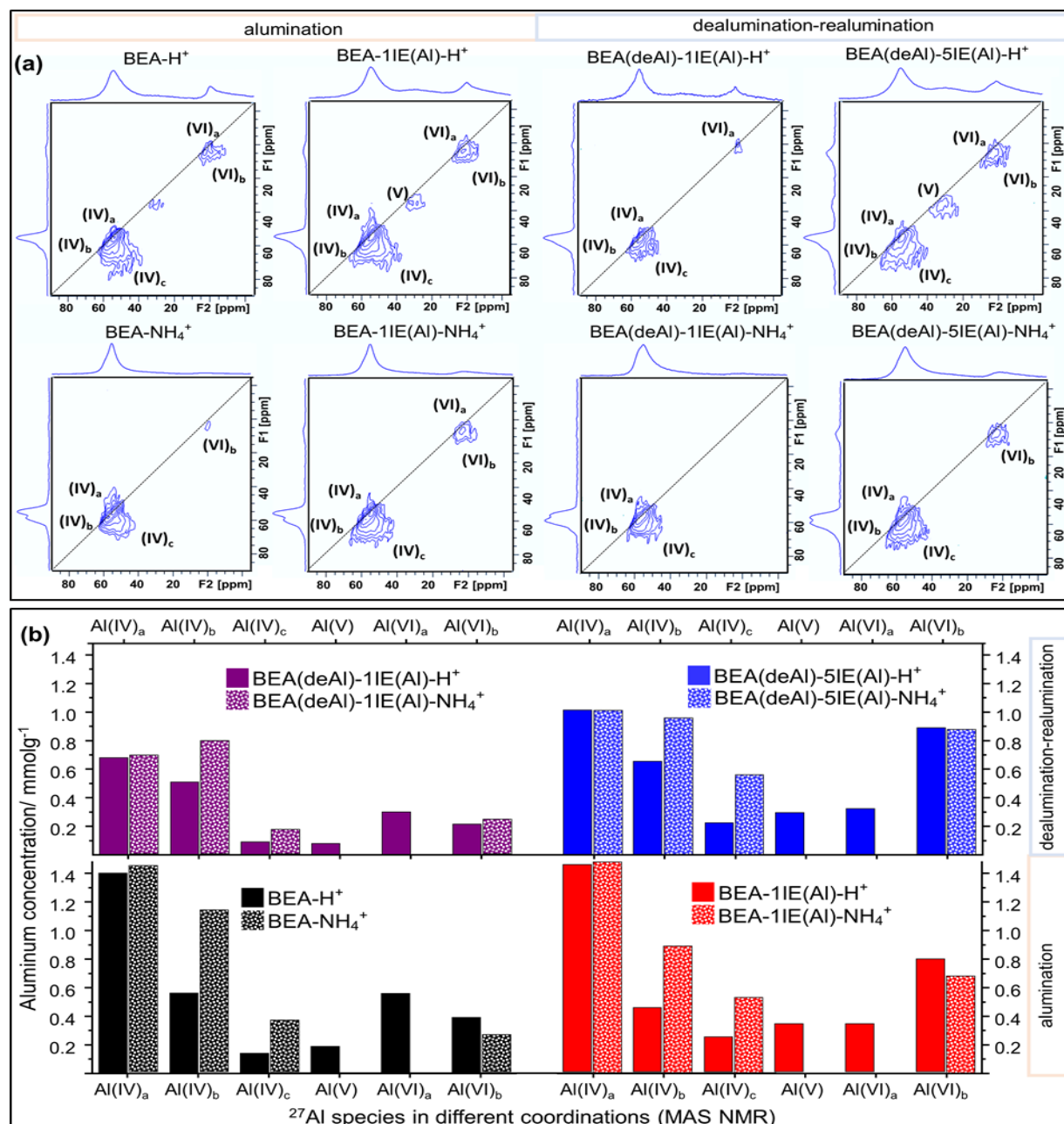


Figure 8.4: (a)  $^{27}\text{Al}$  MQMAS spectra and (b) the quantitative distribution (in  $\text{mmoles g}^{-1}$ ,  $\pm 10\%$ ) of aluminum, i.e. (Al(IV)<sub>a</sub>, Al(IV)<sub>b</sub>, Al(IV)<sub>c</sub>, Al(V), Al(VI)<sub>a</sub>, Al(VI)<sub>b</sub>) species obtained from  $^{27}\text{Al}$  MAS and MQMAS NMR spectra. The F1 axis of MQMAS spectra is an isotropic dimension, whereas the F2 axis shows the anisotropic dimension with second-order quadrupolar interactions.

**Solid-state NMR spectroscopy:** The  $^{27}\text{Al}$  MAS and  $^{27}\text{Al}$  MQMAS NMR spectra of the zeolites, recorded under ambient conditions, are presented in **Figures 8.3c and 8.4a**, respectively. The concentration of aluminum species in different coordinations obtained from MAS NMR spectra using the NMR fitting parameters determined from MQMAS spectra are listed in **Table E4**. For a visual comparison, the quantitative distribution of aluminum species in different coordinations is presented in **Figure 8.4(b)**.

The MAS NMR spectrum of  $\text{BEA-H}^+$  shows a sharp peak at  $\sim 54$  ppm due to tetrahedral aluminum ( $\text{Al(IV}_a\text{)}$ ) in the framework of zeolite <sup>62, 234</sup> (**Figure 3c**). These species have a minimal quadrupolar interaction (**Figure 8.4**) with a  $Q_{cc} \sim 1.7$  MHz (**Table S3**). The resonance at  $\sim 58.5$  ppm due to  $\text{Al(IV}_b\text{)}$  species is associated with small  $Q_{cc} \sim 1.9$  MHz but slightly more significant isotropic expansion (**Figure 4a and Table E3**). Likewise, a broad asymmetric resonance with very large  $Q_{cc}$  ( $\sim 4.5$  MHz) at  $\sim 60$  ppm is attributed to distorted tetrahedral aluminum  $\text{Al(IV}_c\text{)}$  species (**Figures 8.3c and 8.4a**). A broad, less intense feature at  $\sim 30$  ppm, due to pentahedral aluminum, is labeled as  $\text{Al(V)}$  species <sup>63-65</sup>.

The MAS NMR spectrum of  $\text{BEA-H}^+$  also shows two octahedral resonances, i.e., a sharp one at  $\sim 0.1$  ppm ( $Q_{cc} \sim 1.1$  MHz) due to  $\text{Al(VI}_a\text{)}$  species and another overlapping broad asymmetric feature ( $Q_{cc} \sim 2.5$  MHz) at  $\sim 2.7$  ppm due to  $\text{Al(VI}_b\text{)}$  species. The concentration of  $\text{Al(IV}_a\text{)}$ ,  $\text{Al(IV}_b\text{)}$ ,  $\text{Al(IV}_c\text{)}$ ,  $\text{Al(V)}$ ,  $\text{Al(VI}_a\text{)}$ , and  $\text{Al(VI}_b\text{)}$  species is 1.39, 0.56, 0.14, 0.19, 0.56 and 0.39 respectively. The spectrum of  $\text{BEA-NH}_4^+$  (**Figure 8.3c**) reveals the disappearance of peak  $\sim 0.1$  ppm and concurrent increase of intensity in the tetrahedral region, whereas the broad feature at  $\sim 2.7$  ppm still exists. Thus, an ammonium-exchange of  $\text{BEA-H}^+$  increases the concentration of  $\text{Al(IV}_b\text{)}$  species to  $1.14 \text{ mmol g}^{-1}$ , whereas that of  $\text{Al(IV}_a\text{)}$  species remains the same. The  $\text{Al(VI}_a\text{)}$  species that can be reinserted back into the framework of the zeolite upon ammonium-exchange are termed as FA-Al, whereas  $\text{Al(VI}_b\text{)}$  species, retaining their octahedral coordination in proton and ammonium forms of the zeolite, are called as EFAI <sup>50, 62, 180</sup>. According to the literature, <sup>69, 227, 234</sup>,  $\text{Al(IV}_a\text{)}$  represents aluminum at  $T_1$ - $T_2$  sites of the BEA framework, and  $\text{Al(IV}_b\text{)}$  is aluminum positioned at  $T_3$ - $T_9$  sites. The FA-Al, i.e.,  $\text{Al(VI}_a\text{)}$  species are coordinated to  $\text{Al(IV}_b\text{)}$  species of the framework, which in the  $\text{BEA-H}^+$  sample attain octahedral coordination to appear as  $\text{Al(VI}_a\text{)}$  species and increase the concentration of  $\text{Al(IV}_b\text{)}$  species in  $\text{BEA-NH}_4^+$ . Furthermore, the disappearance of  $\text{Al(V)}$  species results in a corresponding increase in the concentration of  $\text{Al(IV}_c\text{)}$  species from 0.14 to  $0.37 \text{ mmol g}^{-1}$  (**Figure 8.3c, 8.4**).

The aluminations of  $\text{BEA-H}^+$  successfully increases the concentration of  $\text{Al(IV}_b\text{)}$  species from 0.39 to  $0.79 \text{ mmol g}^{-1}$ , whereas the concentration of  $\text{Al(VI}_a\text{)}$  species decreases from 0.56 to 0.34



mmol $g^{-1}$ . Furthermore, there is a slight decrease in the concentration of Al(IV<sub>b</sub>) species and a slight increase in that of Al(IV<sub>c</sub>) and Al(V) species. In the corresponding NH<sub>4</sub><sup>+</sup> form, i.e., BEA-1IE(Al)-NH<sub>4</sub><sup>+</sup>, the absence of Al(VI<sub>a</sub>) and Al(V) species is followed by an increase in the concentration of Al(IV<sub>b</sub>) and Al(IV<sub>c</sub>) species, respectively. However, the increase in total aluminum content due to alumination (from 3.23 to 3.59 mmol $g^{-1}$ ) does not solely account for an increase in the content of Al(IV<sub>b</sub>) species (from 0.39 to 0.79 mmol $g^{-1}$ ) BEA-1IE(Al)-H<sup>+</sup> as the alumination also increases the concentration of Al(V) species (from 0.19 to 0.34 mmol $g^{-1}$ ). Another important consequence of alumination is the decrease in the content of Al(IV<sub>b</sub>) species (from 0.56 to 0.34 mmol $g^{-1}$ ). This suggests that the increase in the concentration of Al(IV<sub>b</sub>) species, comparatively higher than total incorporated aluminum, is due to a decrease in the content of Al(IV<sub>a</sub>) species. As Al(IV<sub>a</sub>) species are associated with the framework, some of these aluminum species, upon alumination or calcination, might have been completely dislodged from the framework, thus increasing the content of Al(VI<sub>b</sub>) species.

The spectrum of BEA(deAl)-H<sup>+</sup> does not show any visible signal in the resonance envelope, and the very low aluminum content of BEA(deAl)-H<sup>+</sup> (0.26 mmol $g^{-1}$ ) exists solely as Al(IV<sub>a</sub>) species (**Figure 8.3c, 4a-b, Table E4**). Literature suggests that the dealumination of BEA via inorganic acids completely extracts the aluminum located at T<sub>3</sub>-T<sub>9</sub> sites, whereas the Al(IV<sub>a</sub>) species of T<sub>1</sub>-T<sub>2</sub> sites are only partially removed<sup>234, 261-264</sup>. In this work, the dealumination treatment, due to the severity of its conditions (13M HNO<sub>3</sub> solution and 373K), can effectively remove ~90% of these aluminum species. The first realumination on BEA(deAl)-H<sup>+</sup> can reinsert 0.30 mmol $g^{-1}$  of Al(VI<sub>a</sub>) species in BEA(deAl)-1IE(Al)-H<sup>+</sup>, which is ~50% of the content of these species in BEA-H<sup>+</sup>, whereas the reinserted content of Al(VI<sub>b</sub>) species is comparable to that of BEA-H<sup>+</sup> sample (**Figure 8.3c, 8.4a-b and Table E4**). The most prominent effect of first realumination appears as an increase in the concentration of tetrahedral species, i.e., 0.68, 0.51, 0.09 mmol $g^{-1}$  for Al(VI<sub>a</sub>), Al(VI<sub>b</sub>), and Al(VI<sub>c</sub>) species, respectively.

However, the aluminum incorporated after multiple realuminations of BEA(deAl)-H<sup>+</sup> predominantly increases the concentration of Al(VI<sub>b</sub>) species (0.88 mmol $g^{-1}$ ) in BEA(deAl)-5IE(Al)-H<sup>+</sup>. Unlike alumination, FA-Al species don't completely dislodge from the framework upon further realuminations on BEA(deAl)-IE(Al)-H<sup>+</sup> to make BEA(deAl)-5IE(Al)-H<sup>+</sup>, as the content of Al(VI<sub>a</sub>) remains similar to that of BEA(deAl)-1IE(Al)-H<sup>+</sup>. The concentration of Al(IV<sub>a</sub>), Al(IV<sub>b</sub>), and Al(IV<sub>c</sub>) species increase only slightly (1.01, 0.67, and 0.22 mmol $g^{-1}$ ,

respectively) when compared with the increase in the content of tetrahedral aluminum species in BEA(deAl)-1IE(Al)-H<sup>+</sup>. Even after five realumination treatments, BEA(deAl)-5IE(Al)-H<sup>+</sup> could only regain 70% of the Al(IV<sub>a</sub>) species (compared to the content of these species in BEA-H<sup>+</sup>), whereas the content of Al(IV<sub>b</sub>) species is even greater than that of BEA-H<sup>+</sup>. The content of Al(V) also increases after dealumination-realumination i.e. 0.08 and 0.28 mmolg<sup>-1</sup> for BEA(deAl)-1IE(Al)-H<sup>+</sup> and BEA(deAl)-5IE(Al)-H<sup>+</sup>, respectively. The corresponding NH<sub>4</sub><sup>+</sup> forms, i.e., BEA(deAl)-1IE(Al)-NH<sub>4</sub><sup>+</sup> and BEA(deAl)-5IE(Al)-NH<sub>4</sub><sup>+</sup>, reveal the increase in the concentration of Al(IV<sub>b</sub>) and Al(IV<sub>c</sub>) species at the expense of Al(VI<sub>a</sub>) species and Al(V) species, respectively. These results show that BEA-1IE(Al)-H<sup>+</sup> has the maximum concentration of FA-Al, i.e., Al(VI<sub>a</sub>) species, and BEA(deAl)-5IE(Al)-H<sup>+</sup> has the maximum concentration of EFAl, i.e., Al(VI<sub>b</sub>) species, which suggests that Al-IE protocol used for alumination and realumination, predominantly incorporates EFAl. These observations can also be appreciated from MAS and MQMAS spectra (Figures 3c and 4a). The isotropic and anisotropic expansion of incorporated EFAl species (Q<sub>cc</sub>~2.5 MHz) in dealuminated-realuminated samples is similar to that of Al(VI<sub>b</sub>) species in BEA-H<sup>+</sup> and BEA-1IE(Al)-H<sup>+</sup> samples (**Table E3**).

**Lewis Acidity:** The FTIR spectra in the hydroxyl stretching region of all BEA samples in their protonic and ammonium forms, respectively, are presented in **Figures 8.5a and 8.5a'**. The parent BEA-H<sup>+</sup> shows four distinct bands at 3610, 3670, 3747, and 3780 cm<sup>-1</sup> and one broad and weak band at 3500 cm<sup>-1</sup>. The most intense high-frequency band at 3747 cm<sup>-1</sup> is due to hydroxyl vibrations of isolated/external silanol (Si-OH) groups, and a connected tail at 3736 cm<sup>-1</sup> is due to internal silanols at framework defects<sup>235</sup>. The band at 3610 cm<sup>-1</sup> can be ascribed to strongly acidic bridging Si(OH)Al groups. The weak and broad band centered at 3500 cm<sup>-1</sup> attributes to internal silanols nests, delocalized due to strong hydrogen-bonding connections<sup>242</sup>. These SiOH groups can be generated due to stacking faults, owing to the coexistence of polymorphs in zeolite BEA<sup>233</sup>. The band at 3670 cm<sup>-1</sup> has been assigned to hydroxyls of tri-coordinated aluminum connected to the BEA framework<sup>237</sup> and to EFAl appearing in an octahedral environment in <sup>27</sup>Al NMR<sup>242, 243</sup>. The VHF-OH band with a characteristic vibration at ~3780 cm<sup>-1</sup> is further discussed below (vide infra).

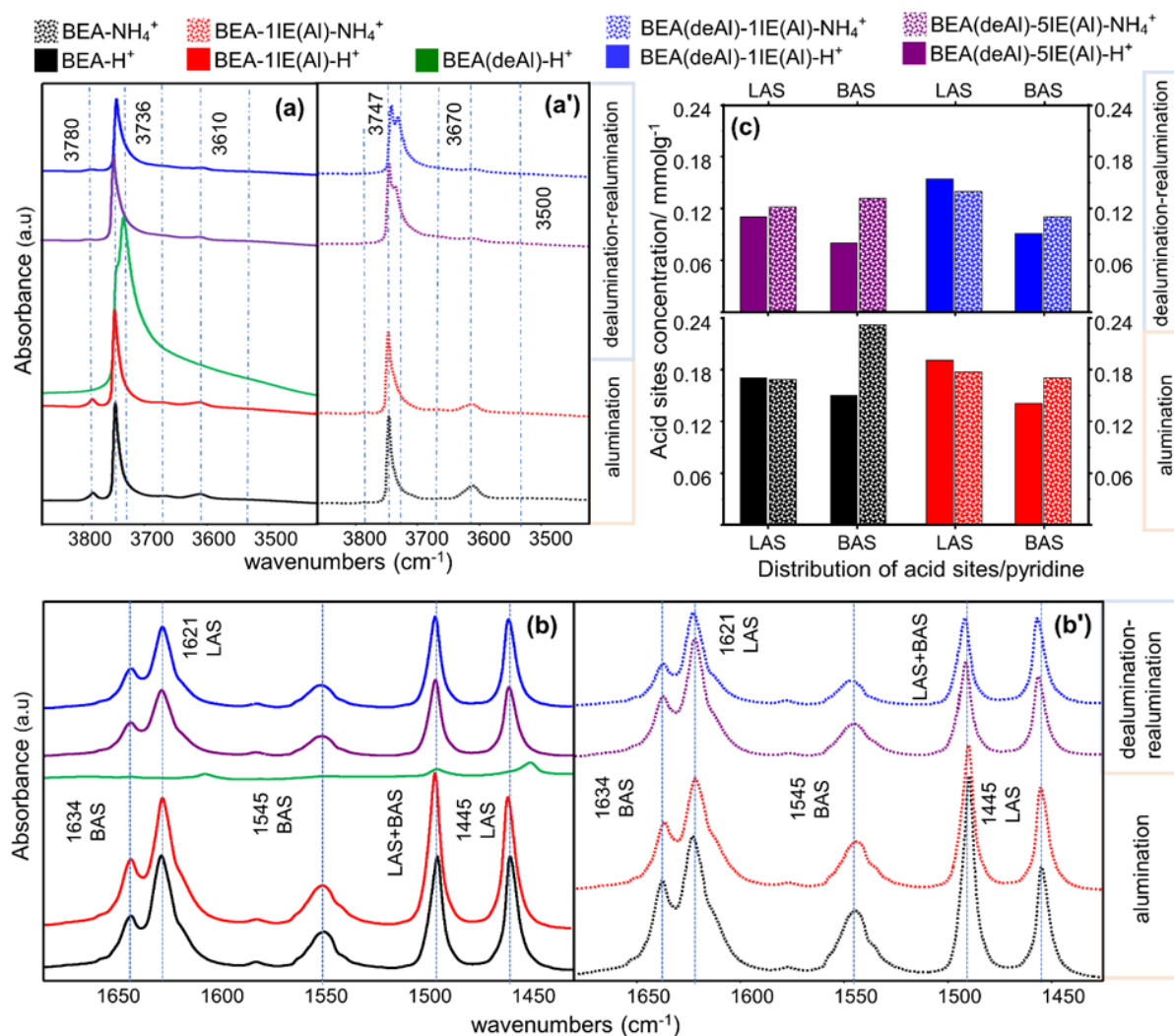


Figure 8.16: FTIR spectra of evacuated samples at 723K in hydroxyl stretching region of (a) H<sup>+</sup> form and (a') NH<sub>4</sub><sup>+</sup> form of BEA samples; Pyridine-FTIR difference spectra in pyridine stretching region of (b) H<sup>+</sup> form and (b') NH<sub>4</sub><sup>+</sup> form of BEA samples; the difference spectra are obtained by subtraction of spectra after activation at 723K from spectra after pyridine adsorption at 423K followed by evacuation at 423K; (c) distribution of acid sites accessed by pyridine in H<sup>+</sup> and NH<sub>4</sub><sup>+</sup> form of BEA samples.

After aluminations, the spectrum profile does not change much for BEA-11E(Al)-H<sup>+</sup>. The dealumination treatment brings drastic changes to the spectrum of BEA-deAl. The signature due to terminal silanols gets broader as the connected tail at 3736 cm<sup>-1</sup>, due to internal SiOH groups, significantly intensifies. Moreover, dealumination follows the complete disappearance of two bands at 3610 and 3670 due to extra-lattice aluminum species and one band at 3780 cm<sup>-1</sup> due to framework aluminum moieties<sup>264</sup>. The band at 3500 cm<sup>-1</sup>, due to hydrogen-bonded silanol nests, also significantly increases in intensity in BEA(deAl)-H<sup>+</sup>. These features

corroborate the almost complete extraction of framework and non-framework aluminum after washing the zeolite BEA with nitric acid, which aligns with previous reports<sup>263, 265, 266</sup>.

The spectrum of BEA(deAl)-1IE(Al)-H<sup>+</sup> illustrates the revival of all characteristic bands typical of BEA-H<sup>+</sup> (**Figure 8.5a**). For instance, three bands at 3610, 3670, and 3780 cm<sup>-1</sup>, responsible for vibrations due to the presence of aluminum, reappear in the spectrum of BEA(deAl)-1IE(Al)-H<sup>+</sup>. The comeback of these bands verifies the significant uptake of aluminum during realumination, again in agreement with XRD and elemental analysis. However, a considerable decrease occurs in the bands' intensity at 3733, 3780, and 3610 cm<sup>-1</sup>. The intensity of the band at 3500 cm<sup>-1</sup> also drops and becomes comparable to BEA-H<sup>+</sup> and BEA-1IE(Al)-H<sup>+</sup>. Multiple realuminations do not cause any significant changes to the spectrum of BEA(deAl)-5IE(Al)-H<sup>+</sup> (**Figure 8.5a**).

Table 4: (a) LAS and BAS concentration in mmoles g<sup>-1</sup> ( $\pm 10\%$ ) from pyridine-FTIR; (b) Carbon monoxide-FTIR analysis; the relative content of acidic sites ( $\pm 10\%$ ) was obtained by the areas of deconvoluted peaks at 2241 cm<sup>-1</sup>, 2230 cm<sup>-1</sup>, 2207 cm<sup>-1</sup> and 2195 cm<sup>-1</sup> for LAS and 2177 cm<sup>-1</sup> for BAS respectively at carbon monoxide dosage of 10 torrs. LAS<sub>all</sub> represent the sum of areas of the peaks 2241 cm<sup>-1</sup>, 2230 cm<sup>-1</sup>, 2207 cm<sup>-1</sup> and 2195 cm<sup>-1</sup> for LAS

Zeolite	pyridine <sup>a</sup>		carbon monoxide <sup>b</sup>					
	LAS	BAS	LAS <sub>V,S</sub> <sup>a</sup>	LAS <sub>S</sub> <sup>b</sup>	LAS <sub>M</sub> <sup>c</sup>	LAS <sub>W</sub> <sup>d</sup>	LAS <sub>all</sub> <sup>b</sup>	BAS <sup>b</sup>
BEA-H <sup>+</sup>	0.17	0.16	0.13	0.60	0.32	0.02	1.10	1.12
BEA-NH <sub>4</sub> <sup>+</sup>	0.16	0.23	0.01	0.52	0.12	-	0.65	1.50
BEA-1IE(Al)-H <sup>+</sup>	0.20	0.15	0.13	0.40	0.56	0.01	1.21	1.29
BEA-1IE(Al)-NH <sub>4</sub> <sup>+</sup>	0.17	0.17	0.01	0.46	0.23	-	0.7	1.40
BEA(deAl)-H <sup>+</sup>	0.02	-	-	-	-	-	0.03	0.07
BEA(deAl)-1IE(Al)-H <sup>+</sup>	0.11	0.08	0.01	0.35	0.30	-	0.66	0.69
BEA(deAl)-1IE(Al)-NH <sub>4</sub> <sup>+</sup>	0.12	0.13	-	0.38	0.16	-	0.54	0.81
BEA(deAl)-5IE(Al)-H <sup>+</sup>	0.14	0.09	0.03	0.59	0.89	0.01	1.51	0.72
BEA(deAl)-5IE(Al)-NH <sub>4</sub> <sup>+</sup>	0.13	0.11	-	0.49	0.48	-	0.97	0.84

Upon ammonium exchange, the most significant (and similar) changes apparent in the spectra of BEA-NH<sub>4</sub><sup>+</sup> and BEA-1IE(Al)-NH<sub>4</sub><sup>+</sup> are (1) the disappearance of 3780 cm<sup>-1</sup> band and (2) the increase in the intensity of the band at 3610 cm<sup>-1</sup> (**Figure 8.5a**). The spectra of ammonium forms of realuminated samples, i.e., BEA(deAl)-1IE(Al)-NH<sub>4</sub><sup>+</sup> and BEA(deAl)-5IE(Al)-NH<sub>4</sub><sup>+</sup> also exhibit a decrease in intensity of the band at 3610 cm<sup>-1</sup>. Unlike the spectra of BEA-NH<sub>4</sub><sup>+</sup> and BEA-1IE(Al)-NH<sub>4</sub><sup>+</sup>, the intensity of the band at 3736 cm<sup>-1</sup> of internal silanols increases in intensity in BEA(deAl)-1IE(Al)-NH<sub>4</sub><sup>+</sup> and BEA(deAl)-5IE(Al)-NH<sub>4</sub><sup>+</sup> samples. The micropore structure of zeolite can explain the increase in the intensity of the 3736 cm<sup>-1</sup> band. As the nitrates (of ammonium nitrate solution used for NH<sub>4</sub><sup>+</sup>-IE) have a slightly acidic nature, it might well be that the acidity of nitrates has enhanced the micro-porosity of zeolites by accessing more internal silanols. This observation also aligns with the changes in the total pore volumes of these BEA samples (**Table E2**).

Pyridine base is used as a probe molecule for quantification of acid sites. The FTIR difference spectra for H<sup>+</sup> and NH<sub>4</sub><sup>+</sup> forms of BEA zeolites in the pyridine stretching region are presented in **Figures 8.5b and 8.5b'**. All spectra (except that of BEA(deAl)-H<sup>+</sup>) exhibit five distinct bands. The feature at 1490 cm<sup>-1</sup> is a structure-insensitive band. The bands at 1455 cm<sup>-1</sup> and 1621 cm<sup>-1</sup> represent pyridine bound to LAS, and those at 1545 cm<sup>-1</sup> and 1634 cm<sup>-1</sup> correspond to pyridine interacting with BAS<sup>49, 220</sup>. Of all the protonic zeolites (**Figure 8.4a**), the intensity of LAS bands is maximum in the spectrum of BEA-1IE(Al)-H<sup>+</sup> and minimum in that of BEA(deAl)-1IE(Al)-H<sup>+</sup>. Similarly, the intensity of BAS bands is maximum for BEA-H<sup>+</sup> and minimum for BEA(deAl)-1IE(Al)-H<sup>+</sup>. However, the spectrum of BEA(deAl)-H<sup>+</sup> does not show any bands responsible for BAS and LAS bands. The intensity of BAS bands increases, and that of LAS decreases in the spectra of NH<sub>4</sub><sup>+</sup> forms of parent, aluminated and realuminated samples.

The concentrations of LAS and BAS quantified using the bands at 1445 and 1545 cm<sup>-1</sup>, respectively<sup>221</sup>, are presented in **Table 8.4**. The dealuminated BEA(deAl)-H<sup>+</sup> comprises only 0.02 mmolg<sup>-1</sup> of LAS and no BAS. The concentration of LAS is 0.17, 0.20, 0.11, and 0.14 mmolg<sup>-1</sup> for BEA-H<sup>+</sup>, BEA-1IE(Al)-H<sup>+</sup>, BEA(deAl)-1IE(Al)-H<sup>+</sup> and BEA(deAl)-5IE(Al)-H<sup>+</sup> respectively. The respective NH<sub>4</sub><sup>+</sup> forms of these samples have LAS concentrations of 0.16, 0.17, 0.12, and 0.13 mmolg<sup>-1</sup>. Similarly, the concentration of BAS in BEA-H<sup>+</sup>, BEA-1IE(Al)-

$\text{H}^+$ , BEA(deAl)-1IE(Al)- $\text{H}^+$  and BEA(deAl)-5IE(Al)- $\text{H}^+$  is 0.16, 0.15, 0.13, and 0.11  $\text{mmolg}^{-1}$  respectively. The respective  $\text{NH}_4^+$  forms of these samples have BAS concentrations of 0.23, 0.17, 0.08, and 0.09  $\text{mmolg}^{-1}$ , respectively (**Table 8.4**). The comparison of these concentrations in **Figure 8.5c** shows that dealumination-realumination treatments can only recover 50% of BAS accessed by pyridine. In contrast, more than 80% of LAS are regenerated that were reached by pyridine. Upon ammonium-exchange, the concentration of LAS decreases with an increase in the concentration of LAS, the effect being more prominent in parent and aluminated BEA. However, the decrease in LAS content in BEA- $\text{NH}_4^+$ , BEA-1IE(Al)- $\text{NH}_4^+$ , and BEA(deAl)-1IE(Al)- $\text{NH}_4^+$  does not correlate to the decrease in the content of BAS in these samples (**Figure 8.5c**).

As a strong base, pyridine probes the acid sites without differentiating between them in terms of their strength, whereas some sites are sterically inaccessible. We also employed carbon monoxide to probe the acid sites, as it is smaller and has acidic strength weaker than pyridine. Therefore it gives additional advantages of differentiating among the acid sites, depending on their strength <sup>72</sup>. **Figure 8.6a** presents the FTIR spectra of absorbed carbon monoxide over for  $\text{H}^+$  and  $\text{NH}_4^+$  forms of all BEA zeolites at low temperatures (100 K). The LAS bound to carbon monoxide shows characteristic bands at 2241, 2230, 2207, and 2195  $\text{cm}^{-1}$ . These bands correspond to very strong LAS ( $\text{LAS}_{\text{V.S}}$ ), strong LAS ( $\text{LAS}_{\text{S}}$ ), medium LAS ( $\text{LAS}_{\text{M}}$ ), and weak LAS ( $\text{LAS}_{\text{W}}$ ), respectively. The bands at 2177 and 2157  $\text{cm}^{-1}$  ascribe to the interaction of carbon monoxide with BAS and silanols, respectively <sup>77, 80</sup>, whereas the rest of the bands below 2180  $\text{cm}^{-1}$  are due to physisorbed carbon monoxide (**Figure 8.6**). The initial doses of carbon monoxide interact with  $\text{LAS}_{\text{V.S}}$  and successively,  $\text{LAS}_{\text{S}}$ ,  $\text{LAS}_{\text{M}}$ , and  $\text{LAS}_{\text{W}}$ ) thus differentiating between them based on their strength. Further amounts of carbon monoxide probe the BAS (2177  $\text{cm}^{-1}$ ) and silanols (2157  $\text{cm}^{-1}$ ).

The relative proportion of BAS and LAS, calculated from the area of deconvoluted peaks, are given in **Table 8.4** and compared in **Figure 8.6b**. Parent BEA- $\text{H}^+$  has all four types of LAS ( $\text{LAS}_{\text{V.S}}$ ,  $\text{LAS}_{\text{S}}$ ,  $\text{LAS}_{\text{M}}$ , and  $\text{LAS}_{\text{W}}$ ), whereas BEA(deAl)- $\text{H}^+$  does not possess any LAS (in line with Py-FTIR analysis). Aluminated BEA- $\text{H}^+$  and realuminations of BEA(deAl)- $\text{H}^+$  significantly increase the intensity of the bands due to  $\text{LAS}_{\text{S}}$  and  $\text{LAS}_{\text{M}}$ . The  $\text{LAS}_{\text{V.S}}$  and  $\text{LAS}_{\text{W}}$  cannot be regenerated upon realumination of BEA(deAl)- $\text{H}^+$  (**Figure 8.6a,b**, and **Table 8.4**). Furthermore, the least intense band of  $\text{LAS}_{\text{W}}$  in the spectrum of BEA- $\text{H}^+$  no more exists after

aluminum. After  $\text{NH}_4^+$ -IE, the bands corresponding to  $\text{LAS}_{\text{V,S}}$  and  $\text{LAS}_{\text{W}}$  disappear, demonstrating the coordination of ammonium cations to the corresponding aluminum LAS.

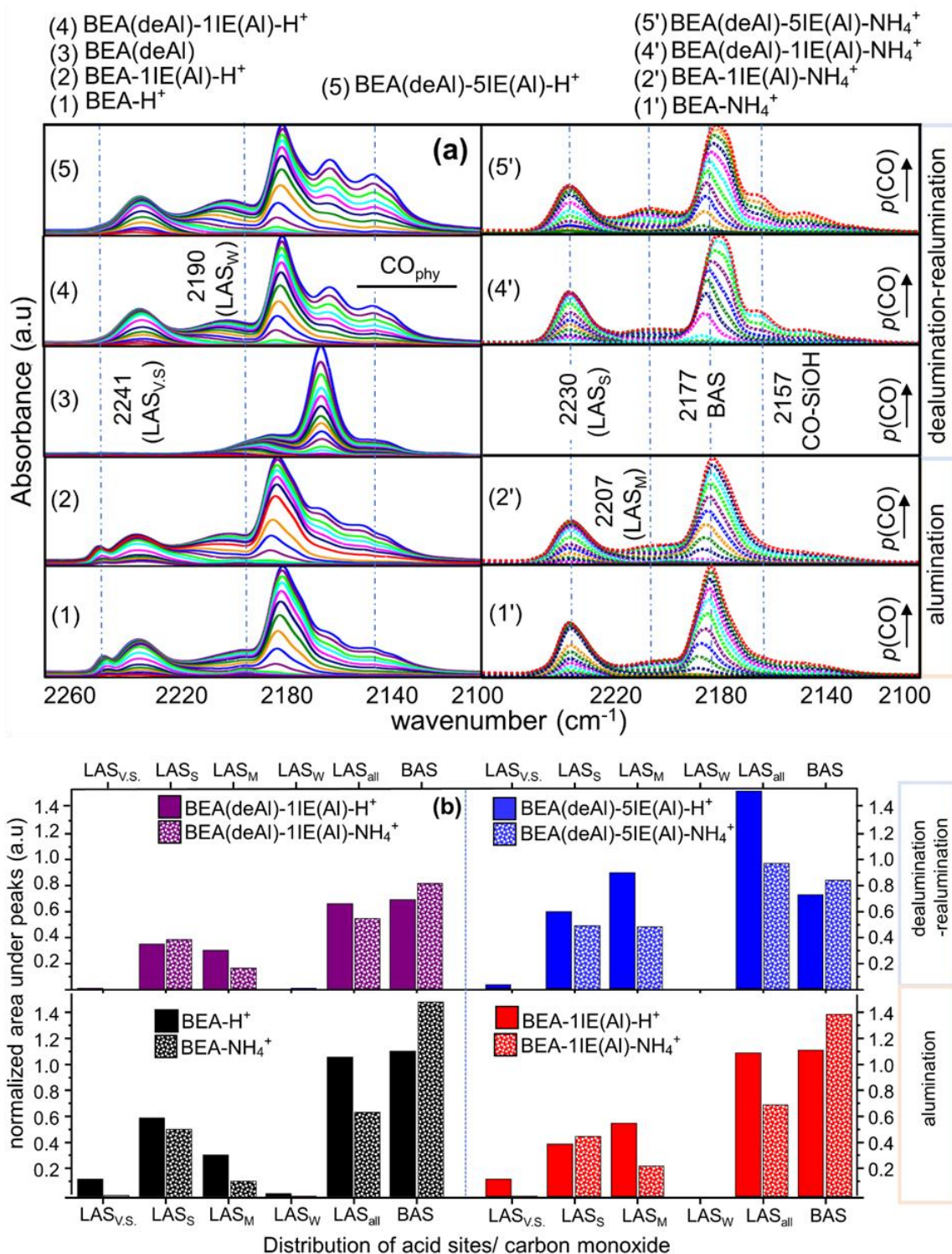


Figure 8.6: (a) FTIR difference spectra over adsorbed carbon monoxide in the carbon monoxide stretching region obtained by subtraction of spectra of cold wafers at 70 K from spectra after CO adsorption at 70K carbon monoxide; The spectra of  $\text{H}^+$  form of samples are marked as 1-5

and those of  $\text{NH}_4^+$  forms are marked as 1'-5' (b) distribution of acid sites accessed by carbon monoxide in  $\text{H}^+$  form and  $\text{NH}_4^+$  form of samples.

The content of LAS probed by carbon monoxide appears to be maximum for BEA(deAl)-5IE(Al)- $\text{H}^+$ . This disagrees with the quantitative FTIR results of adsorbed pyridine but aligns with the aluminum distribution obtained by  $^{27}\text{Al}$  NMR quantification. The samples BEA(deAl)-1IE(Al)- $\text{H}^+$  and BEA(deAl)-5IE(Al)- $\text{H}^+$  have the least (yet comparable) content of BAS. The drop in the content of LAS upon  $\text{NH}_4^+$ -IE does follow the increase in BAS, but not quantitatively. We have previously shown that the increase in the content of LAS, probed by carbon monoxide in aluminum-exchanged FAU, is not as significant as in the case of Py-FTIR<sup>180</sup>. The carbon monoxide interacts with Lewis acid sites mostly electrostatically, which justifies weak strength of interaction, and hence, predominantly strong acid sites are probed. As the Al-IE procedure produces charge-neutral LAS, carbon monoxide does not probe all the incorporated EFAl species. It was also proposed that some of the LAS can also be inaccessible for carbon monoxide, depending on the location of LAS<sup>180</sup>. The increase in LAS content during aluminations and multiple realuminations does not decrease the content of BAS, which is in line with Py-FTIR analysis. These results show that the maximum number of LAS are produced in BEA(deAl)-5IE(Al)- $\text{H}^+$ , which were not fully accessed by pyridine (**Figure 8.6a, 8.6b and Table 8.4**).

**Figure 8.7** shows a quantitative correlation of the MPV reduction rate with the total Lewis acid sites accessed by pyridine and carbon monoxide and the concentration of FA-Al and EFAl obtained by  $^{27}\text{Al}$  MAS NMR. The detailed analysis of geometric coordination and Lewis acidity of aluminum species in  $\text{H}^+$  and  $\text{NH}_4^+$  forms of BEA sheds light on the distribution of aluminum Lewis acid sites as a function of aluminations, dealuminations, and realuminations. Similarly, employing pyridine and carbon monoxide not only considers the differences due to accessibility limitations but also unveils the varying strengths of LAS produced under different treatments. Before aluminations, parent BEA had both FA-Al and EFAl centers, with FA-Al concentration far more significant than EFAl, responsible for Lewis acidic signatures in pyridine- and carbon monoxide-probed FTIR spectra. Many previous findings have proposed that the FA-Al species, coordinated to three framework oxygens and an OH group, are the only active sites in the MPVO-type reactions, whereas EFAl species, despite being Lewis acidic, do not participate<sup>66, 106, 257, 258</sup>. Herein, our findings do not support these proposals as aluminations enhance the Lewis acidity and MPV catalytic activity by only increasing the concentration of EFAl species.



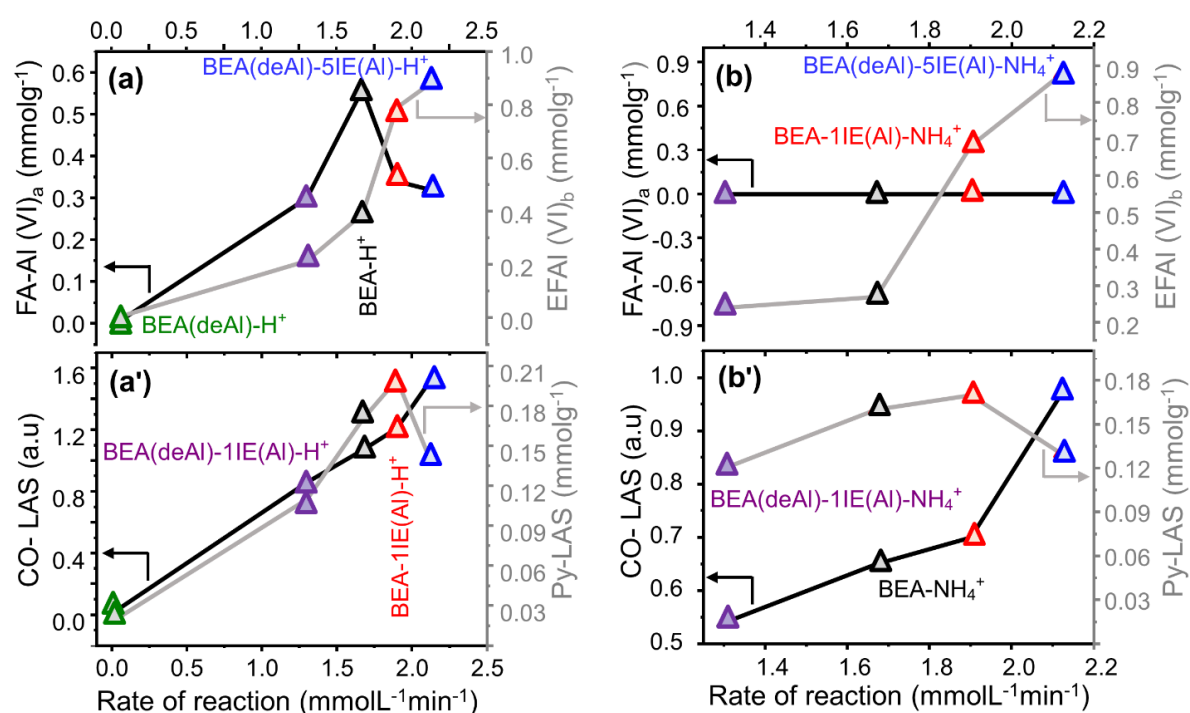


Figure 8.7: The total concentration of octahedral aluminum in H<sup>+</sup> (a) NH<sub>4</sub><sup>+</sup> form (b) of samples plotted as a function of the initial rate of MPV reaction (for 200 mg for catalyst); FA-Al: left axis and EFAl: right axis. Total LAS content of samples in H<sup>+</sup> (a') and NH<sub>4</sub><sup>+</sup> form (b') of samples plotted as a function of the initial rate of MPV reaction (for 200 mg for catalyst); Py-FTIR: left axis and CO-FTIR: right axis.

The disappearance of FA-Al and EFAl of BEA-H<sup>+</sup> after dealumination, followed by a large increase in Si/Al ratio, is in-line with a negligible concentration of Lewis acid sites and associated inactivity in MPV reaction. After the first realumination, a significant contribution to Lewis acidity comes from FA-Al, with their concentration twice that of EFAl. The sum of FA-Al and EFAl species after first realumination, almost half that of BEA before dealumination, is in good agreement with lower Lewis acidity and activity compared to parent and/or aluminated BEA. The maximum drop in Si/Al ratio due to five realuminations of a dealuminated BEA is followed by a maximum concentration of EFAl and the highest catalytic activity in the MPV reaction. However, the LAS quantified by pyridine, lower than those of parent and aluminated BEA, do not correlate to the catalytic activity, aluminum distribution, and the LAS probed by carbon monoxide. Carbon monoxide, in-line with elemental analysis, NMR, and catalytic activity, accesses the maximum content of LAS after five realuminations. Thus, the Py-FTIR results signify the effect of accessibility limitations due to the size of the pyridine molecule.

Notably, the FA-Al and EFAl centers of parent BEA upon interaction with carbon monoxide, are divided into LAS of four different acidic strengths. However, aluminations and realuminations preferably and efficiently increase the strong and medium strength LAS (Figure 6). The increase in EFAl content and aluminum LAS during aluminations and multiple realuminations of BEA does not occur at the expense of BAS. Therefore, the EFAl generated during these treatments exists as charge-neutral oxide and/or hydroxide clusters<sup>180</sup>. The increase in MPV catalytic activity and Lewis acidity with an increase in the concentration of EFAl during aluminations and multiple realuminations proposes that FA-Al is not the sole active site for the MPV hydride transfer mechanism. Instead, both FA-Al and EFAl act as sites for the reduction of ketone. No significant change in selectivity towards *cis*-product for parent, aluminated, and multiple realuminated BEA further supports our findings. Our findings suggest that (1) FA-Al species are the foremost MPV active sites in parent BEA due to their high concentration formed during post-synthetic treatments, explained by the defective framework.<sup>103, 105, 229</sup> (2) EFAl also serve as active sites and preferable tuning of EFAl LAS efficiently improves the activity of BEA without affecting the stereoselectivity to produce commercially viable *ci*-alcohol.

## 8.4. Conclusions

The Lewis acidity of BEA zeolite was modulated via aluminations and dealuminations-realuminations routes, wherein a facile aluminum-exchange was used for aluminations and realuminations treatments. XRD and N<sub>2</sub> physisorption confirm the preservation of the structure and porosity of BEA zeolite after these treatments. The inherent Lewis acidity of parent BEA and associated catalytic activity in MPV reaction is mainly due to FA-Al and partly due to EFAl. Aluminations of BEA increase the catalytic activity that quantitatively correlates to an increase in the number of LAS from FTIR and EFAl from <sup>27</sup>Al NMR. In contrast, the content of FA-Al species does not increase. Dealumination results in the removal of ~90% of aluminum, with a corresponding decrease in Lewis acidity and catalytic activity. The first realumination enhances the catalytic activity and Lewis acidity, primarily due to FA-Al species, whereas the concentration of FA-Al is very small. Further realuminations result in the maximum catalytic activity of zeolite BEA without affecting the selectivity towards *cis* 4-*tert* butylcyclohexanone. The catalytic activity is associated with increased LAS due to the incorporation of EFAl, whereas the content of FA-Al does not change. Thus, both FA-Al and EFAl can act as active sites for the MPV hydride transfer mechanism. The increase in EFAl content and LAS, during aluminations and multiple realuminations of BEA, does not occur at the expense of BAS.

## **Chapter 9**

### **Revisiting the “Very High Frequency” hydroxyls in zeolites**

#### **Contributions**

The synthesis and NMR characterization of materials was performed by the author the thesis

## 9.1. Introduction

The aluminosilicate zeolites are composed of silica and alumina tetrahedra interconnected through the bridged oxygen atoms forming a uniform pore system in zeolites<sup>10,11</sup>. The presence of acidic hydroxyl groups within the pores plays a crucial role in their catalytic activity<sup>12</sup>. Generally, four types of hydroxyl groups may exist in zeolites as follows 1) bridging hydroxyls that connect framework silica and alumina tetrahedra and are acidic (2) terminal, nonacidic hydroxyls present on the outer surface of zeolite (3) hydroxyls attached with extra-framework aluminum species and considered to be acidic and (4) hydroxyls attached to Si atoms in defects sites, termed as silanol defects. The former two types of hydroxyls exist in a defect-free zeolite, whereas the latter two types of hydroxyls may form during the synthesis of a zeolite or post-synthesis treatments, such as high-temperature calcination, acid/base leaching, and steaming<sup>133-135</sup>. **Figure 9.1a** presents a typical FTIR spectrum of zeolite Y in the region of hydroxyl stretching vibration.

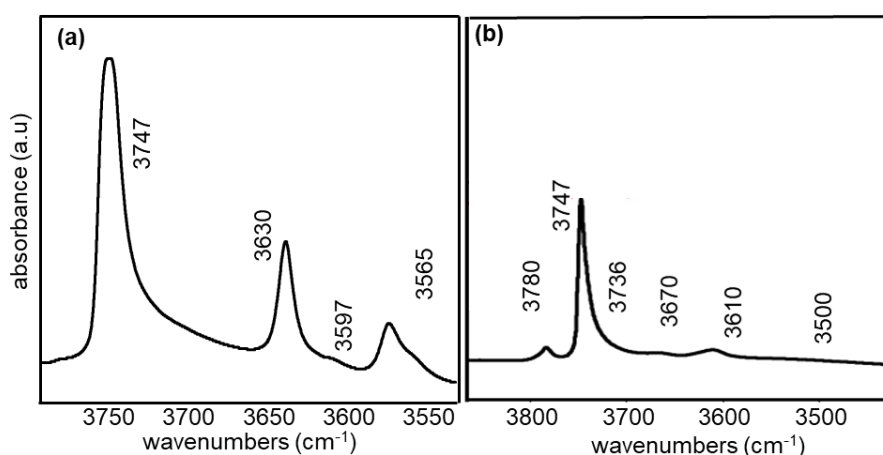


Figure 9.1. Typical FTIR spectra in the hydroxyl stretching region of evacuated (a) zeolite Y (b) zeolite beta.

The four distinct bands at  $3747\text{ cm}^{-1}$ ,  $3630\text{ cm}^{-1}$ ,  $3565\text{ cm}^{-1}$ , and  $3597\text{ cm}^{-1}$  correspond to terminal Si-OH, low-frequency bridging silanols, high-frequency bridging silanols, and the hydroxyls on the EF entities and the interaction of the silanols with the EF species, respectively<sup>77-79</sup>. However, hydroxyl groups lead to a complex infrared pattern in zeolite beta (**Figure 9.1b**). The position of the  $3747\text{ cm}^{-1}$  band is similar in zeolite BEA and Y, whereas  $3736\text{ cm}^{-1}$  is due to internal silanols in BEA. The band at  $3500\text{ cm}^{-1}$  in the spectrum of zeolite BEA is due to the same type of hydroxyls showing bands at  $3597\text{ cm}^{-1}$  in the spectrum of zeolite Y. BEA has only one type of bridging hydroxyls at  $3610\text{ cm}^{-1}$ , whereas the band at  $3670\text{ cm}^{-1}$  is due to hydroxyls of Al-OH species in BEA<sup>233, 235, 237, 242, 243</sup>. Moreover, protonic BEA zeolite, calcined at high

temperatures or steam treated at mild temperatures, exhibits a hydroxyl band with a characteristic vibration at  $\sim 3780\text{ cm}^{-1}$  of the infrared region. As the frequency of this band is very high for zeolites, it was designated as the ‘very high frequency’ (VHF) OH<sup>243</sup>. This low-intensity band, not present in Si-BEA, thus, is associated with the hydroxyls attached to aluminum species (**Figure 9.2**)<sup>267</sup>.

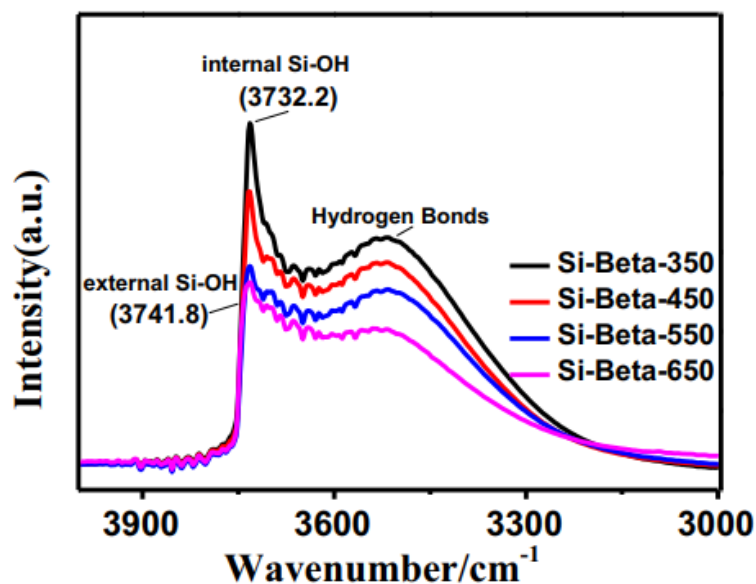


Figure 9.2. FTIR spectra in the hydroxyl stretching region of Si-Beta. Reproduced with permission from Ref<sup>267</sup>.

Besides BEA, this band was also reported in the FTIR spectra of ZSM5 zeolite after no post-synthetic treatment, alkaline treatment, and steam treatment<sup>268</sup> (**Figure 9.3**). Similarly, zeolite MOR was reported to exhibit the broad-shaped VHF band<sup>269</sup> (**Figure 9.4**). This VHF band was previously assigned in many ways to various aluminum-containing species, such as AlOOH or AlOH moieties of transient species leaving the framework<sup>81, 243, 259</sup>. Some researchers associate this band with extra-lattice aluminum species in ZSM-5<sup>241</sup>, while others associate this band to EFAl appearing in an octahedral environment in <sup>27</sup>Al NMR of BEA zeolite<sup>242</sup> or tri-coordinated aluminum<sup>268</sup> connected to the BEA framework<sup>243</sup>. In the case of MOR, this band was observed, but no assignment was given to this band<sup>269</sup>.

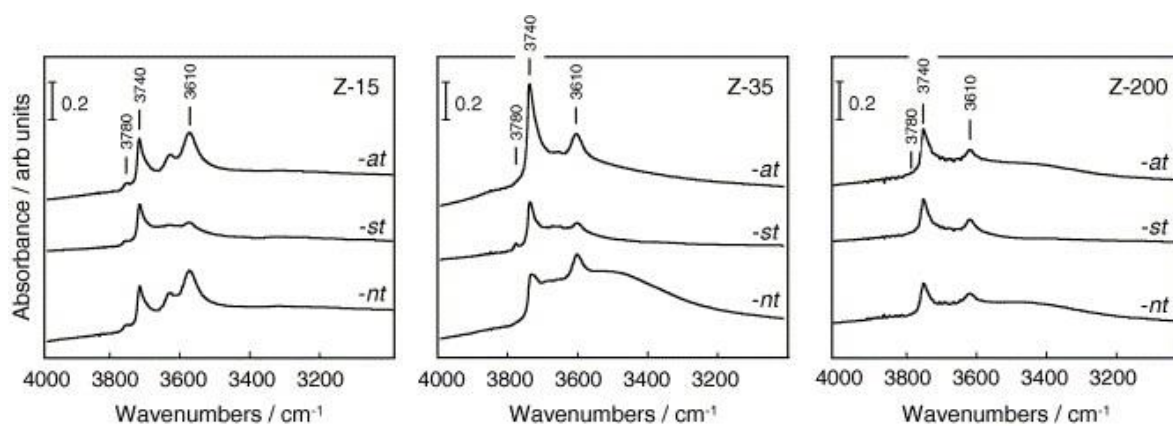


Figure 9.3: FTIR spectra in OH-stretching region of ZSM5-15, ZSM5-35, and ZSM5-200 upon no treatment (-nt), steam treatment (-st), and alkaline treatment (-at) Spectra were recorded in He at 473 K. Reproduced with permission from Ref <sup>268</sup>.

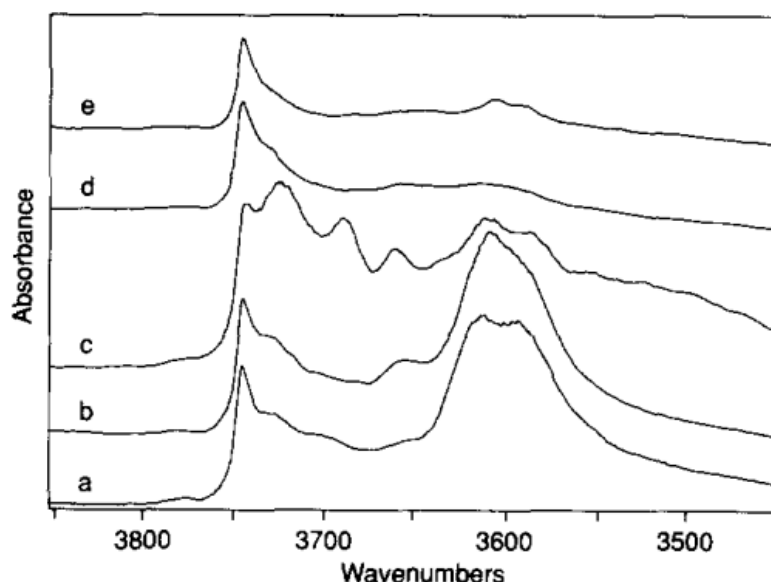


Figure 9.4: Infrared spectra (hydroxyl region): (a) NH<sub>4</sub>-MOR, (b) H-MOR (500), (c) H-MOR (HC1), (d) H-MOR (735), (e) H-MOR (steam). Reproduced with permission from Ref <sup>269</sup>.

Some researchers attribute this band to highly acidic character <sup>66</sup>, while others regard it as non-acidic <sup>270,271</sup>. Later, it was shown that the VHF absorption shifts upon interaction with adsorbed basic molecules; this band has been proposed to be acidic <sup>259</sup>. Samples possessing this type of hydroxyl bands were proposed to have enhanced catalytic activity <sup>66,259</sup>. While this is mostly associated with Lewis acid sites <sup>81,243,259</sup>, there are reports where this band has been assigned to weakly acidic Brønsted acid sites <sup>272</sup>. From infrared studies with the aid of adsorbed bases, it was concluded that this OH is less acidic than a bridging OH <sup>259</sup>.

As explained in **Chapter 8**, zeolite BEA, in its protonic form contains both FA-Al and EFAl species which are formed as a result of post-synthetic treatments<sup>66, 81, 259</sup>. As zeolite BEA demonstrates very high activity in the Lewis acid-catalyzed Meerwein–Ponndorf–Verley reduction<sup>81, 100, 103</sup>, the FA-Al species (coordinated to three framework oxygens and an OH group) have widely been proposed as the active site in the MPV reaction<sup>66, 106, 257, 258</sup>. The activity of BEA zeolite was shown to increase with the increase in temperature; therefore, it was concluded that Lewis acidic Al-sites are the active species<sup>106</sup>. Most importantly, it was proposed that MPV reaction in BEA occurs on the partially hydrolyzed aluminum species that are still attached to the framework, and the VHF hydroxyl groups at  $\sim 3780\text{ cm}^{-1}$  were suggested to be attached with these partially hydrolyzed species<sup>81</sup>. Thus, many publications describe the VHF hydroxyls connected to “partly” framework Al exhibiting strong Lewis properties<sup>81, 106, 243, 273</sup>. Due to the presence of this band in the protonic BEA and consequent disappearance in ammonium forms, VHF has been previously associated with hydroxyls attached to very strong FA-Al species<sup>81, 243, 259</sup>. Even though the VHF hydroxyl band is observed in MOR zeolite<sup>269</sup>, it was proposed that the zeolite Y and MOR do not show any activity in the MPV reaction because it does not have this type of catalytically active aluminum species<sup>106, 274</sup>. Furthermore, extra-framework aluminum sites (EFAl), which are entirely dislocated from the framework, were proposed to be catalytically inactive in the MPV reaction of BEA<sup>161</sup>.

However, the work presented in **Chapter 8** confirms that the activity of zeolite BEA linearly correlates with an increase in EFAl LAS. The samples with lower concentrations of FA-Al and a significantly higher proportion of EFAl show enhanced activity as compared to those having similar content of FA-Al but lower content of EFAl or lower content of EFAl and higher of FA-Al. The assignment of VHF hydroxyls to the active site of the MPV reaction becomes ambiguous as the samples with the negligible intensity of VHF were found to be more active than those with higher intensities (**Chapter 8**). Thus, there are many discrepancies in the literature related to the assignment of these hydroxyl species. FTIR spectroscopy is usually applied to probe the acidity of species employing different bases like pyridine, ammonia, carbon monoxide, carbon dioxide, acetonitrile<sup>275-278</sup>, etc., and many bases, including pyridine carbon dioxide Pyridine, is among the most widely used probe molecules to differentiate and quantify BAS and LAS. However, due to its high basicity, it equally probes the acid sites of variable strength, and, at times, it cannot access some of the acid sites in the smaller zeolite channels because of its bulkiness<sup>49, 69, 71, 238</sup>. In comparison, weaker bases interact with the acidic center by electrostatic forces, which do not lead to proton detachment but hydrogen bond formation.

Thus, using small molecules of weak strength like carbon monoxide and nitrogen can aid the differentiation based on the strength of the acid sites <sup>72-76</sup>.

The literature assignment of VHF hydroxyls to strongly active Lewis acidic species is mostly based on employing pyridine as the probe molecule. <sup>268, 269, 279, 280</sup>. Due to the annihilation of many hydroxyl bands, including VHF OH groups, after adsorption of pyridine accompanied by Lewis acidic bands in the pyridine ring deformation region, these hydroxyls are associated with strong acidity <sup>106, 274, 281</sup>. Thus, as discussed above, many researchers have tried to assign this band. However, the exact assignment of this band and the structure of aluminum species associated with this band still needs to be clarified and remains a matter of discussion. Different probes other than pyridine (mentioned above) are also used for the acidity measurements. However, the literature still needs the simultaneous analysis of the FTIR spectra in the hydroxyl region without the adsorption of the base and with the loadings of the adsorbed base. The systematic comparison of the base stretching region at different conditions and using different bases of fairly different sizes and strengths is also unavailable. Furthermore, combining the information from FTIR spectroscopy with other spectroscopic tools under conditions similar to FTIR can also give some parallels about the structure evaluation.

Therefore, this chapter aims to systematically explore the evolution of VHF in hydroxyl and base stretching regions under different conditions. For this, we utilize the samples used in **Chapter 8** with different cation forms of parent and aluminum-exchanged BEA. The FTIR spectroscopy with and without probe carbon monoxide and pyridine were examined simultaneously in addition to that <sup>27</sup>Al-<sup>1</sup>H HETCOR NMR spectroscopy on evacuated zeolites to accept or rule out the possible structures and coordination of aluminum species associated with VHF hydroxyls. This work describes that the VHF-OH band of BEA, at  $\sim 3780\text{ cm}^{-1}$  in the hydroxyl region, correlates neither to the strongly acidic FA-Al species nor to the EFAl species generated by aluminum-exchange. Instead, this is a weakly acidic band associated with gamma alumina-type octahedral aluminum and possibly weakly acidic FA-Al LAS.

## 9.2. Materials and Methods

**Table 9.1** lists the nomenclature of the samples used in this work. Further details on the material preparation and chemical used are listed in **Section 8.2**.



Table 9.1: List of parent and modified BEA samples with the respective treatment conditions

Sample ID	Treatment conditions
BEA-H <sup>+</sup>	1x calcination of zeolite Beta (CP814E*) in static air
BEA-NH <sub>4</sub> <sup>+</sup>	2x ammonium-exchange of BEA-H <sup>+</sup>
BEA-1IE(Al)-H <sup>+</sup>	1x Al-IE of BEA-H <sup>+</sup> followed by calcination in static air
BEA-1IE(Al)-NH <sub>4</sub> <sup>+</sup>	2x ammonium-exchange of BEA-1IE(Al)-H <sup>+</sup>
BEA(deAl)-H <sup>+</sup>	1x dealumination of BEA-H <sup>+</sup> , followed by calcination in static air
BEA(deAl)-1IE(Al)-H <sup>+</sup>	1x Al-IE of BEA(deAl)-H <sup>+</sup> followed by calcination in static air
BEA(deAl)-1IE(Al)-NH <sub>4</sub> <sup>+</sup>	2x ammonium-exchange of BEA(deAl)-1IE(Al)-H <sup>+</sup>
BEA(deAl)-5IE(Al)-H <sup>+</sup>	5x Al-IE of BEA(deAl)-H <sup>+</sup> followed by calcination in static air
BEA(deAl)-5IE(Al)-NH <sub>4</sub> <sup>+</sup>	2x ammonium-exchange of BEA(deAl)-5IE(Al)-H <sup>+</sup>

**Material Characterization:** Fourier Transform infrared (FTIR) spectra of zeolite samples using pyridine and carbon monoxide as probe molecules were recorded using a Thermo Nicolet iS50 FTIR spectrometer having a DTGS detector (**Section 3.2.1**). All the FTIR spectra presented here were normalized to the weight and area of the sample discs. <sup>27</sup>Al-<sup>1</sup>H HETCOR NMR spectra were recorded using a Bruker 700MHz Ultra-Shield spectrometer using a 1.3 mm MAS probe at a 40 kHz spinning speed. Prior to measurements, samples were evacuated overnight under a high vacuum at 673K. The reactor containing the samples under vacuum was sealed and brought to the glove box. The samples were packed on evacuated rotors in the glove box under an inert atmosphere. To avoid moisture, the packed rotors were placed in an air-tight vial filled with inert gas and brought to the spectrometer.

### 9.3. Results and Discussion

The ‘VHF’ band at 3780 cm<sup>-1</sup> is present in the parent proton form of evacuated BEA, as shown by the FTIR spectra in the hydroxyl stretching region (**Figures 8.5a and 8.5a’**). The disappearance of this band upon dealumination confirms that these hydroxyls are linked to some acidic aluminum species.

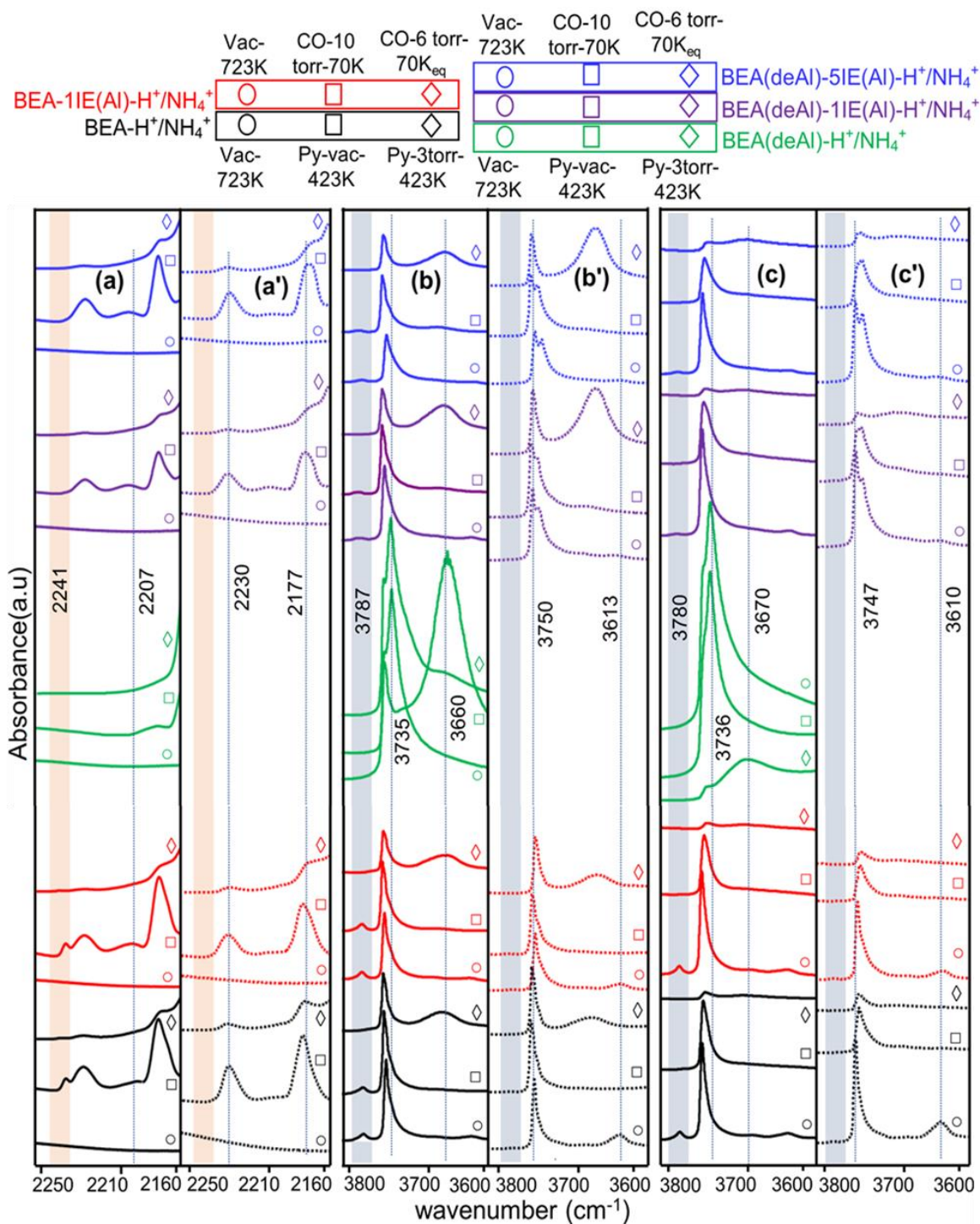


Figure 9.5. CO-FTIR spectra of (a)  $H^+$  and (a')  $NH_4^+$  form of samples in carbon monoxide stretching region; CO-FTIR spectra of (b)  $H^+$  and (b')  $NH_4^+$  of samples in hydroxyl stretching region; (b); Py-FTIR spectra of (c)  $H^+$  and (c')  $NH_4^+$  of samples in hydroxyl stretching region. Orange and grey regions guide the eye to the  $2241\text{ cm}^{-1}$  band of LAS and the  $3780\text{ cm}^{-1}$  band in hydroxyl stretching regimes.

As discussed in **Section 8.3**, the LAS bound to carbon monoxide shows characteristic bands at  $2241$ ,  $2230$ ,  $2207$ , and  $2195\text{ cm}^{-1}$  in the FTIR spectra of absorbed carbon monoxide. Corresponding to very strong LAS ( $LAS_{v,s}$ ), strong LAS ( $LAS_s$ ), medium LAS ( $LAS_M$ ), and

weak LAS (LAS<sub>w</sub>), respectively. In comparison, pyridine-bound LAS appear at 1455 cm<sup>-1</sup> and 1621 cm<sup>-1</sup> <sup>49, 220</sup> Due to the presence of a VHF band in the protonic BEA and consequent disappearance in ammonium forms, this band has been previously associated with hydroxyls attached to very strong FA-Al species <sup>81, 243, 259</sup>. **Figure 9.5a** shows that the strongest LAS probed by CO-FTIR appear at 2241 cm<sup>-1</sup> (LAS<sub>v,s</sub>). To ascribe ‘VHF’ hydroxyls to any LAS, the simultaneous and deeper analysis of the evolution of the ‘VHF’ band, LAS<sub>v,s</sub> band, and other Lewis acidic features under different conditions is essential. As the literature stills lack this comparison, we present in **Figure 9.5a** (orange regions) the CO-FTIR spectra in the carbon monoxide stretching region of protonic and ammonium forms of BEA samples under different conditions. These spectra are compared with the evolution of the ‘VHF’ band in the hydroxyl stretching region of respective Py-FTIR and CO-FTIR spectra (grey areas). The features of interest are listed in **Table 9.1**, whereas the pyridine stretching region is not compared as pyridine probes all acid sites equally.

The FTIR spectra of in H<sup>+</sup> and NH<sub>4</sub><sup>+</sup> form of parent BEA, evacuated at 723K, present no observable features in the CO-stretching region (**Figures 9.5a and 9.5a'**, black spectra with ○ symbol). However, apart from other typical hydroxyl bands, the OH-stretching region in BEA-H<sup>+</sup> reveals the band at 3780 cm<sup>-1</sup>, and the latter disappears upon NH<sub>4</sub><sup>+</sup>-IE (**Figures 9.5b and 9.5b'**, black spectra with ○ symbol). This suggests that the structure responsible for the 3780 cm<sup>-1</sup> band is moisture sensitive and appears only under high vacuum and temperature conditions when most waters of hydration are removed. Additionally, changing the cationic form of zeolite from H<sup>+</sup> to NH<sub>4</sub><sup>+</sup> annihilates these hydroxyls; thus, the NH<sub>4</sub><sup>+</sup> forms of all BEA samples do not show the ‘VHF’ band under any conditions.

Introducing 10 torrs of carbon monoxide at 70K probes all the LAS<sub>v,s</sub> and most of the LAS<sub>s</sub> and LAS<sub>M</sub> in BEA- H<sup>+</sup>. On the contrary, these carbon monoxide doses do not affect the ‘VHF’ band. However, introducing 3 torrs of pyridine at 423K results in the complete disappearance of the ‘VHF’ band. The BEA-NH<sub>4</sub><sup>+</sup> sample does not exhibit LAS<sub>v,s</sub> (2241 cm<sup>-1</sup>) after exposure to 10 torr of carbon monoxide at 70K (**Figures 9.5a-c'**, black spectra with □ symbol). Furthermore, only the equilibrium doses of carbon monoxide interact with and annihilate the ‘VHF’ band of BEA-H<sup>+</sup>, whereas these doses hardly probe LAS. Similar observations hold in the case of aluminated BEA, i.e., BEA-1IE(Al)-H<sup>+</sup> (**Figures 9.5a-c'**, red spectra). Dealumination results in the disappearance of all aluminum bands in the hydroxyl and carbon monoxide stretching region (**Figures 9.5a-c'**, green spectra). The spectra of H<sup>+</sup> forms of

realuminated samples show a ‘VHF’ band with very little intensity, whereas LAS<sub>v,s</sub> does not exist in these spectra.

Table 9.1: Assignment of 3780 cm<sup>-1</sup> band; summary of NMR and FTIR features of BEA zeolites during different treatment and measurement conditions. <sup>a</sup>P (parent BEA) <sup>b</sup>alu (alumination) <sup>c</sup>dealu (dealumination), <sup>d</sup>realu (realumination).

Distinct features (NMR & FTIR)	Conditions	<sup>a</sup> P	<sup>a</sup> alu	<sup>b</sup> dealu	<sup>c</sup> realu
		H <sup>+</sup> / NH <sub>4</sub> <sup>+</sup>	H <sup>+</sup> / NH <sub>4</sub> <sup>+</sup>	H <sup>+</sup> / NH <sub>4</sub> <sup>+</sup>	H <sup>+</sup> / NH <sub>4</sub> <sup>+</sup>
3780 cm <sup>-1</sup> Py-FTIR	vacuum, 723K	✓ / X	✓ / X	X / -	X / X
	3torr-423K	X / X	X / X	X / -	X / X
	3torr-423K <sub>eq</sub>	X / X	X / X	X / -	X / X
1445 cm <sup>-1</sup> Py-FTIR	vacuum, 723K	X / X	X / X	X / -	X / X
	3torr-423K	✓ / ✓	✓ / ✓	X / -	✓ / ✓
	3torr-423K <sub>eq</sub>	✓ / ✓	✓ / ✓	X / -	✓ / ✓
3787 cm <sup>-1</sup> CO-FTIR	vacuum, 723K	✓ / X	✓ / X	X / -	* ✓ / X
	10torr-70K	✓ / X	✓ / X	X / -	* ✓ / X
	5.5torr-70K <sub>eq</sub>	X / X	X / X	X / -	X / X
2241 cm <sup>-1</sup> CO-FTIR	vacuum, 723K	X / X	X / X	X / -	X / X
	10torr-70K	✓ / X	✓ / X	X / -	* ✓ / X
	5.5torr-70K <sub>eq</sub>	X / X	X / X	X / -	X / X
0.8 ppm <sup>1</sup> H NMR	vacuum, 673K	✓ / X	✓ / X	-	X / X
21 ppm <sup>27</sup> Al NMR		✓ / X	✓ / X	-	X / X

These observations ascribe that the ‘VHF’ hydroxyls are weakly acidic structures that interact with carbon monoxide only at very high doses. As a strong base, pyridine does not have any differential interaction with accessible sites but probes all of them equally. Therefore, the ‘VHF’ band disappears at 3 torr of pyridine at 423K. Furthermore, the intactness of the ‘VHF’ band under the conditions when all CO-LAS bands disappear corresponds to the fact that these hydroxyls are not associated with any of these LAS. The LAS<sub>v,s</sub> seem to be highly unsaturated Lewis acid sites with no hydroxyls attached to them, and these LAS cannot be regenerated after dealumination-realumination treatments. The simultaneous disappearance of bands of LAS<sub>v,s</sub>

and ‘VHF’ hydroxyls in  $\text{NH}_4^+$  BEA zeolites is just a coincidence and has no mutual structural correlation (**Table 9.1** and **Figure 9.5**). These results, thus, rule out the correlation of ‘VHF’ hydroxyls to strong FA-Al LAS.

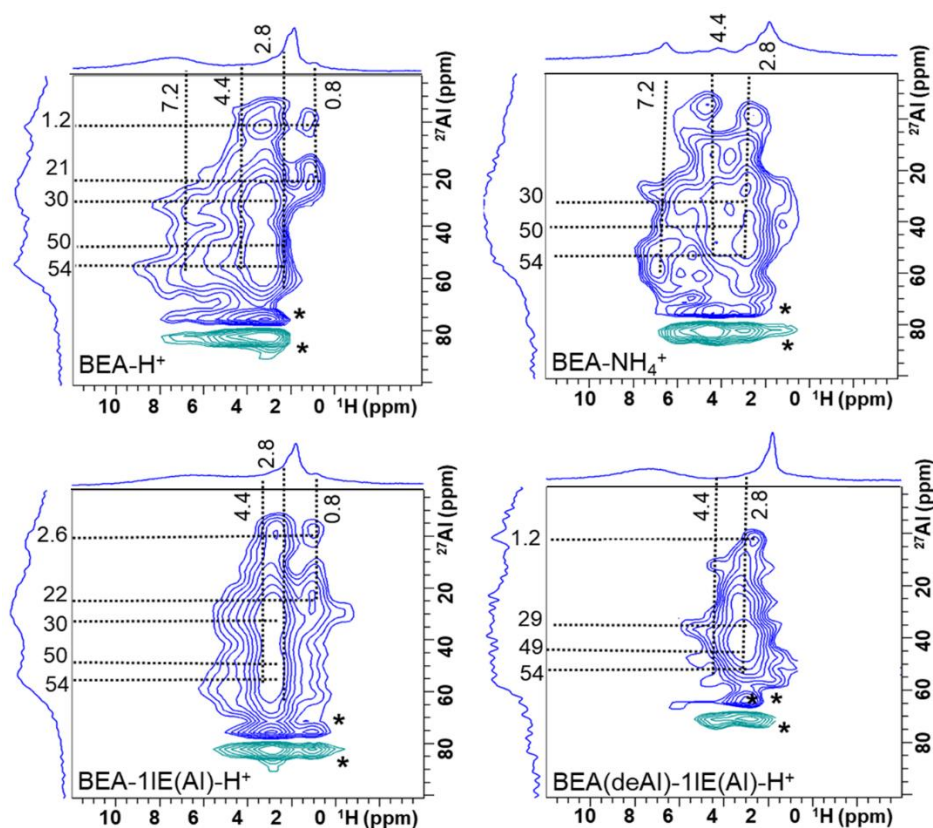


Figure 9.6:  $^{27}\text{Al}$ - $^1\text{H}$  HETCOR NMR spectra of evacuated samples; the negative-positive contours shown by an asterisk (\*) are due to the data acquisition program and thus don't represent structural features. The independent  $^1\text{H}$  NMR and  $^{27}\text{Al}$  NMR spectra from  $^{27}\text{Al}$ - $^1\text{H}$  HETCOR experiments performed on evacuated samples are presented in Figure F.1.

For a deeper insight into the structure of aluminum attached to these hydroxyls, we performed  $^{27}\text{Al}$ - $^1\text{H}$  HETCOR NMR spectroscopy on evacuated BEA samples (**Figures 9.6** and **F.1**), and the features of interest are listed in **Table 9.1**. As  $^1\text{H}$  MAS NMR on evacuated zeolites is the fingerprint of the hydroxyl region from FTIR spectra,  $^{27}\text{Al}$ -H HETCOR experiments can inform us about the nature of aluminum attached to ‘VHF’ hydroxyls. **Figure 9.6** shows that the  $^1\text{H}$  NMR feature at 0.8 ppm, corresponding to the ‘VHF’ hydroxyls, is present in the  $\text{H}^+$  form of parent and aluminated BEA and absent in respective  $\text{NH}_4^+$  forms, which is in line with observations from FTIR. As the intensity of the ‘VHF’ band in the FTIR spectrum of  $\text{BEA}(\text{deAl})\text{-1IE}(\text{Al})\text{-H}^+$  was negligible, this sample does not exhibit the  $^1\text{H}$  NMR feature at 0.8 ppm. The ‘VHF’ hydroxyls, at 0.8 ppm, correlate to octahedral aluminum ( $^{27}\text{Al}$  NMR feature at 1.2 ppm) and to another sharp aluminum feature at 21 ppm. Interestingly, the  $^{27}\text{Al}$  NMR

feature at 21 ppm exclusively exists in the  $H^+$  form of parent and aluminated BEA and is absent in respective  $NH_4^+$  forms. In contrast, the peak at 1.2 ppm is present in all samples (with varied intensity). As different types of alumina show this kind of feature in the range of 15-22 ppm, our results suggest that the VHF hydroxyl may be attached to some aluminum oxide/hydroxide-like species. A  $^1H$  and  $^{27}Al$  NMR studies on the dehydration of pseudo-boehmites showed that the dehydrated pseudo-boehmite (ambient pressure dehydration at 1373K followed by room temperature evacuation) shows a single octahedral NMR resonance at  $\sim 15$  ppm (**Figure 9.7**)<sup>282</sup>. In comparison, the low-temperature dehydration of pseudo-boehmites generates a peak at 8.8 ppm due to octahedral aluminum sites, which is similar to that observed for crystalline boehmite and diaspore<sup>282</sup>. Likewise, a dehydrated  $\gamma$ -alumina sample that underwent ambient pressure heating at 1553K before dehydration also shows the octahedral feature at  $\sim 15$  ppm<sup>282</sup>.

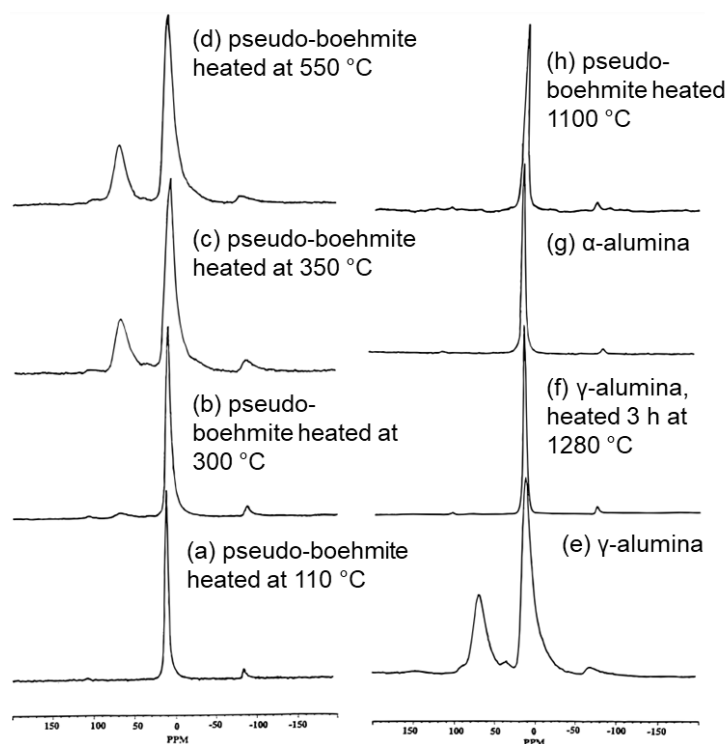


Figure 9.7:  $^{27}Al$ -MAS NMR spectra of pseudo-boehmites dehydrated at different temperatures. Reproduced with permission from Ref<sup>282</sup>.

Similarly, the silylation of zeolite BEA results in an octahedral aluminum feature at  $\sim 18$  ppm, whose appearance was dependent on the nature of the silylating agents used (**Figure 9.8**)<sup>283</sup>. Using octamethylcyclotetrasiloxane (OMTS) as the silylating agent resulted in the appearance of this feature. In comparison, silylating agents like tetra-ethoxysilane (TEOS), tetra-propoxysilane (TPOS), and tetra-butoxysilane (TPOS) do not result in the appearance of this peak.

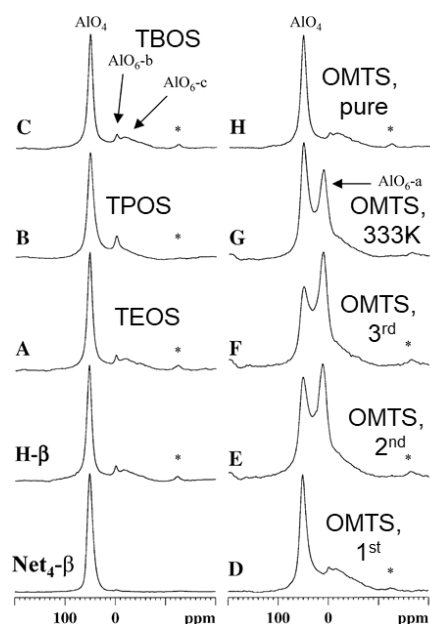


Figure 9.8:  $^{27}\text{Al}$ -MAS NMR spectra of parent protonic and silylated BEA. Reproduced with permission from Ref <sup>283</sup>.

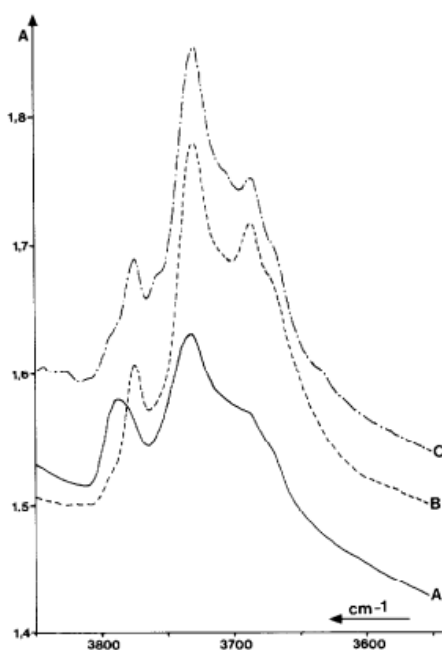


Figure 9.9: IR spectra in the OH absorption range of the amorphous (A), well-crystallized (B), and reference (C) samples. Reproduced with permission from Ref <sup>284</sup>.

In another study to evaluate the effects of crystallinity and morphology on the surface properties of alumina, it was shown that the VHF band was not presented in crystalline alumina samples. In comparison, amorphous alumina samples showed the band at  $3780\text{ cm}^{-1}$ , suggesting the amorphous nature of these species (**Figure 9.9**) <sup>284</sup>. An FTIR spectroscopic study to evaluate the surface chemistry and surface structure of catalytic aluminas showed that the FTIR spectrum

of evacuated  $\gamma$ -AlOOH activated at 300K does not show VHF. In comparison, the activation of  $\gamma$ -Al<sub>2</sub>O<sub>3</sub> at 773K results in the appearance of this band at 3778 cm<sup>-1</sup>. Likewise, the activation of  $\eta$ -Al<sub>2</sub>O<sub>3</sub> at 773K also results in the presence of this band. In comparison, the  $\theta$ -Al<sub>2</sub>O<sub>3</sub> and  $\alpha$ -Al<sub>2</sub>O<sub>3</sub> do not show this feature at similar activation temperatures (**Figure 9.10**)<sup>285</sup>. This suggests that the VHF hydroxyl band can be associated with forming  $\eta$ -Al<sub>2</sub>O<sub>3</sub> or  $\gamma$ -Al<sub>2</sub>O<sub>3</sub> like species during high-temperature activation of zeolitic materials. The temperatures at which the zeolite samples are activated prior to FTIR and NMR studies on dehydrated samples are also similar. The possibility of the presence of  $\alpha$ -Al<sub>2</sub>O<sub>3</sub> can be simply excluded as this is a highly crystalline material and is formed at very high-temperature activations<sup>286</sup>.

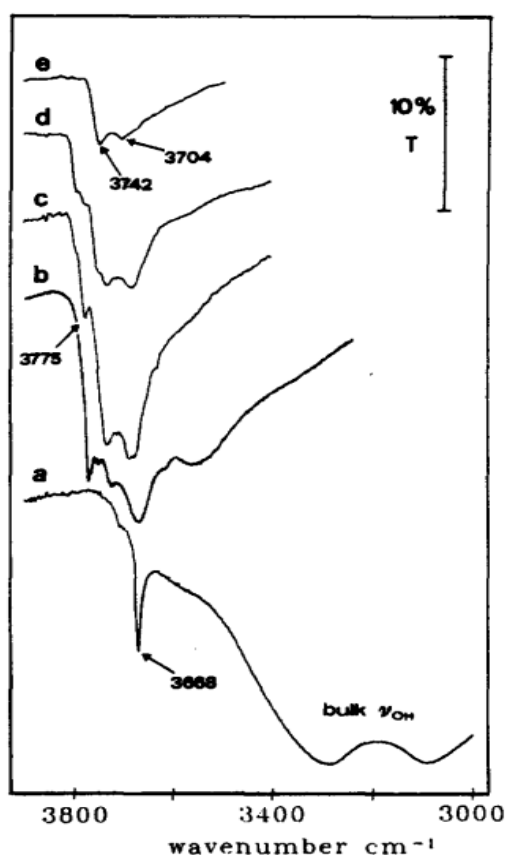


Figure 9.10: The high wavenumbers region of the OH spectrum of some Al oxides. (a):  $\gamma$ -AlOOH activated at 300 K. (b-e):  $\eta$ -Al<sub>2</sub>O<sub>3</sub>,  $\gamma$ -Al<sub>2</sub>O<sub>3</sub>,  $\theta$ -Al<sub>2</sub>O<sub>3</sub>, and  $\alpha$ -Al<sub>2</sub>O<sub>3</sub> activated at 773 K. Reproduced with permission from Ref<sup>285</sup>.



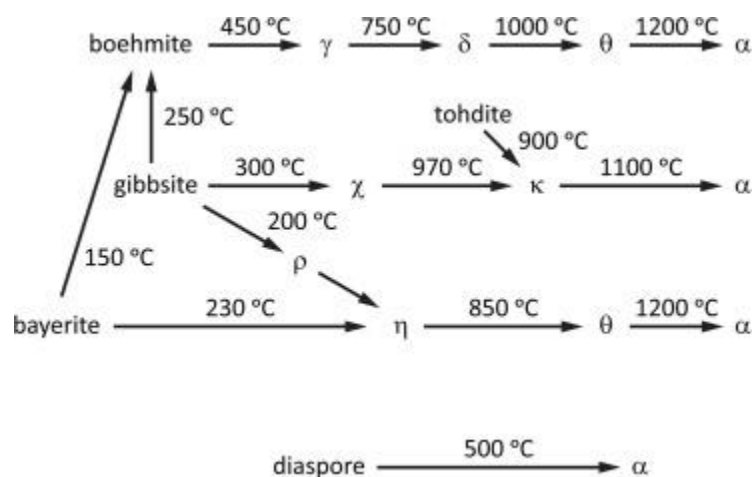


Figure 9.11: The transformation sequences that are most common for aluminum oxides and hydroxides. Greek letters indicate aluminas. Included are indicative values of the transition temperatures. Reproduced with permission from Ref <sup>286</sup>.

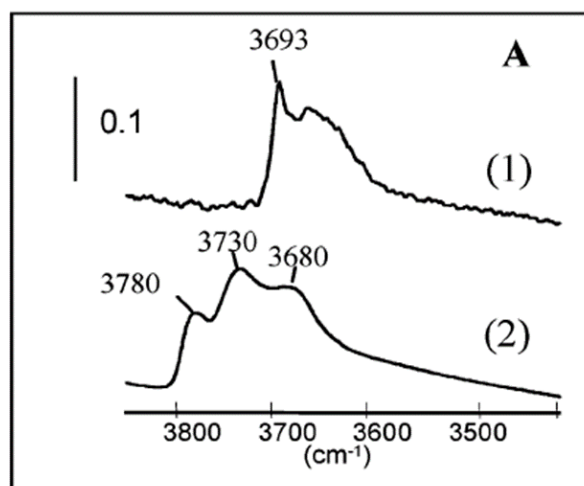


Figure 9.12: FTIR spectra of  $\gamma$ - $\text{Ga}_2\text{O}_3$  and  $\gamma$ - $\text{Al}_2\text{O}_3$  samples pretreated at 673 K. Reproduced with permission from Ref <sup>287</sup>.

The transformation of aluminum oxides/hydroxides to transitional aluminas as a function of temperatures is presented in **Figure 9.11**. The  $\gamma$ - $\text{Al}_2\text{O}_3$  are generally produced from the boehmite phase upon heating the boehmites to temperatures  $\sim 773\text{K}$ , whereas  $\eta$ - $\text{Al}_2\text{O}_3$  is formed at  $\sim 573\text{K}$ . Thus, among the two candidates mentioned above to be the possible structures of aluminum-bearing VHF hydroxyls,  $\gamma$ - $\text{Al}_2\text{O}_3$  is the best contender. Another infrared spectroscopic study presented that the ‘VHF’ band at  $3780\text{ cm}^{-1}$  does exist in the spectrum of  $\gamma$ - $\text{Al}_2\text{O}_3$  by performing the pretreatment at 673K **Figure 9.12)** <sup>287</sup>. Additionally, comparing the FTIR spectra of  $\gamma$ - $\text{Al}_2\text{O}_3$  with  $\gamma$ - $\text{Ga}_2\text{O}_3$  pretreated at this temperature confirms that  $\gamma$ - $\text{Ga}_2\text{O}_3$  does not have such hydroxyls <sup>287</sup>. Thus, based on our findings from FTIR using two different probes and NMR after evacuation at similar temperatures and available literature about the <sup>27</sup>Al NMR

peak at ~15-22 ppm and VHF feature of aluminas<sup>282, 283, 287, 288</sup>, we propose that VHF hydroxyls are neither strongly acidic nor attached to FA-Al species. Instead, they are weakly acidic hydroxyls. We suggest that the microparticles of boehmite, like AlOOH species, are present in zeolite BEA as impurities or are formed as a result of post-synthetic treatments. These types of structures, upon removal of waters of hydration in the temperature range of 673-773K, form  $\gamma$ -Al<sub>2</sub>O<sub>3</sub>, resulting in the appearance of the so-called 'VHF' hydroxyls band in the range 3775-3790 cm<sup>-1</sup>. Moreover, the post-synthetic Al-IE treatments, followed by calcination on parent BEA do not affect this band. In comparison, due to realumination on a dealuminated BEA, the intensity of the VHF hydroxyls was drastically lower than that of parent and aluminum-exchanged samples. This proposes that the aluminum bearing these hydroxyls is most likely produced during the synthesis of BEA, or, at least, alumination and realumination-dealumination treatments do not favor the generation of these species.

#### 9.4. Conclusions

FTIR spectroscopy of adsorbed carbon monoxide and pyridine was performed on the parent, aluminated, and dealuminated-realumnated BEA in their proton and ammonium forms. The <sup>27</sup>Al-<sup>1</sup>H HETCOR NMR spectroscopy under similar conditions of sample evacuation without probe molecules gave useful insight into the acidity of the so-called very high frequency 'VHF' hydroxyls at 3780 cm<sup>-1</sup> and the structure of aluminum species bearing these hydroxyls. Our findings, in combination with the literature search, suggest that 'VHF' hydroxyls are predominantly associated with  $\gamma$ -Al<sub>2</sub>O<sub>3</sub>-type octahedral aluminum species formed at high-temperature treatments, most likely from an AlOOH-like boehmite phase. However, a very small fraction of these hydroxyls may be coordinated to FA-Al species, which do not correspond to very strong LAS. The disappearance of very strong and medium-strength LAS does not accompany the disappearance of the VHF band in the proton form of zeolite; thus, this band is weakly acidic and is not linked to strongly acidic FA-Al LAS.

# Chapter 10

## Conclusions and Outlook

### 10.1 Conclusions

Zeolites are an essential class of heterogeneous catalysts because of their hydrothermal stability, large micropore volume, structural pores' suitability, tunability for catalytic reactions, and co-presence of LAS and BAS. Unlike BAS, which originates from a hydroxyl group bridging framework silicon and aluminum atoms, the structure of LAS remains ambiguous. This is due to the multiplicity of aluminum structures responsible for Lewis acidity in zeolites. This is due to the mult (Chapter 1). Even though considerable research has been carried out on the Lewis acidity of zeolites, the literature still lacks a sound understanding of the structure and strength of aluminum LAS in zeolites. In particular, the open questions about the nature and the structure-performance relations of extra-framework aluminum (EFAI) motifs must be carefully addressed (Chapter 2). Therefore, the rational design of aluminum LAS and establishing the quantitative structure-activity relations was the objective of this work. The emphasis was given to carefully assigning different types of aluminum LAS in zeolites using various spectroscopic techniques (Chapter 3).

Firstly, Lewis acidity was introduced into Zeolite Y through a simple ion-exchange protocol using an aluminum nitrate aqueous solution (Chapter 4). X-ray diffraction and nitrogen physisorption suggest that the zeolitic framework is retained after these treatments. With an increase in the total extra-framework aluminum in the modified zeolites, there was a pronounced increase in the number of LAS, as illustrated by FTIR spectroscopy of adsorbed pyridine and carbon monoxide. In contrast, no significant change in the number of Brønsted acid sites was observed. The number of LAS, determined by FTIR of adsorbed pyridine and carbon monoxide, quantitatively correlated to the rate of reaction for MPV reduction of 4-*tert* butyl cyclohexanone and to the octahedrally coordinated extra-framework aluminum determined by  $^{27}\text{Al}$  MAS NMR. The findings conclude that ion-exchange of extra-framework cations is a feasible way to introduce and/or enhance the Lewis acidity of pristine zeolite. These species, however, do not result in charge-compensating aluminum ions; instead, they form neutral extra-framework clusters. Thus, the Lewis acid sites will likely present as charge-neutral

Al(OH)<sub>3</sub>H<sub>2</sub>O and/or nano-sized Al<sub>2</sub>O<sub>3</sub> clusters. Multiple Al-IE treatments with a lower concentration of aluminum precursor maximize the generation of LAS.

Like other post-synthetic treatments, the extent of generation of LAS by the Al-IE route also depends on many factors. Consequently, **Chapter 5** explores the role of aluminum-exchange conditions, the Si/Al ratio of parent zeolite, and nature of co-cation in generating the EFAl LAS by Al-IE. The results indicate that higher Si/Al ratios of parent Y zeolite favor maximum incorporation of EFAl while retaining the BAS, intrinsic pore structure, and zeolite framework. The LAS incorporated in zeolites of higher Si/Al ratios quantitatively correlate with the aluminum content determined by ICP, the octahedrally coordinated EFAl determined by NMR, and the catalytic activity for MPV reduction of 4-*tert* butyl cyclohexanone. Aluminum-exchange performed under combined heating and stirring conditions yielded zeolites with lower catalytic activity and lower content of LAS despite the maximum concentration of EFAl. However, the Al-IE under stirring conditions is most favorable to incorporate large amounts of EFAl with the maximum catalytic activity and the concentration of LAS. The presence of sodium as co-cation negatively affects the generation of EFAl LAS and the catalytic activity.

The consequences of post-synthetic modifications are not the same for all zeolite structures. Therefore, Chapter 6 compares the generation and activity of aluminum-exchanged LAS in zeolites with BEA, MOR, MFI, and FAU topologies. The results indicate that this procedure efficiently incorporates a significant amount of LAS in BEA and Y zeolites, as determined by FTIR of adsorbed pyridine. The incorporated LAS in these zeolites and the framework ones have a quantitative correlation with the aluminum content determined by ICP, the octahedrally coordinated EFAl determined by <sup>27</sup>Al MAS NMR, and the catalytic activity for MPV reduction of 4-*tert* butyl cyclohexanone. Like in Y zeolite, Lewis acidity in BEA is not incorporated at the expense of BAS; therefore, neutral LAS are present. These LAS could not be generated in MFI zeolite due to its small pore size and in MOR zeolite due to accessibility limitations caused by side pockets and potential positions of these EFAl LAS in MOR, respectively. Consequently, no significant change in the content of EFAl and MPV catalytic activity was observable in these zeolites. The respective selectivity, determined by the zeolite pore size of all zeolite catalysts, towards *cis* to *trans* 4-*tert* butylcyclohexanol does not vary after Al-IE treatments.

The MPV reduction of ketones occurs under mild conditions as it uses secondary alcohols for the hydride transfer reaction; thus, it can also be catalyzed by weak or medium-strength LAS. Therefore, Chapter 7 evaluated the catalytic performance of zeolite Y with different Si/Al ratios

and the respective aluminum-exchanged samples for n-butane dehydrogenation. The parent protonic zeolites at low Si/Al ratios, despite having maximum content of LAS and BAS, show minimal conversion compared to the ammonium forms. Increasing the Si/Al ratio increases the conversion of parent zeolites; after Si/Al=15, the activity lowers. Aluminum-exchanged LAS species significantly increase the conversion of parent zeolites with a substantial increase in selectivity for dehydrogenation. Despite lowering BAS due to Na-IE before and after Al-IE, the dehydrogenation selectivity of aluminum-exchanged samples does not change. The preservation of structure and Lewis acidity of EFAl species in the regenerated catalysts confirms that the thermal stability and strength of neutral EFAl LAS, produced by Al-IE, are capable of cleaving the C-H bonds of alkanes. Higher selectivities of isobutane propose that the protolysis of n-butane to form carbenium ion occurs on LAS, followed by the skeletal isomerization to isobutane.

To evaluate the distribution of aluminum LAS in zeolite BEA and the associated MPV activity, the Lewis acidity of BEA zeolite was modulated via alumination and dealumination-realumination routes. Al-IE was used for alumination and realumination treatments and nitric acid treatment for dealumination, respectively. The inherent Lewis acidity of parent BEA and the associated catalytic activity in the MPV reaction is mainly due to FA-Al and only partly due to EFAl. Aluminations and multiple realuminations of dealuminated BEA increase the activity that quantitatively correlates to increased LAS from FTIR and EFAl from NMR. In contrast, the content of FA-Al does not increase. Thus, both FA-Al and EFAl can act as active sites for the MPV hydride transfer mechanism without changing the product selectivity.

The insights about the structure of the MPV active site were employed to revisit the so-called ‘very high frequency’ (VHF) hydroxyls at  $\sim 3780\text{cm}^{-1}$  of zeolites and the structure of aluminum species attached (**Chapter 9**). FTIR spectroscopy of adsorbed carbon monoxide and pyridine, combined with  $^{27}\text{Al}$ - $^1\text{H}$  HETCOR NMR spectroscopy of dehydrated aluminated, dealuminated-realuminated, and parent BEA was performed. Our findings, in combination with the literature search, suggest that ‘VHF’ hydroxyls are predominantly associated with  $\gamma\text{-Al}_2\text{O}_3$ -type octahedral aluminum species formed at high-temperature treatments, most likely from an ALOOH-like boehmite phase. However, a tiny fraction of these hydroxyls may be coordinated to FA-Al species, which do not correspond to very strong LAS. The disappearance of very strong and medium-strength LAS does not accompany the disappearance of the VHF band in the proton form of zeolite; thus, this band is weakly acidic and is not linked to strongly acidic FA-Al LAS.

In conclusion, this work provides significant insights into the rational design of EFAl LAS in zeolites without Brønsted acidity of zeolite. Evaluating the factors affecting the generation of aluminum-exchanged LAS guides the pathways towards maximizing the Lewis acidity yet preserving the intrinsic properties of zeolite. A combination of different spectroscopic techniques, catalytic evaluation, and diverse treatment conditions can be used to quantitatively discern the different Lewis acidic aluminum species and address the open questions related to the Lewis acidity of extra-framework aluminum in zeolites.

## 10.2. Outlook

Investigating the Lewis acidity of extra-framework aluminum in zeolites is a highly active and interdisciplinary research field that holds great promise for developing novel and efficient heterogeneous catalysts for various industrial processes. The research on extra-framework aluminum in zeolites not only contributes to a fundamental understanding of catalysis at the molecular level but also has significant implications for the development of practical and sustainable industrial processes. The present work provided significant development toward synthesis-structure-performance correlations of aluminum LAS via different experimental and spectroscopic approaches. However, this topic offers many avenues for future research in structure analysis, material design, and catalysis.

### Strategies for rational engineering of aluminum Lewis acid sites

In the present work, ion-exchange of aluminum species is presented as an efficient strategy for dedicated modulation of aluminum Lewis acid sites in zeolites. However, there is a continuing demand to rationalize the approaches to control and tailor the Lewis acidity of extra-framework aluminum in zeolites to achieve the desired catalytic properties. The efficiency and/or the structure of Lewis acid sites can be dictated by the systematic control of zeolite morphology, the presence of defect sites, and the aluminum content of the parent zeolite<sup>289</sup>. Therefore, the development of novel methods for the introduction of Lewis acidic aluminum, as well as the optimization of available approaches, is crucial<sup>60, 142, 262, 273, 290</sup>. For example, tri-coordinated aluminum, associated with strong Lewis acidity, was rationally constructed by precise tailoring of acid-treatment time for ultra-stable Y zeolite<sup>291</sup>. These Lewis acid sites were confirmed to be the catalytic active sites for oxidative desulfurization with hydrogen peroxide as an oxidant<sup>291</sup>. Similarly, the controlled thermal treatment of protonic zeolite Y at temperatures above 900K is recently reported to generate naked Al<sup>3+</sup> species. These moieties were proposed to be

charge balanced by a triplet of adjacent framework oxygens with a net charge of -1 for each Si-O-Al moiety<sup>292</sup>.

For some methods, like desilication, the formation of Lewis acid sites is accompanied by the developing of a secondary pore structure, which can be favorable for processes that convert bulky molecules<sup>293</sup>. While modulating the Lewis acidity of zeolite with gallium substitution is frequently explored<sup>294, 295</sup>, the generation of extra-framework Lewis acid sites by combined aluminum and gallium exchange is worth trying. Another yet very novel possible way is the cooperative Lewis acidity of aluminum and the isolated framework heteroatom. A systematic desilication of zeolite followed by dealumination and heteroatom grafting creates aluminum Lewis acid sites, which favor the enhancement of the inherent acidity of heteroatom<sup>296</sup>. Furthermore, integrating zeolites with other materials or modification strategies can also offer new avenues for developing efficient aluminum Lewis acid sites, thus enhancing materials' catalytic activity and selectivity in various industrial applications.

### Bridging the gaps in analysis conditions

In the present work, we presented sound correlations of the generation of extra-framework aluminum with the enhanced Lewis acidity from FTIR and increased activity in Lewis acid-catalyzed reaction. However, these correlations still face challenges pertaining to the difference in conditions under which the structure, acidity, and activity are analyzed. For example, the structure of aluminum species is typically analyzed by obtaining solid-state NMR on the air-exposed/hydrated samples. In comparison, the acidity associated with the aluminum species is measured by FTIR spectroscopy when the samples are dehydrated under high vacuum and temperature conditions before the adsorption of basic probe molecules. In comparison, the acidity associated with the aluminum species is measured by FTIR spectroscopy when the samples are dehydrated under high vacuum and temperature conditions before the adsorption of basic probe molecules.

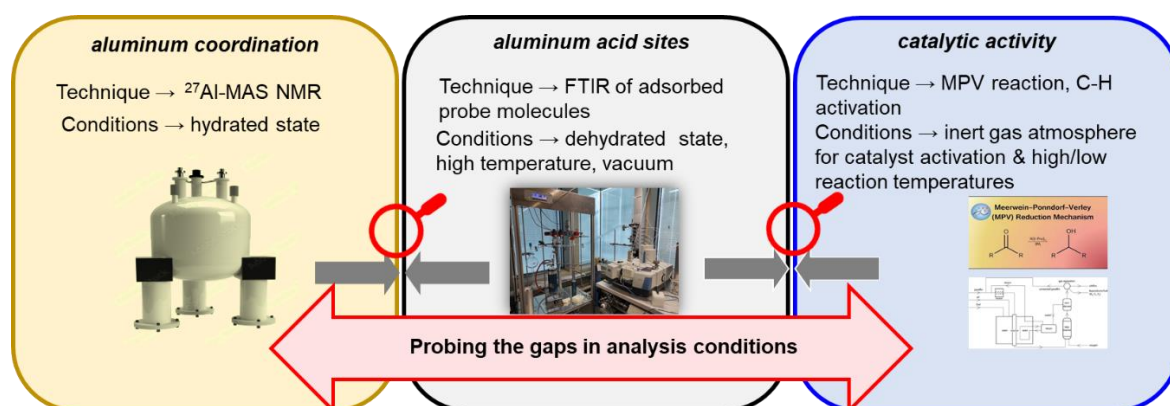


Figure 10.1: Highlighting the gaps in conditions of different techniques for analyzing and establishing structure-activity relations of aluminum active sites.

The catalytic activity in the MPV reaction was evaluated by activating catalysts under an inert atmosphere, followed by catalytic reaction under an inert atmosphere at temperatures lower than 373K (**Figure 10.1**). In contrast, the activity in C-H activation was evaluated at temperatures above 673K. As described in **Chapter 1** and the following, the structure of aluminum Lewis acid sites is highly sensitive to the conditions in which zeolite exists. Therefore, the gaps between the conditions under which different aspects of the aluminum species are typically studied suggest that not all the structures of aluminum species may likely be present under different conditions of evaluation. To probe these gaps, strategies should be developed to get insights from one technique under the conditions of the other and vice versa. For example, in **Chapter 9**, we performed  $^{27}\text{Al}$ - $^1\text{H}$  HETCOR NMR spectroscopy of material evacuated under conditions similar to that of FTIR spectroscopy, and these studies gave information that cannot be extracted from typical measurements of FTIR or NMR. However, there is a pressing demand to improve the utilization of these methods for better structure-performance correlations. A possible continuation of this approach can be to study the aluminum structure under conditions of IR by measuring MQMAS NMR after the adsorption of probe molecules on dehydrated samples<sup>55</sup>. In contrast, the evolution of Lewis acidity of the aluminum species under NMR conditions can be evaluated by performing FTIR measurements with pre-adsorbed water<sup>60</sup>. Similarly, adsorption of the secondary alcohol can be done on zeolite after activation to temperatures used for MPV catalysts. Consequently, the NMR spectroscopy on these materials can give valuable insights into the final structure and coordination of catalytically active sites for MPV reaction.

### **Expanding the characterization strategies for mechanistic insights**

While the literature presents extensive information about the correlation of activity with increased Lewis acidity, very little focus is given to exploring the actual structure of responsible aluminum species. This present work provided valuable insights into the structure of aluminum in combination with activity and Lewis acidity. Future research efforts may focus on further elucidating the mechanisms by which extra-framework aluminum affects the catalytic performance of zeolite catalysts. Consequently, coupling MAS NMR spectroscopy with double and triple quantum resonance will enable the study of proximity and anisotropy of aluminum sites associated with different acidity types<sup>297</sup>. In addition, applying advanced characterization techniques such as in situ and operando spectroscopy and microscopy can provide a more comprehensive understanding of the nature and behavior of extra-framework aluminum in zeolites under realistic reaction conditions. This can further accelerate the development of



zeolite catalysts with improved performance and selectivity. For example, the presence and evolution of tetrahedral, octahedral, and under-coordinated aluminum species during all steps of zeolite treatment can be efficiently revealed by X-ray absorption spectroscopy (XAS)<sup>173, 178</sup>.

Similarly, the Rietveld refinement of XRD patterns can identify migration of aluminum to extra-framework positions and reveal occupancy of extra-framework cations as a function of temperature<sup>298</sup>. As the cooperative catalysis of LAS and BAS is of significant relevance in the catalytic industry, precise characterization of diverse aluminum LAS and their proximity and interaction with BAS and the zeolite framework are of primary importance. In this context, measurement of NMR on nuclei other than aluminum, such as <sup>1</sup>H and <sup>29</sup>Si, including 2D correlation spectroscopy, can give valuable information on the local aluminum environment. Similarly, the analysis of adsorbed probe molecules through NMR spectroscopy of <sup>13</sup>C, <sup>15</sup>N, and <sup>31</sup>P nuclei can directly probe the acidity of aluminum centers. For instance, <sup>27</sup>Al-<sup>31</sup>P or <sup>27</sup>Al-<sup>15</sup>N REDOR and TRAPDOR experiments employing trimethylphosphine and pyridine probes and quantify BAS and LAS, respectively<sup>299, 300</sup>. Detailed information about the strength of different LAS is also essential to correlate it with the structure and activity. In this respect, in combination with quantifying acid sites using pyridine, weaker bases such as nitrogen and carbon monoxide should be routinely used for different Lewis acid sites of varying coordination. The information on the strength of acid sites can also be obtained by a combination of FTIR spectroscopy with temperature-programmed desorption of probe molecules<sup>301</sup>. Thus, an optimized combination of characterization techniques can provide valuable mechanistic insights into the structural, electronic, and chemical properties of extra-framework aluminum in zeolites and their correlation with Lewis acidity.

### **Theoretical approaches**

The acid site distribution in the zeolite framework is firmly related to the locations of aluminum species, which results in different reaction environments, including reaction space and activation ability of acid sites, and hence, a significant difference in catalytic performance. In this respect, knowledge of structural proximity and structure under reaction conditions will significantly contribute to understanding the role of Lewis acid sites in catalysis by zeolites. However, this point has just received considerable attention in recent years, although zeolites and their catalytic properties have been extensively studied. This is because the aluminum locations in aluminosilicates are challenging to be accurately determined by the present experimental characterization techniques<sup>302-305</sup>. For a thorough understanding of the chemical phenomena at the molecular scale, the information from experimental characterization should

also be supported by theoretical, computational approaches to design next-generation catalysts optimally. The molecular modeling and DFT calculations can thus provide a pool of information on the stabilization of aluminum in zeolite and reaction rates<sup>306-308</sup>.

Overall, the study of EFAl LAS in zeolites presents a promising opportunity to develop more efficient and selective heterogeneous catalysts for industrial processes through the manipulation of Lewis acidity. Further investigation and optimization of extra-framework aluminum in zeolites can pave the way for developing sustainable and environmentally friendly chemical processes. Therefore, a detailed understanding of the nature and reactivity of EFAl in zeolites is crucial for the design and optimization of zeolite catalysts with improved activity, selectivity, and stability.

## References

1. Primo, A.; Garcia, H., Zeolites as catalysts in oil refining. *Chemical Society Reviews* **2014**, *43* (22), 7548-7561.
2. Martínez, A.; Prieto, G.; García-Trenco, A.; Peris, E., Advanced Catalysts Based on Micro-and Mesoporous Molecular Sieves for the Conversion of Natural Gas to Fuels and Chemicals. *Zeolites and Catalysis: Synthesis, Reactions and Applications* **2010**, 649-685.
3. Vogt, E. T. C.; Weckhuysen, B. M., Fluid catalytic cracking: recent developments on the grand old lady of zeolite catalysis. *Chemical Society Reviews* **2015**, *44* (20), 7342-7370.
4. Montalvo, S.; Huiliñir, C.; Borja, R.; Sánchez, E.; Herrmann, C., Application of zeolites for biological treatment processes of solid wastes and wastewaters – A review. *Bioresource Technology* **2020**, *301*, 122808.
5. Feng, C.; E, J.; Han, W.; Deng, Y.; Zhang, B.; Zhao, X.; Han, D., Key technology and application analysis of zeolite adsorption for energy storage and heat-mass transfer process: A review. *Renewable and Sustainable Energy Reviews* **2021**, *144*, 110954.
6. Zhu, Z.; Xu, H.; Jiang, J.; Wu, P., Postsynthesis and Effective Baeyer–Villiger Oxidation Properties of Hierarchical FAU-type Stannosilicate. *The Journal of Physical Chemistry C* **2016**, *120* (41), 23613-23624.
7. Venuto, P. B.; Habib, T., Catalyst-Feedstock-Engineering Interactions in Fluid Catalytic Cracking. *Catalysis Reviews* **1978**, *18* (1), 1-150.
8. Zhu, L.; Ren, L.; Zeng, S.; Yang, C.; Zhang, H.; Meng, X.; Rigutto, M.; Made, A. v. d.; Xiao, F.-S., High temperature synthesis of high silica zeolite Y with good crystallinity in the presence of N-methylpyridinium iodide. *Chemical Communications* **2013**, *49* (89), 10495-10497.
9. Chen, G.; Liu, G.; Pan, Y.; Liu, G.; Gu, X.; Jin, W.; Xu, N., Zeolites and metal–organic frameworks for gas separation: the possibility of translating adsorbents into membranes. *Chemical Society Reviews* **2023**, *52* (14), 4586-4602.
10. Martínez, C.; Pérez-Pariente, J., Zeolites and ordered porous solids: fundamentals and applications. *Valencia, Spain: FEZA* **2011**.
11. Burton, A., Recent trends in the synthesis of high-silica zeolites. *Catalysis Reviews* **2018**, *60* (1), 132-175.
12. Li, Y.; Yu, J., New stories of zeolite structures: their descriptions, determinations, predictions, and evaluations. *Chemical reviews* **2014**, *114* (14), 7268-7316.
13. Sudarsanam, P.; Peeters, E.; Makshina, E.; Parvulescu, V. I.; Sels, B., Advances in porous and nanoscale catalysts for viable biomass conversion. *Chemical Society Reviews* **2019**, *48*.
14. Cejka, J.; Corma, A.; Zones, S., *Zeolites and catalysis: synthesis, reactions and applications*. John Wiley & Sons: 2010.
15. Niwa, M.; Katada, N.; Okumura, K., *Characterization and design of zeolite catalysts: solid acidity, shape selectivity and loading properties*. Springer Science & Business Media: 2010; Vol. 141.
16. Loewenstein, W., The distribution of aluminum in the tetrahedra of silicates and aluminates. *American Mineralogist: Journal of Earth and Planetary Materials* **1954**, *39* (1-2), 92-96.
17. Howden, M. G., Zeolite ZSM-5 containing boron instead of aluminium atoms in the framework. *Zeolites* **1985**, *5* (5), 334-338.
18. Guo, P.; Strohmaier, K.; Vroman, H.; Afeworki, M.; Ravikovitch, P. I.; Paur, C. S.; Sun, J.; Burton, A.; Zou, X., Accurate structure determination of a borosilicate zeolite EMM-26 with two-dimensional 10× 10 ring channels using rotation electron diffraction. *Inorganic Chemistry Frontiers* **2016**, *3* (11), 1444-1448.
19. Fan, X.; Jiao, Y., Porous materials for catalysis: Toward sustainable synthesis and applications of zeolites. In *Sustainable nanoscale engineering*, Elsevier: 2020; pp 115-137.

20. Kulprathipanja, S., *Zeolites in industrial separation and catalysis*. John Wiley & Sons: 2010.
21. McCusker, L.; Liebau, F.; Engelhardt, G., Nomenclature of structural and compositional characteristics of ordered microporous and mesoporous materials with inorganic hosts (IUPAC Recommendations 2001). *Pure and Applied Chemistry* **2001**, *73* (2), 381-394.
22. McCusker, C. B. a. L. B. International zeolite Association (IZA), Database of Zeolite Structures. <http://www.iza-structure.org/databases/>.
23. Fyfe, C.; Gobbi, G.; Klinowski, J.; Thomas, J.; Ramdas, S., Resolving crystallographically distinct tetrahedral sites in silicalite and ZSM-5 by solid-state NMR. *Nature* **1982**, *296* (5857), 530-533.
24. Haag, W.; Lago, R.; Weisz, P., The active site of acidic aluminosilicate catalysts. *Nature* **1984**, *309* (5969), 589-591.
25. Chai, Y.; Shang, W.; Li, W.; Wu, G.; Dai, W.; Guan, N.; Li, L., Noble metal particles confined in zeolites: synthesis, characterization, and applications. *Advanced Science* **2019**, *6* (16), 1900299.
26. Li, Y.; Li, L.; Yu, J., Applications of zeolites in sustainable chemistry. *Chem* **2017**, *3* (6), 928-949.
27. Pérez-Botella, E.; Valencia, S.; Rey, F., Zeolites in Adsorption Processes: State of the Art and Future Prospects. *Chemical Reviews* **2022**, *122* (24), 17647-17695.
28. Jacobs, P. A.; Dusselier, M.; Sels, B. F., Will Zeolite-Based Catalysis be as Relevant in Future Biorefineries as in Crude Oil Refineries? *Angewandte Chemie International Edition* **2014**, *53* (33), 8621-8626.
29. Speight, J. G., *The refinery of the future*. Gulf Professional Publishing: 2020.
30. Chen, N. Y.; Lucki, S. J.; Garwood, W. E., Dewaxing of oils by shape selective cracking and hydrocracking over zeolites zsm-5 and zsm-8. Google Patents: 1972.
31. Yuen, C. N.; Garwood, W. E., Selective catalytic conversion with a crystalline aluminosilicate. Google Patents: 1968.
32. Saravanamurugan, S.; Paniagua, M.; Melero, J. A.; Riisager, A., Efficient Isomerization of Glucose to Fructose over Zeolites in Consecutive Reactions in Alcohol and Aqueous Media. *Journal of the American Chemical Society* **2013**, *135* (14), 5246-5249.
33. Minachev, K. M.; Garanin, V. I.; Kharlamov, V. V.; Isakova, T. A.; Senderov, E. E., Catalytic properties of synthetic mordenite in the isomerization, hydrogenation, and hydroisomerization of certain hydrocarbons. *Russian Chemical Bulletin* **1969**, *18* (8), 1611-1615.
34. Galadima, A.; Muraza, O., Role of zeolite catalysts for benzene removal from gasoline via alkylation: A review. *Microporous and Mesoporous Materials* **2015**, *213*, 169-180.
35. Tian, P.; Wei, Y.; Ye, M.; Liu, Z., Methanol to olefins (MTO): from fundamentals to commercialization. *Acs Catalysis* **2015**, *5* (3), 1922-1938.
36. Bjørgen, M.; Joensen, F.; Holm, M. S.; Olsbye, U.; Lillerud, K.-P.; Svelle, S., Methanol to gasoline over zeolite H-ZSM-5: Improved catalyst performance by treatment with NaOH. *Applied Catalysis A: General* **2008**, *345* (1), 43-50.
37. Kubička, D.; Kubičková, I.; Čejka, J., Application of molecular sieves in transformations of biomass and biomass-derived feedstocks. *Catalysis Reviews* **2013**, *55* (1), 1-78.
38. Taarning, E.; Osmundsen, C. M.; Yang, X.; Voss, B.; Andersen, S. I.; Christensen, C. H., Zeolite-catalyzed biomass conversion to fuels and chemicals. *Energy & Environmental Science* **2011**, *4* (3), 793-804.
39. Luo, H. Y.; Lewis, J. D.; Román-Leshkov, Y., Lewis Acid Zeolites for Biomass Conversion: Perspectives and Challenges on Reactivity, Synthesis, and Stability. *Annual Review of Chemical and Biomolecular Engineering* **2016**, *7* (1), 663-692.
40. Xu, B.; Bordiga, S.; Prins, R.; van Bokhoven, J. A., Effect of framework Si/Al ratio and extra-framework aluminum on the catalytic activity of Y zeolite. *Applied Catalysis A: General* **2007**, *333* (2), 245-253.
41. Kwak, B. S.; Lee, J. S.; Lee, J. S.; Choi, B.-H.; Ji, M. J.; Kang, M., Hydrogen-rich gas production from ethanol steam reforming over Ni/Ga/Mg/Zeolite Y catalysts at mild temperature. *Applied energy* **2011**, *88* (12), 4366-4375.
42. Chica, A., Zeolites: promised materials for the sustainable production of hydrogen. *International Scholarly Research Notices* **2013**, *2013*.

43. Wang, Y.; Kazumi, S.; Gao, W.; Gao, X.; Li, H.; Guo, X.; Yoneyama, Y.; Yang, G.; Tsubaki, N., Direct conversion of CO<sub>2</sub> to aromatics with high yield via a modified Fischer-Tropsch synthesis pathway. *Applied Catalysis B: Environmental* **2020**, *269*, 118792.
44. Wei, J.; Yao, R.; Ge, Q.; Xu, D.; Fang, C.; Zhang, J.; Xu, H.; Sun, J., Precisely regulating Brønsted acid sites to promote the synthesis of light aromatics via CO<sub>2</sub> hydrogenation. *Applied Catalysis B: Environmental* **2021**, *283*, 119648.
45. Dai, C.; Zhao, X.; Hu, B.; Zhang, J.; Hao, Q.; Chen, H.; Guo, X.; Ma, X., Hydrogenation of CO<sub>2</sub> to aromatics over Fe–K/alkaline Al<sub>2</sub>O<sub>3</sub> and P/ZSM-5 tandem catalysts. *Industrial & Engineering Chemistry Research* **2020**, *59* (43), 19194-19202.
46. Wang, X.; Zeng, C.; Gong, N.; Zhang, T.; Wu, Y.; Zhang, J.; Song, F.; Yang, G.; Tan, Y., Effective suppression of CO selectivity for CO<sub>2</sub> hydrogenation to high-quality gasoline. *Acs Catalysis* **2021**, *11* (3), 1528-1547.
47. Rongxian, B.; Yisheng, T.; Yizhuo, H., Study on the carbon dioxide hydrogenation to iso-alkanes over Fe–Zn–M/zeolite composite catalysts. *Fuel processing technology* **2004**, *86* (3), 293-301.
48. Injongkol, Y.; Khemthong, P.; Yodsin, N.; Wongnongwa, Y.; Sosa, N.; Youngjan, S.; Butburee, T.; Rungtaweivoranit, B.; Kiatphuengporn, S.; Wittayakun, J., Combined in situ XAS and DFT studies on the role of Pt in zeolite-supported metal catalysts for selective n-hexane isomerization. *Fuel* **2022**, *314*, 123099.
49. Zholobenko, V.; Freitas, C.; Jendrlin, M.; Bazin, P.; Travert, A.; Thibault-Starzyk, F., Probing the acid sites of zeolites with pyridine: Quantitative AGIR measurements of the molar absorption coefficients. *Journal of Catalysis* **2020**, *385*, 52-60.
50. Ravi, M.; Sushkevich, V. L.; van Bokhoven, J. A., On the location of Lewis acidic aluminum in zeolite mordenite and the role of framework-associated aluminum in mediating the switch between Brønsted and Lewis acidity. *Chemical Science* **2021**, *12* (11), 4094-4103.
51. Buurmans, I. L.; Pidko, E. A.; de Groot, J. M.; Stavitski, E.; van Santen, R. A.; Weckhuysen, B. M., Styrene oligomerization as a molecular probe reaction for zeolite acidity: a UV-Vis spectroscopy and DFT study. *Physical Chemistry Chemical Physics* **2010**, *12* (26), 7032-7040.
52. Dai, W.; Lei, Q.; Wu, G.; Guan, N.; Hunger, M.; Li, L., Spectroscopic signature of Lewis acidic framework and extraframework Sn sites in beta zeolites. *ACS Catalysis* **2020**, *10* (23), 14135-14146.
53. Klinowski, J., Solid-state NMR studies of molecular sieve catalysts. *Chemical reviews* **1991**, *91* (7), 1459-1479.
54. Wouters, B. H.; Chen, T.; Grobet, P. J., Steaming of zeolite Y: Formation of transient Al species. *The Journal of Physical Chemistry B* **2001**, *105* (6), 1135-1139.
55. Jiao, J.; Kanellopoulos, J.; Wang, W.; Ray, S. S.; Foerster, H.; Freude, D.; Hunger, M., Characterization of framework and extra-framework aluminum species in non-hydrated zeolites Y by <sup>27</sup>Al spin-echo, high-speed MAS, and MQMAS NMR spectroscopy at B<sub>0</sub> = 9.4 to 17.6 T. *Physical Chemistry Chemical Physics* **2005**, *7* (17), 3221-3226.
56. Omegna, A.; van Bokhoven, J. A.; Prins, R., Flexible Aluminum Coordination in Alumino–Silicates. Structure of Zeolite H– USY and Amorphous Silica– Alumina. *The Journal of Physical Chemistry B* **2003**, *107* (34), 8854-8860.
57. Kanellopoulos, J.; Unger, A.; Schwioger, W.; Freude, D., Catalytic and multinuclear MAS NMR studies of a thermally treated zeolite ZSM-5. *Journal of Catalysis* **2006**, *237* (2), 416-425.
58. Kentgens, A. P.; Iuga, D.; Kalwei, M.; Koller, H., Direct observation of Brønsted acidic sites in dehydrated zeolite H-ZSM5 using DFS-enhanced <sup>27</sup>Al MQMAS NMR spectroscopy. *Journal of the American Chemical Society* **2001**, *123* (12), 2925-2926.
59. Haag, W. O.; Lago, R. M.; Weisz, P. B., The active site of acidic aluminosilicate catalysts. *Nature* **1984**, *309* (5969), 589-591.
60. Ravi, M.; Sushkevich, V. L.; van Bokhoven, J. A., Lewis Acidity Inherent to the Framework of Zeolite Mordenite. *The Journal of Physical Chemistry C* **2019**, *123*, 15139-15144.
61. Gackowski, M.; Podobinski, J.; Broclawik, E.; Datka, J., IR and NMR Studies of the Status of Al and Acid Sites in Desilicated Zeolite Y. *Molecules* **2019**, *25* (1).

62. Ravi, M.; Sushkevich, V. L.; van Bokhoven, J. A., Towards a better understanding of Lewis acidic aluminium in zeolites. *Nat Mater* **2020**, *19* (10), 1047-1056.
63. Ray, G. J.; Samoson, A., Double rotation and variable field 27Al n.m.r. study of dealuminated Y zeolites. *Zeolites* **1993**, *13* (6), 410-413.
64. Kosslick, H.; Tuan, V. A.; Fricke, R.; Martin, A.; Storek, W., Study on the nature of aluminum in dealuminated zeolite ZSM-20. In *Studies in Surface Science and Catalysis*, Weitkamp, J.; Karge, H. G.; Pfeifer, H.; Hölderich, W., Eds. Elsevier: 1994; Vol. 84, pp 1013-1020.
65. Remy, M. J.; Stanica, D.; Poncelet, G.; Feijen, E. J. P.; Grobet, P. J.; Martens, J. A.; Jacobs, P. A., Dealuminated H-Y Zeolites: Relation between Physicochemical Properties and Catalytic Activity in Heptane and Decane Isomerization. *The Journal of Physical Chemistry* **1996**, *100* (30), 12440-12447.
66. Bourgeat-Lami, E.; Massiani, P.; Di Renzo, F.; Espiau, P.; Fajula, F.; Des Courières, T., Study of the state of aluminium in zeolite- $\beta$ . *Applied catalysis* **1991**, *72* (1), 139-152.
67. Wang, W.; Xu, J.; Deng, F., Recent advances in solid-state NMR of zeolite catalysts. *National Science Review* **2022**, *9* (9), nwac155.
68. Brouwer, D. H.; Brouwer, C. C.; Mesa, S.; Semelhago, C. A.; Steckley, E. E.; Sun, M. P.; Mikolajewski, J. G.; Baerlocher, C., Solid-state 29Si NMR spectra of pure silica zeolites for the International Zeolite Association Database of Zeolite Structures. *Microporous and Mesoporous Materials* **2020**, *297*, 110000.
69. Maache, M.; Janin, A.; Lavalley, J. C.; Joly, J. F.; Benazzi, E., Acidity of zeolites Beta dealuminated by acid leaching: An FTi.r. study using different probe molecules (pyridine, carbon monoxide). *Zeolites* **1993**, *13* (6), 419-426.
70. Emeis, C. A., Determination of Integrated Molar Extinction Coefficients for Infrared Absorption Bands of Pyridine Adsorbed on Solid Acid Catalysts. *Journal of Catalysis* **1993**, *141* (2), 347-354.
71. Nesterenko, N. S.; Thibault-Starzyk, F.; Montouillout, V.; Yuschenko, V. V.; Fernandez, C.; Gilson, J. P.; Fajula, F.; Ivanova, I. I., Accessibility of the acid sites in dealuminated small-pore mordenites studied by FTIR of co-adsorbed alkylpyridines and CO. *Microporous and Mesoporous Materials* **2004**, *71* (1), 157-166.
72. Sushkevich, V. L.; Ivanova, I. I.; Tolborg, S.; Taarning, E., Meerwein-Ponndorf-Verley-Oppenauer reaction of crotonaldehyde with ethanol over Zr-containing catalysts. *Journal of Catalysis* **2014**, *316*, 121-129.
73. Bordiga, S.; Lamberti, C.; Bonino, F.; Travert, A.; Thibault-Starzyk, F., Probing zeolites by vibrational spectroscopies. *Chemical Society Reviews* **2015**, *44* (20), 7262-7341.
74. Hadjiivanov, K. I.; Vayssilov, G. N., Characterization of oxide surfaces and zeolites by carbon monoxide as an IR probe molecule. *Advances in Catalysis* **2002**, *47*, 307-511.
75. Catana, G.; Baetens, D.; Mommaerts, T.; Schoonheydt, R. A.; Weckhuysen, B. M., Relating structure and chemical composition with lewis acidity in zeolites: A spectroscopic study with probe molecules. *The Journal of Physical Chemistry B* **2001**, *105* (21), 4904-4911.
76. Wischert, R.; Copéret, C.; Delbecq, F.; Sautet, P., Dinitrogen: a selective probe for tri-coordinate Al "defect" sites on alumina. *Chemical Communications* **2011**, *47* (17), 4890-4892.
77. Daniell, W.; Topsøe, N. Y.; Knözinger, H., An FTIR Study of the Surface Acidity of USY Zeolites: Comparison of CO, CD3CN, and C5H5N Probe Molecules. *Langmuir* **2001**, *17* (20), 6233-6239.
78. Barthomeuf, D., Amorphous silica alumina debris in zeolites and zeolitic-type clusters in amorphous silica-alumina catalysts. *Zeolites* **1990**, *10* (2), 131-133.
79. Hadjiivanov, K., Chapter Two - Identification and Characterization of Surface Hydroxyl Groups by Infrared Spectroscopy. In *Advances in Catalysis*, Jentoft, F. C., Ed. Academic Press: 2014; Vol. 57, pp 99-318.
80. Ravi, M.; Sushkevich, V. L.; van Bokhoven, J. A., Lewis acidity inherent to the framework of zeolite mordenite. *The Journal of Physical Chemistry C* **2019**, *123* (24), 15139-15144.
81. Kunkeler, P.; Zuurdeeg, B.; Van Der Waal, J.; van Bokhoven, J. A.; Koningsberger, D.; Van Bekkum, H., Zeolite beta: the relationship between calcination procedure, aluminum configuration, and Lewis acidity. *Journal of catalysis* **1998**, *180* (2), 234-244.

82. Lanzafame, P.; Temi, D. M.; Perathoner, S.; Spadaro, A. N.; Centi, G., Direct conversion of cellulose to glucose and valuable intermediates in mild reaction conditions over solid acid catalysts. *Catalysis Today* **2012**, *179* (1), 178-184.
83. Ramli, N. A. S.; Amin, N. A. S., Kinetic study of glucose conversion to levulinic acid over Fe/HY zeolite catalyst. *Chemical Engineering Journal* **2016**, *283*, 150-159.
84. Boronat, M.; Corma, A.; Renz, M.; Viruela, P. M., Predicting the activity of single isolated Lewis acid sites in solid catalysts. *Chemistry—A European Journal* **2006**, *12* (27), 7067-7077.
85. Konwar, L. J.; Mäki-Arvela, P.; Begum, P.; Kumar, N.; Thakur, A. J.; Mikkola, J.-P.; Deka, R. C.; Deka, D., Shape selectivity and acidity effects in glycerol acetylation with acetic anhydride: Selective synthesis of triacetin over Y-zeolite and sulfonated mesoporous carbons. *Journal of Catalysis* **2015**, *329*, 237-247.
86. Corma, A.; Domine, M. E.; Valencia, S., Water-resistant solid Lewis acid catalysts: Meerwein–Ponndorf–Verley and Oppenauer reactions catalyzed by tin-beta zeolite. *Journal of Catalysis* **2003**, *215* (2), 294-304.
87. Dapsens, P. Y.; Mondelli, C.; Pérez-Ramírez, J., Design of Lewis-acid centres in zeolitic matrices for the conversion of renewables. *Chemical Society Reviews* **2015**, *44* (20), 7025-7043.
88. Wolf, P.; Hammond, C.; Conrad, S.; Hermans, I., Post-synthetic preparation of Sn-, Ti- and Zr-beta: a facile route to water tolerant, highly active Lewis acidic zeolites. *Dalton Transactions* **2014**, *43* (11), 4514-4519.
89. Dapsens, P. Y.; Mondelli, C.; Kusema, B. T.; Verel, R.; Pérez-Ramírez, J., A continuous process for glyoxal valorisation using tailored Lewis-acid zeolite catalysts. *Green Chemistry* **2014**, *16* (3), 1176-1186.
90. Dapsens, P. Y.; Mondelli, C.; Pérez-Ramírez, J., Highly Selective Lewis Acid Sites in Desilicated MFI Zeolites for Dihydroxyacetone Isomerization to Lactic Acid. *ChemSusChem* **2013**, *6* (5), 831-839.
91. Saravanamurugan, S.; Riisager, A., Zeolite-catalyzed isomerization of tetroses in aqueous medium. *Catalysis Science & Technology* **2014**, *4* (9), 3186-3190.
92. Dijkmans, J.; Gabriëls, D.; Dusselier, M.; de Clippel, F.; Vanelderden, P.; Houthoofd, K.; Malfliet, A.; Pontikes, Y.; Sels, B. F., Productive sugar isomerization with highly active Sn in dealuminated  $\beta$  zeolites. *Green Chemistry* **2013**, *15* (10), 2777-2785.
93. Rajabbeigi, N.; Torres, A. I.; Lew, C. M.; Elyassi, B.; Ren, L.; Wang, Z.; Je Cho, H.; Fan, W.; Daoutidis, P.; Tsapatsis, M., On the kinetics of the isomerization of glucose to fructose using Sn-Beta. *Chemical Engineering Science* **2014**, *116*, 235-242.
94. Cho, H. J.; Chang, C.-C.; Fan, W., Base free, one-pot synthesis of lactic acid from glycerol using a bifunctional Pt/Sn-MFI catalyst. *Green Chemistry* **2014**, *16* (7), 3428-3433.
95. Bermejo-Deval, R.; Gounder, R.; Davis, M. E., Framework and Extraframework Tin Sites in Zeolite Beta React Glucose Differently. *ACS Catalysis* **2012**, *2* (12), 2705-2713.
96. Gunther, W. R.; Wang, Y.; Ji, Y.; Michaelis, V. K.; Hunt, S. T.; Griffin, R. G.; Román-Leshkov, Y., Sn-Beta zeolites with borate salts catalyse the epimerization of carbohydrates via an intramolecular carbon shift. *Nature Communications* **2012**, *3* (1), 1109.
97. Gounder, R.; Davis, M. E., Monosaccharide and disaccharide isomerization over Lewis acid sites in hydrophobic and hydrophilic molecular sieves. *Journal of Catalysis* **2013**, *308*, 176-188.
98. Holm, M. S.; Saravanamurugan, S.; Taarning, E., Conversion of Sugars to Lactic Acid Derivatives Using Heterogeneous Zeotype Catalysts. *Science* **2010**, *328* (5978), 602-605.
99. Jae, J.; Mahmoud, E.; Lobo, R. F.; Vlachos, D. G., Cascade of Liquid-Phase Catalytic Transfer Hydrogenation and Etherification of 5-Hydroxymethylfurfural to Potential Biodiesel Components over Lewis Acid Zeolites. *ChemCatChem* **2014**, *6* (2), 508-513.
100. Luo, H. Y.; Consoli, D. F.; Gunther, W. R.; Román-Leshkov, Y., Investigation of the reaction kinetics of isolated Lewis acid sites in Beta zeolites for the Meerwein–Ponndorf–Verley reduction of methyl levulinate to  $\gamma$ -valerolactone. *Journal of Catalysis* **2014**, *320*, 198-207.
101. Nakagawa, Y.; Tamura, M.; Tomishige, K., Perspective on catalyst development for glycerol reduction to C3 chemicals with molecular hydrogen. *Research on Chemical Intermediates* **2018**, *44*, 1-25.

102. Klomp, D.; Maschmeyer, T.; Hanefeld, U.; Peters, J. A., Mechanism of Homogeneously and Heterogeneously Catalysed Meerwein–Ponndorf–Verley–Oppenauer Reactions for the Racemisation of Secondary Alcohols. *Chemistry – A European Journal* **2004**, *10* (8), 2088-2093.
103. Creighton, E.; Ganeshie, S.; Downing, R.; Van Bekkum, H., Stereoselective Meerwein–Ponndorf–Verley and Oppenauer reactions catalysed by zeolite BEA. *Journal of Molecular Catalysis A: Chemical* **1997**, *115* (3), 457-472.
104. Anwander, R.; Palm, C.; Gerstberger, G.; Groeger, O.; Engelhardt, G., Enhanced catalytic activity of MCM-41-grafted aluminium isopropoxide in MPV reductions. *Chemical Communications* **1998**, (17), 1811-1812.
105. Jansen, J. C.; Creighton, E. J.; Njo, S. L.; van Koningsveld, H.; van Bekkum, H., On the remarkable behaviour of zeolite Beta in acid catalysis. *Catalysis today* **1997**, *38* (2), 205-212.
106. Van der Waal, J.; Creighton, E.; Kunkeler, P.; Tan, K.; Van Bekkum, H., Beta-type zeolites as selective and regenerable catalysts in the Meerwein–Ponndorf–Verley reduction of carbonyl compounds. *Topics in Catalysis* **1997**, *4*, 261-268.
107. Caspary, K. J.; Gehrke, H.; Heinritz-Adrian, M.; Schwefer, M., Dehydrogenation of Alkanes. In *Handbook of Heterogeneous Catalysis*, pp 3206-3229.
108. James, O. O.; Mandal, S.; Alele, N.; Chowdhury, B.; Maity, S., Lower alkanes dehydrogenation: Strategies and reaction routes to corresponding alkenes. *Fuel Processing Technology* **2016**, *149*, 239-255.
109. Resasco, D. E., Dehydrogenation – Heterogeneous. In *Encyclopedia of Catalysis*.
110. Sommer, J.; Jost, R., Carbenium and carbonium ions in liquid- and solid-superacid-catalyzed activation of small alkanes. **2000**, *72* (12), 2309-2318.
111. Rovik, A. K.; Hagen, A.; Schmidt, I.; Dahl, S.; Chorkendorff, I.; Christensen, C. H., Dehydrogenation of Light Alkanes Over Rhenium Catalysts on Conventional and Mesoporous MFI Supports. *Catalysis Letters* **2006**, *109* (3), 153-156.
112. Pidko, E. A.; van Santen, R. A., Activation of Light Alkanes over Zinc Species Stabilized in ZSM-5 Zeolite: A Comprehensive DFT Study. *The Journal of Physical Chemistry C* **2007**, *111* (6), 2643-2655.
113. Meitzner, G. D.; Iglesia, E.; Baumgartner, J. E.; Huang, E. S., The Chemical State of Gallium in Working Alkane Dehydrocyclodimerization Catalysts. In situ Gallium K-Edge X-Ray Absorption Spectroscopy. *Journal of Catalysis* **1993**, *140* (1), 209-225.
114. van Bokhoven, J. A.; Tromp, M.; Koningsberger, D. C.; Miller, J. T.; Pieterse, J. A. Z.; Lercher, J. A.; Williams, B. A.; Kung, H. H., An Explanation for the Enhanced Activity for Light Alkane Conversion in Mildly Steam Dealuminated Mordenite: The Dominant Role of Adsorption. *Journal of Catalysis* **2001**, *202* (1), 129-140.
115. Kostyniuk, A.; Bajec, D.; Likožar, B., Catalytic hydrogenation, hydrocracking and isomerization reactions of biomass tar model compound mixture over Ni-modified zeolite catalysts in packed bed reactor. *Renewable Energy* **2021**, *167*, 409-424.
116. Ivanushkin, G.; Dusselier, M., Engineering Lewis Acidity in Zeolite Catalysts by Electrochemical Release of Heteroatoms during Synthesis. *Chemistry of Materials* **2023**.
117. Sushkevich, V. L.; Ivanova, I. I.; Taarning, E., Ethanol conversion into butadiene over Zr-containing molecular sieves doped with silver. *Green Chemistry* **2015**, *17* (4), 2552-2559.
118. Hammond, C.; Conrad, S.; Hermans, I., Simple and scalable preparation of highly active Lewis acidic Sn-β. *Angewandte Chemie International Edition* **2012**, *51* (47), 11736-11739.
119. Perego, C.; Carati, A.; Ingallina, P.; Mantegazza, M. A.; Bellussi, G., Production of titanium containing molecular sieves and their application in catalysis. *Applied Catalysis A: General* **2001**, *221* (1-2), 63-72.
120. Al-Nayili, A.; Albdiry, M.; Salman, N., Dealumination of Zeolite Frameworks and Lewis Acid Catalyst Activation for Transfer Hydrogenation. *Arabian Journal for Science and Engineering* **2021**, *46* (6), 5709-5716.
121. Astorino, E.; Peri, J. B.; Willey, R. J.; Busca, G., Spectroscopic characterization of silicalite-1 and titanium silicalite-1. *Journal of Catalysis* **1995**, *157* (2), 482-500.



122. Corma, A.; Domine, M. E.; Nemeth, L.; Valencia, S., Al-free Sn-beta zeolite as a catalyst for the selective reduction of carbonyl compounds (Meerwein– Ponndorf– Verley reaction). *Journal of the American Chemical Society* **2002**, *124* (13), 3194-3195.
123. Li, K.; Beaver, M.; Speronello, B.; García-Martínez, J., Mesoporous zeolites: Preparation, characterization and applications. Wiley-VCH Weinheim: 2015.
124. Deng, C.; Zhang, J.; Dong, L.; Huang, M.; Bin, L.; Jin, G.; Gao, J.; Zhang, F.; Fan, M.; Zhang, L.; Gong, Y., The effect of positioning cations on acidity and stability of the framework structure of Y zeolite. *Sci Rep* **2016**, *6*, 23382.
125. Rhodes, C. J., Properties and applications of Zeolites. *Science Progress* **2010**, *93* (3), 223-284.
126. Li, G.; Pidko, E. A., The nature and catalytic function of cation sites in zeolites: a computational perspective. *ChemCatChem* **2019**, *11* (1), 134-156.
127. Tromp, M.; van Bokhoven, J. A.; Garriga Oostenbrink, M. T.; Bitter, J. H.; de Jong, K. P.; Koningsberger, D. C., Influence of the Generation of Mesopores on the Hydroisomerization Activity and Selectivity of n-Hexane over Pt/Mordenite. *Journal of Catalysis* **2000**, *190* (2), 209-214.
128. Bañares, M. A., Supported metal oxide and other catalysts for ethane conversion: a review. *Catalysis Today* **1999**, *51* (2), 319-348.
129. Hernández-Beltrán, F.; Moreno-Mayorga, J. C.; Quintana-Solórzano, R.; Sánchez-Valente, J.; Pedraza-Archila, F.; Pérez-Luna, M., Sulfur reduction in cracked naphtha by a commercial additive: effect of feed and catalyst properties. *Applied Catalysis B: Environmental* **2001**, *34* (2), 137-148.
130. Yardimci, D.; Serna, P.; Gates, B., A Highly Selective Catalyst for Partial Hydrogenation of 1, 3-Butadiene: MgO-Supported Rhodium Clusters Selectively Poisoned with CO. *ChemCatChem* **2012**, *4* (10), 1547-1550.
131. Ogino, I.; Gates, B. C., Molecular chemistry in a zeolite: genesis of a zeolite Y-supported ruthenium complex catalyst. *Journal of the American Chemical Society* **2008**, *130* (40), 13338-13346.
132. Martínez-Macias, C.; Chen, M.; Dixon, D. A.; Gates, B. C., Single-Site Zeolite-Anchored Organoiridium Carbonyl Complexes: Characterization of Structure and Reactivity by Spectroscopy and Computational Chemistry. *Chemistry (Weinheim an der Bergstrasse, Germany)* **2015**, *21* (33), 11825-11835.
133. Klinowski, J.; Fyfe, C. A.; Gobbi, G. C., High-resolution solid-state nuclear magnetic resonance studies of dealuminated zeolite Y. *Journal of the Chemical Society, Faraday Transactions 1: Physical Chemistry in Condensed Phases* **1985**, *81* (12), 3003-3019.
134. Bevilacqua, M.; Busca, G., A study of the localization and accessibility of Brønsted and Lewis acid sites of H-mordenite through the FT-IR spectroscopy of adsorbed branched nitriles. *Catalysis Communications* **2002**, *3* (11), 497-502.
135. Marques, J.; Gener, I.; Ayrault, P.; Bordado, J.; Lopes, J.; Ribeiro, F. R.; Guisnet, M., Infrared spectroscopic study of the acid properties of dealuminated BEA zeolites. *Microporous and mesoporous materials* **2003**, *60* (1-3), 251-262.
136. Kühn, G., The coordination of aluminum and silicon in zeolites as studied by x-ray spectrometry. *Journal of Physics and Chemistry of Solids* **1977**, *38* (11), 1259-1263.
137. Hunger, M.; Freude, D.; Pfeifer, H., Magic-angle spinning nuclear magnetic resonance studies of water molecules adsorbed on Brønsted-and Lewis-acid sites in zeolites and amorphous silica–aluminas. *Journal of the Chemical Society, Faraday Transactions* **1991**, *87* (4), 657-662.
138. Ma, D.; Deng, F.; Fu, R.; Han, X.; Bao, X., MAS NMR studies on the dealumination of zeolite MCM-22. *The Journal of Physical Chemistry B* **2001**, *105* (9), 1770-1779.
139. Brus, J.; Kobera, L.; Schoefberger, W.; Urbanová, M.; Klein, P.; Sazama, P.; Tabor, E.; Sklenak, S.; Fishchuk, A. V.; Dědeček, J., Structure of framework aluminum Lewis sites and perturbed aluminum atoms in zeolites as determined by  $^{27}\text{Al}$  {1H} REDOR (3Q) MAS NMR spectroscopy and DFT/molecular mechanics. *Angewandte Chemie International Edition* **2015**, *54* (2), 541-545.
140. Busca, G., Acidity and basicity of zeolites: A fundamental approach. *Microporous and Mesoporous Materials* **2017**, *254*, 3-16.

141. Zhang, Y.; Zhao, R.; Sanchez-Sanchez, M.; Haller, G. L.; Hu, J.; Bermejo-Deval, R.; Liu, Y.; Lercher, J. A., Promotion of protolytic pentane conversion on H-MFI zeolite by proximity of extra-framework aluminum oxide and Brønsted acid sites. *Journal of Catalysis* **2019**, *370*, 424-433.
142. Gil, B.; Zones, S. I.; Hwang, S.-J.; Bejblova, M.; Čejka, J., Acidic properties of SSZ-33 and SSZ-35 novel zeolites: a complex infrared and MAS NMR study. *The Journal of Physical Chemistry C* **2008**, *112* (8), 2997-3007.
143. Phung, T. K.; Busca, G., On the Lewis acidity of protonic zeolites. *Applied Catalysis A: General* **2015**, *504*, 151-157.
144. Ward, J. W., The nature of active sites on zeolites: I. The decationated Y zeolite. *Journal of Catalysis* **1967**, *9* (3), 225-236.
145. Li, S.; Zheng, A.; Su, Y.; Zhang, H.; Chen, L.; Yang, J.; Ye, C.; Deng, F., Brønsted/Lewis acid synergy in dealuminated HY zeolite: a combined solid-state NMR and theoretical calculation study. *Journal of the American Chemical Society* **2007**, *129* (36), 11161-11171.
146. Pidko, E. A.; Hensen, E. J.; Zhidomirov, G. M.; van Santen, R. A., Non-localized charge compensation in zeolites: A periodic DFT study of cationic gallium-oxide clusters in mordenite. *Journal of Catalysis* **2008**, *255* (2), 139-143.
147. Jiao, J.; Ray, S.; Wang, W.; Weitkamp, J.; Hunger, M., Effect of Dehydration on the Local Structure of Framework Silicon Atoms in Zeolites Y Investigated by Solid-State NMR Spectroscopy. *Zeitschrift für anorganische und allgemeine Chemie* **2005**, *631* (2-3), 484-490.
148. Li, G.; Pidko, E. A.; Van Santen, R. A.; Feng, Z.; Li, C.; Hensen, E. J., Stability and reactivity of active sites for direct benzene oxidation to phenol in Fe/ZSM-5: A comprehensive periodic DFT study. *Journal of catalysis* **2011**, *284* (2), 194-206.
149. Shannon, R. D.; Gardner, K. H.; Staley, R. H.; Bergeret, G.; Gallezot, P.; Auroux, A., The nature of the nonframework aluminum species formed during the dehydroxylation of HY. *The Journal of Physical Chemistry* **1985**, *89* (22), 4778-4788.
150. Bhering, D. L.; Ramírez-Solís, A.; Mota, C. J. A., A Density Functional Theory Based Approach to Extraframework Aluminum Species in Zeolites. *The Journal of Physical Chemistry B* **2003**, *107* (18), 4342-4347.
151. Yu, Z.; Zheng, A.; Wang, Q.; Chen, L.; Xu, J.; Amoureux, J. P.; Deng, F., Insights into the Dealumination of Zeolite HY Revealed by Sensitivity-Enhanced <sup>27</sup>Al DQ-MAS NMR Spectroscopy at High Field. *Angewandte Chemie International Edition* **2010**, *49* (46), 8657-8661.
152. Pu, X.; Liu, N.-w.; Shi, L., Acid properties and catalysis of USY zeolite with different extra-framework aluminum concentration. *Microporous and Mesoporous Materials* **2015**, *201*, 17-23.
153. Macedo, A.; Raatz, F.; Boulet, R.; Janin, A.; Lavalley, J. C., Characterization of the Acidity of Highly Dealuminated Y Zeolites. Comparison Between Conventional Treatments and Isomorphous Substitution. In *Studies in Surface Science and Catalysis*, Elsevier: 1988; Vol. 37, pp 375-383.
154. Lohse, U.; Löffler, E.; Hunger, M.; Stöckner, J.; Patzelová, V., Hydroxyl groups of the non-framework aluminium species in dealuminated Y zeolites. *Zeolites* **1987**, *7* (1), 11-13.
155. Menezes, S. M. C.; Camorim, V. L.; Lam, Y. L.; San Gil, R. A. S.; Bailly, A.; Amoureux, J. P., Characterization of extra-framework species of steamed and acid washed faujasite by MQMAS NMR and IR measurements. *Applied Catalysis A: General* **2001**, *207* (1-2), 367-377.
156. Sommer, J.; Jost, R.; Hachoumy, M., Activation of small alkanes on strong solid acids: mechanistic approaches. *Catalysis Today* **1997**, *38* (3), 309-319.
157. Huang, J.; Jiang, Y.; Marthala, V. R. R.; Thomas, B.; Romanova, E.; Hunger, M., Characterization and Acidic Properties of Aluminum-Exchanged Zeolites X and Y. *The Journal of Physical Chemistry C* **2008**, *112* (10), 3811-3818.
158. Zholobenko, V. L.; Kustov, L. M.; Kazansky, V. B.; Loeffler, E.; Lohser, U.; Peuker, C.; Oehlmann, G., On the possible nature of sites responsible for the enhancement of cracking activity of HZSM-5 zeolites dealuminated under mild steaming conditions. *Zeolites* **1990**, *10* (4), 304-306.
159. Zholobenko, V. L.; Kustov, L. M.; Kazansky, V. B.; Loeffler, E.; Lohse, U.; Oehlmann, G., On the nature of the sites responsible for the enhancement of the cracking activity of HZSM-5 zeolites dealuminated under mild steaming conditions: part 2. *Zeolites* **1991**, *11* (2), 132-134.

160. Anand, R.; Maheswari, R.; Hanefeld, U., Catalytic properties of the novel mesoporous aluminosilicate AlTUD-1. *Journal of Catalysis* **2006**, *242* (1), 82-91.
161. Kunkeler, P. J.; Zuurdeeg, B. J.; Van der Waal, J. C.; van Bokhoven, J. A.; Koningsberger, D. C.; Van Bekkum, H., Zeolite Beta: the relationship between calcination procedure, aluminum configuration, and Lewis acidity. *Journal of catalysis* **1998**, *180* (2), 234-244.
162. DeCanio, S. J.; Sohn, J. R.; Fritz, P. O.; Lunsford, J. H., Acid catalysis by dealuminated zeolite-Y: I. Methanol dehydration and cumene dealkylation. *Journal of Catalysis* **1986**, *101* (1), 132-141.
163. Marques, J. P.; Gener, I.; Ayrault, P.; Bordado, J. C.; Lopes, J. M.; Ribeiro, F. R.; Guisnet, M., Infrared spectroscopic study of the acid properties of dealuminated BEA zeolites. *Microporous and mesoporous materials* **2003**, *60* (1-3), 251-262.
164. Anunziata, O. A.; Martínez, M. L.; Costa, M. G., Characterization and acidic properties of Al-SBA-3 mesoporous material. *Materials Letters* **2010**, *64* (4), 545-548.
165. Xia, Z.; Fu, J.; Duan, A.; Han, L.; Wu, H.; Zhao, Z.; Xu, C.; Wang, D.; Wang, B.; Meng, Q., Post Synthesis of Aluminum Modified Mesoporous TUD-1 Materials and Their Application for FCC Diesel Hydrodesulfurization Catalysts. *Catalysts* **2017**, *7* (5), 141-160.
166. Raatz, F.; Freund, E.; Marcilly, C., Study of small-port and large-port mordenite modifications. Part 2.—Ion-exchange properties of thermally treated ammonium forms. *Journal of the Chemical Society, Faraday Transactions 1: Physical Chemistry in Condensed Phases* **1985**, *81* (2), 299-310.
167. Jiao, J.; Altwasser, S.; Wang, W.; Weitkamp, J.; Hunger, M., State of aluminum in dealuminated, nonhydrated zeolites Y investigated by multinuclear solid-state NMR spectroscopy. *The Journal of Physical Chemistry B* **2004**, *108* (38), 14305-14310.
168. Wouters, B. H.; Chen, T. H.; Grobet, P. J., Reversible Tetrahedral– Octahedral Framework Aluminum Transformation in Zeolite Y. *Journal of the American Chemical Society* **1998**, *120* (44), 11419-11425.
169. Haouas, M.; Kogelbauer, A.; Prins, R., The effect of flexible lattice aluminium in zeolite beta during the nitration of toluene with nitric acid and acetic anhydride. *Catalysis letters* **2000**, *70* (1-2), 61-65.
170. Remy, M. J.; Genet, M. J.; Poncelet, G.; Lardinois, P. F.; Notté, P. P., Investigation of dealuminated mordenites by X-ray photoelectron spectroscopy. *The Journal of Physical Chemistry* **1992**, *96* (6), 2614-2617.
171. Collignon, F.; Jacobs, P. A.; Grobet, P.; Poncelet, G., Investigation of the coordination state of aluminum in  $\beta$  zeolites by X-ray photoelectron spectroscopy. *The Journal of Physical Chemistry B* **2001**, *105* (29), 6812-6816.
172. Esquivel, D.; Cruz-Cabeza, A. J.; Jiménez-Sanchidrián, C.; Romero-Salguero, F. J., Local environment and acidity in alkaline and alkaline-earth exchanged  $\beta$  zeolite: Structural analysis and catalytic properties. *Microporous and Mesoporous Materials* **2011**, *142* (2-3), 672-679.
173. van Bokhoven, J. A., In-situ Al K-edge spectroscopy on zeolites: instrumentation, data-interpretation and catalytic consequences. *Physica Scripta* **2005**, *2005* (T115), 76-79.
174. van Bokhoven, J. A.; Koningsberger, D. C.; Kunkeler, P.; Van Bekkum, H.; Kentgens, A. P. M., Stepwise dealumination of zeolite  $\beta$  at specific T-sites observed with  $^{27}\text{Al}$  MAS and  $^{27}\text{Al}$  MQ MAS NMR. *Journal of the American Chemical Society* **2000**, *122* (51), 12842-12847.
175. Abraham, A.; Lee, S.-H.; Shin, C.-H.; Hong, S. B.; Prins, R.; van Bokhoven, J. A., Influence of framework silicon to aluminium ratio on aluminium coordination and distribution in zeolite Beta investigated by  $^{27}\text{Al}$  MAS and  $^{27}\text{Al}$  MQ MAS NMR. *Physical Chemistry Chemical Physics* **2004**, *6* (11), 3031-3036.
176. Xu, B.; Rotunno, F.; Bordiga, S.; Prins, R.; van Bokhoven, J. A., Reversibility of structural collapse in zeolite Y: Alkane cracking and characterization. *Journal of Catalysis* **2006**, *241* (1), 66-73.
177. Altwasser, S.; Jiao, J.; Steuernagel, S.; Weitkamp, J.; Hunger, M., Elucidating the dealumination mechanism of zeolite HY by solid-state NMR spectroscopy. In *Studies in Surface Science and Catalysis*, Elsevier: 2004; Vol. 154, pp 3098-3105.
178. van Bokhoven, J. A.; Van der Eerden, A. M. J.; Koningsberger, D. C., Three-coordinate aluminum in zeolites observed with in situ X-ray absorption near-edge spectroscopy at the Al K-edge:

- flexibility of aluminum coordinations in zeolites. *Journal of the American Chemical Society* **2003**, *125* (24), 7435-7442.
179. Moreno-Recio, M.; Santamaría-González, J.; Maireles-Torres, P., Brønsted and Lewis acid ZSM-5 zeolites for the catalytic dehydration of glucose into 5-hydroxymethylfurfural. *Chemical Engineering Journal* **2016**, *303*, 22-30.
180. Batool, S. R.; Sushkevich, V. L.; van Bokhoven, J. A., Correlating Lewis acid activity to extra-framework aluminum species in zeolite Y introduced by Ion-exchange. *Journal of Catalysis* **2022**, *408*, 24-35.
181. Almutairi, S. M. T.; Mezari, B.; Filonenko, G. A.; Magusin, P. C. M. M.; Rigutto, M. S.; Pidko, E. A.; Hensen, E. J. M., Influence of Extraframework Aluminum on the Brønsted Acidity and Catalytic Reactivity of Faujasite Zeolite. *ChemCatChem* **2013**, *5* (2), 452-466.
182. Valand, R.; Tanna, S.; Lawson, G.; Bengtström, L., A review of Fourier Transform Infrared (FTIR) spectroscopy used in food adulteration and authenticity investigations. *Food Additives & Contaminants: Part A* **2020**, *37* (1), 19-38.
183. Smith, B. C., *Fundamentals of Fourier transform infrared spectroscopy*. CRC press: 2011.
184. Khan, S. A.; Khan, S. B.; Khan, L. U.; Farooq, A.; Akhtar, K.; Asiri, A. M., Fourier transform infrared spectroscopy: fundamentals and application in functional groups and nanomaterials characterization. *Handbook of materials characterization* **2018**, 317-344.
185. Ojeda, J. J.; Dittrich, M., Fourier transform infrared spectroscopy for molecular analysis of microbial cells. *Microbial Systems Biology: Methods and Protocols* **2012**, 187-211.
186. Opella, S. J., Solid-state NMR and membrane proteins. *Journal of magnetic resonance* **2015**, *253*, 129-137.
187. Sels, B.; Kustov, L., Zeolites and zeolite-like materials. **2016**.
188. Chmelka, B. F., Materializing opportunities for NMR of solids. *Journal of Magnetic Resonance* **2019**, *306*, 91-97.
189. HUNGER, M., Brønsted acid sites in zeolites characterized by multinuclear solid-state nmr spectroscopy. *Catalysis Reviews* **1997**, *39* (4), 345-393.
190. Reif, B.; Ashbrook, S. E.; Emsley, L.; Hong, M., Solid-state NMR spectroscopy. *Nature Reviews Methods Primers* **2021**, *1* (1), 2.
191. Massiot, D.; Fayon, F.; Capron, M.; King, I.; Le Calvé, S.; Alonso, B.; Durand, J. O.; Bujoli, B.; Gan, Z.; Hoatson, G., Modelling one- and two-dimensional solid-state NMR spectra. *Magnetic resonance in chemistry* **2002**, *40* (1), 70-76.
192. Czjzek, G.; Fink, J.; Götz, F.; Schmidt, H.; Coey, J.; Rebouillat, J.-P.; Liénard, A., Atomic coordination and the distribution of electric field gradients in amorphous solids. *Physical Review B* **1981**, *23* (6), 2513.
193. Harrington, G. F.; Santiso, J., Back-to-Basics tutorial: X-ray diffraction of thin films. *Journal of Electroceramics* **2021**, *47* (4), 141-163.
194. Fatimah, S.; Ragadhita, R.; Al Husaeni, D. F.; Nandiyanto, A. B. D., How to calculate crystallite size from x-ray diffraction (XRD) using Scherrer method. *ASEAN Journal of Science and Engineering* **2022**, *2* (1), 65-76.
195. Gawas, U. B.; Mandrekar, V. K.; Majik, M. S., Structural analysis of proteins using X-ray diffraction technique. In *Advances in biological science research*, Elsevier: 2019; pp 69-84.
196. Lowell, S.; Shields, J. E.; Thomas, M. A.; Thommes, M., *Characterization of porous solids and powders: surface area, pore size and density*. Springer Science & Business Media: 2006; Vol. 16.
197. Naderi, M., Surface area: brunauer–emmett–teller (BET). In *Progress in filtration and separation*, Elsevier: 2015; pp 585-608.
198. Aguilera, J. A.; Aragón, C.; Cristoforetti, G.; Tognoni, E., Application of calibration-free laser-induced breakdown spectroscopy to radially resolved spectra from a copper-based alloy laser-induced plasma. *Spectrochimica Acta Part B: Atomic Spectroscopy* **2009**, *64* (7), 685-689.
199. Khan, S. R.; Sharma, B.; Chawla, P. A.; Bhatia, R., Inductively Coupled Plasma Optical Emission Spectrometry (ICP-OES): a Powerful Analytical Technique for Elemental Analysis. *Food Analytical Methods* **2022**, *15* (3), 666-688.

200. Donati, G. L.; Amais, R. S.; Williams, C. B., Recent advances in inductively coupled plasma optical emission spectrometry. *Journal of Analytical Atomic Spectrometry* **2017**, *32* (7), 1283-1296.
201. Ghosh, S.; Prasanna, V. L.; Sowjanya, B.; Srivani, P.; Alagaraja, M.; Banji, D., Inductively coupled plasma–optical emission spectroscopy: a review. *Asian Journal of Pharmaceutical Analysis* **2013**, *3* (1), 24-33.
202. Soria, A.; Rodríguez-Sánchez, S.; Sanz, J.; Martínez-Castro, I., Gas Chromatographic Analysis of Food Bioactive Oligosaccharides. 2014; pp 370-398.
203. Krupčík, J.; Gorovenko, R.; Špánik, I.; Sandra, P.; Armstrong, D. W., Flow-modulated comprehensive two-dimensional gas chromatography with simultaneous flame ionization and quadrupole mass spectrometric detection. *Journal of Chromatography A* **2013**, *1280*, 104-111.
204. Lónyi, F.; Lunsford, J. H., The development of strong acidity in hexafluorosilicate-modified Y-type zeolites. *Journal of Catalysis* **1992**, *136* (2), 566-577.
205. Beyerlein, R.; Choi-Feng, C.; Hall, J.; Huggins, B.; Ray, G., Effect of steaming on the defect structure and acid catalysis of protonated zeolites. *Topics in Catalysis* **1997**, *4* (1), 27-42.
206. van Bokhoven, J. A.; Roest, A.; Koningsberger, D.; Miller, J.; Nachtegaal, G.; Kentgens, A., Changes in structural and electronic properties of the zeolite framework induced by extraframework Al and La in H-USY and La (x) NaY: A <sup>29</sup>Si and <sup>27</sup>Al MAS NMR and <sup>27</sup>Al MQ MAS NMR study. *The Journal of Physical Chemistry B* **2000**, *104* (29), 6743-6754.
207. Siantar, D. P.; Millman, W. S.; Fripiat, J. J., Structural defects and cation exchange capacity in dealuminated Y zeolites. *Zeolites* **1995**, *15* (6), 556-560.
208. Luo, H. Y.; Lewis, J. D.; Román-Leshkov, Y., Lewis acid zeolites for biomass conversion: Perspectives and challenges on reactivity, synthesis, and stability. *Annual review of chemical and biomolecular engineering* **2016**, *7*, 663-692.
209. Zhang, R.; Xu, S.; Raja, D.; Khusni, N. B.; Liu, J.; Zhang, J.; Abdulridha, S.; Xiang, H.; Jiang, S.; Guan, Y.; Jiao, Y.; Fan, X., On the effect of mesoporosity of FAU Y zeolites in the liquid-phase catalysis. *Microporous and Mesoporous Materials* **2019**, *278*, 297-306.
210. Araujo, A. S.; Silva, A. O. S.; Souza, M. J. B.; Coutinho, A. C. S. L. S.; Aquino, J. M. F. B.; Moura, J. A.; Pedrosa, A. M. G., Crystallization of ZSM-12 Zeolite with Different Si/Al Ratio. *Adsorption* **2005**, *11* (2), 159-165.
211. Etim, U.; Bai, P.; Wang, Y.; Subhan, F.; Liu, Y.; Yan, Z., Mechanistic insights into structural and surface variations in Y-type zeolites upon interaction with binders. *Applied Catalysis A: General* **2019**, *571*, 137-149.
212. Higgins, F. M.; de Leeuw, N. H.; Parker, S. C., Modelling the effect of water on cation exchange in zeolite A. *Journal of Materials Chemistry* **2002**, *12* (1), 124-131.
213. Dabbawala, A. A.; Suresh kumar Reddy, K.; Mittal, H.; Al Wahedi, Y.; Vaithilingam, B. V.; Karanikolos, G. N.; Singaravel, G.; Morin, S.; Berthod, M.; Alhassan, S. M., Water vapor adsorption on metal-exchanged hierarchical porous zeolite-Y. *Microporous and Mesoporous Materials* **2021**, *326*, 111380.
214. Shannon, R. D.; Gardner, K. H.; Staley, R. H.; Bergeret, G.; Gallezot, P.; Auroux, A., The nature of the nonframework aluminum species formed during the dehydroxylation of H-Y. *The Journal of Physical Chemistry* **1985**, *89* (22), 4778-4788.
215. Li, S.; Zheng, A.; Su, Y.; Zhang, H.; Chen, L.; Yang, J.; Ye, C.; Deng, F., Brønsted/Lewis Acid Synergy in Dealuminated HY Zeolite: A Combined Solid-State NMR and Theoretical Calculation Study. *Journal of the American Chemical Society* **2007**, *129* (36), 11161-11171.
216. Li, S.; Huang, S.-J.; Shen, W.; Zhang, H.; Fang, H.; Zheng, A.; Liu, S.-B.; Deng, F., Probing the Spatial Proximities among Acid Sites in Dealuminated H-Y Zeolite by Solid-State NMR Spectroscopy. *The Journal of Physical Chemistry C* **2008**, *112* (37), 14486-14494.
217. Mota, C. J.; Bhering, D. L.; Rosenbach Jr, N., A DFT study of the acidity of ultrastable Y zeolite: where is the Brønsted/Lewis acid synergism? *Angewandte Chemie* **2004**, *116* (23), 3112-3115.
218. Li, S.; Zheng, A.; Su, Y.; Fang, H.; Shen, W.; Yu, Z.; Chen, L.; Deng, F., Extra-framework aluminium species in hydrated faujasite zeolite as investigated by two-dimensional solid-state NMR

- spectroscopy and theoretical calculations. *Physical Chemistry Chemical Physics* **2010**, *12* (15), 3895-3903.
219. Liu, C.; Li, G.; Hensen, E. J. M.; Pidko, E. A., Nature and Catalytic Role of Extraframework Aluminum in Faujasite Zeolite: A Theoretical Perspective. *ACS Catalysis* **2015**, *5* (11), 7024-7033.
220. Gould, N. S.; Xu, B., Quantification of acid site densities on zeolites in the presence of solvents via determination of extinction coefficients of adsorbed pyridine. *Journal of Catalysis* **2018**, *358*, 80-88.
221. Gabrienko, A. A.; Danilova, I. G.; Arzumanov, S. S.; Pirutko, L. V.; Freude, D.; Stepanov, A. G., Direct Measurement of Zeolite Brønsted Acidity by FTIR Spectroscopy: Solid-State <sup>1</sup>H MAS NMR Approach for Reliable Determination of the Integrated Molar Absorption Coefficients. *The Journal of Physical Chemistry C* **2018**, *122* (44), 25386-25395.
222. Cairon, O.; Chevreau, T. r.; Lavalley, J.-C., Brnsted acidity of extraframework debris in steamed Y zeolites from the FTIR study of CO adsorption. *Journal of the Chemical Society, Faraday Transactions* **1998**, *94* (19), 3039-3047.
223. Wakabayashi, F.; Fujino, T.; Kondo, J. N.; Domen, K.; Hirose, C., FT-IR Studies of Interaction between Zeolitic Hydroxyl Groups and Small Molecules. 2. Adsorption of Oxygen, Hydrogen, and Rare Gases on H-Mordenite at Low Temperatures. *The Journal of Physical Chemistry* **1995**, *99* (40), 14805-14812.
224. Otero Areán, C.; Turnes Palomino, G.; Geobaldo, F.; Zecchina, A., Characterization of Gallosilicate MFI-Type Zeolites by IR Spectroscopy of Adsorbed Probe Molecules. *The Journal of Physical Chemistry* **1996**, *100* (16), 6678-6690.
225. Sigl, M.; Ernst, S.; Weitkamp, J.; Knözinger, H., Characterization of the acid properties of [Al]-, [Ga]- and [Fe]-HZSM-5 by low-temperature FTIR spectroscopy of adsorbed dihydrogen and ethylbenzene disproportionation. *Catalysis Letters* **1997**, *45* (1), 27-33.
226. Lin, J.-S.; Wang, J.-J.; Wang, J.; Wang, I.; Balasamy, R. J.; Aitani, A.; Al-Khattaf, S.; Tsai, T.-C., Catalysis of alkaline-modified mordenite for benzene alkylation of diolefin-containing dodecene for linear alkylbenzene synthesis. *Journal of Catalysis* **2013**, *300*, 81-90.
227. Li, J.; Liu, H.; An, T.; Yue, Y.; Bao, X., Carboxylic acids to butyl esters over dealuminated–realuminated beta zeolites for removing organic acids from bio-oils. *RSC advances* **2017**, *7* (54), 33714-33725.
228. McGlone, J.; Prielcel, P.; Da Vià, L.; Majdal, L.; Lopez-Sanchez, J. A., Desilicated ZSM-5 zeolites for the production of renewable p-xylene via Diels–Alder cycloaddition of dimethylfuran and ethylene. *Catalysts* **2018**, *8* (6), 253.
229. Treacy, M. M. J.; Newsam, J. M., Two new three-dimensional twelve-ring zeolite frameworks of which zeolite beta is a disordered intergrowth. *Nature* **1988**, *332* (6161), 249-251.
230. Simoncic, P.; Armbruster, T., Peculiarity and defect structure of the natural and synthetic zeolite mordenite: A single-crystal X-ray study. *American Mineralogist* **2004**, *89* (2-3), 421-431.
231. Simoncic, P.; Armbruster, T., Se incorporated into zeolite mordenite-Na: a single-crystal X-ray study. *Microporous and Mesoporous Materials* **2004**, *71* (1), 185-198.
232. Kalvachev, Y.; Todorova, T.; Popov, C., Recent Progress in synthesis and application of nanosized and hierarchical mordenite—A Short Review. *Catalysts* **2021**, *11* (3), 308.
233. Li, P.; Liu, G.; Wu, H.; Liu, Y.; Jiang, J.-g.; Wu, P., Postsynthesis and Selective Oxidation Properties of Nanosized Sn-Beta Zeolite. *The Journal of Physical Chemistry C* **2011**, *115* (9), 3663-3670.
234. van Bokhoven, J. A.; Koningsberger, D.; Kunkeler, P.; Van Bekkum, H.; Kentgens, A., Stepwise dealumination of zeolite beta at specific T-sites observed with <sup>27</sup>Al MAS and <sup>27</sup>Al MQ MAS NMR. *Journal of the American Chemical Society* **2000**, *122* (51), 12842-12847.
235. Zecchina, A.; Bordiga, S.; Spoto, G.; Marchese, L.; Petrini, G.; Leofanti, G.; Padovan, M., Silicalite characterization. 2. IR spectroscopy of the interaction of carbon monoxide with internal and external hydroxyl groups. *The Journal of Physical Chemistry* **1992**, *96* (12), 4991-4997.
236. Wu, P.; Komatsu, T.; Yashima, T., IR and MAS NMR studies on the incorporation of aluminum atoms into defect sites of dealuminated mordenites. *The Journal of Physical Chemistry* **1995**, *99* (27), 10923-10931.

237. Nogier, J.-P.; Millot, Y.; Man, P. P.; Shishido, T.; Che, M.; Dzwigaj, S., Probing the Incorporation of Ti(IV) into the BEA Zeolite Framework by XRD, FTIR, NMR, and DR UV–jp810722bis. *The Journal of Physical Chemistry C* **2009**, *113* (12), 4885-4889.
238. Holm, M. S.; Svelle, S.; Joensen, F.; Beato, P.; Christensen, C. H.; Bordiga, S.; Bjørgen, M., Assessing the acid properties of desilicated ZSM-5 by FTIR using CO and 2,4,6-trimethylpyridine (collidine) as molecular probes. *Applied Catalysis A: General* **2009**, *356* (1), 23-30.
239. Daniell, W.; Topsøe, N.-Y.; Knözinger, H., An FTIR study of the surface acidity of USY zeolites: Comparison of CO, CD<sub>3</sub>CN, and C<sub>5</sub>H<sub>5</sub>N probe molecules. *Langmuir* **2001**, *17* (20), 6233-6239.
240. Hadjiivanov, K., Identification and characterization of surface hydroxyl groups by infrared spectroscopy. In *Advances in Catalysis*, Elsevier: 2014; Vol. 57, pp 99-318.
241. Otero-Áreón, C., Low-temperature Fourier-transform infrared investigation of the interaction of CO with nanosized ZSM5 and silicalite. *Journal of the Chemical Society, Faraday Transactions* **1992**, *88* (19), 2959-2969.
242. Kiricsi, I.; Flego, C.; Pazzuconi, G.; Parker, W. O., Jr.; Millini, R.; Perego, C.; Bellussi, G., Progress toward Understanding Zeolite .beta. Acidity: An IR and 27Al NMR Spectroscopic Study. *The Journal of Physical Chemistry* **1994**, *98* (17), 4627-4634.
243. Vimont, A.; Thibault-Starzyk, F.; Lavalley, J., Infrared spectroscopic study of the acidobasic properties of beta zeolite. *The Journal of Physical Chemistry B* **2000**, *104* (2), 286-291.
244. Cannan, T.; Hinchey, R., Synthesis of Zeolite Beta. *US5139759A, August* **1992**, 18.
245. Kumar, N.; Lindfors, L.; Byggningsbacka, R., Synthesis and characterization of H-ZSM-22, Zn-H-ZSM-22 and Ga-H-ZSM-22 zeolite catalysts and their catalytic activity in the aromatization of n-butane. *Applied Catalysis A: General* **1996**, *139* (1-2), 189-199.
246. Yue, Y.; Fu, J.; Wang, C.; Yuan, P.; Bao, X.; Xie, Z.; Basset, J.-M.; Zhu, H., Propane dehydrogenation catalyzed by single Lewis acid site in Sn-Beta zeolite. *Journal of Catalysis* **2021**, *395*, 155-167.
247. Pidko, E. A.; Hensen, E. J. M.; van Santen, R. A., Dehydrogenation of Light Alkanes over Isolated Gallium Ions in Ga/ZSM-5 Zeolites. *The Journal of Physical Chemistry C* **2007**, *111* (35), 13068-13075.
248. Li, B.; Xu, Z.; Chu, W.; Luo, S.; Jing, F., Ordered mesoporous Sn-SBA-15 as support for Pt catalyst with enhanced performance in propane dehydrogenation. *Chinese Journal of Catalysis* **2017**, *38* (4), 726-735.
249. Machado, F. J.; López, C. M.; Campos, Y.; Bolívar, A.; Yunes, S., The transformation of n-butane over Ga/SAPO-11: The role of extra-framework gallium species. *Applied Catalysis A: General* **2002**, *226* (1-2), 241-252.
250. Beyer, H.; Horvath, J.; Reti, F., Catalytic cracking and dehydrogenation of butanes and neopentane on reduced copper-exchanged Y-zeolites. *Reaction Kinetics and Catalysis Letters* **1980**, *14*, 395-401.
251. van Bokhoven, J. A.; Koningsberger, D. C.; Kunkeler, P.; van Bekkum, H., Influence of Steam Activation on Pore Structure and Acidity of Zeolite Beta: An Al K Edge XANES Study of Aluminum Coordination. *Journal of Catalysis* **2002**, *211* (2), 540-547.
252. Van Bokhoven, J. A., In-situ Al K-edge spectroscopy on zeolites: Instrumentation, data-interpretation and catalytic consequences. *Physica Scripta T* **2005**, *T115*, 76-79.
253. Frash, M. V.; van Santen, R., Quantum-chemical modeling of the hydrocarbon transformations in acid zeolite catalysts. *Topics in Catalysis* **1999**, *9*, 191-205.
254. Reddy, K.; Rao, B.; Shiralkar, V., Alkylation of benzene with isopropanol over zeolite beta. *Applied Catalysis A: General* **1993**, *95* (1), 53-63.
255. Tsai, T.-C.; Ay, C.-L.; Wang, I., Cumene disproportionation over zeolite β: I. comparison of catalytic performances and reaction mechanisms of zeolites. *Applied catalysis* **1991**, *77* (2), 199-207.
256. Hoefnagel, A.; Van Bekkum, H., Direct Fries reaction of resorcinol with benzoic acids catalyzed by zeolite H-beta. *Applied Catalysis A: General* **1993**, *97* (2), 87-102.
257. Chuah, G.; Jaenicke, S.; Zhu, Y.; Liu, S., Meerwein-Ponndorf-Verley reduction over heterogeneous catalysts. *Current Organic Chemistry* **2006**, *10* (13), 1639-1654.

258. Bortnovsky, O.; Sobalík, Z.; Wichterlová, B.; Bastl, Z., Structure of Al–Lewis Site in beta zeolite active in the Meerwein–Ponndorf–Verley reduction of ketone to alcohol. *Journal of Catalysis* **2002**, *210* (1), 171-182.
259. Kiricsi, I.; Flego, C.; Pazzuconi, G.; Parker, W. J.; Millini, R.; Perego, C.; Bellussi, G., Progress toward understanding zeolite. beta. acidity: an IR and 27Al NMR spectroscopic study. *The Journal of Physical Chemistry* **1994**, *98* (17), 4627-4634.
260. Dzwigaj, S.; Millot, Y.; Méthivier, C.; Che, M., Incorporation of Nb(V) into BEA zeolite investigated by XRD, NMR, IR, DR UV–vis, and XPS. *Microporous and Mesoporous Materials* **2010**, *130* (1), 162-166.
261. Baran, R.; Millot, Y.; Onfroy, T.; Krafft, J.-M.; Dzwigaj, S., Influence of the nitric acid treatment on Al removal, framework composition and acidity of BEA zeolite investigated by XRD, FTIR and NMR. *Microporous and Mesoporous Materials* **2012**, *163*, 122-130.
262. Oumi, Y.; Nemoto, S.; Nawata, S.; Fukushima, T.; Teranishi, T.; Sano, T., Effect of the framework structure on the dealumination–realumination behavior of zeolite. *Materials Chemistry and Physics* **2003**, *78* (2), 551-557.
263. Zaiku, X.; Qingling, C.; Chengfang, Z.; Jiaqing, B.; Yuhua, C., Influence of Citric Acid Treatment on the Surface Acid Properties of Zeolite Beta. *The Journal of Physical Chemistry B* **2000**, *104* (13), 2853-2859.
264. Omegna, A.; Vasic, M.; Anton van Bokhoven, J.; Pirngruber, G.; Prins, R., Dealumination and realumination of microcrystalline zeolite beta: an XRD, FTIR and quantitative multinuclear (MQ) MAS NMR study. *Physical Chemistry Chemical Physics* **2004**, *6* (2), 447-452.
265. Tang, B.; Dai, W.; Wu, G.; Guan, N.; Li, L.; Hunger, M., Improved Postsynthesis Strategy to Sn-Beta Zeolites as Lewis Acid Catalysts for the Ring-Opening Hydration of Epoxides. *ACS Catalysis* **2014**, *4* (8), 2801-2810.
266. Tang, B.; Dai, W.; Sun, X.; Guan, N.; Li, L.; Hunger, M., A procedure for the preparation of Ti-Beta zeolites for catalytic epoxidation with hydrogen peroxide. *Green Chemistry* **2014**, *16* (4), 2281-2291.
267. Yi, F.; Chen, Y.; Tao, Z.; Hu, C.; Yi, X.; Zheng, A.; Wen, X.; Yun, Y.; Yang, Y.; Li, Y., Origin of weak Lewis acids on silanol nests in dealuminated zeolite Beta. *Journal of Catalysis* **2019**, *380*, 204-214.
268. Groen, J. C.; Moulijn, J. A.; Pérez-Ramírez, J., Decoupling mesoporosity formation and acidity modification in ZSM-5 zeolites by sequential desilication–dealumination. *Microporous and Mesoporous Materials* **2005**, *87* (2), 153-161.
269. Miller, J. T.; Hopkins, P. D.; Meyers, B. L.; Ray, G. J.; Roginski, R. T.; Zajac, G. W.; Rosenbaum, N. H., The effect of nonframework aluminum on acidity in dealuminated mordenite. *Journal of Catalysis* **1992**, *138* (1), 115-128.
270. Loeffler, E.; Lohse, U.; Peuker, C.; Oehlmann, G.; Kustov, L.; Zholobenko, V.; Kazansky, V., Study of different states of nonframework aluminum in hydrothermally dealuminated HZSM-5 zeolites using diffuse reflectance ir spectroscopy. *Zeolites* **1990**, *10* (4), 266-271.
271. Zholobenko, V.; Kustov, L.; Kazansky, V.; Loeffler, E.; Lohser, U.; Peuker, C.; Oehlmann, G., On the possible nature of sites responsible for the enhancement of cracking activity of HZSM-5 zeolites dealuminated under mild steaming conditions. *Zeolites* **1990**, *10* (4), 304-306.
272. Su, B.-L.; Norberg, V., Characterization of the Brønsted Acid Properties of H(Na)-Beta Zeolite by Infrared Spectroscopy and Thermal Analysis. *Zeolites* **1997**, *19* (1), 65-74.
273. Jia, C.; Massiani, P.; Barthomeuf, D., Characterization by infrared and nuclear magnetic resonance spectroscopies of calcined beta zeolite. *Journal of the Chemical Society, Faraday Transactions* **1993**, *89* (19), 3659-3665.
274. Ivanov, V.; Bachelier, J.; Audry, F.; Lavalley, J., Study of the Meerwein–Ponndorf–Verley reaction between ethanol and acetone on various metal oxides. *Journal of molecular catalysis* **1994**, *91* (1), 45-59.



275. Florian, J.; Kubelkova, L., Proton transfer between H-Zeolite and adsorbed acetone or acetonitrile: quantum chemical and FTIR study. *The Journal of Physical Chemistry* **1994**, *98* (35), 8734-8741.
276. Hadjiivanov, K. I.; Vayssilov, G. N., Characterization of oxide surfaces and zeolites by carbon monoxide as an IR probe molecule. **2002**.
277. Pulido, A.; Delgado, M.; Bludský, O.; Rubeš, M.; Nachtigall, P.; Areán, C. O., Combined DFT/CC and IR spectroscopic studies on carbon dioxide adsorption on the zeolite H-FER. *Energy & Environmental Science* **2009**, *2* (11), 1187-1195.
278. Gil, B.; Kafahurska, K.; Kowalczyk, A., A study of the external and internal sites of 2D and 3D zeolites through the FTIR investigation of the adsorption of ammonia and pivalonitrile. *Applied Catalysis A: General* **2019**, *578*, 63-69.
279. Sushkevich, V. L.; Ivanova, I. I.; Yakimov, A. V., Revisiting acidity of SnBEA catalysts by combined application of FTIR spectroscopy of different probe molecules. *The Journal of Physical Chemistry C* **2017**, *121* (21), 11437-11447.
280. Radu, D.; Coman, S.; Parvulescu, V.; De Vos, D.; Jacobs, P.; Sobalik, Z., Investigation of acidic properties of Ir-\* BEA zeolites by Py-, DTBP-, and Qu-FTIR. In *Studies in Surface Science and Catalysis*, Elsevier: 2005; Vol. 158, pp 909-916.
281. Vimont, A.; Thibault-Starzyk, F.; Lavalley, J. C., Infrared Spectroscopic Study of the Acidobasic Properties of Beta Zeolite. *Journal of Physical Chemistry B* **2000**, *104* (2), 286-291.
282. Fitzgerald, J. J.; Piedra, G.; Dec, S. F.; Seger, M.; Maciel, G. E., Dehydration studies of a high-surface-area alumina (pseudo-boehmite) using solid-state <sup>1</sup>H and <sup>27</sup>Al NMR. *Journal of the American Chemical Society* **1997**, *119* (33), 7832-7842.
283. Parker Jr, W.; De Angelis, A.; Flego, C.; Millini, R.; Perego, C.; Zanardi, S., Unexpected destructive dealumination of zeolite beta by silylation. *The Journal of Physical Chemistry C* **2010**, *114* (18), 8459-8468.
284. Nortier, P.; Fourre, P.; Saad, A. B. M.; Saur, O.; Lavalley, J. C., Effects of crystallinity and morphology on the surface properties of alumina. *Applied Catalysis* **1990**, *61* (1), 141-160.
285. Morterra, C.; Magnacca, G., A case study: surface chemistry and surface structure of catalytic aluminas, as studied by vibrational spectroscopy of adsorbed species. *Catalysis Today* **1996**, *27* (3), 497-532.
286. van Gog, H., First-principles study of dehydration interfaces between diaspore and corundum, gibbsite and boehmite, and boehmite and  $\gamma$ -Al<sub>2</sub>O<sub>3</sub>: Energetic stability, interface charge effects, and dehydration defects. *Applied Surface Science* **2021**, *541*, 148501.
287. Vimont, A.; Lavalley, J.; Sahibed-Dine, A.; Otero Areán, C.; Rodríguez Delgado, M.; Daturi, M., Infrared spectroscopic study on the surface properties of  $\gamma$ -gallium oxide as compared to those of  $\gamma$ -alumina. *The Journal of Physical Chemistry B* **2005**, *109* (19), 9656-9664.
288. Chandran, C. V.; Kirschhock, C. E.; Radhakrishnan, S.; Taulelle, F.; Martens, J. A.; Breynaert, E., Alumina: discriminative analysis using 3D correlation of solid-state NMR parameters. *Chemical Society Reviews* **2019**, *48* (1), 134-156.
289. Dědeček, J.; Tabor, E.; Sklenak, S., Tuning the Aluminum Distribution in Zeolites to Increase their Performance in Acid-Catalyzed Reactions. *ChemSusChem* **2019**, *12* (3), 556-576.
290. Maier, S. M.; Jentys, A.; Lercher, J. A., Steaming of zeolite BEA and its effect on acidity: a comparative NMR and IR spectroscopic study. *The Journal of Physical Chemistry C* **2011**, *115* (16), 8005-8013.
291. Zhu, Z.; Ma, H.; Liao, W.; Tang, P.; Yang, K.; Su, T.; Ren, W.; Lü, H., Insight into tri-coordinated aluminum dependent catalytic properties of dealuminated Y zeolites in oxidative desulfurization. *Applied Catalysis B: Environmental* **2021**, *288*, 120022.
292. Khivantsev, K.; Gramatikov, S. P.; Jaegers, N. R.; Derewinski, M. A.; Vayssilov, G. N.; Szanyi, J.; Aleksandrov, H. A., Direct observation of a new aluminum Lewis acid site in a zeolite. **2022**.
293. Zhu, P.; Meier, S.; Saravanamurugan, S.; Riisager, A., Modification of commercial Y zeolites by alkaline-treatment for improved performance in the isomerization of glucose to fructose. *Molecular Catalysis* **2021**, *510*, 111686.

294. Zhou, Y.; Thirumalai, H.; Smith, S. K.; Whitmire, K. H.; Liu, J.; Frenkel, A. I.; Grabow, L. C.; Rimer, J. D., Ethylene dehydroaromatization over Ga-ZSM-5 catalysts: nature and role of gallium speciation. *Angewandte Chemie International Edition* **2020**, *59* (44), 19592-19601.
295. Orlyk, S.; Kantserova, M.; Chedryk, V.; Kyriienko, P.; Balakin, D.; Millot, Y.; Dzwigaj, S., Ga (Nb, Ta) SiBEA zeolites prepared by two-step postsynthesis method: acid–base characteristics and catalytic performance in the dehydrogenation of propane to propylene with CO<sub>2</sub>. *Journal of Porous Materials* **2021**, *28* (5), 1511-1522.
296. Bai, J.; Ling, W.; Chen, W.; Liu, Y.; Sun, P.; Wang, H.; Wang, C., The role of aluminum in Sn-Al-beta zeolite catalyzing the conversion of glucose to methyl lactate. *Molecular Catalysis* **2023**, *541*, 113071.
297. Zheng, A.; Li, S.; Liu, S.-B.; Deng, F., Acidic properties and structure–activity correlations of solid acid catalysts revealed by solid-state nmr spectroscopy. *Accounts of chemical research* **2016**, *49* (4), 655-663.
298. Agostini, G.; Lamberti, C.; Palin, L.; Milanese, M.; Danilina, N.; Xu, B.; Janousch, M.; Van Bokhoven, J. A., In situ XAS and XRPD parametric Rietveld refinement to understand dealumination of Y zeolite catalyst. *Journal of the American Chemical Society* **2009**, *132* (2), 667-678.
299. Kao, H.-M.; Grey, C. P., Probing the Brønsted and Lewis acidity of zeolite HY: a <sup>1</sup>H/<sup>27</sup>Al and <sup>15</sup>N/<sup>27</sup>Al TRAPDOR NMR study of monomethylamine adsorbed on HY. *The Journal of Physical Chemistry* **1996**, *100* (12), 5105-5117.
300. Kao, H.-M.; Liu, H.; Jiang, J.-C.; Lin, S.-H.; Grey, C. P., Determining the structure of trimethylphosphine bound to the Brønsted acid site in zeolite HY: Double-resonance NMR and ab initio studies. *The Journal of Physical Chemistry B* **2000**, *104* (20), 4923-4933.
301. Jin, F.; Li, Y., A FTIR and TPD examination of the distributive properties of acid sites on ZSM-5 zeolite with pyridine as a probe molecule. *Catalysis Today* **2009**, *145* (1-2), 101-107.
302. Van der Mynsbrugge, J.; Janda, A.; Lin, L.-C.; Van Speybroeck, V.; Head-Gordon, M.; Bell, A. T., Understanding Brønsted-Acid Catalyzed Monomolecular Reactions of Alkanes in Zeolite Pores by Combining Insights from Experiment and Theory. *ChemPhysChem* **2018**, *19* (4), 341-358.
303. Van Speybroeck, V.; Hemelsoet, K.; Joos, L.; Waroquier, M.; Bell, R. G.; Catlow, C. R. A., Advances in theory and their application within the field of zeolite chemistry. *Chemical Society Reviews* **2015**, *44* (20), 7044-7111.
304. Van Speybroeck, V.; De Wispelaere, K.; Van der Mynsbrugge, J.; Vandichel, M.; Hemelsoet, K.; Waroquier, M., First principle chemical kinetics in zeolites: the methanol-to-olefin process as a case study. *Chemical Society Reviews* **2014**, *43* (21), 7326-7357.
305. Wang, S.; He, Y.; Jiao, W.; Wang, J.; Fan, W., Recent experimental and theoretical studies on Al siting/acid site distribution in zeolite framework. *Current Opinion in Chemical Engineering* **2019**, *23*, 146-154.
306. Nimlos, C. T.; Hoffman, A. J.; Hur, Y. G.; Lee, B. J.; Di Iorio, J. R.; Hibbitts, D. D.; Gounder, R., Experimental and theoretical assessments of aluminum proximity in MFI zeolites and its alteration by organic and inorganic structure-directing agents. *Chemistry of Materials* **2020**, *32* (21), 9277-9298.
307. Antúñez-García, J.; Galván, D.; Petranovskii, V.; Murrieta-Rico, F. N.; Yocupicio-Gaxiola, R. I.; Shelyapina, M. G.; Fuentes-Moyado, S., Aluminum distribution in mordenite-zeolite framework: A new outlook based on density functional theory calculations. *Journal of Solid State Chemistry* **2022**, *306*, 122725.
308. Kolganov, A. A.; Gabrienko, A. A.; Chernyshov, I. Y.; Stepanov, A. G.; Pidko, E. A., The accuracy challenge of the DFT-based molecular assignment of <sup>13</sup>C MAS NMR characterization of surface intermediates in zeolite catalysis. *Physical Chemistry Chemical Physics* **2020**, *22* (41), 24004-24013.

## Publications and presentations

### Publications

1. Pan, Z., Puente-Urbina, A., **Batool, S. R.**, Bodi, A., Wu, X., Zhang, Z., van Bokhoven, J. A. & Hemberger, P. (2023) Tuning the Zeolite Acidity Enables Selectivity Control by Suppressing Ketene Formation in Lignin Catalytic Pyrolysis, *Nature Communications*, 14, 4512. (doi.org/10.1038/s41467-023-40179-z)
2. **Batool, S. R.**, Sushkevich, V. L., & van Bokhoven, J. A. (2023) Factors affecting the generation and catalytic activity of extra-framework aluminum Lewis acid sites in aluminum-exchanged zeolites, *ACS Catalysis* (Under Review).
3. **Batool, S. R.**, Sushkevich, V. L., & van Bokhoven, J. A. (2022). Correlating Lewis acid activity to extraframework aluminum species in zeolite Y introduced by Ion-exchange. *Journal of Catalysis*, 408, 24-35.
4. **Batool, S. R.**, Malana, M. A., Alfryyan, N., Ashiq, M. N., Aftab, F., Aman, S., & Alomairy, S. (2022). Synthesis, characterization, dielectric and magnetic properties of substituted Y-type hexaferrites. *Journal of Materials Science: Materials in Electronics*, 33(20), 16183-16196.
5. Farid, M. A., Ijaz, S., Ashiq, M. N., Ehsan, M. F., Gul, F., **Batool, S. R.**, & Noor ul Hassan, S. (2022). Synthesis of mesoporous zirconium manganese mixed metal oxide nanowires for photocatalytic reduction of CO<sub>2</sub>. *Journal of Materials Research*, 1-11.
6. Fiaz, M., Kashif, M., Shah, J. H., Ashiq, M. N., Gregory, D. H., **Batool, S. R.**, & Athar, M. (2021). Incorporation of MnO<sub>2</sub> nanoparticles into MOF-5 for efficient oxygen evolution reaction. *Ionics*, 27, 2159-2167.
7. Fiaz, M., Kashif, M., Fatima, M., **Batool, S. R.**, Asghar, M. A., Shakeel, M., & Athar, M. (2020). Synthesis of efficient TMS@ MOF-5 catalysts for oxygen evolution reaction. *Catalysis Letters*, 150, 2648-2659.
8. Malana, M. A., Aftab, F., & **Batool, S. R.** (2019). Synthesis and characterization of stimuli-responsive hydrogel based on starch and methyl-3-aminocrotonate: swelling and degradation kinetics. *Polymer Bulletin*, 76, 3073-3092

## Presentations

- 2023 **Syeda Rabia Batool**, Sushkevich L. Vitaly, Paunović Vladimir, Jeroen A. van Bokhoven, 9th Conference of the Federation of the European Zeolite Associations (FEZA) Poster and Oral Presentation
- 2022 **Syeda Rabia Batool**, Sushkevich L. Vitaly, Paunović Vladimir, Jeroen A. van Bokhoven, Insights into Lewis acidic nature of extra-framework aluminum centers incorporated in zeolites by ion-exchange University of Zurich, Switzerland Swiss Chemical Society Fall, Meeting Poster Presentation
- 2022 **Syeda Rabia Batool**, Sushkevich L. Vitaly, Paunović Vladimir, Jeroen A. van Bokhoven, Lewis acid activity of extra-framework Aluminum introduced in Zeolite Y by ion-exchange San Diego, USA American Chemical Society Spring Meeting, Poster and Oral
- 2021 **Syeda Rabia Batool**, Sushkevich L. Vitaly, Jeroen A. van Bokhoven, Correlating Lewis acid activity to extra-framework aluminum species in zeolite Y introduced by ion-exchange (online due to Covid) Swiss Chemical Society Fall Meeting Poster Presentation
- 2021 **Syeda Rabia Batool**, Sushkevich L. Vitaly, Jeroen A. van Bokhoven, Introducing Lewis acidity in zeolites by Ion-Exchanging Extra-Framework Cations (online due to Covid) Swiss Chemical Society Fall Meeting Poster Presentation

## Appendix A

### Appendix to Chapter 4

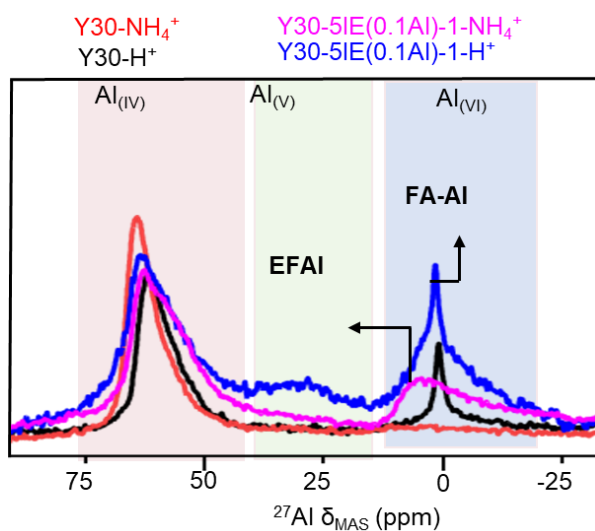


Figure A.1:  $^{27}\text{Al}$  MAS NMR spectra; Y30 in H form (black) has sharp octahedral resonance at ~0ppm ( $\text{VI}_a$ ), after aluminum ion-exchange and calcination to proton form in Y30-5IE(0.1Al)-1-H form (red), sharp resonance at ~0 ppm still persists together with emergence of broad asymmetrical resonance ~3ppm ( $\text{VI}_b$ ); after conversion of aluminum exchanged sample to  $\text{NH}_4$  for, the sharp peak at ~0ppm disappears followed by increase in intensity of the tetrahedral resonance at ~61ppm and only broad, asymmetrical feature continues to be present.

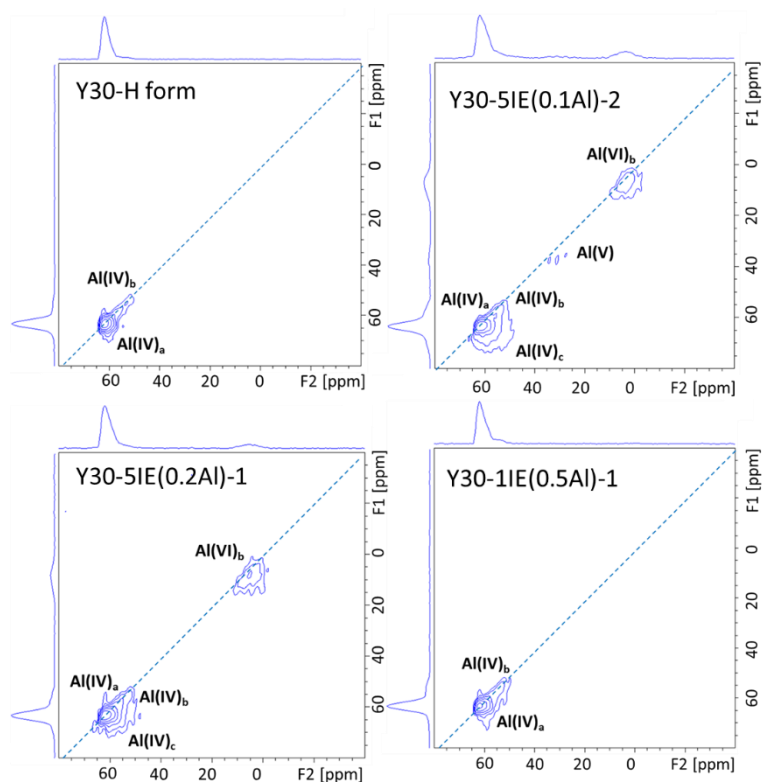


Figure A.2:  $^{27}\text{Al}$  MQMAS spectra of pristine zeolite Y and aluminum ion-exchanged zeolites.

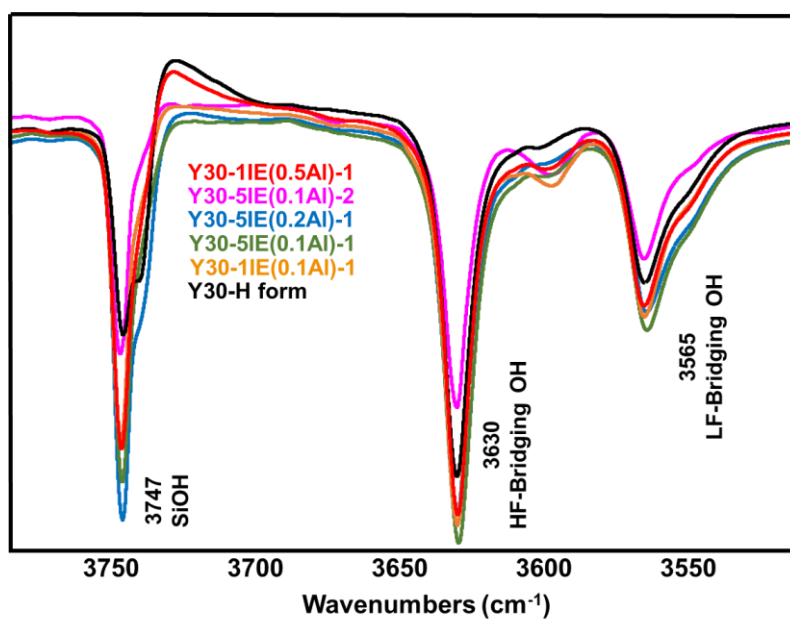


Figure A.3: Py-FTIR difference spectra in OH stretching region obtained by subtraction of spectra after activation at 723K from spectra after Py adsorption at 423K followed by evacuation at 423K

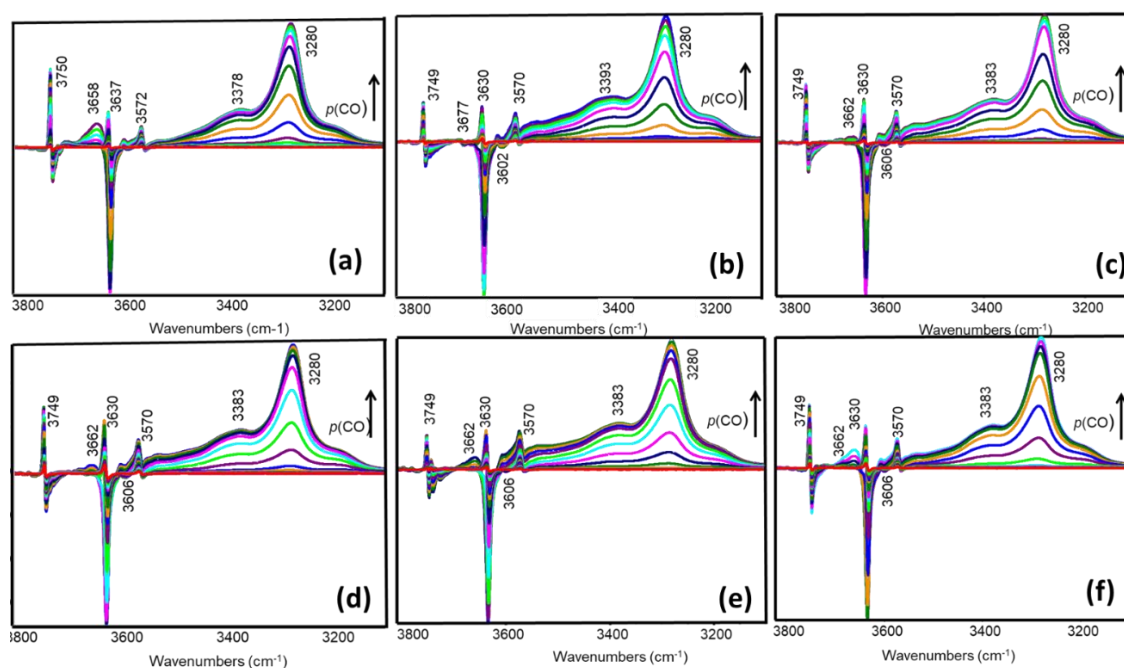


Figure A.4: CO-FTIR difference spectra in OH stretching region obtained by subtraction of spectra of cold wafers at 70K from spectra after CO adsorption at 70K. (a) Y30-H form (b) Y30-1IE(0.1Al)-1 (c) Y30-5IE(0.1Al)-1 (d) Y30-5IE(0.1Al)-2 (e) Y30-5IE(0.2Al)-1 (f) Y30-1IE(0.5Al)-1

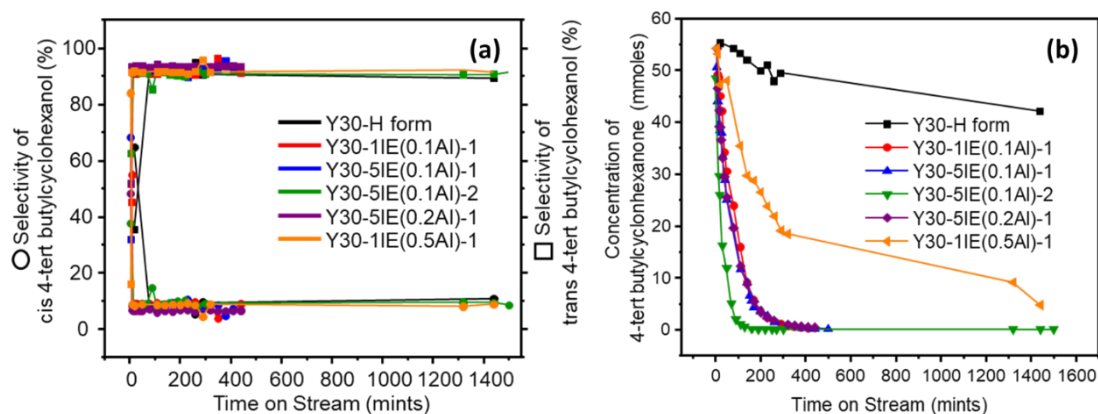


Figure A.5: (a) Differential selectivity of cis and trans products of catalytic reaction over pristine and modified zeolites. (b) Conc. of 4-tert butyl cyclohexanone during time of stream.

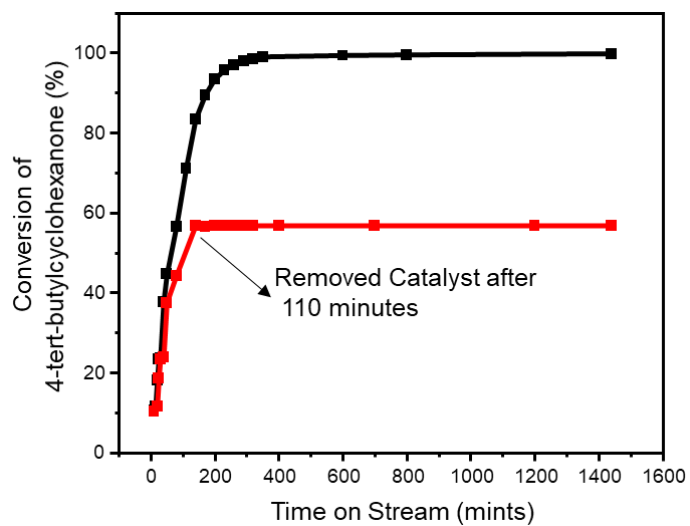


Figure A.6: Hot filtration test with Y30-1IE(0.1Al)-1; black curve is for 1<sup>st</sup> experiment with catalyst during the whole time on stream, red curve is for 2<sup>nd</sup> experiment under same reaction conditions but the catalyst was removed by filtration after 110 minutes and the filtrate was allowed to run on its own for rest of time



# Appendix B

## Appendix to Chapter 5

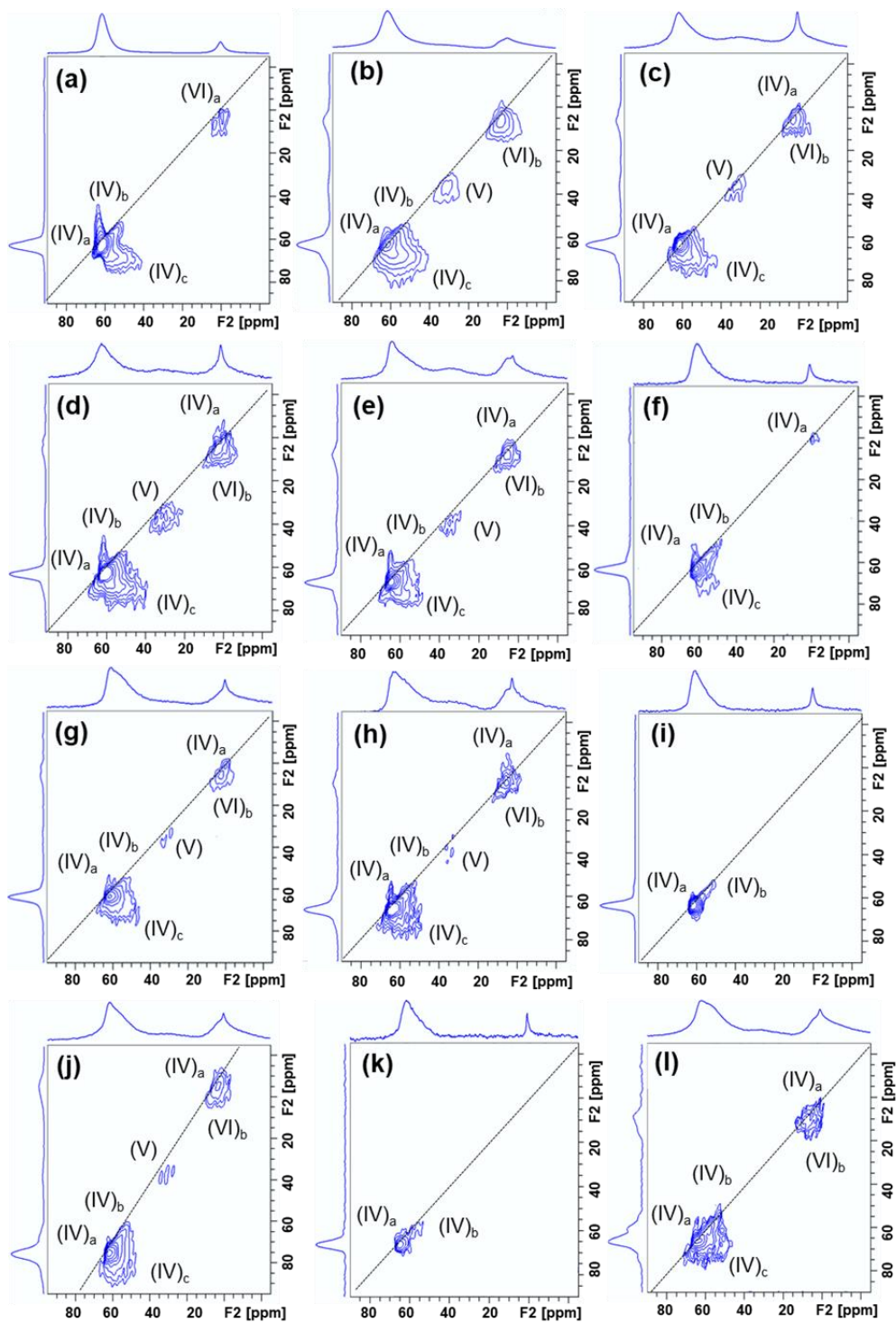


Figure B.1:  $^{27}\text{Al}$  MQMAS spectra of pristine zeolite Y with different Si/Al ratios and aluminum ion-exchanged zeolites. (a) Y2.5- $\text{H}^+$  (b) Y2.5-1IE(0.1Al) (c) Y6- $\text{H}^+$  (d) Y6-1IE(0.1Al) (e) Y6-5IE(0.1Al) (f) Y15- $\text{H}^+$  (g) Y15-1IE(0.1Al) (h) Y17-5IE(0.1Al) (i) Y30- $\text{H}^+$  (j) Y30-5IE(0.1Al) (k) Y40- $\text{H}^+$  (l) Y40-1IE(0.1Al).

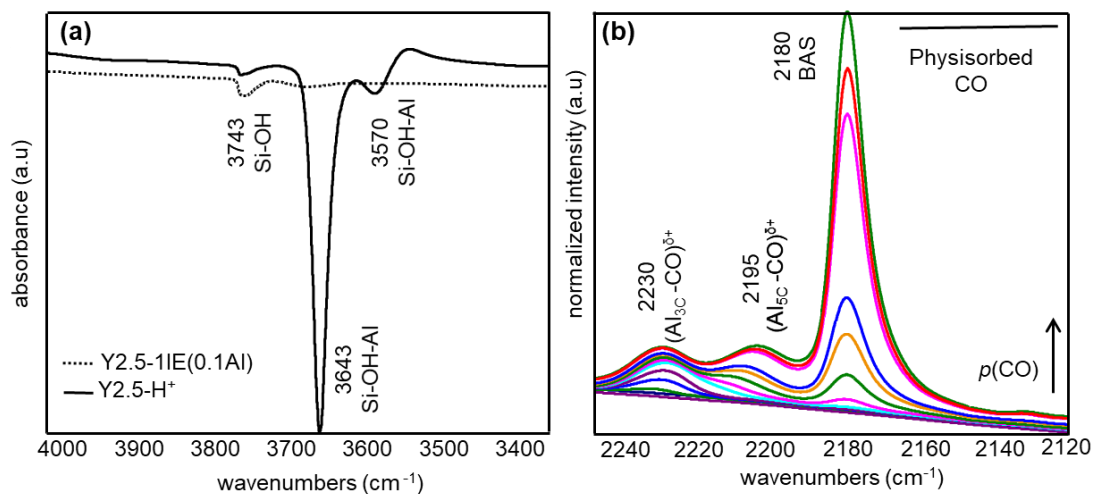


Figure B.2: (a) Py-FTIR difference spectra in OH stretching region obtained by subtraction of spectra after activation at 723K from spectra after Py adsorption at 423K followed by evacuation at 423K. (b) FTIR difference spectra in carbon monoxide stretching region of Y2.5-1IE(0.1Al).

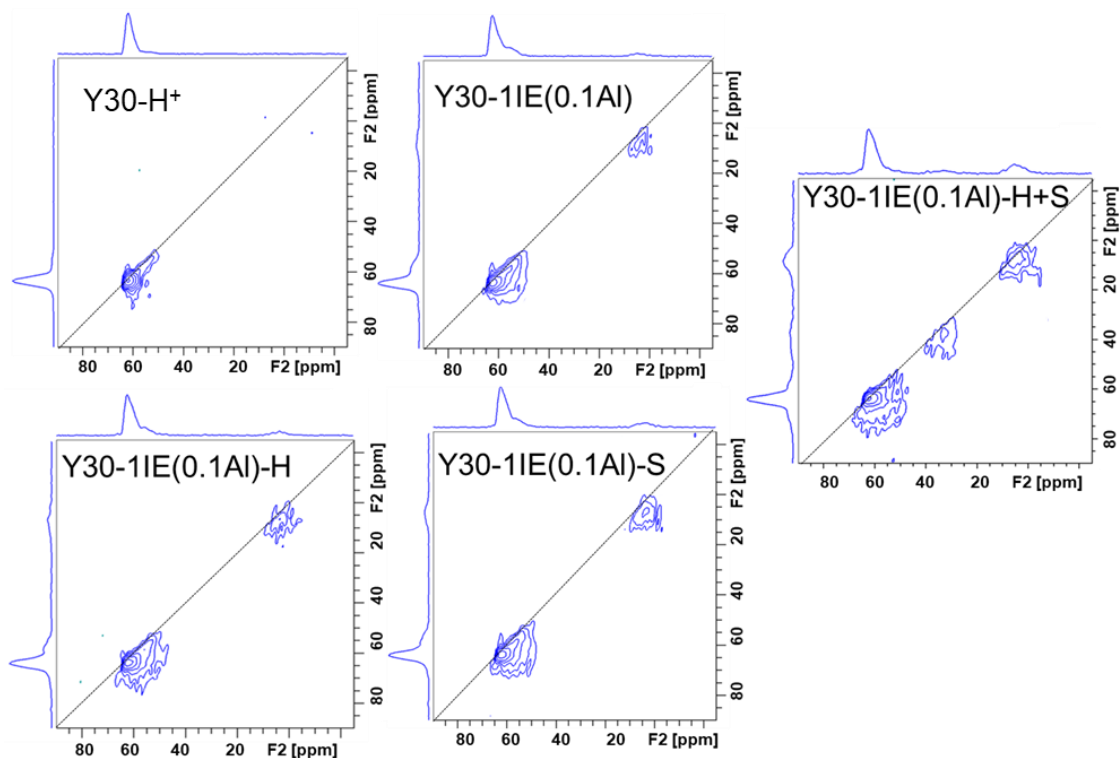


Figure B.3:  $^{27}\text{Al}$  MQMAS spectra of pristine zeolite Y30- $\text{H}^+$  and aluminum-exchanged samples under different Al-IE conditions.

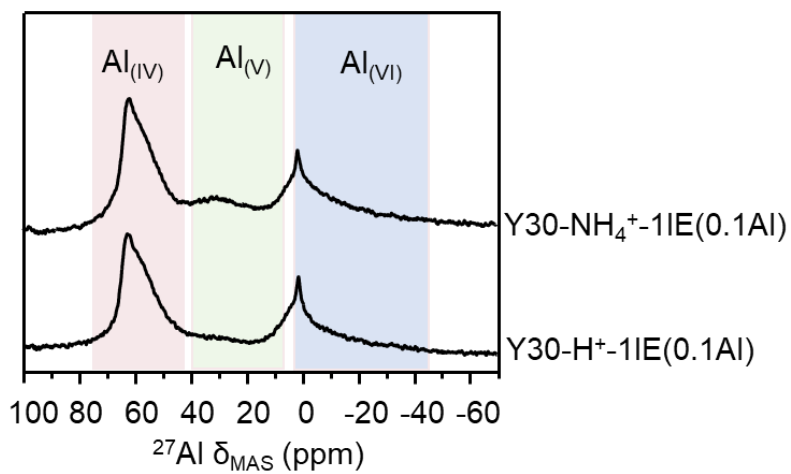


Figure B.4:  $^{27}\text{Al}$  MAS NMR spectra of aluminum-exchanged samples starting with Y30 in parent and ammonium forms.

Table B.1: (a) the concentration of sodium, silicon, and aluminum (mmoles g<sup>-1</sup>) obtained from ICP; (b) the concentration of aluminum (mmoles g<sup>-1</sup>) in different geometrical coordinations obtained by deconvolution of <sup>27</sup>Al MAS NMR spectra using NMR parameters from <sup>27</sup>Al MQMAS NMR.

Zeolite	<sup>a</sup> Na	<sup>a</sup> Si	<sup>a</sup> Al	<sup>b</sup> Al <sub>(IV)a</sub>	<sup>b</sup> Al <sub>(IV)b</sub>	<sup>b</sup> Al <sub>(IV)c</sub>	<sup>b</sup> Al <sub>(V)</sub>	<sup>b</sup> Al <sub>(VI)a</sub>	<sup>b</sup> Al <sub>(VI)b</sub>
Y2.5-H <sup>+</sup>	1.80	24.01	8.86	4.83	0.30	1.51	0.00	2.21	0.00
Y2.5-1IE(0.1Al)	1.50	23.10	9.24	2.30	0.23	2.93	0.57	-	3.21
Y2.5-5IE(0.1Al)	1.60	24.20	10.94	1.57	0.44	3.75	1.10	-	4.08
Y6-H <sup>+</sup>	0.15	30.28	5.41	2.56	0.33	0.66	0.02	1.34	0.50
Y6-1IE(0.1Al)	0.13	30.07	5.65	2.52	0.21	0.79	0.11	1.30	0.72
Y6-5IE(0.1Al)	0.14	29.73	6.03	2.59	0.22	0.83	0.34	1.22	0.83
Y15-H <sup>+</sup>	0.05	30.6	2.04	1.21	0.26	0.14	0.04	0.39	0.00
Y15-1IE(0.1Al)	0.04	31	3.40	1.24	0.14	0.33	0.25	0.36	1.08
Y15-5IE(0.1Al)	0.06	30.33	4.05	1.31	0.31	0.45	0.41	0.39	1.18
Y30-H <sup>+</sup>	0.10	34.50	1.13	0.54	0.37	0.00	0.00	0.24	0.00
Y30-1IE(0.1Al)	0.10	33.50	2.20	0.50	0.30	0.41	0.00	0.16	1.12
Y30-5IE(0.1Al)	0.26	32.50	3.25	0.59	0.38	0.68	0.10	0.21	1.29
Y30-1IE(0.1Al)-H	0.11	34.20	2.02	0.51	0.29	0.43	0.03	0.15	0.61
Y30-1IE(0.1Al)-S	0.13	34.60	2.61	0.57	0.35	0.38	0.12	0.22	0.97
Y30-1IE(0.1Al)-H+S	0.10	33.90	2.63	0.45	0.22	0.50	0.21	0.22	1.03
Y30-Na	0.98	32.90	1.08	0.52	0.56	0.00	0.00	0.00	0.00
Y30-Na-1IE(0.1Al)	0.20	34.50	1.98	0.51	0.22	0.27	0.13	0.29	0.56
Y30-1IE(0.1Al)-Na	0.66	33.50	2.24	0.50	0.51	0.38	0.08	0.00	0.77
Y(40)-H <sup>+</sup>	0.09	36.42	0.91	0.41	0.38	0.00	0.00	0.12	0.00
Y40-1IE(0.1Al)	0.08	32.80	2.50	0.42	0.39	0.43	0.10	0.13	1.03
Y40-5IE(0.1Al)	10.00	31.26	3.60	0.46	0.46	0.72	0.19	0.15	1.62

Table B.2: LAS and BAS concentration in mmoles g<sup>-1</sup> ( $\pm 10\%$ ) obtained from pyridine-FTIR spectroscopy (a); catalytic data of MPV reduction of 4-*tert* butylcyclohexanone ( $\pm 5\%$ ); conversion of 4-*tert* butylcyclohexanone over after 7.4 h (b); initial rate of reaction in mmolesL<sup>-1</sup>min<sup>-1</sup>(c); cumulative selectivity after 7.4 h to *cis* and *trans* 4-*tert* butylcyclohexanol (d).

<b>Zeolite</b>	<b>Py-LAS<sup>a</sup></b>	<b>Py-BAS<sup>a</sup></b>	<b>Coversion<sup>b</sup></b>	<b>Initial Rate<sup>c</sup></b>	<b><i>trans:cis</i><sup>d</sup></b>
Y2.5-H <sup>+</sup>	0.22	0.75	15.2	0.05	04:96
Y2.5-1IE(0.1Al)	0.62	0.08	10.3	0.04	41:59
Y2.5-5IE(0.1Al)	0.67	0.01	8.2	0.04	45:55
Y6-H <sup>+</sup>	0.11	0.25	25.2	0.07	68:32
Y6-1IE(0.1Al)	0.14	0.24	38.3	0.17	90:10
Y6-5IE(0.1Al)	0.18	0.24	98.3	0.24	92:08
Y15-H <sup>+</sup>	0.08	0.18	24	0.08	75:25
Y15-1IE(0.1Al)	0.13	0.19	99	0.26	90:10
Y15-5IE(0.1Al)	0.19	0.17	99.9	0.44	86:14
Y30-H <sup>+</sup>	0.07	0.14	21	0.02	75:25
Y30-1IE(0.1Al)	0.15	0.13	99.4	0.34	90:10
Y30-5IE(0.1Al)	0.23	0.12	99.9	0.45	87:13
Y30-1IE(0.1Al)-H	0.13	0.13	92.5	0.27	85:15
Y30-1IE(0.1Al)-S	0.20	0.14	99.9	0.38	86:14
Y30-1IE(0.1Al)-H+S	0.11	0.12	81.2	0.22	85:15
Y30-Na	0.02	0.02	10.3	0.01	20:80
Y30-Na-1IE(0.1Al)	0.11	0.09	80.1	0.27	84:16
Y30-1IE(0.1Al)-Na	0.09	0.06	36	0.10	90:10
Y(40)-H <sup>+</sup>	0.02	0.08	22.2	0.06	76:24
Y40-1IE(0.1Al)	0.17	0.09	99.6	0.42	88:12
Y40-5IE(0.1Al)	0.26	0.08	100	0.51	88:12

# Appendix C

## Appendix to Chapter 6

### C2. Lewis acid catalytic activity in MOR and MFI

**Figure 6.7a** shows that, before aluminum-exchange, MOR(11) and MFI(15) show very little conversion of 4-*tert* butylcyclohexanone during the time on stream, even after 7 h reaching the maximum conversion of only 10% and 9% respectively (**Table 6.4**). The corresponding initial rates of ketone conversion are also very low accounting for 0.03 and 0.04 mmolL<sup>-1</sup>min<sup>-1</sup>, respectively (**Figure 6.7d and Table 6.4**). MFI(15) and MOR(11) are more selective towards *trans*-ol with *cis:trans* selectivity of 37:63 and 25:75 respectively.

After aluminum-exchange, no significant difference in the conversion of MOR(11)-IE(Al) and MFI(15)-IE(Al) is observed during the reaction (**Figure 6.7b**). The maximum conversion achieved also remains similar as that of respective parent zeolites i.e. 9% and 10% at a reaction rate of 0.04 and 0.05 mmolL<sup>-1</sup>min<sup>-1</sup>, respectively (**Figure 6.7d and Table 6.4**). Also, the ratio of *cis:trans* selectivity does not vary (within the range of error limits) for these two samples after aluminum modification. It is an established fact that Si/Al ratio plays an important role in determining the catalytic activity of zeolite catalysts in many different reactions. Therefore, MFI and MOR zeolites with higher Si/Al ratio i.e. MFI(40) and MOR(45) were also tested for this reaction before and after aluminum-exchange treatment (**Table C3**). However, the catalytic conversion and the initial rate of reaction for MFI(40), MFI(40)-IE(Al), MOR(45) and MOR(45)-IE(Al) samples remain comparable to those at lower Si/Al ratios (**Table C3**).

### C3. Factors affecting the generation and activity of extra-framework Lewis acid sites in different zeolites

In order to understand and establish any (negative/positive) structure-performance correlations in the studied zeolites, it is essential to evaluate the factors affecting the generation and activity of LAS in these zeolites (*vide infra*).

Zeolite FAU (zeolite Y), however, is a large pore zeolite consisting of a three-dimensional structure of pores made of large supercages (1.2 nm) with and small sodalite cages (0.74 nm)

connecting them and the MPV reaction in case of FAU occurs inside the micropores. Zeolite MOR is large pore and a semi-two-dimensional channel system (**Table 6.1**). Apart from 12-MR, it has intersecting 8-MR channels with a window spanning of 5.7 x 2.6 Å. The strongly compressed 8-MR rings, with no/very little flexibility are termed as “side pockets” of zeolite MOR. It has been proposed that a major proportion of FA-Al species of MOR zeolite are located inside these 8-MR “side pockets”. Therefore, pyridine, being a bulky molecule could not access the aluminum sitting deep inside the “side pockets” of zeolite MOR. This corroborates why MOR(11), despite having maximum and very large concentration of FA-Al species, detected using NMR spectroscopy, does not give consistently higher content of LAS probed by pyridine (**Figures 6.8a, b**). Not only LAS, but also BAS moieties tend to sit inside side pockets of MOR. This is substantiated by significant intensity of the band at 3587 cm<sup>-1</sup>, in the FTIR spectrum of adsorbed pyridine over MOR(11), associated to BAS, not accessed by pyridine (**Figure 6.5**). The very low catalytic conversion in MPV reaction, yet with very high concentration of FA-Al and very wide pore openings of MOR(11) can be explained in terms of accessibility limitations. After Al-IE, in the it is very likely that the EFAl can only be stabilized in the side pockets of MOR. Consequently, the aluminum precursor could face steric constraints diffusing through these narrow pores of otherwise uni-dimensional channel system. As a result Al-IE becomes ineffective to generate EFAl LAS in MOR(11)-IE(Al).

The very low Lewis acidity (accessed by pyridine) and the very low catalytic conversion in MPV reaction in case of MOR(11), yet with a very high concentration of FA-Al and wide pore openings, can be explained in terms of accessibility limitations offered by 8-MR “side pockets”. Similarly, the lowest incorporation of EFAl after Al-IE is also proposed to be potentially because of the position of these sites and the side pockets. There is also a second possibility that, these species could not be formed/stabilized in the side pockets of zeolite due to the FA-Al already sitting in there. The latter proposal can be supported by the fact that in MOR(45)-IE(Al), only little fraction of FA-Al is formed (**Figure C2**). However, due to the accessibility limitation, these species were neither able to show an equivalent increase in LAS content, nor to efficiently catalyze the MPV reaction (**Figure C2, Table C3**).

In the MPV mechanism, the reaction is initiated by the formation of aluminum isopropoxide species by interaction of aluminum center with isopropanol. This is then followed by coordination of aluminum isopropoxide species to the ketone and results in a six-membered ring transition state complex (**Figure C3**). Since the most of the Lewis acidic aluminum of MOR(11) (FA-Al Al(VI<sub>a</sub>) species) are located in the side pockets, it is highly unlikely, that 8-

MR side pockets can accommodate isopropanol and 4-*tert* butyl cyclohexanone to form a six-membered transition state. Therefore, the reaction shown by MOR(11) is supposed to occur over FA-Al, which are not located in the side pockets (**Figure 6.8a, and 6.8b**). This is the reason why this zeolite exhibits greater selectivity towards *trans*-ol rather than *cis*-ol.

In the case of MFI (ZSM5), although the channels of this zeolite are relatively small, it was shown that naphthalene molecules with a diameter of even 0.74 nm can adsorb in the pores. This is because, a molecule can diffuse in the c-dimension by alternatively navigating along first two dimensions which explains the flexibility of 10-MR structures. This is the reason that, MFI(15) zeolite, with the sum of concentration of FA-Al Al(VI<sub>a</sub>) and FA-Al Al(VI<sub>b</sub>) species, way lower as compared to MOR(11), exhibits Lewis acid content comparable to the latter (**Figure 6.8b**). The very low conversion and rate of reaction for MFI(15), comparable to that of MOR(11), can also be explained in terms of steric restrictions associated with the entry and exit of 4-*tert* butyl cyclohexanone and *cis/trans* 4-*tert* butyl cyclohexanol and formation of the MPV transition state (**Figure 6.8 a and 6.8b**).

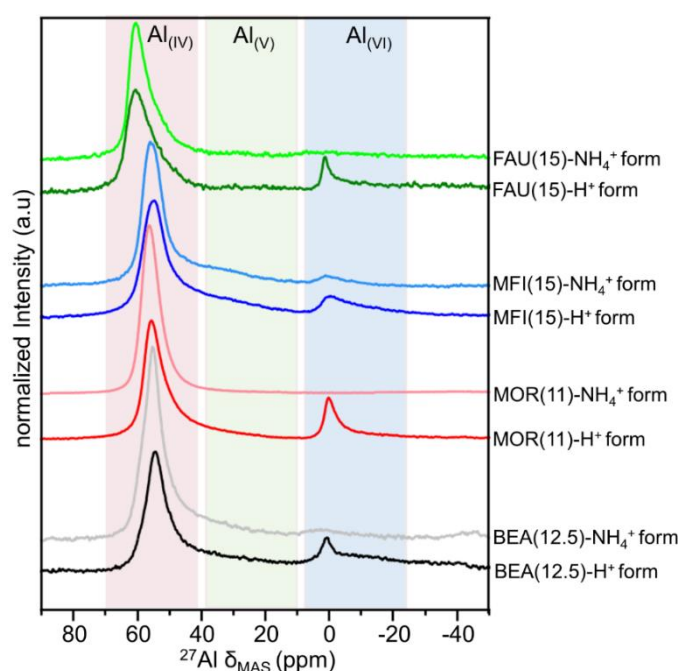


Figure C1.  $^{27}\text{Al}$  MAS NMR spectra of parent zeolites in their proton forms ( $\text{H}^+$ -forms and ammonium forms ( $\text{NH}_4^+$ -forms).



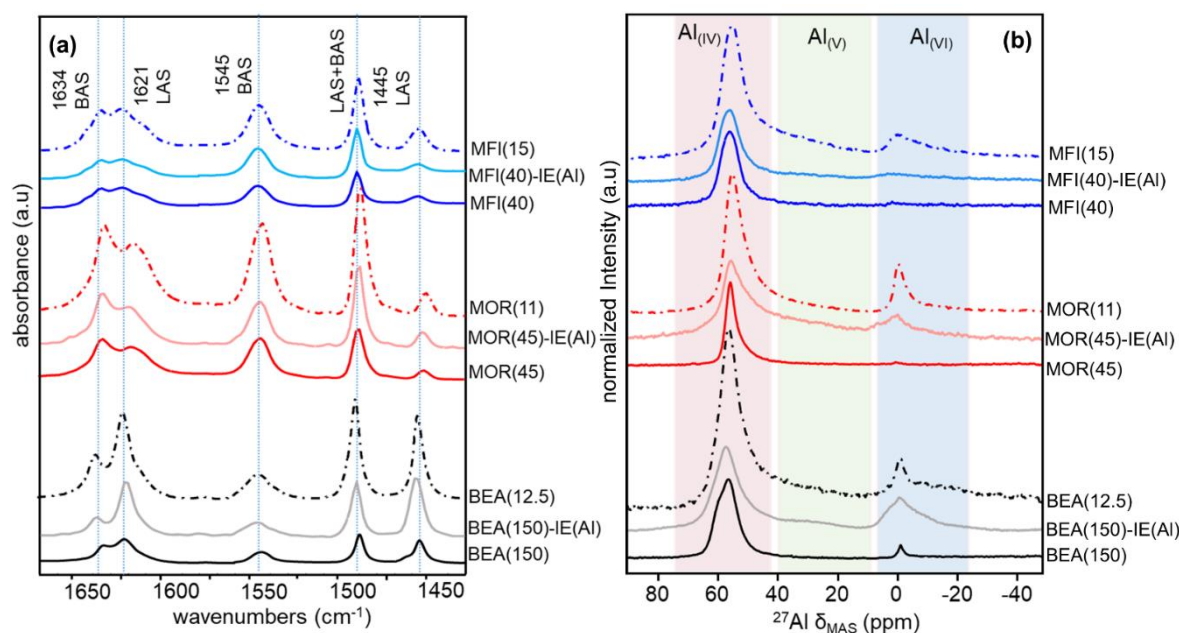


Figure C2. Pyridine-FTIR difference spectra in pyridine stretching region obtained by subtraction of spectra after activation at 723K from spectra after pyridine adsorption at 423K followed by evacuation at 423K (a) and  $^{27}\text{Al}$  MQMAS spectra (b). For comparison, pyridine-FTIR difference spectra and  $^{27}\text{Al}$  MQMAS spectra of MOR(11) and MFI(15) are shown as dotted spectra, in (a) and (b), respectively

Table C1. Silicon (a) and aluminum (b) concentration (mmoles  $\text{g}^{-1}$ ) obtained from ICP; concentration of aluminum (mmoles  $\text{g}^{-1}$ ) in different geometrical coordinations obtained by deconvolution of  $^{27}\text{Al}$  MAS NMR spectra using NMR parameters from  $^{27}\text{Al}$  MQMAS NMR (c).

	<sup>a</sup> Si content	<sup>a</sup> Al content	<sup>c</sup> Al <sub>(IV)a</sub>	<sup>c</sup> Al <sub>(IV)b</sub>	<sup>c</sup> Al <sub>(IV)c</sub>	<sup>c</sup> Al <sub>(V)</sub>	<sup>c</sup> Al <sub>(VD)a</sub>	<sup>c</sup> Al <sub>(VD)b</sub>
BEA(12.5)	40.4	3.23	1.39	0.56	0.14	0.19	0.56	0.39
BEA(12.5)-IE(Al)	37.4	3.59	1.44	0.44	0.24	0.34	0.34	0.79
MOR(11)	32.9	2.98	1.9	-	0.39	-	0.69	-
MOR(11)-IE(Al)	35.0	3.03	1.82	-	0.48	-	0.73	-
MFI(15)	30.7	2.13	1.26	-	0.45	-	0.4	0.02
MFI(15)-IE(Al)	30.7	2.37	1.15	-	0.51	0.13	0.49	0.07
FAU(15)	30.6	2.04	1.21	0.26	0.14	0.04	0.39	-
FAU(15)-IE(Al)	31.0	3.40	1.24	0.14	0.33	0.25	0.36	1.08

Table C2. Physicochemical characterization of parent and aluminum-exchanged zeolites

<b>Zeolite</b>	<sup>a</sup> <b>S<sub>BET</sub></b> <b>m<sup>2</sup>g<sup>-1</sup></b>	<sup>b</sup> <b>V<sub>total</sub></b> <b>cm<sup>3</sup>g<sup>-1</sup></b>	<sup>c</sup> <b>V<sub>micro</sub></b> <b>cm<sup>3</sup>g<sup>-1</sup></b>	<sup>c</sup> <b>S<sub>micro</sub></b> <b>m<sup>2</sup>g<sup>-1</sup></b>	<sup>c</sup> <b>S<sub>meso</sub></b> <b>m<sup>2</sup>g<sup>-1</sup></b>	<sup>f</sup> <b>Crystallinity<sub>rel</sub></b> <b>(%)</b>
MOR(45)	400	0.25	0.19	350	50	100
MOR(45)-IE(Al)	480	0.26	0.18	340	140	93
MFI(40)	370	0.16	0.16	310	60	100
MFI(40)-IE(Al)	360	0.15	0.15	300	60	95
BEA(150)	490	0.22	0.21	350	170	100
BEA(150)-IE(Al)	480	0.23	0.20	360	180	91

<sup>a</sup>calculated from BET method, <sup>b</sup>based on single point adsorption at p/p<sub>0</sub> = 0.97, <sup>c</sup>calculated from t-plot method, <sup>d</sup>calculated by a previously described method<sup>180</sup>, assuming the crystallinity of parent zeolites as 100%,

Table C3. LAS and BAS concentration in mmoles g<sup>-1</sup> ( $\pm$  10 %) obtained from pyridine-FTIR spectroscopy (a) Catalytic data of MPV reduction of 4-tert butylcyclohexanone ( $\pm$  5 %); Percentage conversion of 4-tert butylcyclohexanone over time on stream (b) Initial Rate of reaction in mmolesL<sup>-1</sup> min<sup>-1</sup> (c) Percentage cumulative selectivity to cis and trans 4-tert butylcyclohexanol (d).

<b>Zeolite</b>	<b>Py-LAS<sup>a</sup></b>	<b>Py-BAS<sup>a</sup></b>	<b>Initial Rate<sup>b</sup></b>	<b>Conversion<sup>c</sup></b>	<b>cis:trans<sup>d</sup></b>
MOR(45)	0.02	0.15	0.04	7	40:60
MOR(45)-IE(Al)	0.05	0.14	0.06	11	33:67
MFI(40)	0.01	0.09	0.02	5	88:12
MFI(40)-IE(Al)	0.01	0.10	0.02	5	90:10
BEA(150)	0.03	0.06	0.3	42	92:08
BEA(150)-IE(Al)	0.18	0.07	1.59	100	89:11

# Appendix D

## Appendix to Chapter 7

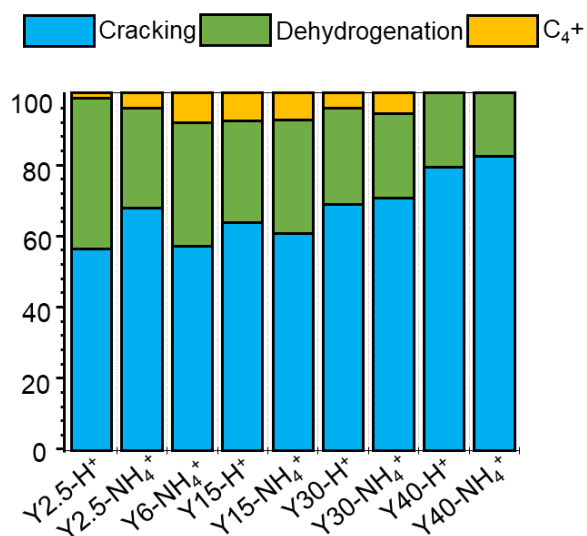


Figure D.1. Selectivity (%) of cracking (CH<sub>4</sub>, C<sub>2</sub>H<sub>4</sub>, C<sub>2</sub>H<sub>6</sub>, C<sub>3</sub>H<sub>6</sub>, and C<sub>3</sub>H<sub>8</sub>), dehydrogenation (*i*-C<sub>4</sub>H<sub>10</sub>, *i*-C<sub>4</sub>H<sub>8</sub>, 1-C<sub>4</sub>H<sub>8</sub>, and 2-C<sub>4</sub>H<sub>8</sub>) and C<sub>4</sub><sup>+</sup> products over parent Y zeolites in their proton and ammonium forms at 823K.

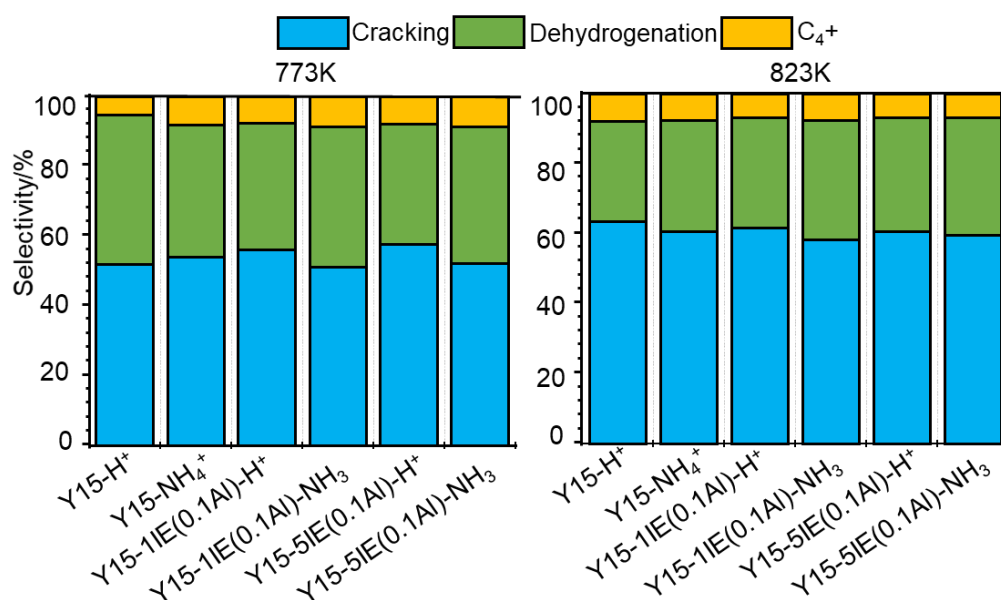


Figure D.2. Selectivity (%) of cracking (CH<sub>4</sub>, C<sub>2</sub>H<sub>4</sub>, C<sub>2</sub>H<sub>6</sub>, C<sub>3</sub>H<sub>6</sub>, and C<sub>3</sub>H<sub>8</sub>), dehydrogenation (*i*-C<sub>4</sub>H<sub>10</sub>, *i*-C<sub>4</sub>H<sub>8</sub>, 1-C<sub>4</sub>H<sub>8</sub>, and 2-C<sub>4</sub>H<sub>8</sub>) and C<sub>4</sub><sup>+</sup> products over parent Y15 and aluminum-exchanged samples in their proton and ammonium forms at two different reaction temperatures at 773 K (left) and 823K (right).

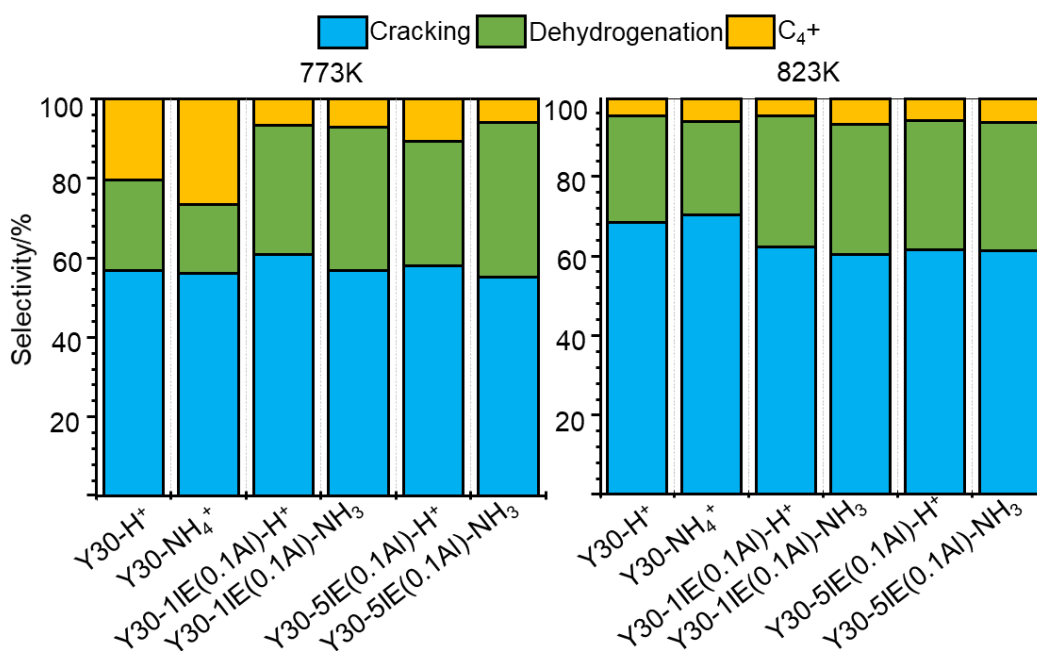


Figure D.3. Selectivity (%) of cracking ( $\text{CH}_4$ ,  $\text{C}_2\text{H}_4$ ,  $\text{C}_2\text{H}_6$ ,  $\text{C}_3\text{H}_6$ , and  $\text{C}_3\text{H}_8$ ), dehydrogenation ( $i$ - $\text{C}_4\text{H}_{10}$ ,  $i$ - $\text{C}_4\text{H}_8$ ,  $1$ - $\text{C}_4\text{H}_8$ , and  $2$ - $\text{C}_4\text{H}_8$ ) and  $\text{C}_4^+$  products over parent Y30 and aluminum-exchanged samples in their proton and ammonium forms at two different reaction temperatures of 773 K (left) and 823K (right).

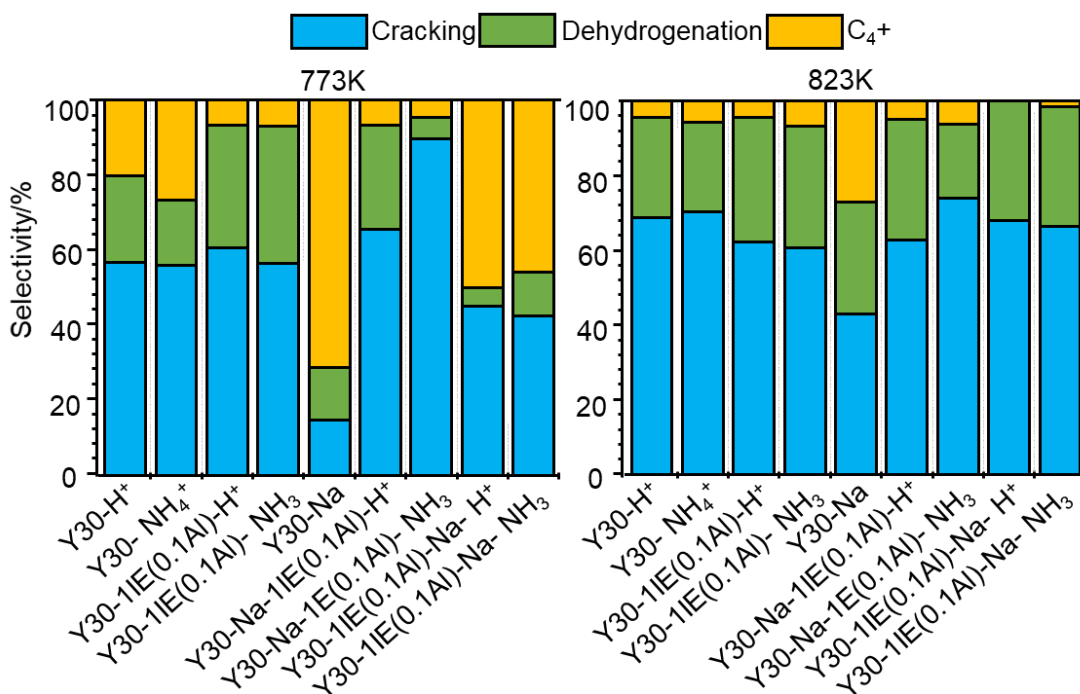


Figure D.4. Selectivity (%) of cracking ( $\text{CH}_4$ ,  $\text{C}_2\text{H}_4$ ,  $\text{C}_2\text{H}_6$ ,  $\text{C}_3\text{H}_6$ , and  $\text{C}_3\text{H}_8$ ), dehydrogenation ( $i$ - $\text{C}_4\text{H}_{10}$ ,  $i$ - $\text{C}_4\text{H}_8$ ,  $1$ - $\text{C}_4\text{H}_8$ , and  $2$ - $\text{C}_4\text{H}_8$ ) and  $\text{C}_4^+$  products over proton and ammonium forms of parent and aluminum-exchanged Y30 samples, having sodium cations, at two different reaction temperatures of 773 K (left) and 823K (right).

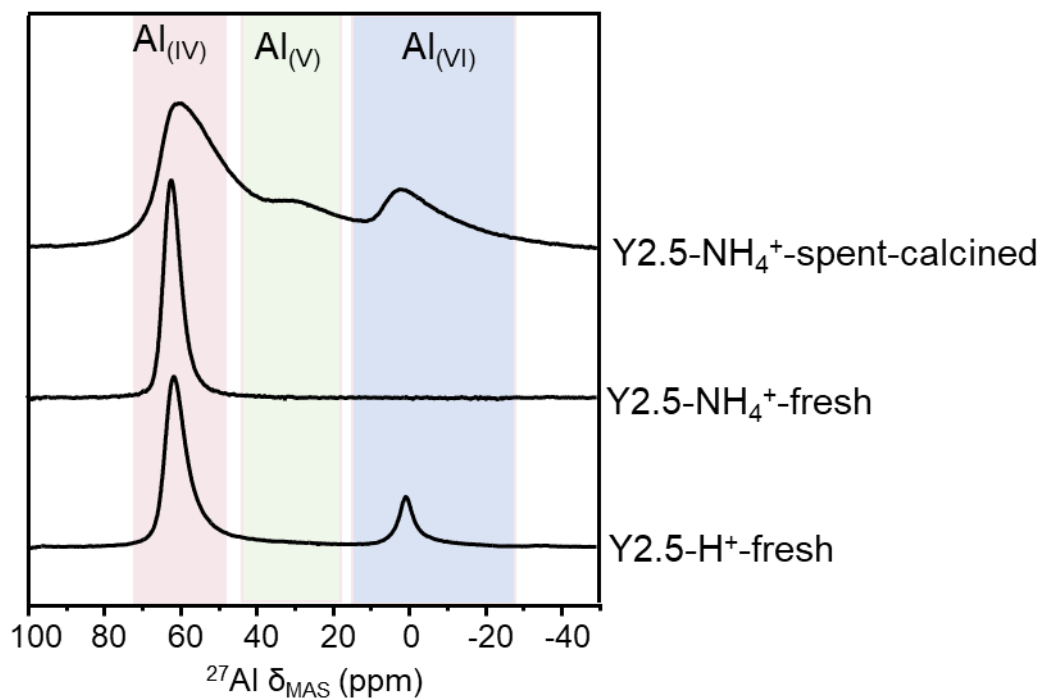


Figure D.4.  $^{27}\text{Al}$  MAS NMR spectra of fresh and regenerated Y2.5 in parent and ammonium forms. The presented spectra are normalized to the weight of the sample used. Colored regions are added to guide the eye.

Table D1. (a) Conversion (X) % and (b) Selectivity (%) of cracking, dehydrogenation, and C<sub>4</sub><sup>+</sup> products over all zeolites at 5% conversion of n-butane. Selectivities for samples marked by \* and \*\* are given at 2% and 1.5 conversion, respectively.

<b>Zeolite</b>	<b><sup>a</sup>Conversion</b>	<b><sup>b</sup>Cracking</b>	<b><sup>b</sup>Dehydrogenation</b>	<b><sup>b</sup>C<sub>4</sub><sup>+</sup></b>
Y2.5-H <sup>+</sup>	4.6	*56	*42	*02
Y2.5-NH <sub>4</sub> <sup>+</sup>	9.8	65	27	08
Y6- NH <sub>4</sub> <sup>+</sup>	17.3	48	43	10
Y15-H <sup>+</sup>	22	52	39	09
Y15-NH <sub>4</sub> <sup>+</sup>	20	49	44	07
Y15-1IE(0.1Al)-H <sup>+</sup>	15	49	38	13
Y15-1IE(0.1Al)-NH <sub>3</sub>	16.8	48	43	09
Y15-5IE(0.1Al)-H <sup>+</sup>	17	61	34	06
Y15-5IE(0.1Al)-NH <sub>3</sub>	17.5	50	37	12
Y30-H <sup>+</sup>	5.3	74	22	04
Y30- NH <sub>4</sub> <sup>+</sup>	5.0	71	24	05
Y30-1IE(0.1Al)-H <sup>+</sup>	9.1	61	35	04
Y30-1IE(0.1Al)- NH <sub>3</sub>	10.4	57	37	7
Y30-5IE(0.1Al)-H <sup>+</sup>	12.2	56	39	6
Y30-5IE(0.1Al)- NH <sub>3</sub>	12.7	54	40	06
Y30-Na	1.3	**43	**30	**27
Y30-Na-1IE(0.1Al)-H <sup>+</sup>	7.1	63	32	05
Y30-Na-1IE(0.1Al)- NH <sub>3</sub>	8.2	74	20	06
Y30-1IE(0.1Al)-Na-H <sup>+</sup>	2.1	*68	*32	-
Y30-1IE(0.1Al)-Na-NH <sub>3</sub>	2.5	*67	*31	*02
Y(40)-H <sup>+</sup>	3.5	*65	*27	*8
Y(40)- NH <sub>4</sub> <sup>+</sup>	2.1	*55	*35	*10

Table D.2: Total carbon deposits (wt %) calculated from TGA profiles of the spent catalysts in n-butane dehydrogenation.

<b>Zeolite</b>	<b>Total carbon deposit (wt %)</b>	<b>Zeolite</b>	<b>Total carbon deposit (wt %)</b>
Y2.5-H <sup>+</sup>	2.1	Y30-H <sup>+</sup>	0.4
Y2.5-NH <sub>4</sub> <sup>+</sup>	2.3	Y30- NH <sub>4</sub> <sup>+</sup>	0.08
Y6- NH <sub>4</sub> <sup>+</sup>	2.07	Y30-1IE(0.1Al)-H <sup>+</sup>	1.35
Y15-H <sup>+</sup>	1.95	Y30-1IE(0.1Al)- NH <sub>4</sub> <sup>+</sup>	0.6
Y15- NH <sub>4</sub> <sup>+</sup>	1.38	Y30-5IE(0.1Al)-H <sup>+</sup>	0.9
Y15-1IE(0.1Al)-H <sup>+</sup>	1.41	Y30-5IE(0.1Al)- NH <sub>4</sub> <sup>+</sup>	0.9
Y15-1IE(0.1Al)- NH <sub>4</sub> <sup>+</sup>	3.07	Y30-Na-1IE(0.1Al)-H <sup>+</sup>	1.05
Y15-5IE(0.1Al)-H <sup>+</sup>	0.4	Y30-Na-1IE(0.1Al)- NH <sub>4</sub> <sup>+</sup>	0.8
Y15-5IE(0.1Al)- NH <sub>4</sub> <sup>+</sup>	1.87	Y(40)- NH <sub>4</sub> <sup>+</sup>	0.33

# Appendix E

## Appendix to Chapter 8

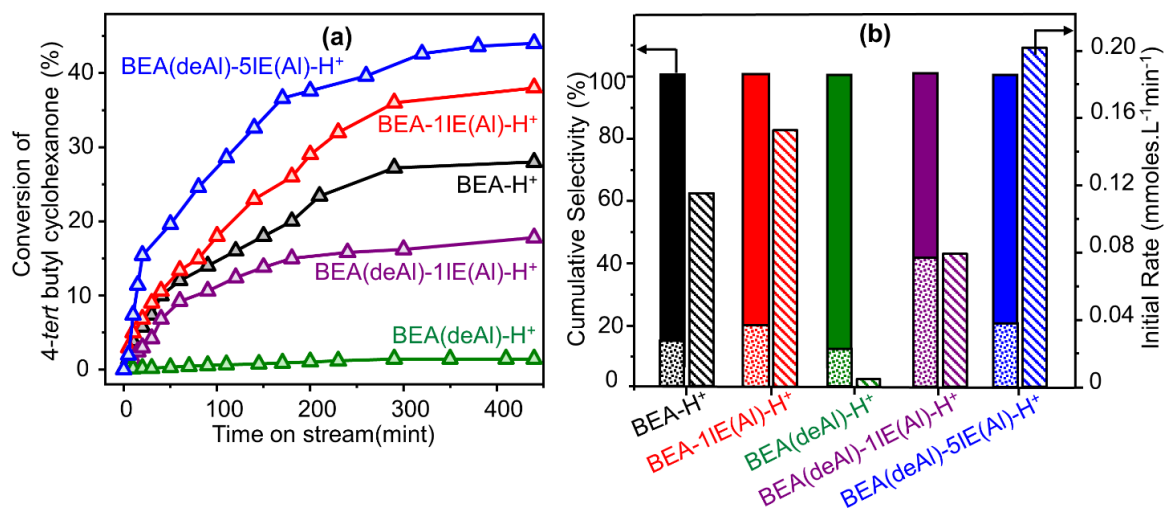


Figure E1. (a) Catalytic conversion (%) of 4-*tert* butyl cyclohexanone as a function of time on stream over 20mg of BEA zeolites. (b) Cumulative selectivity towards *cis* (solid bars) and *trans* (dotted bars) 4-*tert* butylcyclohexanol after 7.4 h and initial rate of reaction (bars with diagonal stripes). The initial rate of reaction is determined as the slope of the linear regression in the time-concentration plot between zero time and 110 minutes of reaction time.

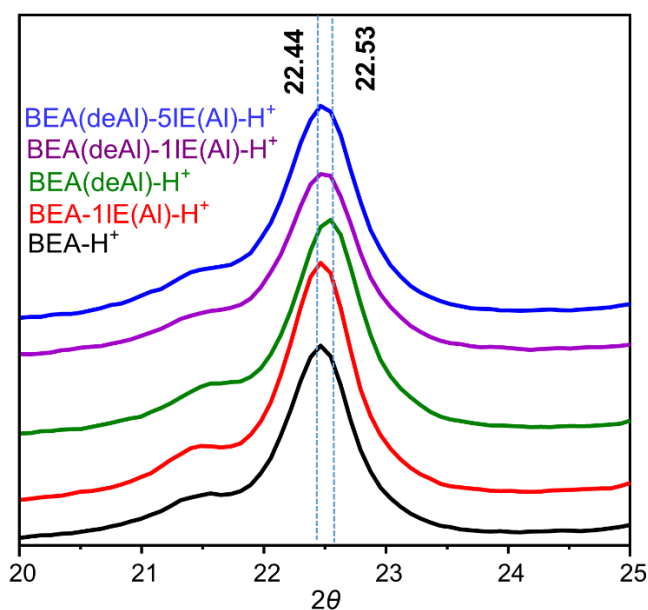


Figure E2. PXRD patterns of a protonic form of BEA zeolites in the  $2\theta$  region of 22–23°.



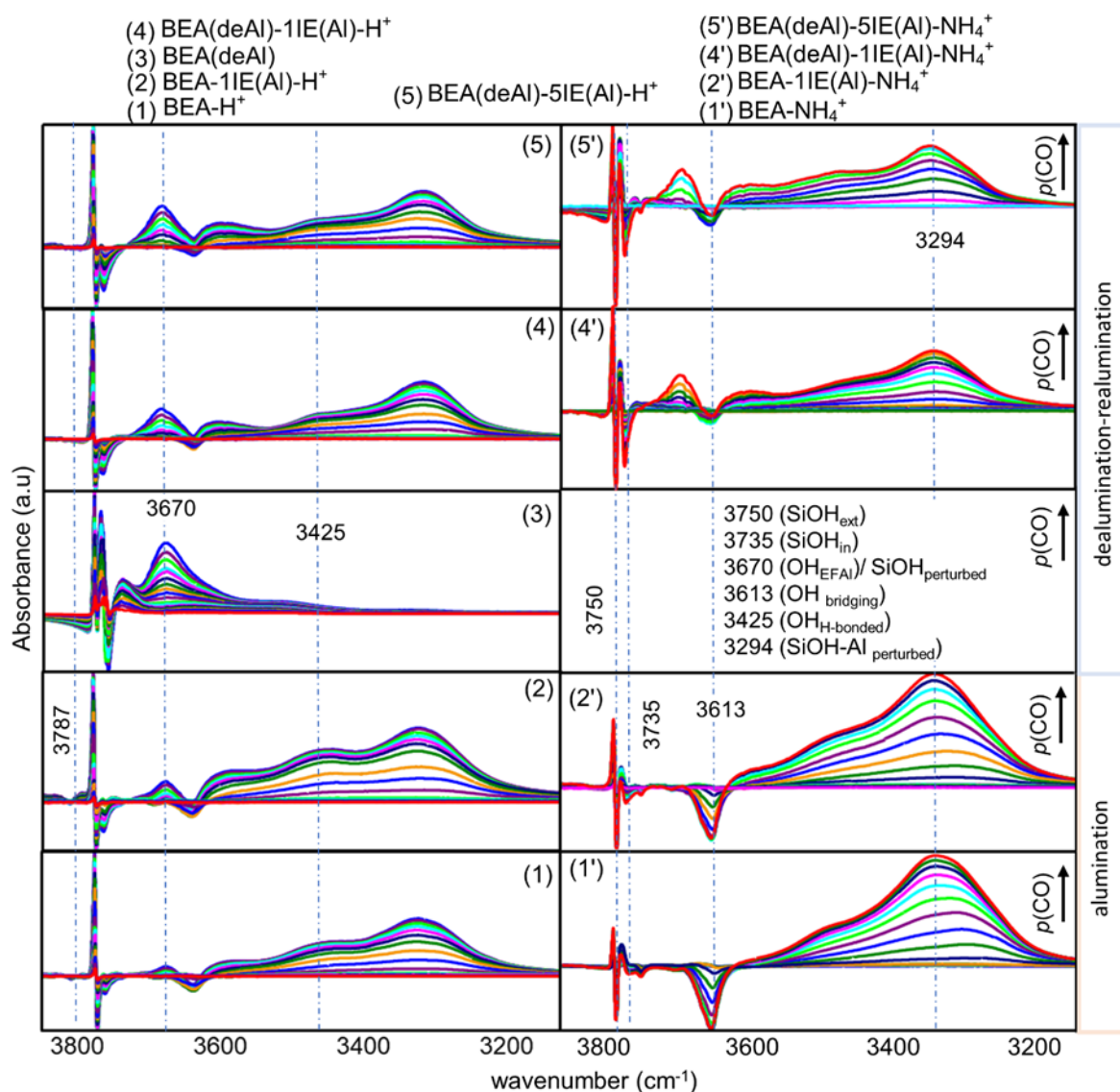


Figure E3. FTIR difference spectra over adsorbed carbon monoxide in the hydroxyl stretching region obtained by subtraction of spectra of cold wafers at 70 K from spectra after CO adsorption at 70K carbon monoxide; The spectra of H<sup>+</sup> form of samples are marked as 1-5, and those of NH<sub>4</sub><sup>+</sup> forms are marked as 1'-5'.

Table E1. The tetrahedral sites (T-sites) in zeolite BEA crystal, with the average crystallographic T-O-T angles in degrees and the corresponding  $^{27}\text{Al}$  isotropic chemical shifts ( $\delta_{\text{iso}}$ ) in ppm.

Type of symmetrical aluminum of BEA framework	T-site Locations	T-O-T angle	$\delta_{\text{iso}} = -0.5(\theta) + 132$
1	T <sub>1</sub> , T <sub>2</sub>	155.3-155.9	54-54.4
2	T <sub>3</sub> , T <sub>4</sub> , T <sub>5</sub> , T <sub>6</sub> , T <sub>7</sub> , T <sub>8</sub> & T <sub>9</sub>	148-152.8	55.6-58

Table E2. Physicochemical characterization of  $\text{NH}_4^+$  form of a parent, aluminated and dealuminated-realuminated BEA zeolite.

Zeolite	<sup>a</sup> Si/Al ratio	<sup>b</sup> S <sub>BET</sub> m <sup>2</sup> g <sup>-1</sup>	<sup>c</sup> V <sub>total</sub> cm <sup>3</sup> g <sup>-1</sup>	<sup>d</sup> V <sub>micro</sub> cm <sup>3</sup> g <sup>-1</sup>
BEA-NH <sub>4</sub> <sup>+</sup>	12.4	460	0.21	0.19
BEA-1IE(Al)-NH <sub>4</sub> <sup>+</sup>	10.3	440	0.22	0.21
BEA(deAl)-1IE(Al)-NH <sub>4</sub> <sup>+</sup>	14.2	480	0.28	0.23
BEA(deAl)-5IE(Al)-NH <sub>4</sub> <sup>+</sup>	9.6	470	0.29	0.23

<sup>a</sup>calculated from ICP, <sup>b</sup>calculated from BET method <sup>c</sup>based on single point adsorption at p/po = 0.97, <sup>d</sup>calculated from t-plot method

Table E3. Aluminum concentration (mmoles g<sup>-1</sup>) obtained from ICP (a) and concentration of aluminum (mmoles g<sup>-1</sup>) in different geometrical coordinations obtained by deconvolution of <sup>27</sup>Al MAS NMR spectra using NMR parameters from <sup>27</sup>Al MQMAS NMR (b). The values marked by \* and \*\* in brackets correspond to an isotropic chemical shift in ppm ( $\delta_{\text{iso}}$ ,  $\pm 0.5$ ) and quadrupolar coupling constant in MHz ( $C_Q$ ,  $\pm 0.3$ ), respectively, for each peak, obtained from deconvolution <sup>27</sup>Al MQMAS NMR spectra using the Czjzek line shape model.

Sample ID	<sup>a</sup> Al content	<sup>b</sup> Al <sub>(IV)a</sub> (54*, 1.7**)	<sup>b</sup> Al <sub>(IV)b</sub> (58.5, 1.9)	<sup>b</sup> Al <sub>(IV)c</sub> (60, 4.5)	<sup>b</sup> Al <sub>(V)</sub> (30, 2.5)	<sup>b</sup> Al <sub>(VD)a</sub> (0.1, 1.1)	<sup>b</sup> Al <sub>(VD)b</sub> (2.7, 2.5)
BEA-H <sup>+</sup>	3.23	1.39	0.56	0.14	0.19	0.56	0.39
BEA-NH <sub>4</sub> <sup>+</sup>	3.21	1.43	1.14	0.37	-	-	0.27
BEA-1IE(Al)-H <sup>+</sup>	3.59	1.44	0.44	0.24	0.34	0.34	0.79
BEA-1IE(Al)-NH <sub>4</sub> <sup>+</sup>	3.57	1.47	0.89	0.53	-	-	0.68
H <sup>+</sup> -BEA(deAl)-H <sup>+</sup>	0.26	0.26	-	-	-	-	-
BEA(deAl)-1IE(Al)-H <sup>+</sup>	1.87	0.68	0.51	0.09	0.08	0.30	0.21
BEA(deAl)-1IE(Al)-NH <sub>4</sub> <sup>+</sup>	1.89	0.69	0.79	0.17	-	-	0.24
BEA(deAl)-5IE(Al)-H <sup>+</sup>	3.38	1.01	0.67	0.22	0.28	0.32	0.88
BEA(deAl)-5IE(Al)-NH <sub>4</sub> <sup>+</sup>	3.34	0.99	0.95	0.54	-	-	0.87

# Appendix F

## Appendix to Chapter 9

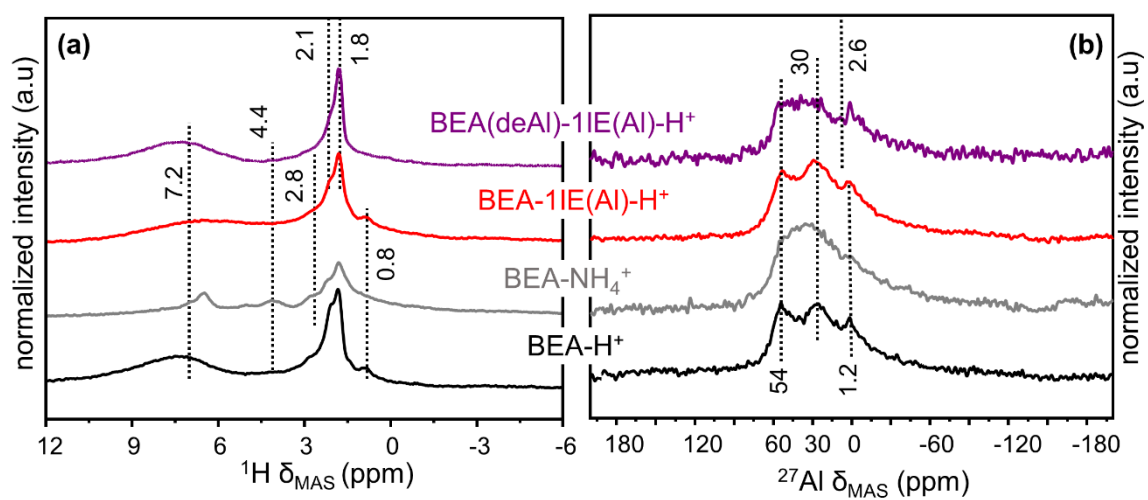


Figure S4. (a) The  $^1\text{H}$  NMR and (b)  $^{27}\text{Al}$  NMR spectra extracted from  $^{27}\text{Al}$ - $^1\text{H}$  HETCOR experiments performed on evacuated BEA samples